Spin dynamics in high-mobility two-dimensional electron systems embedded in GaAs/AlGaAs quantum wells

vorgelegt von

Dipl. Phys. Michael Griesbeck
geboren am 01.10.1982 in Kemnath

im Oktober 2012

Die Arbeit wurde von Prof. Dr. Christian Schüller angeleitet.
Das Promotionsgesuch wurde am 25. Juni 2012 eingereicht.
Das Kolloquium hat am 22. November 2012 stattgefunden.

Contents

Chapter 1

Introduction

Scientific research in many fields facilitated the enormous technical progress in the 20th century. Three of the main milestones of physical research are the development of the theory of relativity [Ein05; Ein16], (relativistic) quantum mechanics [Pla01; Hei25; Sch26; Dir28] and huge advances on the field of solid state electronics, starting with the implementation of the first transistor [Bar48] at Bell Telephone Laboratories. Advances in semiconductor technology like the invention of molecular beam epitaxy (MBE) [Cho71; Cho81] or the modulation doping of heterostructures [Din78] led in the following years to the development of many sophisticated devices like the high electron mobility transistor [Mim80], suitable for operation at highest frequencies in the GHz range. Moreover, semiconductor heterostructures were used for the realization of quantum mechanical model systems, like potential steps, tunnel barriers or potential wells, representing the famous quantum mechanical problem of the "particle in the box". Thus, semiconductor physics evolved to a perfect playground for testing quantum mechanical concepts, like the size quantization in the finite potential well or the Landau quantization in external magnetic fields, leading to the quantum Hall effect [Kli80] in two-dimensional electron systems. Advances in materials science finally gave rise for the development of extremely clean and well-defined two-dimensional electron systems, where the electrons can move ballistically over distances on the order of a few hundred microns.

Besides the detailed investigation of carrier dynamics, the spin properties of electrons, holes and the lattice nuclei attracted wide attention, as well. In contrast to the case of free electrons, where the spin and the orbital degrees of freedom are just weakly coupled, the spin-orbit interaction (SOI) is strongly enhanced in semiconductors [Ras06]. This leads to a couple of effects observable in transport measurements, like beatings in the Shubnikov-de Haas oscillations [Nit97], the weak anti-localization effect [Kog02] or in photocurrent measurements [Gan04]. Furthermore, due to the presence of the SOI the spin orientation of a carrier is not a conserved quantity, in contrast to what one finds for the corresponding charge. This manifests itself in relatively short spin dephasing times, after which a nonequilibrium spin population returns to its equilibrium value. The most relevant spin dephasing mechanism in noncentrosymmetric semiconductors was developed at the A. F. Ioffe Physicotechnical Institute in the former USSR by Dyakonov and coworkers [Dya71b; Dya71a; Dya86]. Later it was pointed out that the symmetry of the spin-orbit fields (SOFs) is crucial for electron spin dephasing in low dimensional electron systems: interference effects of two independent contributions to the SOI in GaAs can lead to anisotropic spin dephasing, which was studied by Averkiev et al. [Ave99; Ave06]. In addition, anisotropic spin dephasing can be found in electron

systems quantized along the [110] crystallographic direction, resulting from the different symmetry of the involved SOFs [Döh04; Mül08; Gri12]. In certain cases, the SOI also leads to coherent dynamics and a precessional motion of a nonequilibrium spin ensemble about the SOF [Bra02; Ley07b; Sti07c; Gri09]. This situation can be especially found in samples, showing a high electron mobility.

A widely used approach for the investigation of spin dynamics is based on the all-optical generation of a nonequilibrium spin polarization, often denoted as optical orientation [Mei84]. In the early years, mainly the analysis of the polarization properties of photoluminescence light after non-resonant excitation gave access to spin dynamics properties of the investigated materials. Since tuneable ultrafast light sources like the Ti:sapphire lasers became available, the time-resolved observation of spin dynamics became possible [Aws85; Bau94], based on the magneto-optic Faraday/Kerr effect [Far46].

The availability of both, high-quality suitable materials (in particular magnetic semiconductors), as well as the relevant measurement techniques, opened the way to a new, interdisciplinary research field: the usage of the spin degree of freedom for the purpose of information processing[1] is the main goal in the research field of spin electronics, or short spintronics [Wol01; Zut04; Wu10]. Essential parts are the generation of spin polarization, its manipulation within the spin lifetime and finally, the readout. Though a variety of solutions exist for each of these three important steps, the basic concept of spintronics can be explained by help of the proposal of the spin field effect transistor (sFET) by Datta and Das [Dat90]. This probably most famous concept[2] of spintronics pushed this
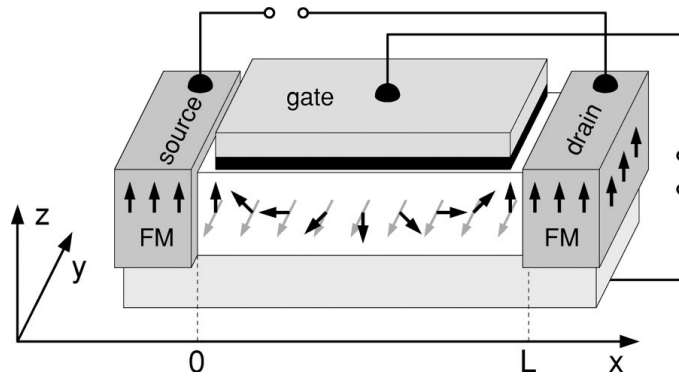
Figure 1.1: *Scheme of the sFET proposed by Datta and Das [Dat90]. The spin polarization is injected from a ferromagnetic source contact into the semiconducting channel. There, the spin is exposed to a spin-orbit field controlled via the applied gate voltage. Depending on the relative orientation of the spin and the magnetization of the ferromagnetic drain contact, the transmission into the contact is either high or low. (taken from [Win04]).*

research field since the year 1990. Fig. 1.1 depicts a scheme of the Datta/Das sFET: a ferromagnetic source contact provides spin polarized electrons which are injected into the semiconducting channel. There, the spin is exposed to a spin-orbit field, which is

---

[1]Related to the research field of spintronics is the field of *quantum* information processing [DiV95; DiV97]. There, in contrast, the main focus is on the search for systems suitable for the realization of quantum bits (qubits), the building blocks of future quantum computers. In contrast to a classical bit, the qubit can represent, in addition to the one and the zero state, *any superposition* of these two states. It was pointed out [DiV95] that quantum computation would be suitable for the treatment of otherwise untractable numerical tasks, as for example the prime factoring of large integers.

[2]A korean group [Koo09] recently demonstrated the sFET action under laboratory conditions. However, some drawbacks like the bad scalability make the Datta-Das sFET unlikely to be used in real devices.

controlled via the applied gate voltage. After *ideally ballistic* electron motion through the channel, the electron is transmitted into or reflected at the ferromagnetic drain contact, depending on the relative spin orientation and the magnetization of the drain contact. A comparable concept for an sFET in the non-ballistic regime was proposed by Schliemann et al. [Sch03b], requiring the presence of a special symmetry of the SOF.

In this work, the focus will be on the dynamics of an optically generated spin ensemble in GaAs-based heterostructures, which are well-suited for studying spin dynamics: the direct band gap allows for an efficient creation of a nonequilibrium electron spin population via optical orientation. Moreover, advances in materials science facilitate the fabrication of well-defined MBE-grown samples, where the band profile can be tailored precisely, resulting in high electron mobilities. In such samples, the time until a nonequilibrium spin ensemble is returned to its equilibrium value (i.e., the spin dephasing time) can be studied in dependence of several parameters. The spin dephasing time will be shown to depend on several parameters like the relative orientation of the spin and the crystallographic axes, the sample temperature, the excitation conditions and some other sample properties. It should be emphasized that in comparison with previously reported similar experiments [Ohn99; Mal00b; Bra02; Ave06; Ley07b; Sti07c; Mül08; Eld11], all the investigated GaAs-based samples have a higher electron mobility. This can be attributed to optimized growth conditions during sample growth and the precise control of the band profile of the heterostructures. The outstanding properties of the investigated state of the art samples make it possible to reveal interesting effects which were previously masked by imperfections of the samples: the extremely high mobility allows for the observation of spin dynamics of ballistic electrons, as well as a novel effect, which can be observed, when the ballistic electrons are forced to move on cyclotron orbits by an external magnetic field. Moreover, the precisely controlled band profile in the investigated samples allows for the study of electron spin dephasing anisotropies.

This work is organized as follows:

In Chap. 2, some theoretical aspects of carrier dynamics in GaAs-based heterostructures are elucidated, being essential for the understanding of the experimental results. In addition, the origin and the consequences of the importance of spin-orbit interaction in the investigated systems is discussed. Finally, a short overview on interactions between the electron spin system and the system of the lattice nuclei is given.

After the presentation of the basic theoretical concepts, the structure of the investigated MBE-grown samples is presented in Chap. 3. The fundamental prerequisites as well as a sophisticated growth scheme for the fabrication of heterostructures showing an ultra-high electron mobility is discussed. Moreover, the relevant steps of sample processing after sample growth are shown, which allow for the fabrication of optically thin samples, as well as semi-transparent metall top gates.

Chap. 4 deals with the applied all-optical measurement techniques, which are used for sample characterization and in particular for the investigation of spin dynamics. Besides a description of the basic measurement principle of the widely used time-resolved Kerr/Faraday rotation technique, the concept of so-called resonant spin amplification (RSA) [Kik98; Kik99] measurements is presented there. The chapter closes with a brief overview on photoluminescence experiments, suitable for the characterization of semiconductor structures.

Some experimental results on spin dynamics in two-dimensional electron systems with an asymmetric band profile are given in Chap. 5. There, the dependences of spin dynamics on some parameters such as the width of the two-dimensional electron system, the sample orientation with respect to the magnetic field direction and the sample temperature is discussed in detail. In addition, experimentally observed dependencies

on the excitation conditions, as well as the influence of an applied gate voltage on spin dynamics are presented.

In Chap. 6, spin dynamics in ultra-high-mobility two-dimensional electron systems embedded in GaAs-based heterostructures having a highly symmetric conduction band profile is elucidated. There, coherent dynamics of an optically generated spin ensemble in the spin-orbit field is shown in a sample grown along the [001] crystallographic direction; the crucial influence of a weak magnetic field oriented perpendicular to the sample plane is discussed, as well. The second part of this chapter deals with the observation of a large spin dephasing anisotropy in a (110)-grown sample: the RSA method is shown to be applicable for the determination of the relevant parameters describing spin dynamics. After the discussion of an a priori unexpected temperature dependence of the observed spin dephasing anisotropy, spin dynamics is demonstrated to be strongly affected by continuously illuminating the sample with short-wavelength laserlight. Moreover, strong evidence is presented for an efficient interaction of the electron spin system and the system of the lattice nuclei, resulting from the extremely long spin dephasing times accessible in the sample under certain conditions.

The work closes with a final summary of the experimental results presented in Chaps. 5 and 6, which is the subject of Chap. 7. There, the most relevant results of this work are put together. The high relevance of the (a)symmetry of the band profile is emphasized, as well as the dependence of spin dynamics on other parameters like the choice of the growth direction.

Chapter 2

Theory

The experimental results presented in chapter 5 and 6 are based on the unique properties of the investigated samples, and the particular symmetries of the spin-orbit fields involved. In the first part of this chapter the main characteristics of confined electrons in a GaAs/AlGaAs quantum well relevant for this work will be discussed. Of particular interest are the mobility μ of the electrons and the corresponding transport scattering time τ_p, as well as the electron-electron scattering time τ_{ee} at a given temperature T. Moreover, also the dynamics in an external magnetic field $\boldsymbol{B}$ will be discussed. The second part of this chapter will focus on the coupling of the spatial and the spin degree of freedom of the confined electrons. The origin and some effects of spin-orbit coupling leading to spin dephasing, coherent spin dynamics and spin dephasing anisotropies will be shown in the formalism of kinetic spin Bloch equations, as far as they are neccessary for understanding the experimental results presented below. The last part of this chapter covers the coupling between the electron spins and the nuclear spins, which is important in the case of very long electron spin dephasing times and high spin polarization of the electron system.

2.1 Special properties of GaAs/AlGaAs heterostructures

In the last decades there has been great progress in the fabrication of very clean electron systems based on the GaAs/AlGaAs system, which allow for the observation of quantum effects in transport measurements. Only a few points of this wide research field are illustrated here, because of their relevance for the experimental results of this work. Basic details concerning the crystal structure and the calculation of the electron band structure can be found in standard solid state and semiconductor physics textbooks (see, e.g. [Ash03; Sze81]). A review on basic parameters of GaAs, AlAs and AlGaAs can be found, e.g., in Refs. [Ada85; Lev99].

2.1.1 Heterostructures and the influence of doping

For the realization of high-mobility electron systems one often uses heterostructures, i.e., samples that consist of different materials grown on top of each other. By choosing materials with different bandgaps, quantum mechanical systems like tunnel barriers, potential steps and quantum wells can be realized.

The GaAs/Al_xGa$_{1-x}$As system crystallizes in the zincblende structure (Fig. 2.1), and is perfectly suited for fabricating various heterostructures from it. One important point
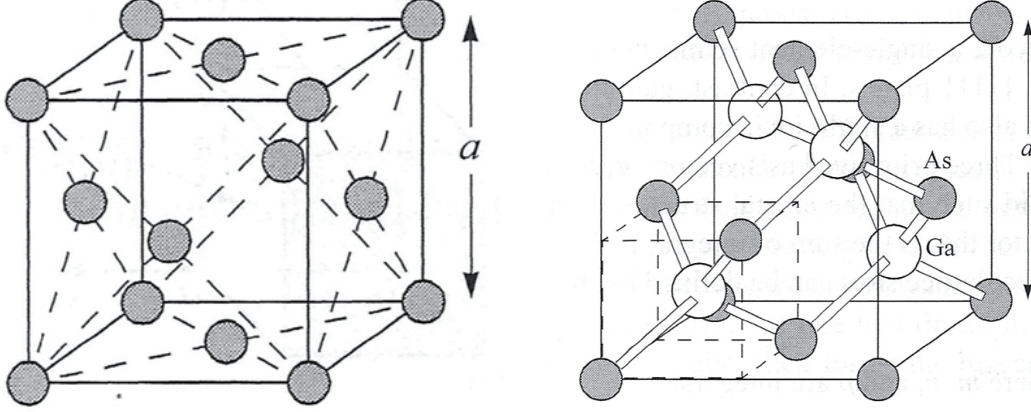
Figure 2.1: *left: unit cell of the face-centered cubic lattice with the cubic lattice constant a. right: cubic unit cell of the zincblende crystal GaAs (taken from [Sze81]).*

is the nearly perfect matching of the lattice constants of the GaAs crystal and the ternary semiconductor compound $Al_xGa_{1-x}As$, where a fraction x of the Ga atoms is replaced by Al atoms. The dependence of the lattice constant a and the band gap energy E_G in $Al_xGa_{1-x}As$ with $0 < x < 0.45$ at room temperature follow the relations [Lev99]

$$a = 5.6533 + 0.0078x \, [\text{Å}] \tag{2.1}$$

and

$$E_{G,x} = 1.424 + 1.247x \, [\text{eV}]. \tag{2.2}$$

For a higher Al content $0.45 < x < 1$ the band gap becomes indirect, with the minimum of the conduction band lying in the X valley. The band gap energy E_G is temperature dependent and can be described by a relation[1] proposed by Varshni [Var67]. At low temperatures the energy difference between the top of the valence band and the bottom of the Γ valley in the conduction band $E_{\Gamma,x}$ is given by [Lev99][2]

$$E_{\Gamma,x} = 1.519 + 1.155x + 0.37x^2 \, [\text{eV}]. \tag{2.3}$$

As depicted in Fig. 2.2, GaAs/AlGaAs interfaces show a type 1 band alignment, caused by the different electron affinities χ in the two materials [And62][3]. Consequently, there exist bound states for both electrons and holes in GaAs/AlGaAs quantum wells[4]. The transverse energy of the conduction as well as the valence band states in an undoped heterostructure can be estimated in the model of a rectangular potential well with infinitely high walls[5] [Lan81] leading to the quantization of the z component of the $\boldsymbol{k}$-vector

$$k_{z,n} = n'\frac{\pi}{d}, \tag{2.4}$$

---

[1] The band gap energy E_g was proposed to follow the relation $E_g(T) = E_g(T = 0) - \tilde{\alpha}T^2/(T + \tilde{\beta})$, where $\tilde{\alpha}$ and $\tilde{\beta} \approx \Theta_D$ are material dependent phenomenological constants. Θ_D is the Debye temperature.

[2] A slightly deviating dependence of $E_{\Gamma,x} = 1.519 \cdot (1-x) + 3.009 \cdot x + x \cdot (1-x) \cdot (0.127 - 1.310x) \, [\text{eV}]$ being cubic in the aluminum content x can be found in Refs. [Asp86; Vur01].

[3] The widely used Anderson rule should be taken more as a qualitative behavior. It was shown that the band edge discontinuity is unequal to $E_c \neq \Delta\chi$ for most heterojunction systems [Bau83].

[4] The existence of bound states for electrons and holes is of particular importance for the so-called optical gating process, for details see Sec. 2.1.3.

[5] Though the barriers in the real sample are of finite height, this is an often-used approximation for the lowest electron level.
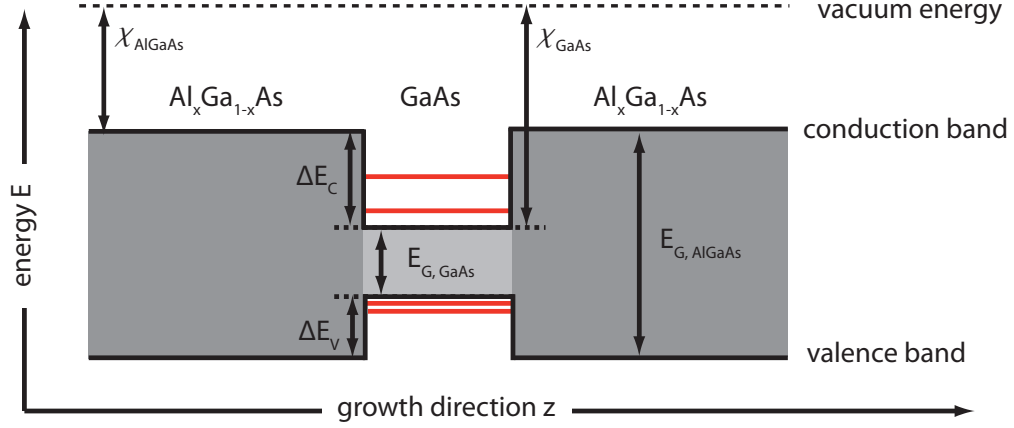
Figure 2.2: *Schematic band edge profile of a GaAs/AlGaAs quantum well with bound states for electrons and holes. The band edge discontinuities ΔE_c and ΔE_v as consequences of the conduction band alignment with respect to the vacuum energy [And62] and the difference in the band gaps of $Al_x Ga_{1-x} As$ and $GaAs$ [Lev99] are shown.*

and quantized energy levels

$$E_n' = \frac{\hbar^2}{2m_{e,h}^*} \left(\frac{n'\pi}{d} \right)^2 + \frac{\hbar^2 k_{||}^2}{2m_{e,h}^*},\tag{2.5}$$

where n' is the transverse subband index, d the quantum well width, $m_{e,h}^*$ the effective mass of the carriers, and $k_{||} = \sqrt{k_x^2 + k_y^2}$ the inplane component of the $\boldsymbol{k}$ vector. The energy subbands are filled with free electrons up to the Fermi energy E_F (at T=0 K).

By modulation doping, where the dopant atoms are separated from the position of the quantum well by a thin undoped spacer layer, high mobilities in two-dimensional electron systems (2DESs) can be achieved [Dru81]. The distance between the ionized doping atoms and the 2DES leads to a drastically reduced scattering at ionized impurities. To achieve even higher mobilities, more sophisticated growth schemes [Uma09] have to be used (details in Sec. 3), including more than one doping layer. In such structures a highly symmetric band edge profile of the quantum well can be achieved. In contrast, a built-in electric field $E_z = -\nabla\Phi$ exists in a single-sided doped (ssd) heterostructure, which is related to a band edge gradient (see Fig. 2.3). Here, Φ is the electrostatic potential. The band edge gradient results in an asymmetric electronic wavefunction,
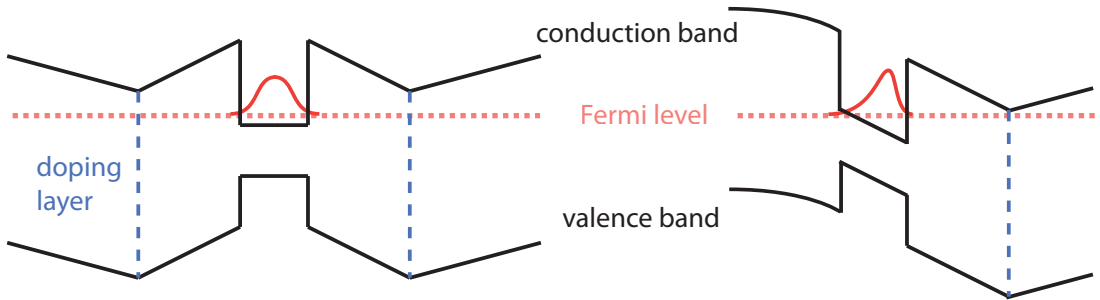
Figure 2.3: *Simplified band profiles of a double-sided doped (left) and a single-sided doped (right) quantum well.*

shifted towards one of the two interfaces. Thus, the wavefunction penetrates deeper into the AlGaAs than in the case of a double-sided doped (dsd) heterostructure. The penetration of the wavefunction into the AlGaAs barrier also influences the electron g factor [Yug07], see also Secs. 2.2.5 and 5.1.3. If the penetration of the electrons' wavefunction into the low-mobility AlGaAs barrier material [Sax81] is reduced by using symmetric dsd heterostructures where the wavefunction is centered in the middle of the quantum well [Uma09], the mobility of a 2DES can be further increased. The higher mobility in such structures results also from a reduction of interface scattering at the GaAs/AlGaAs boundaries.

The different symmetry of dsd and ssd heterostructures is also of great importance for the spin-orbit (SO) field acting on the electron spin, as will be pointed out in Sec. 2.2.2. The dependence of the symmetry properties of the SO field on the relative orientation of the quantum well with respect to the crystallographic axis will be elucidated there, too.

2.1.2 Mobility and electron scattering processes in a 2DES
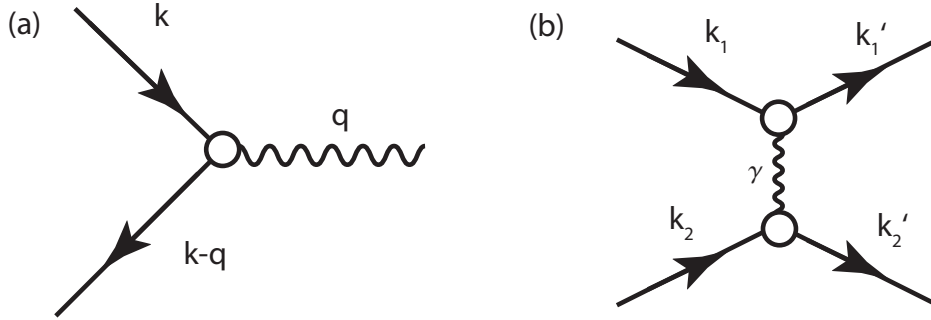
Figure 2.4: *(a) An electron with wave vector $\boldsymbol{k}$ is scattered on lattice vibrations and a phonon is emitted with wave vector $\boldsymbol{q}$. Energy is transferred to the lattice. (b) An electron is scattered by another electron. Energy and momentum of the electron system is conserved.*

In the semiclassical transport model [Ash03], the motion of free electrons in a high-mobility 2DES is a sequence of ballistic classical motion over distances on the order of the mean free path, interrupted by quantum scattering events. The corresponding scattering rate τ_p^{-1} describes the number of momentum scattering events per time unit, and has contributions from various scattering processes [Sze81]. The scattering time τ_p is proportional to the electron mobility

$$\mu = \frac{e\tau_p}{m_e^*}, \tag{2.6}$$

and can be determined from magneto-transport measurements. Panel (a) of Fig. 2.4 shows a diagram of an electron-phonon scattering process, which transfers the energy $E_{Ph} = \hbar\omega(q)$ and the momentum $\boldsymbol{q}$ from the electron system to the lattice.

Advances in technology allow for the design of high-quality 2DESs with electron mobilities higher than $10^7 \, \mathrm{cm^2/Vs}$ [Uma09], and corresponding scattering times on the order of a few hundred ps. In such systems, the transport scattering time τ_p can exceed the time τ_{ee} between collisions of two electrons, which then dominates the microscopic relaxation rate [Ash03]

$$\frac{1}{\tau} = \frac{1}{\tau_p} + \frac{1}{\tau_{ee}} \tag{2.7}$$

of an electron. It was pointed out that the microscopic scattering time τ is the relevant timescale for spin dephasing properties [Gla04b]. Electron-electron (ee) collisions do not change the total quasi-momentum of the electron system, and therefore do not directly affect the electron mobility, but are of major importance for coherent spin dynamics [Ley07a; Gri09]. In panel (b) of Fig. 2.4 the corresponding diagramm of an electron-electron scattering process is shown. The electron-electron scattering rate for strictly two-dimensional carriers, which are located at the Fermi surface, is given at low temperatures by

$$\tau_{ee}^{-1} = \left(\frac{\pi}{4}\right) \ln\left(\frac{E_F}{k_B T_e}\right) \frac{E_F}{\hbar} \left(\frac{k_B T_e}{E_F}\right)^2, \tag{2.8}$$

and depends strongly on the temperature[6] T_e and the Fermi wave vector $\boldsymbol{k}_F$ of the electron system [Jun96]. For quasi-two-dimensional electrons in a quantum well (QW) of a finite width d, an additional factor

$$H(\tilde{q}) = \frac{-32\pi^4 + 32\pi^4 e^{-\tilde{q}d} + 3(\tilde{q}d)^5 + 20(\tilde{q}d)^3\pi^2 + 32\pi^4\tilde{q}d}{[(\tilde{q}d)^2 + 4\pi^2]^2(\tilde{q}d)^2} < 1 \tag{2.9}$$

has to be considered, where $\tilde{q}$ is the wave vector, which is transferred in the scattering event. $H(\tilde{q})$ describes the weakening of the ee interaction in the quasi-two-dimensional electron system in comparison with the strictly two-dimensional case [Gla03; Gla04b]. Thus, the ee scattering time τ_{ee} at the Fermi energy E_F of a 2DES residing in a QW of finite width d can be estimated as

$$\tau_{ee}^{-1} = H^2(k_F) \left(\frac{\pi}{4}\right) \ln\left(\frac{E_F}{k_B T_e}\right) \frac{E_F}{\hbar} \left(\frac{k_B T_e}{E_F}\right)^2, \tag{2.10}$$

assuming that the transferred wave vector $\tilde{q}$ is on the order of the Fermi wave vector, $\tilde{q} = k_F$. Experimentally, the ee scattering rate can be determined by four-wave-mixing measurements [Kim92] or transport measurements [Slu96]. Moreover, novel experiments on coherent spin dynamics, as shown in Sec. 6.1.2 and [Gri09], allow for the determination of a lower limit of the ee scattering time.

As can be seen from Eq. (2.8), the ee scattering time strongly depends on the electron temperature T_e (if defined, see footnote), which can exceed the lattice temperature T_L in low-dimensional systems by far [Rya84]. This is especially the case in high-mobility samples where the electron system is weakly coupled to the lattice, resulting in an electron system which is not in thermal equilibrium with the lattice. Photoluminescence (PL) measurements, being discussed in Sec. 4.3, were found to be a convenient technique for the determination of the electron temperature T_e from the high-energy tail of the PL in early [Rya84; Sha84] and recent high-mobility 2DESs [Bas08]. More effects of the temperature of electrons in low-dimensional systems, which was also shown to influence the electron mobility μ [Sha84], are reviewed in Ref. [Rid91].

2.1.3 Variation of the carrier density by gating

The carrier density n of a modulation-doped 2DES is given by the number of carriers transferred from the doping layer into the quantum well. It depends strongly on the growth process, doping concentrations, the width of the spacer between the doping layer and the quantum well and many other parameters. To study dependencies of any effect

---

[6]The temperature T_e of an electron system with an arbitrary energy distribution function $f(E)$ deviating from a Maxwellian distribution is in general not well-defined (for details see, e.g. [Esi86], and references therein). The typical timescale, on which an ensemble of out-of-equilibrium electrons relaxes back into a Maxwellian distribution, where it has a defined temperature, is on the order of the microscopic scattering time τ.
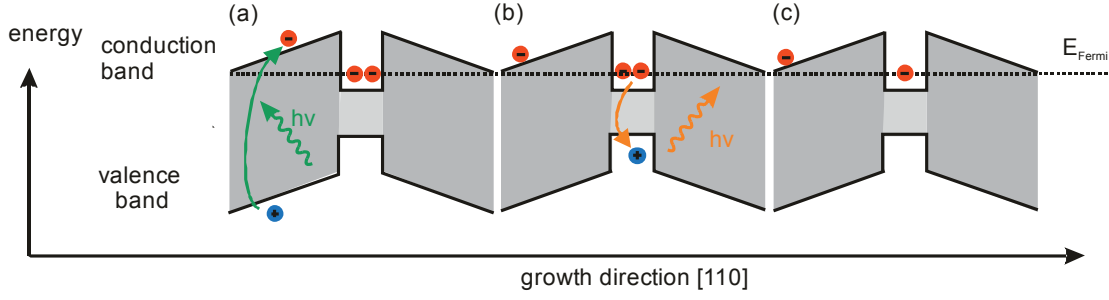
Figure 2.5: *(a) Shining weak above-barrier light on the sample excites electron-hole pairs in the barrier material AlGaAs. (b) Due to the built-in electric fields the electron moves towards the doping layer, whereas the hole falls into the quantum well. There it recombines with a resident electron. (c) After the recombination process one is left with a reduced carrier density in the quantum well and an electron removed to the position of the doping layer.*

on the carrier density, one would need a series of samples with different carrier densities or one has to tune the carrier density of one sample to different values. This can be done by electrostatic or optical gating.

Electrostatic gating of a 2DES with a semi-transparent top gate

The carrier density n of a 2DES can be varied by changing the band edge profile of the heterostructure, due to an applied external electric field. This can be realized by applying the field between the 2DES as one contact and a metallic top gate, which, in the case of this work, needs to be semi-transparent (for details, see Sec. 3.2.1) because of the all-optical measurement techniques employed, presented in Chap. 4.

The carrier density n for a given value U_G of the external applied gate voltage can be calculated by self-consistently solving the Schroedinger and the Poisson equation for the particular sample parameters, including the external applied electrostatic field.

Optical gating of a 2DES with weak above-barrier illumination

In semiconductor heterostructures with built-in electric fields in the barriers surrounding the active region, an all-optical technique can be used as well to change the carrier density n of quantum wells [Cha86] or modulation-doped heterojunctions [Kuk89]. By shining low-intensity above-barrier light on the sample, electron-hole pairs are generated in the AlGaAs barriers around the quantum well, as depicted in panel (a) of Fig. 2.5. If built-in electric fields are present, a separation of the optically excited charges occurs. If the band edge profile has a shape as shown in Fig. 2.5, the electrons are moved by the potential gradient towards the position of the doping layers, whereas the holes fall into the quantum well (panel (b) of Fig. 2.5). There, they recombine within the minority carrier lifetime τ_{PL} with resident electrons. At the end one is left with a reduced carrier density in the quantum well, and an electron removed to the position of the doping layers where it reduces the number N^+ of ionized donors (see panel (c) of Fig. 2.5). Due to thermal or optical activation or due to tunneling processes through the potential barrier [Cha86], a redistribution of charge carriers between the doping layer and the 2DES is possible. Under excitation with a continuous wave (cw) laser a steady state is achieved, where the rate of electrons, which are returning into the quantum well from the doping layer, is equal to the recombination rate of resident electrons and holes injected in the quantum well by charge separation in the barriers. In Refs.

[Cha86; Car99] a simple theoretical model was presented relating the adjusted steady-state carrier density n_s to the intensity I of a cw laser, which is necessary to change the carrier density from the value n_0 without illumination to the steady-state value n_s:

$$I = C(n_0 - n_s) \exp(-D\sqrt{n_s}). \tag{2.11}$$

The parameters C and D in this model are fitting parameters. D can be understood as the effective height of the tunnel barrier, which is realized by the spacer between the doping layer and the quantum well. It should be noted that to the knowledge of the author a model for a dsd quantum well has not been developed yet.

With this gating technique, which is often referred to as "optical gating", also an inversion of the carrier type from p to n in a p-modulation doped structure was reported [Syp07].

2.1.4   High-mobility heterostructures in external magnetic fields

The carrier dynamics in a two-dimensional electron system in an external magnetic field $\boldsymbol{B} = \nabla \times \boldsymbol{A}$ is governed by the Hamilton operator

$$\hat{H} = \frac{1}{2m_e^*}(\hat{p} + e\boldsymbol{A})^2 + V(\hat{z}) \tag{2.12}$$

with the vector potential $\boldsymbol{A}$ and the confinement potential in z direction, $V(z)$. Whereas the density of states splits into discrete Landau levels in a strong magnetic field $\boldsymbol{B} = (0, 0, B_z)$ with $\omega_c \tau_p > 1$, which allows for the observation of the quantum Hall effect [Kli80], the carrier dynamics can be treated semiclassically for weak magnetic fields $\boldsymbol{B}$. The semiclassical equation of motion in the Drude model [Dru00] then reads

$$m_e^* \frac{d\boldsymbol{v}}{dt} = -e\boldsymbol{v} \times \boldsymbol{B} - \frac{m_e^*\boldsymbol{v}}{\tau_p}, \tag{2.13}$$

which describes the cyclotron motion of an electron with reduced mass m_e^* with the cyclotron frequency

$$\omega_c = \frac{eB}{m_e^*}, \tag{2.14}$$

and the momentum relaxation time τ_p. From the cyclotron frequency ω_c at a nonzero magnetic field B, also the effective mass m_e^* of the charge carriers can be determined. The results of the determination of the effective mass m_e^* of an electron in a 30 nm wide GaAs/AlGaAs quantum well, using a novel, all-optical technique will be presented in Sec. 6.1.2.

2.2   Spin of free electrons in semiconductor nanostructures

In this section the most important facts of spin dynamics in a two-dimensional electron system, embedded in a GaAs/AlGaAs quantum well, are presented. The importance of the spin-orbit interaction (SOI), coupling the electron spin and its wave vector $\boldsymbol{k}$ and governing spin dynamics in the investigated samples (see Chap. 3 for details) is discussed in detail in Sec. 2.2.1, whereas in Sec. 2.2.2, the particular situation in low-dimensional systems is treated. After a short overview about how to generate spin polarization in GaAs/AlGaAs nanostructures (Sec. 2.2.3), the dynamics of an optically generated spin ensemble will be discussed in the framework of a kinetic equation approach (Sec. 2.2.4), followed by some words about the electron spin g factor (Sec. 2.2.5). Finally, the direct consequences of the presence and the symmetry of the SOI, leading to (anisotropic) spin dephasing (Secs. 2.2.6 and 2.2.7) and coherent spin precession (details in Sec. 2.2.8), are pointed out.

2.2.1 Spin-orbit interaction

Often, the physics of the solid state is described in terms of wave functions, which are solutions of the Schroedinger equation [Sch26]

$$i\hbar \frac{\partial}{\partial t}\Psi = \hat{H}\Psi \tag{2.15}$$

with the Hamiltonian $\hat{H}$ for the particular problem. A more general approach is the four-component Dirac Equation [Dir28], which includes relativistic effects. This leads after some algebra in first order of $(mc)^{-2}$ [Con35; Ell54] directly to the spin-orbit interaction term

$$\widehat{H_{SO}} = \frac{\hbar}{4m_0^2 c^2}(\nabla V(\boldsymbol{r}) \times \hat{\boldsymbol{p}}) \cdot \hat{\boldsymbol{\sigma}}. \tag{2.16}$$

Here, $V(\boldsymbol{r})$ is the spin-independent lattice potential at the position $\boldsymbol{r}$; $\hat{\boldsymbol{p}} = -i\hbar\nabla$ is the electron momentum operator and $\hat{\boldsymbol{\sigma}}$ is the vector of the Pauli spin matrices. Eq. (2.16) can be rewritten as

$$H_{SO} = \frac{\hbar}{2}\boldsymbol{\Omega}(\boldsymbol{k}) \cdot \hat{\boldsymbol{\sigma}}, \tag{2.17}$$

where $\boldsymbol{\Omega}(\boldsymbol{k})$ can be interpreted as an effective $\boldsymbol{k}$-dependent magnetic field. The explicit form of $\boldsymbol{\Omega}(\boldsymbol{k})$ strongly depends on the potential $V(\boldsymbol{r})$. A particular situation can be found in systems which lack of inversion symmetry, like the zinkblende crystal structure (Fig. 2.1) or asymmetrically grown heterostructures (right panel of Fig. 2.3). Resulting from the bulk inversion asymmetry (BIA) of the zinkblende crystal structure, $\boldsymbol{\Omega}(\boldsymbol{k})$ always has a contribution of the so-called Dresselhaus term [Dre55; Dya71a]

$$\Omega_D\left(k\right) = \begin{pmatrix} \Omega_{100} \\ \Omega_{010} \\ \Omega_{001} \end{pmatrix} = \frac{\gamma}{\hbar} \begin{pmatrix} k_{100}\left(k_{010}^2 - k_{001}^2\right) \\ k_{010}\left(k_{001}^2 - k_{100}^2\right) \\ k_{001}\left(k_{100}^2 - k_{010}^2\right) \end{pmatrix} \tag{2.18}$$

with

$$\gamma = \frac{\alpha_c \hbar^3}{m^*\sqrt{2m^* E_G}}. \tag{2.19}$$

α_c is a dimensionless parameter, which determines the strength of the Dresselhaus SO field. In moderately n-doped bulk GaAs this parameter has a value of $\alpha_c = 0.07$ [Mar83].

Eq. (2.19) directly shows the major importance of SO coupling in semiconductors, in comparison to the vanishing impact on free electrons in vacuum: the relevant energy scale for the SOI in the case of free electrons is the electron-positron gap $2m_0 c^2 \approx$ 1 MeV, whereas in a semiconductor a much smaller band gap $E_G \approx 1$ eV leads to an enhancement of the SO coupling by a factor of about $m_0 c^2 / E_G$ [Ras06].

SO fields resulting from the structure inversion asymmetry (SIA) in asymmetrically grown heterostructures will be presented in detail in Sec. 2.2.2.

2.2.2 Spin-orbit fields in nanostructures

In the case of low-dimensional electron systems, where the wave function is confined in the quantum well, the electron wave vector component parallel to the growth direction z is quantized: $k_{z,n'} = n'\pi/d$. By replacing the quantized values k_z by $\langle k_z \rangle = 0$ and k_z^2 by $\langle k_z^2 \rangle = \pi^2/d^2$ for electrons occupying the lowest subband, one can simplify Eq. (2.18) and ends up with the expressions for $\boldsymbol{\Omega}(\boldsymbol{k})$, which now depend on the particular choice of the quantization axis z. Following [Dya86; Zut04], here the most important cases of electron systems should be discussed, having the quantization axis z along the [001] and
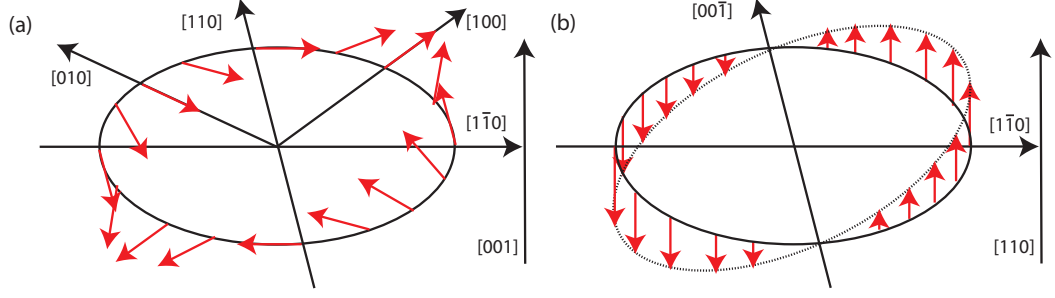
Figure 2.6: *Symmetry of the Dresselhaus SO field for electrons at the Fermi surface in a (001)-grown (a) and a (110)-grown 2DES (b). Whereas for (001)-oriented 2DESs the Dresselhaus SO field has only in-plane components, the SO field is strictly oriented out-of-plane for (110)-grown 2DESs.*

[110] axis, respectively. For systems grown along the [001] direction, i. e., if a coordinate system $x||[100]$, $y||[010]$ and $z||[001]$ is used, the expression for $\mathbf{\Omega}(\mathbf{k})$ reads

$$\Omega_{D,\,2D,\,001} = \frac{\gamma}{\hbar} \begin{pmatrix} k_{100}\left(k_{010}^2 - \langle k_{001}^2 \rangle\right) \\ k_{010}\left(\langle k_{001}^2 \rangle - k_{100}^2\right) \\ 0 \end{pmatrix}. \tag{2.20}$$

Usually, in narrow or not too highly doped 2DESs the expectation value $\langle k_{001}^2 \rangle$ is large compared to the square of the in-plane wave vectors $k_{010,100}^2$. In this case, Eq. (2.20) can be approximated by

$$\Omega_{D,\,2D,\,001} \approx \frac{\beta}{\hbar} \begin{pmatrix} -k_{100} \\ k_{010} \\ 0 \end{pmatrix}, \tag{2.21}$$

where

$$\beta = \gamma \langle k_{001}^2 \rangle = \gamma \left(\frac{\pi}{d}\right)^2 \tag{2.22}$$

is the linear Dresselhaus parameter, depending on the confinement length d. The $\mathbf{\Omega}(\mathbf{k})$ shown in Eq. (2.21), being linear in the electron wave vector $\mathbf{k}$, is the so-called $\mathbf{k}$-linear Dresselhaus field. The symmetry of the linear Dresselhaus field, which has only in-plane components in this case, is shown in the left panel of Fig. 2.6.

If the growth axis is the [110] crystallographic direction, the Dresselhaus field $\mathbf{\Omega}(\mathbf{k})$ has a quite different shape. Typically, in this case one uses the coordinate system $x||[1\bar{1}0]$, $y||[00\bar{1}]$, $z||[110]$ and ends up with the expression [Dya86; Has97]

$$\mathbf{\Omega}_D^{(110)}(\mathbf{k}) = \frac{\gamma}{\hbar} \left[0, 0, k_x(\langle k_z^2 \rangle - (k_x^2 - 2k_y^2))\right] \tag{2.23}$$

for the Dresselhaus field. As can be seen from Eq. (2.23) and the sketch of $\mathbf{\Omega}(\mathbf{k})$ in the right panel of Fig. 2.6, the Dresselhaus field $\mathbf{\Omega}(\mathbf{k})$ points along the growth direction [110] for all allowed wave vectors $\mathbf{k}$ [Has97; Win04].

In low-dimensional structures the effective SO field $\mathbf{\Omega}(\mathbf{k})$ can also have SIA contributions if a built-in electric field E_z is present in the region of the structure where the electrons are confined [Ras60; Byc84b; Byc84a]. The SIA contribution (also called Rashba field) to $\mathbf{\Omega}(\mathbf{k})$ then reads

$$\Omega_{SIA,\,2D} = \frac{2\alpha_R E_z}{\hbar} \begin{pmatrix} k_y \\ -k_x \\ 0 \end{pmatrix} = \frac{\alpha}{\hbar} \begin{pmatrix} k_y \\ -k_x \\ 0 \end{pmatrix} \tag{2.24}$$
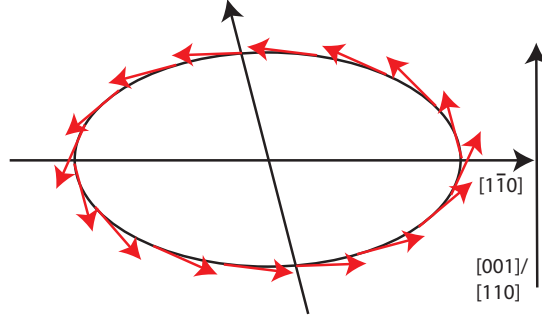
Figure 2.7: *Symmetry of the SIA or Rashba contribution to the SO field $\mathbf{\Omega}(\mathbf{k})$. The Rashba contribution to the SO field is always parallel to the plane of the 2DES.*

and is illustrated in Fig. 2.7. $\alpha = 2\alpha_R E_z$ usually is called Rashba parameter, where $\alpha_R = 5$ eÅ^2 is the so-called Rashba coefficient of GaAs [Win03].

The symmetry of the Rashba field in a 2DES does not depend on the growth axis, which is in stark contrast to what one finds for the Dresselhaus field. So, the Rashba contribution to $\mathbf{\Omega}(\mathbf{k})$ is always parallel to the quantum well plane and perpendicular to the electrons in-plane $\mathbf{k}$-vector.

An experimental separation of the Rashba and the Dresselhaus contribution to the SOF is of high interest, and can be done in different ways, using different experimental approaches: besides photocurrent measurements based on the magnetogyrotropic photogalvanic effect [Gan04; Lec09] and combined electric and optical approaches [Mei07], also all-optical measurements can be used [Ave06; Sti07a; Lar08; Eld11].

The dramatic differences in the symmetries of the Dresselhaus fields in heterostructures grown along the [001] and the [110] direction in connection with the invariant symmetry of the Rashba contribution to the SO field finally lead to interesting effects on spin dynamics, which will be presented in Sec. 2.2.7.

For the sake of completeness, at the end of this section the particular case of (111)-grown QWs should be mentioned: Here, both the Dresselhaus and the Rashba contribution to the SO field have the symmetry as shown in Fig. 2.7. Therefore, by tuning the strength of the Rashba term via an external gate, the Dresselhaus and Rashba SO fields can cancel each other for a certain applied gate voltage. Due to this, a suppression of spin relaxation can be expected [Sun10; Bal11].

2.2.3 Generation of spin polarization / Optical orientation

Nonmagnetic semiconductors have, in equilibrium and in the absence of an external magnetic field, equal numbers of charge carriers with spin-up and spin-down. If an imbalance exists between the occupation of the spin-up and the spin-down states, then one speaks of a polarization of the spin system. The dimensionless degree of spin polarization P is defined as the difference of the carrier densities with spin-up and spin-down related to the total carrier density:

$$P = \frac{n_{e_\uparrow} - n_{e_\downarrow}}{n_{e_\uparrow} + n_{e_\downarrow}}. \tag{2.25}$$

Electrical spin injection

One possibility to generate electron spin polarization in a semiconductor is the electrical injection of spin-polarized carriers from a ferromagnetic material like iron [Cro05b] or the diluted magnetic semiconductor Galliummanganesearsenide (GaMnAs) [VD04] into

the semiconductor. The largest problems to overcome are, in the case of iron, the huge difference in the density of states of the carriers (the so-called conductivity mismatch), and, in the case of GaMnAs, the fact that the ferromagnetism is mediated by holes. To solve these problems, commonly tunnel barriers are used. In the case of GaMnAs one can use a spin-conserving Esaki tunnel diode allowing for the tunneling of spin-polarized electrons from the valence band of GaMnAs into the GaAs conduction band [Cio09]. Also, alloys of Nickel and Iron have been used recently for electrical spin injection by Koo et al. [Koo09], who were the first to implement the Datta-Das spin field effect transistor[7] using an Indiumarsenide (InAs) channel. A promising scheme for electrical spin injection in materials with strong spin-orbit coupling makes use of the extrinsic spin-Hall effect [Kat04], leading to a spatial separation of the spin-up and spin-down carriers. In this case, spin injection can be achieved without using any ferromagnetic material.

Optical spin injection

An easy and widely used method to generate spin polarization in a direct-gap semiconductor is optical spin polarization, where due to the absorption of circularly polarized light a spin-polarized electron-hole pair is generated. This method is based on the conservation of the angular momentum of the absorbed photon, which leads to selection rules for the total angular momentum J of the electron and its z-component m_J:

$$\Delta J = 0, \pm 1 \tag{2.26}$$

and

$$\Delta m_J = \pm 1, \tag{2.27}$$

for light propagation in z direction. In Fig. 2.8 the allowed optical transitions in a low-dimensional GaAs system near the Γ-point fullfilling Eqs. (2.26) and (2.27) are shown, following [Dya84]. The numbers in the circles represent the relative transition
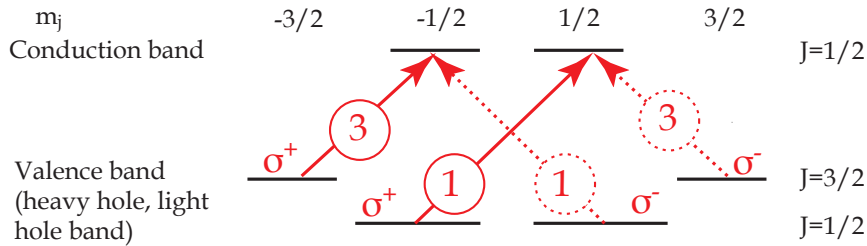
Figure 2.8: *Simplified electronic band structure in a GaAs quantum well in the vicinity of the Γ point, following [Dya84]. The arrows mark the allowed optical transitions under excitation with σ^+ and σ^- light.*

probabilities between the different states. The maximum degree of spin polarization, which can be achieved by the excitation with σ^+ light, can be calculated using Eq. (2.25). In a case where both the heavy and the light hole valence band are involved in optical transitions (e.g., in bulk GaAs, where they are degenerate), both spin states in the conduction band are filled with different probabilities. This results in a spin polarization of the conduction band of

$$P = \frac{3-1}{3+1} = \frac{1}{2}. \tag{2.28}$$

---

[7]However, a non-local detection scheme was used in their measurements.

If the spectral width of the exciting light is much narrower than the heavy/light hole splitting, and the optical transition occurs only between the heavy hole and the conduction band, the electrons in the conduction band can be completely spin polarized.

In doped systems, the resulting degree of spin polarization is always lower than in the undoped case because also the resident, in general unpolarized electrons with sheet density n have to be considered. The spin polarization, which can be generated by a single laser pulse, is then

$$P = \frac{n_{e_{\uparrow}} - n_{e_{\downarrow}}}{n_{e_{\uparrow}} + n_{e_{\downarrow}} + n}. \tag{2.29}$$

The density $n_{\text{opt}} = n_{e_{\uparrow}} + n_{e_{\downarrow}}$ of the optically generated electrons is related to the number N_{Ph} of photons in a single laser pulse. N_{Ph} can be estimated from the mean power $\bar{P}$ of the exciting laser with wavelength λ and repetition frequency f_{rep} by

$$N_{Ph} = \frac{\bar{P}\lambda}{hcf_{\text{rep}}}. \tag{2.30}$$

A fraction $\alpha' N_{Ph}$ of the photons of a single pulse are absorbed in the active region, leading to an optically generated carrier density

$$n_{\text{opt}} \approx 0.86 \frac{\alpha' N_{Ph}}{\pi r^2} \tag{2.31}$$

in the illuminated area. Here, α' is the absorption coefficient, r is the focal radius of the gaussian laser beam and the factor 0.86 is a correction factor, taking into account that only a fraction 0.86 of the laser intensity is inside the gaussian beam radius[8] r. By combining equations (2.29) - (2.31), one can estimate the initial degree of spin polarization present in the sample.

2.2.4   Spin dynamics

The dynamics of the total spin $\boldsymbol{s}$ of an optically generated spin ensemble in an external magnetic field $\boldsymbol{B}$ can be described in terms of the phenomenological semi-classical Bloch-Torrey equations [Blo46; Tor56] or in terms of a kinetic equation approach [Bro04], which has the form

$$\frac{d\boldsymbol{s}}{dt} + \boldsymbol{s} \times \boldsymbol{\Omega}_L + \hat{\Gamma}\boldsymbol{s} = 0, \tag{2.32}$$

where $\hat{\Gamma}$ is the spin relaxation rates tensor and

$$\boldsymbol{\Omega}_L = \frac{\mu_B \hat{\boldsymbol{g}} \cdot \boldsymbol{B}}{\hbar} \tag{2.33}$$

represents the Larmor frequency including the electron g factor tensor $\hat{\boldsymbol{g}}$, see Sec. 2.2.5 for details. Mechanisms leading to spin dephasing, which determine $\hat{\Gamma}$ in detail, will be shown in Sec. 2.2.6. The solution of Eq. (2.32) depends strongly on the properties of the investigated systems. In the following and in the Secs. 2.2.7 and 2.2.8 some particular cases will be discussed, which are important for the understanding of the experimental data presented in Secs. 5 and 6.

---

[8]The gaussian beam radius r is commonly defined as the radius at which the intensity of the laser beam drops to $1/e^2$ of the maximal value.

Standard case: Isotropic spin dephasing and spin precession in an external magnetic field $\boldsymbol{B} = (B_x, 0, 0)$

In the case of isotropic spin dephasing times (SDTs) $T_{xx} = T_{yy} = T_{zz} = T_2$ and spin precession in an applied external magnetic field $\boldsymbol{B} = (B_x, 0, 0)$ aligned parallel to the sample plane, the kinetic equations for the components s_x, s_y and s_z of the total spin $\boldsymbol{s}$ read

$$\frac{\partial s_x}{\partial t} + \frac{s_x}{T_2} = 0, \quad \frac{\partial s_y}{\partial t} + \Omega_L s_z + \frac{s_y}{T_2} = 0, \quad \frac{\partial s_z}{\partial t} - \Omega_L s_y + \frac{s_z}{T_2} = 0, \tag{2.34}$$

with the scalar Larmor frequency $\Omega_L = g\mu_B B_x/\hbar$. The solution of the first expression in Eq. (2.34) can be easily determined and one gets

$$s_x(t) = s_{0,x} \exp(-t/T_2), \tag{2.35}$$

with the initial value $s_{0,x}$. Under the conditions of optical spin injection under normal incidence the in-plane spin component $s_{0,x} = 0$, therefore, one can focus on the behaviour of s_y and s_z. For sufficiently high values of B_x one gets the oscillatory behavior of

$$s_y(t) = s_0 \exp(-t/T_2)\sin(\Omega t) \quad \text{and} \quad s_z(t) = s_0 \exp(-t/T_2)\cos(\Omega t), \tag{2.36}$$

where it is assumed that $s_z(t = 0) = s_0$ and $s_y(t = 0) = 0$.

2.2.5 The electron g factor

The spin $\boldsymbol{S}$ of a s-type conduction band electron is coupled with its magnetic moment $\boldsymbol{\mu}_s$ by the electron spin g factor[9] as

$$\boldsymbol{\mu}_s = \frac{g\mu_B}{\hbar}\boldsymbol{S}, \tag{2.37}$$

where μ_B is the Bohr magneton and $\hbar$ the reduced Planck constant. The electron g factor, also called Landé factor, of quasi-free electrons inside a semiconductor deviates from the value $g_0 = 2.00231930436170(76)$ [Odo06] of free electrons in vaccuum due to influences of the SO interaction [Ell54]. This can lead to large negative values of the g factor with $|g| \approx 50$ in small-bandgap materials with strong SO coupling like Indiumantimonide (InSb) [Rot59; Lit08]. For GaAs the SO interaction leads to a negative electron g factor of about $g = -0.44$ for bulk GaAs at $T = 4\,\mathrm{K}$. This value depends on the sample temperature as well as on the doping concentration [Oes95; Oes96].

In electron systems with lower dimensionality, the electron g factor shows a dependence on the confinement energy, what was demonstrated for undoped [Yug07] as well as asymmetrically doped 2DESs [Lec11] embedded in GaAs/AlGaAs heterostructures. Additionally, in 2DESs with reduced point group symmetry[10] C_{2v}, the g factor is no longer isotropic, but has to be treated in terms of a $\hat{\boldsymbol{g}}$ factor tensor. The C_{2v} point group symmetry can be found in asymmetric (001)-grown heterostructures or in symmetric heterostructures grown along the [110] crystallographic direction, leading to non-zero off-diagonal elements $g_{xy} = g_{yx}$ of the $\hat{\boldsymbol{g}}$ factor tensor [Kal93; Eld11; Hüb11].

Besides electron spin resonance (ESR) experiments [Ste83; Nef11], different all-optical experimental techniques, such as spin-flip Raman scattering [Sap92], optical orientation [Sne91], optically detected magnetic resonance (ODMR) [Kes90] or spin quantum beat spectroscopy in emission [Heb94], absorption [BA91] and Kerr/Faraday rotation [Bau94], were used in the past for the determination of the elements of the electron

---

[9]g in the context of electrons is usually simply called the electron g factor.

[10]The symmetry point group C_{2v} has only 4 elements: The identity $\mathcal{I}$, two mirror planes σ_v/σ_v' and a twofold axial symmetry, the C_2 axis [Lan81]. A prominent molecule showing C_{2v} symmetry is the water molecule H_2O.

$\hat{\boldsymbol{g}}$ factor tensor. In this work, for this purpose the time-resolved Kerr rotation, as well as the resonant spin amplification technique, were used, which will be discussed in detail in Chap. 4.

2.2.6   Spin dephasing mechanisms

For the spins of conduction band electrons in a semiconductor nanostructure, there exist a couple of spin dephasing mechanisms, which bring an artificially generated spin polarization back to the equilibrium value. In the following, the most important mechanisms for electron spin dephasing in semiconductors will be discussed.

The Elliot-Yafet mechanism

As it was shown by Elliot [Ell54] and Yafet [Yaf63], the electron Bloch states are not eigenstates of the spin operator $\hat{\boldsymbol{S}} = \frac{\hbar}{2}\hat{\boldsymbol{\sigma}}$, due to the SO interaction

$$\widehat{H_{SO}} = \frac{\hbar}{4m^2c^2}(\nabla V(r) \times \hat{\boldsymbol{p}}) \cdot \hat{\boldsymbol{\sigma}}. \tag{2.38}$$

Here, $V(r)$ is the spin-independent lattice potential, $\hat{\boldsymbol{p}} = -i\hbar\nabla$ the electron momentum operator and $\hat{\boldsymbol{\sigma}}$ the vector of the Pauli spin matrices. Consequently, the electron states are superpositions of the spin-up and spin-down states $|\uparrow\rangle$ and $|\downarrow\rangle$. An electron Bloch state having mainly spin-up character thus can be written as

$$\psi("\uparrow", \boldsymbol{k}, \boldsymbol{r}) = [a_{\boldsymbol{k}}|\uparrow\rangle + b_{\boldsymbol{k}}|\downarrow\rangle] e^{i\boldsymbol{k}\cdot\boldsymbol{r}}, \tag{2.39}$$

where $a_{\boldsymbol{k}}$ and $b_{\boldsymbol{k}}$ are functions with the periodicity of the lattice, while for $a_{\boldsymbol{k}}$ and $b_{\boldsymbol{k}}$ the relation $|a_{\boldsymbol{k}}| \gg |b_{\boldsymbol{k}}|$ holds. The absolute value of b is determined by the ratio $\Delta E_{SO}/\Delta E_G$ of the spin-orbit energy ΔE_{SO} and the band gap energy E_G. Due to the superposition of the spin-up and the spin-down states, the dominant spin component of the electron can change at a scattering event with a finite probability on the order of b^2. The particular scattering mechanism is not relevant in this case; even spin-conserving scattering processes like electron-phonon scattering or scattering by nonmagnetic impurities can lead to a change of the spin state and thus to spin dephasing. The spin dephasing time T_1 of the Elliot-Yafet (EY) mechanism is, therefore, proportional to the microscopic scattering time τ (see Sec. 2.1.2):

$$T_1 \propto \tau. \tag{2.40}$$

Due to the dependence on the band gap energy E_G, the EY mechanism dominates spin dephasing in narrow-gap semiconductors and especially in metals, whereas it is of minor importance in most GaAs-based semiconductor systems.

The Dyakonov-Perel' mechanism

The very important spin dephasing mechanism in GaAs-based electron systems is the Dyakonov-Perel' (DP) mechanism [Dya71b; Dya71a]. In contrast to the EY mechanism, where the spin dephasing results from a small admixture of the opposite spin state and a spin flip *during* the scattering processes, the DP mechanism appears in all systems without an inversion center, and spin dephasing takes place *between* the scattering events. The lack of inversion symmetry can be due to a particular crystal structure (e.g., the zinkblende crystal structure, see Fig. 2.1), an asymmetric growth profile of a heterostructure (see right panel of Fig. 2.3), applied strain [Cro05a] or the so-called interface inversion asymmetry [Rös02].

In a system which lacks inversion symmetry, a spin splitting $\Delta E_{SO}(\boldsymbol{k}) = E_{\uparrow}(\boldsymbol{k}) - E_{\downarrow}(\boldsymbol{k})$ occurs between the spin-up and the spin-down states for a certain $\boldsymbol{k}$ vector, while the Kramers relation $E_{\uparrow}(\boldsymbol{k}) = E_{\downarrow}(-\boldsymbol{k})$ still holds. The spin splitting $\Delta E_{SO}(\boldsymbol{k})$ can be interpreted in terms of a $\boldsymbol{k}$ dependent effective magnetic field acting on the electrons' spin. This can also be seen from the SO term in the Hamiltonian in Eq. (2.16), which can be rewritten in the form

$$\widehat{H_{SO}} = \frac{\hbar}{2}\hat{\boldsymbol{\sigma}} \cdot \boldsymbol{\Omega}(\boldsymbol{k}), \tag{2.41}$$

where $\hat{\boldsymbol{\sigma}}$ is the vector of the Pauli spin matrices and $\boldsymbol{\Omega}(\boldsymbol{k})$ is the effective SO field, which leads to the spin splitting $\Delta E_{SO}(\boldsymbol{k}) = 2\hbar|\boldsymbol{\Omega}(\boldsymbol{k})|$. The explicit form of $\boldsymbol{\Omega}(\boldsymbol{k})$ depends strongly on the particular electron system and was shown in detail in Secs. 2.2.1 and 2.2.2.
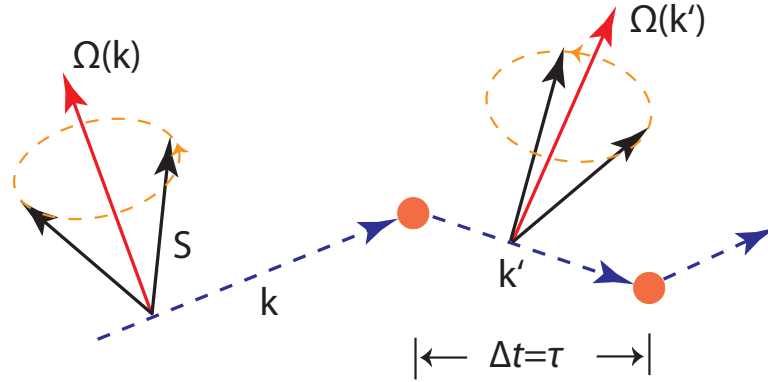

Figure 2.9: *The spin of an electron precesses about the SO field $\boldsymbol{\Omega}(\boldsymbol{k})$ while the electron moves through the crystal with a wave vector $\boldsymbol{k}$. After a scattering event the wave vector $\boldsymbol{k}'$ as well as the SO field $\boldsymbol{\Omega}(\boldsymbol{k}')$ are different. Randomization about many scattering processes leads to dephasing of a spin ensemble.*

Due to the presence of the SO field $\boldsymbol{\Omega}(\boldsymbol{k})$, the electron spin precesses about $\boldsymbol{\Omega}(\boldsymbol{k})$ when the electron moves through the crystal with a wave vector $\boldsymbol{k}$. After a time interval Δt, being on the order of the microscopic scattering time τ, the electron will be scattered, resulting in a new electron wave vector $\boldsymbol{k}'$ and a new spin precession axis $\boldsymbol{\Omega}(\boldsymbol{k}')$, about which the electron spin precesses until the next scattering event. This situation is shown in Fig. 2.9. As a consequence of many subsequent random scattering events, an ensemble of electron spins finally dephases completely.

There are two interesting limiting cases of the DP mechanism, classified by the value of the product $\boldsymbol{\Omega}(\boldsymbol{k})\tau$, which is the number of revolutions the electron spin precesses before being scattered. In the case of $\boldsymbol{\Omega}(\boldsymbol{k})\tau < 1$, which is denoted as the motional narrowing regime, the spin can precess only about a small angle before being scattered. The spin dephasing time T_2 can then be estimated using a random walk modell [Dya71a; Sli78]. The electron spin precesses between two scattering events about the small angle

$$\phi = \Omega(\boldsymbol{k}_F)\tau. \tag{2.42}$$

The expectation value of the rotation angle after $N = \Delta t/\tau$ random walk steps is given by

$$\langle(\Delta\phi)^2\rangle = (\tau\Omega(\boldsymbol{k}_F))^2 N = \Omega^2(\boldsymbol{k}_F)\tau\Delta t. \tag{2.43}$$

Using the definition of the spin dephasing time $\langle(\Delta\phi)^2\rangle \approx 1$ for $\Delta t = T_2$ and the number $N = \Delta t/\tau$ of random walk steps performed per time unit Δt, one gets the relation

$$\frac{1}{T_2} = \Omega^2(\boldsymbol{k}_F)\tau \tag{2.44}$$

between the microscopic scattering time τ, the square of the SO field $\Omega^2(\boldsymbol{k}_F)$ and the spin dephasing rate $1/T_2$. A qualitative picture of Eq. (2.44) is that the spin cannot follow the rapidly changing SO fields and the rapidly changing precession axis caused by the frequent scattering processes, and thereby gets stabilized.

The second limiting case of the DP mechanism is the clean limit with $\boldsymbol{\Omega}(\boldsymbol{k})\tau > 1$, in which the electron spin can precess more than a full revolution before being scattered. This regime, which is often called weak scattering regime, can be found in high-mobility samples at low temperatures [Bra02; Ley07b; Sti07c; Gri09]. In this regime one can observe coherent oscillations of the spin ensemble, which are damped out as a consequence of scattering events on the timescale of the microscopic scattering time τ. Thus, the spin dephasing time T_2 in this case is proportional to the microscopic scattering time τ:

$$T_2 \propto \tau. \tag{2.45}$$

In Sec. 6.1 some experimental results, where spin dynamics in the weak scattering limit of the DP mechanism could be observed, will be shown.

The Bir-Aronov-Pikus (BAP) mechanism

In p-doped semiconductor systems, or in the presence of optically generated holes, the exchange interaction between electrons and holes opens an additional dephasing channel for the electron spin. In scattering processes between electrons and holes an existing electron spin polarization can be transferred to the hole system where it is rapidly lost, due to the in general short hole spin dephasing time [Dam91; Hil02]. In the case of crystals with cubic symmetry, the underlying contact-type interaction between electrons and holes involving spin flips can be written in the form

$$\widehat{H_{\mathrm{BAP}}} = A\hat{\boldsymbol{S}} \cdot \hat{\boldsymbol{J}}\delta(\hat{\boldsymbol{r}}), \tag{2.46}$$

as was shown by Bir, Aronov and Pikus [Bir75]. Here, A is a constant proportional to the exchange integral between conduction and valence states [Zut04], $\hat{\boldsymbol{S}}$ and $\hat{\boldsymbol{J}}$ are the operators of the electron spin and the total angular momentum of the hole, respectively, and $\hat{\boldsymbol{r}}$ is the distance operator between the electron and hole. The dephasing rate $1/\tau_{\mathrm{BAP}}$ of the electron spins resulting from the exchange with nondegenerate holes is proportional to the hole concentration p [Bir75]:

$$\frac{1}{\tau_{\mathrm{BAP}}} \propto p. \tag{2.47}$$

All the measurements presented in this work were done on n-doped samples, so the BAP mechanism can affect electron spin dephasing only due to optically created holes. All-optical measurement techniques, based on the optical orientation of carriers and exclusively used in this work (see also Chap. 4) lead to the creation of a nonequilibrium hole concentration, decaying with the minority carrier lifetime τ_{PL}. In the absence of other dephasing processes, the optically generated hole density was reported to be the limiting spin dephasing mechanism in n-doped two-dimensional electron systems at low temperatures [Döh04; Mül08; Völ11]. A different situation with an optically excited nonequilibrium hole concentration can be found under the conditions of optical gating (see Sec. 2.1.3). Some results of measurements performed under this conditions are shown in Sec. 6.2.3, which most likely can be attributed to the BAP mechanism. There, for a rough estimation of the dephasing rate Γ_{BAP} of the BAP mechanism the expression [Pik84]

$$\Gamma_{BAP} = \frac{1}{\tau_{\mathrm{BAP}}} = \frac{2}{\tau_0}pa_B^3\frac{v_k}{v_B} \tag{2.48}$$

will be used. Here, v_k is the Fermi velocity of the electrons, $a_B \approx 114$ Å is the effective exciton Bohr radius of GaAs, $\tau_0 \approx 1 \times 10^{-8}$ s is an exchange splitting parameter and $v_B = \hbar/m^* a_B \approx 1.7 \times 10^7$ cm/s [Aro83].

Spin dephasing via the hyperfine interaction

Similar to the contact-type interaction of electrons and holes in the BAP mechanism, there is also a contact-type interaction of the electron spins with the nuclear spin system, coupling the spin of the electrons and the surrounding nuclear spin bath [Fer30; Abr61]. This interaction leads to dynamical nuclear polarization [Lam68] (discussed in more detail in Sec. 2.3) and to electron spin dephasing caused by spatial and temporal fluctuations of the hyperfine field acting on the electron spins [Dya73; Dya74]. The fluctuations of the hyperfine field translate into fluctuations of the Larmor frequency and the precession axis of different subsets of an electron spin ensemble, leading to a dephasing of the spin ensemble. In systems where the electron wave function has an overlap with a huge number of nuclei, like in the case of free electrons, the fluctuations of the hyperfine field are averaged out efficiently. Therefore, spin dephasing due to the hyperfine mechanism is expected predominantly in the case of localized electrons, when the single electron experiences just a small number of nuclei. This situation can be found particularly for electrons confined in quantum dot systems [Kha03; Pet05], where, in addition, spin dephasing via the SO interaction is slow [Kha01]. Hence, the hyperfine interaction can limit spin dephasing in such systems.

An efficient way to suppress the hyperfine mechanism is to apply a finite magnetic field [Coi04]. Flip-flop processes between the electron and nuclear spin, which contribute to electron spin dephasing, are then strongly suppressed because of the large Zeeman energy mismatch.

A system also containing highly localized carriers can also be found in the case of a strongly depleted two-dimensional electron gas, which is tuned near to or into the excitonic regime. This case may be experimentally achieved under certain conditions listed in this work. Experimental findings, which could be related to the hyperfine interaction, will be shown in Sec. 6.2.3.

2.2.7 Anisotropic spin dephasing

In Sec. 2.2.4 the solution of the kinetic equation (2.32) was presented for isotropic electron spin dephasing, as it can be found, for example, in unstrained bulk GaAs. If one considers systems with lower symmetry, many situations with strongly anisotropic spin dephasing can be found, in which T_{xx}, T_{yy}, and T_{zz} are no longer equal. This anisotropy indicates a suppression of the DP mechanism for a certain spin orientation. Two different cases of anisotropic spin dephasing are investigated in this work:

- One case is to be found in (001)-grown systems, where the Dresselhaus and the Rashba contributions to the SO field are both inplane and can interfere with each another. Due to the different symmetry of the two contributions, a large inplane spin dephasing anisotropy (SDA) was predicted [Ave99] and observed [Ave06; Sti07b].

- A second case for strongly anisotropic spin dephasing is noticed in (110)-grown systems with a highly symmetric band edge profile. Here, the Dresselhaus contribution to the SO field is oriented perpendicular to the sample plane, whereas the remaining, vanishingly small Rashba field has only inplane components. In such systems significantly different spin dephasing times parallel to the growth direction and parallel to the sample plane can be expected.

Anisotropic spin dephasing in asymmetric, (001)-grown 2DESs

As pointed out in Sec. 2.2.2, in (001)-grown heterostructures the Dresselhaus and the Rashba contribution to the SO field $\boldsymbol{\Omega}(\boldsymbol{k})$ have different symmetries. If they are equal in strength[11], i. e., if $\alpha = \pm\beta$, the total SO field resulting from the interference of the Dresselhaus and the Rashba contribution points along the $[1(\pm1)0]$ direction for all allowed values of the $\boldsymbol{k}$ vector (see Fig. 2.10). In the following, the discussion will be restricted to $\alpha \approx +\beta$. The case $\alpha \approx -\beta$ could be treated analogously showing the same effects, but resulting in a preferential direction of the SO fields parallel to the $[1\bar{1}0]$ crystallographic axis. With increasing deviation of the ratio α/β from 1, the strict orientation of the SO field parallel to the $[110]$ direction is more and more lost. However, for not too large deviations from $\alpha/\beta = 1$, the preferential direction of the SO field still remains parallel to the $[110]$ direction, as can be seen in the right panel of Fig. 2.10, which depicts the situation of $\alpha/\beta = 0.67$. For large deviations from $\alpha/\beta = 1$, i. e., if the strengths of the Rashba and the Dresselhaus field are strongly different, the total SO field has the symmetry of the larger contribution, its amplitude is proportional to $|k|$, and the $[110]$-direction is no longer a preferential direction.
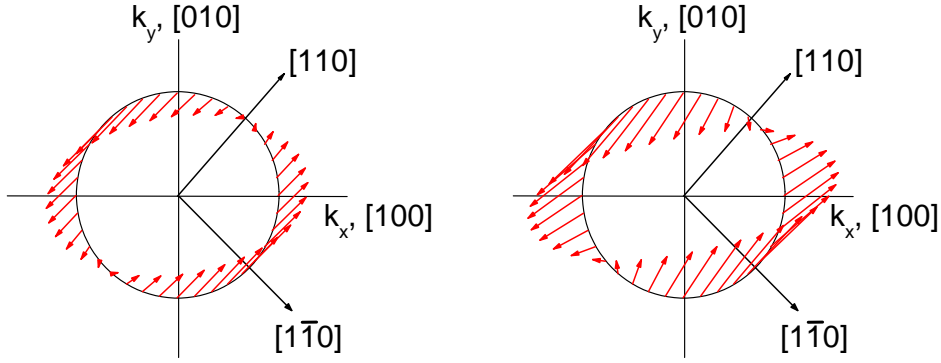
Figure 2.10: *Symmetry of the total SO field for $\alpha/\beta = 1$ (left panel) and $\alpha/\beta = 0.67$ (right panel).*

A direct consequence of the anisotropic SO field is a strong spin dephasing anisotropy (SDA) for spins oriented along different in-plane crystallographic directions. In the ideal case $\alpha/\beta = 1$, spins oriented along the $[110]$ direction are parallel to the total SO field and are therefore protected from dephasing via the DP mechanism; a long spin dephasing time $T_{[110]}$ for spins oriented along the $[110]$ direction can be expected. In contrast, the DP mechanism is active for spins oriented along any other direction, leading to $T_{[1\bar{1}0]} < T_{[110]}$. For values of α/β deviating slightly from 1, spins oriented along the $[110]$ direction still experience less dephasing than spins oriented along other directions.

The appearance of an in-plane SDA in turn allows the determination of the relative

---

[11]This is also the condition, for which the persistent spin helix (PSH) state was predicted [Ber06] and observed [Kor09], where the cubic Dresselhaus terms are responsible for spin dephasing. Based on the PSH state ($\alpha = \beta$) and the inverted PSH state ($\alpha = -\beta$), very recently, also a spin complementary field effect transistor was proposed [Kun12].

strength

$$\left| \frac{\beta}{\alpha} \right| = \frac{\sqrt{T_{[110]}} + \sqrt{T_{[1\bar{1}0]}}}{\sqrt{T_{[110]}} - \sqrt{T_{[1\bar{1}0]}}} \tag{2.49}$$

of the Rashba and the Dresselhaus contribution to the SO field, as it was shown in Refs. [Ave99; Ave06]. There, it was also emphasized, that the right hand side of Eq. (2.49) yields either the ratio β/α or its reciprocal value α/β. In the case of this work, most likely β/α is observed, as will be pointed out in Sec. 5.3.

In the considered case of anisotropic spin dephasing in an (001)-grown sample with interfering Rashba and Dresselhaus contributions to the SO field, the components of the kinetic equation (cf. Eq. (2.32)) for s read

$$\frac{\partial s_x}{\partial t} + \frac{s_x}{T_{xx}} = 0, \quad \frac{\partial s_y}{\partial t} + \Omega_L s_z + \frac{s_y}{T_{yy}} = 0, \quad \frac{\partial s_z}{\partial t} - \Omega_L s_y + \frac{s_z}{T_{zz}} = 0. \tag{2.50}$$

Here, the coordinate system $x||[110]$, $y||[1\bar{1}0]$ and $z||[001]$ is used, and the magnetic field $B = (B, 0, 0)$ is assumed to point along the x-direction. With regard to Glazov and Ivchenko [Gla08][12], the solution of Eq. (2.50) can be written as

$$s_z(t) = s_0 e^{-t/\overline{T}} \left[\cos \tilde{\Omega} t - \left(\frac{1}{T_{zz}} - \frac{1}{T_{yy}} \right) \frac{\sin \tilde{\Omega} t}{2\tilde{\Omega}} \right], \tag{2.51}$$

where

$$\frac{1}{\overline{T}} = \frac{1}{2} \left(\frac{1}{T_{zz}} + \frac{1}{T_{yy}} \right) \quad \text{and} \quad \tilde{\Omega} = \sqrt{\Omega_L^2 - \frac{1}{4} \left(\frac{1}{T_{zz}} - \frac{1}{T_{yy}} \right)^2}. \tag{2.52}$$

If $\tilde{\Omega}$ is real, i.e., if the anisotropy between T_{yy} and T_{zz} is not too large and the magnetic field B is not too small, spin precession with a modified precession frequency $\tilde{\Omega}$ can be observed. To experimentally access T_{xx} instead of T_{yy}, the magnetic field B must be applied along the y-direction.

Experimental results on the in-plane spin dephasing anisotropy and its temperature dependence for a set of samples will be presented in Chap. 5.

Anisotropic spin dephasing in highly symmetric, (110)-grown 2DESs

As it was pointed out in Sec. 2.2.2 and discussed in [Gri11], the symmetry of the Dresselhaus field in a 2DES depends strongly on the quantization axis. In the case of a (110)-grown heterostructure, the Dresselhaus SO field reads [Dya86; Has97]

$$\boldsymbol{\Omega}_D^{(110)}(\boldsymbol{k}) = \frac{\gamma}{\hbar} \left[0, 0, k_x(\langle k_z^2 \rangle - (k_x^2 - 2k_y^2)) \right], \tag{2.53}$$

using the coordinate system $x||[1\bar{1}0]$, $y||[00\bar{1}]$ and $z||[110]$. It follows from Eq. (2.53) that the SO field $\Omega_D^{(110)}$ is perpendicular to the sample plane for any value and direction of the in-plane wave vector $\boldsymbol{k}$ [Has97; Win04]. The symmetry of $\Omega_D^{(110)}$ is schematically shown in panel (a) of Fig. 2.11. A second possible contribution to the SO field, caused by the structure inversion asymmetry, leads to in-plane components of the effective SO field $\boldsymbol{\Omega}_R \propto (k_y, -k_x, 0)$, which is illustrated in panel (b) of Fig. 2.11. In the special case of a symmetrically grown and doped heterostructure, the Rashba contribution to the SO field is negligible, and the Dresselhaus term determines the symmetry of the SO field. In such systems, spins oriented perpendicular to the sample plane are parallel to the

---

[12]A hint [Gla10a] by the corresponding author of Ref. [Gla08] is acknowledged, indicating that there is a misprint in sign in Eq. (7) of Ref. [Gla08].

SO field, and are protected from spin dephasing via the DP mechanism. Therefore, the out-of-plane spin dephasing time T_{zz} is no longer limited by the DP mechanism. For all other spin orientations there is a non-vanishing component of the SO field perpendicular to the spin orientation and ordinary DP spin dephasing can take place. The in-plane spin dephasing rates $1/T_{xx,yy} = \Omega_D^2(\boldsymbol{k})\tau$ are depending on the strength of the SO field $\Omega_D^{(110)}$ and the microscopic scattering rate $1/\tau$, which was discussed in detail in Sec. 2.1.2. As a result, one can expect a strong spin dephasing anisotropy for in-plane and out-of-plane spin orientations in symmetric (110)-grown QWs. This is still valid, if, in addition, a small Rashba field has to be taken into account, which can be a regular Rashba field resulting from a residual asymmetry of the band edge profile or a random Rashba field [She03; Gla05; Gla10b; Gla10c], generated by fluctuations of the remote donor density.
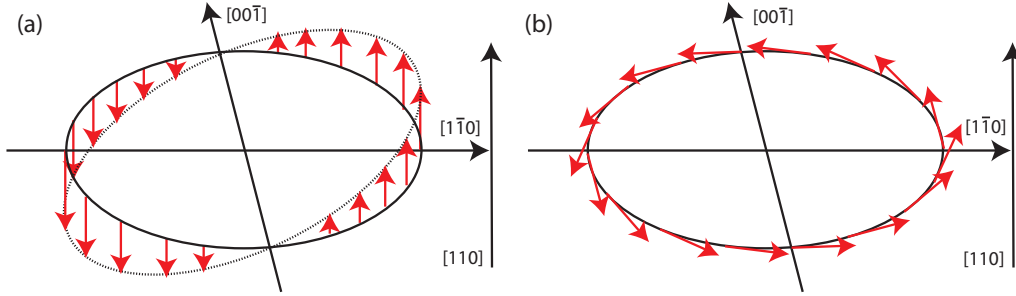

Figure 2.11: *Symmetry of the Dresselhaus (a) and Rashba (b) contribution to the SO field* $\boldsymbol{\Omega}$ *in a (110)-grown 2DES.*

Also in this case, spin dynamics can be described in the framework of a kinetic equation approach. Here, the case of a slightly asymmetric (110) grown QW will be considered, in which the spin relaxation rates tensor has the form [Tar09]

$$\hat{\Gamma} = \begin{pmatrix} \Gamma_{xx} & 0 & 0 \\ 0 & \Gamma_{yy} & \Gamma_{yz} \\ 0 & \Gamma_{zy} & \Gamma_{zz} \end{pmatrix}, \tag{2.54}$$

with the two non-zero off-diagonal elements $\Gamma_{yz} = \Gamma_{zy}$. Further it was shown [Tar09] that the components of $\hat{\Gamma}$ are given by

$$\Gamma_{xx} = \Gamma_{yy} = (\alpha^2 + \beta^2)C, \quad \Gamma_{zz} = 2\alpha^2 C, \quad \Gamma_{yz} = \Gamma_{zy} = \alpha\beta C, \tag{2.55}$$

with the Rashba constant α, the Dresselhaus constant β and a parameter C, depending on the microscopic scattering rate $1/\tau$ and the Fermi wave vector $\boldsymbol{k}_F$ of the electrons. From Eq. (2.55) it follows that the components of $\hat{\Gamma}$ are connected to one another by the relation

$$\Gamma_{yz} = \Gamma_{zy} = \pm\frac{1}{2}\sqrt{\Gamma_{zz}(2\Gamma_{yy} - \Gamma_{zz})}. \tag{2.56}$$

The solution of Eq. (2.32) with the spin relaxation rates tensor in Eq. (2.54) reads

$$s_z(t) = s_0 e^{-t/\overline{T}}\left[\cos\tilde{\Omega}t + \frac{\Gamma_{yy} - \Gamma_{zz}}{2\tilde{\Omega}}\sin\tilde{\Omega}t\right], \tag{2.57}$$

where

$$\frac{1}{\overline{T}} = \frac{\Gamma_{yy} + \Gamma_{zz}}{2} \quad \text{and} \quad \tilde{\Omega} = \sqrt{\Omega_L^2 - \frac{\Gamma_{yy}^2}{4}}. \tag{2.58}$$

The quantity $\tilde{\Omega}$ is real for magnetic fields B leading to a Larmor frequency $\Omega_L > \Gamma_{yy}/2$. In this case an oscillatory behavior of the spin ensemble can be observed, whereas for lower values of the magnetic field B, the spin decays exponentially similar to the mechanical analog, i.e., an overdamped oscillator.

2.2.8 Coherent spin dynamics in the intrinsic spin-orbit fields

In high-mobility samples, which are in the weak scattering regime of the DP mechanism, coherent oscillations of an optically excited spin ensemble about the SO field can be observed [Bra02; Ley07b; Sti07a]. The kinetic equation for this case reads

$$\frac{d\boldsymbol{s_k}}{dt} + \boldsymbol{s_k} \times \boldsymbol{\Omega_k} + \boldsymbol{Q}\{\boldsymbol{s_k}\} = 0, \tag{2.59}$$

where

$$\boldsymbol{\Omega_k} = \frac{\gamma}{\hbar} \begin{pmatrix} k_x(\langle k_z^2 \rangle - k_y^2) \\ -k_y(k_x^2 - \langle k_z^2 \rangle) \\ 0 \end{pmatrix} \tag{2.60}$$

is the Dresselhaus SO field for a (001)-grown 2DES. In the case of narrow or low-doped quantum wells, where $\langle k_z^2 \rangle = (\pi/d)^2 \gg k_F^2$ with the width d of the quantum well, $\boldsymbol{\Omega_k}$ becomes linear in $\boldsymbol{k}$ and Eq. (2.60) reads

$$\boldsymbol{\Omega_k} = \frac{\gamma}{\hbar}\langle k_z^2 \rangle \begin{pmatrix} k_x \\ -k_y \\ 0 \end{pmatrix}. \tag{2.61}$$

A solution for the z-component of Eq. (2.59) can be found in the form of an exponentially damped cosine function $s_z(t) = \exp(-t/\tau)\cos(\boldsymbol{\Omega_k}t)$, where the frequency $\boldsymbol{\Omega_k}$ is determined by the strength of the SO field, and the damping occurs on the timescale τ of the microscopic scattering time (see Sec. 2.1.2).

If, in addition, a magnetic field normal to the sample plane is applied, the electrons are forced to move on cyclotron orbits. Similar to the cyclotron motion in real space, there is also cyclotron motion in k space, where the electrons are moving along an orbit on the Fermi surface (for details, see, e.g. [Ash03]). Due to the time-dependence of $\boldsymbol{k}$, the total time derivative in Eq. (2.32) evolves into

$$\frac{d\boldsymbol{s_k}}{dt} = \frac{\partial \boldsymbol{s_k}}{\partial t} + \frac{\partial \boldsymbol{s_k}}{\partial \varphi_{\boldsymbol{k}}}\frac{\partial \varphi_{\boldsymbol{k}}}{\partial t} = \frac{\partial \boldsymbol{s_k}}{\partial t} + \omega_c \frac{\partial \boldsymbol{s_k}}{\partial \varphi_{\boldsymbol{k}}}, \tag{2.62}$$

where $\omega_c = |e|B/m_c$ is the cyclotron frequency with the charge e and the cyclotron mass m_c of the carriers. $\varphi_{\boldsymbol{k}}$ is the angle between the $\boldsymbol{k}$ vector and the x axis. The full kinetic equation for coherent spin precession of an electron ensemble, which is moving on a cyclotron orbit, reads then [Gla04a]

$$\frac{\partial \boldsymbol{s_k}}{\partial t} + \omega_c \frac{\partial \boldsymbol{s_k}}{\partial \varphi_{\boldsymbol{k}}} + \boldsymbol{s_k} \times \boldsymbol{\Omega_k} + \boldsymbol{Q}\{\boldsymbol{s_k}\} = 0. \tag{2.63}$$

Here, as it was noted in Ref. [Gla07], the effect of Larmor spin precession about the applied external magnetic field can be neglected because the Larmor frequency Ω_L is much smaller than the cyclotron frequency ω_c and the frequency of spin precession about the SO field, $\boldsymbol{\Omega_k}$.

Under the assumptions that $\Omega_{k_F}\tau \gg 1$ and $\omega_c\tau \gg 1$, the solution of Eq. (2.63) can be recast as [Gla07; Gri09]

$$\frac{s_{z,k_F}(t)}{s_{z,k_F}(0)} = \mathcal{A}e^{-t/\tau_s} + \mathcal{B}e^{-t/\tau_b}\cos(\Omega_{eff}t); \tag{2.64}$$

here, $\Omega_{eff} = \sqrt{\omega_c^2 + \Omega_{k_F}^2}$ is the modified Larmor frequency and $\mathcal{A} = \omega_c^2/\Omega_{eff}^2$ is the amplitude of the non-oscillating, long-lived tail of the spin polarization with the damping rate

$$\tau_s^{-1} = \mathcal{B}/\tau, \tag{2.65}$$

where τ is the microscopic scattering time.

$$\mathcal{B} = \Omega_{k_F}^2/\Omega_{eff}^2 \tag{2.66}$$

is the amplitude of the spin beats, damped out with the rate

$$\tau_b^{-1} = (1 + \mathcal{A}) / (2\tau). \tag{2.67}$$

Experimental results on coherent spin dynamics in the intrinsic SO fields and the cyclotron effect on coherent spin precession will be presented in Sec. 6.1.

2.3   Dynamical polarization of nuclei in nanostructures

In Sec. 2.2.6, electron spin dephasing caused by the hyperfine interaction was briefly discussed. In GaAs, the hyperfine interaction between electron spins and the spins of the lattice nuclei is of major importance, because all the stable isotopes ^{69}Ga and ^{71}Ga, as well as ^{75}As have a non-zero nuclear spin of $I = 3/2$. In the following, a basic overview on the hyperfine interaction is presented. Being of particular importance for the understanding of the experimental results shown in Sec. 6.2.4, the back action of a non-zero nuclear spin polarization on electron spin dynamics will be elucidated, as well.

The Hamilton operator $\widehat{\mathcal{H}_{HF}}$ of the Fermi contact hyperfine interaction for s-type electrons can be written as [Fer30; Abr61]

$$\widehat{\mathcal{H}_{HF}} = \frac{2\mu_0}{3} g_0 \mu_B \mu_I \hat{\boldsymbol{I}} \cdot \hat{\boldsymbol{S}} \delta(\hat{\boldsymbol{r}}), \tag{2.68}$$

where $\mu_I = g_I \mu_N$ are the magnetic moments of the relevant nuclear species. g_I represents the nuclear g factor, and μ_N is the nuclear magneton. Due to the structure of $\mathcal{H}_{HF}$, Eq. (2.68) can be rewritten as

$$\widehat{\mathcal{H}_{HF}} = \frac{2\mu_0}{3} g_0 \mu_B \mu_I \left[\frac{1}{2}(\hat{I}_+\hat{S}_- + \hat{I}_-\hat{S}_+) + \hat{I}_z\hat{S}_z \right] \delta(\hat{\boldsymbol{r}}). \tag{2.69}$$

Here, $\hat{I}_\pm = \hat{I}_x \pm i\hat{I}_y$ and $\hat{S}_\pm = \hat{S}_x \pm i\hat{S}_y$ are the standard quantum mechanical ladder operators, leading to an increase or decrease of the corresponding projection $m_{I,S}$ of the state $|j_{I,S}m_{I,S}\rangle$ with total angular momentum $j_{I,S}$ of the nuclear or the electron spin. Thus, the term $(\hat{I}_+\hat{S}_- + \hat{I}_-\hat{S}_+)$ induces simultaneous flips

$$\hat{I}_\pm\hat{S}_\mp|j_I m_I\rangle|j_S m_S\rangle =$$
$$= \hbar\sqrt{(j_I \mp m_I)(j_I \pm m_I + 1)}|j_I m_I \pm 1\rangle \times \tag{2.70}$$
$$\times \hbar\sqrt{(j_S \pm m_S)(j_S \mp m_S + 1)}|j_S m_S \mp 1\rangle$$

of electron and nuclear spin states, and is therefore denoted as Flip-Flop term. This term leads in the presence of an imbalance in the occupation of the electron spin states $|j_S m_S\rangle$ - as it is the case for a finite, nonequilibrium spin polarization - to a polarization of the nuclear spin system. Due to the fact that this process is slow and was reported to happen on the timescale of minutes to hours [Kik00; Mal00a; Sal01a; VD05; Köl12], it is also denoted as dynamic nuclear polarization (DNP) [Abr59; Lam68].

Static effects of the hyperfine interaction were first observed in nuclear magnetic resonance (NMR) and electron spin resonance (ESR) measurements. Shifts in the positions of the NMR resonance lines could be attributed to the hyperfine field [Pag77]

$$\vec{B}_e^i = -\frac{2\mu_0}{3} g_0 \mu_N \sum_k \vec{S}_k \, |\psi_k(\vec{r}_i)|^2 \tag{2.71}$$

of the occupied electron states q, acting on the nuclei i at position $\vec{r}_i$ [Kni49]. Analogously, the electron in an orbital state q is exposed to the hyperfine field [Pag77]

$$\vec{B}_n^k = \frac{2\mu_0}{3} \frac{g_0}{g} \sum_i \mu_{I,i} \vec{I}_i \, |\psi_k(\vec{r}_i)|^2 \tag{2.72}$$

of the lattice nuclei, resulting in the so-called Overhauser shift [Ove53]. The Overhauser field leads also to observable effects in experiments on electron spin dynamics: due to the additional nuclear magnetic field, a change in the Larmor frequency of the electron spin precession can be observed. In the following, this is shortly discussed for bulk semiconductor systems, where these effects were observed first, as well as for the case of 2DESs.

2.3.1 Dynamical nuclear polarization in bulk material

The first measurements on the interaction between the nuclear and the electron spin systems were performed on bulk semiconductor crystals. An overview on early optical measurements of the nuclear polarization is provided in Refs. [Dya84; Fle84; Pag84]. Due to the long spin dephasing times usually found in such systems, the optical generation of a large electron spin polarization is possible. Consequently, the nonequilibrium electron spin polarization leads to a dynamic polarization of the nuclear spin system due to the hyperfine interaction (see Eq. (2.69)). The nuclear polarization can be mapped, e.g., in all-optical experiments via an Overhauser shift (see Eq. (2.72)) in the electron Larmor precession frequency [Kik00].

In addition to the long spin dephasing times, in bulk semiconductors the localization of a fraction of the electrons at donor sites supports an efficient transfer of spin polarization from the electron to the nuclear spin system: in bulk semiconductors, the donor atoms providing the excess carriers are randomly distributed in the active layer. Localized electrons, which are weakly bound to the donor atoms, are widely accepted to be the centers of the DNP process in bulk semiconductors. In contrast, itinerant electrons are found to be coupled more weakly to the nuclear spin system [Hua12].

2.3.2 Dynamical nuclear polarization in 2DESs

In two-dimensional electron systems, the situation for dynamic polarization of the nuclear spin system is quite different: First, fewer localization centers are present due to remote doping schemes (see Chap. 3), where the dopant atoms and the electron system is separated by a thin spacer layer. Thus, spin transfer from localized electrons to the nuclear spin system is less likely. Secondly, the electron spin dephasing times are comparatively short, resulting in a lower achievable electron spin polarization. These two points, unfavorable for a dynamic nuclear polarization process, are compensated to some degree by the confinement of the two-dimensional electrons in a narrow region of the sample: due to the confinement, the electron wave function amplitude is enhanced inside the quantum well, leading to a stronger coupling between the electron and the nuclear spin system. However, DNP processes could be observed in investigations on 2DESs grown along the [110] crystallographic direction with reduced spin dephasing

rates [Sal01a; Sal01b] (see also Sec. 2.2.7), and in nominally undoped excitonic two-dimensional systems [Mal00a; Dzh02].

An adaption of Eqs. (2.71)-(2.72) for the case of a 2DES is provided in [Ţif03; Ţif04; Ţif11]. In low-dimensional structures, the electron wave function $\psi_k(\vec{r}_i) = \phi_k(\vec{r}_i)u_k(\vec{r}_i)$ can be written as a product of an envelope function $\phi_k(\vec{r}_i)$ and a Bloch function $u_k(\vec{r}_i)$. Thus, the amplitude $|\psi_k(\vec{r}_i)|^2$ of the electronic wave function at the position of the i-th nucles can be expressed as $\eta |\phi_k(\vec{r}_i)|^2$, where $\eta = |u_k(\vec{r}_i)|^2$ represents the enhanced probability density of the Bloch function at the position $\vec{r}_i$ of the i-th nucleus [Pag77; Sch03a]. In the case of GaAs, the values of η can be estimated to be $\eta_{Ga} \approx 2.7 \cdot 10^3$ and $\eta_{As} \approx 4.5 \cdot 10^3$ [Pag77; Sch03a]. Herewith, in combination with Eq. (2.72) and the relevant nuclear g factors $g_I(^{69}\text{Ga}) = 2.0166$, $g_I(^{71}\text{Ga}) = 2.5623$ and $g_I(^{75}\text{As}) = 1.4395$, the Overhauser field in low-dimensional structures can be calculated. If the Overhauser field is known from experiment, from Eq. (2.72) the degree of nuclear spin polarization can be estimated. This is presented in App. C for the Overhauser field, generated via an efficient DNP process in sample G, which will be introduced in Sec. 3.1.2.

Chapter 3

Design and preparation of the investigated samples

In this chapter the design and the preparation of the investigated samples will be shown. The experimental results presented in Chaps. 5 and 6 require a precise control of sample parameters, such as the width of the quantum well, the aluminum content in the barriers or the sheet density of donor atoms in the doping layers. To meet this demand, the samples investigated in this work were fabricated in the former workgroup of Prof. Dr. Wegscheider at Regensburg University using molecular beam epitaxy (MBE). With
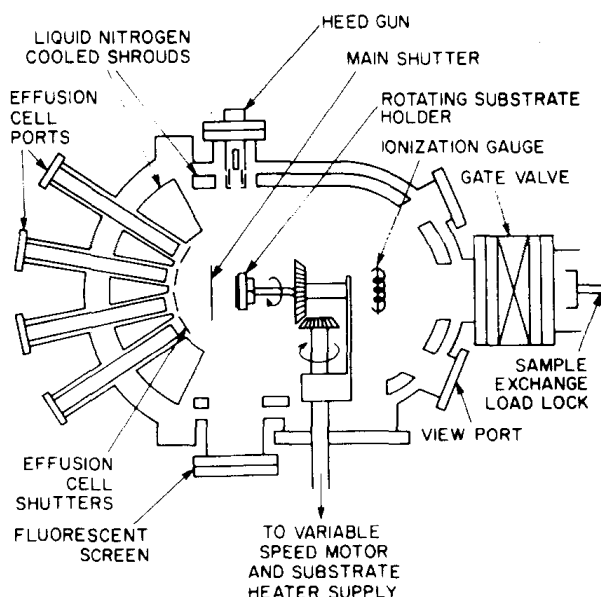
Figure 3.1: *Scheme of a MBE machine, which can be used for the growth of high-quality semiconductor heterostructures. (Taken from [Cho81].)*

this technique invented at the Bell Telephone Laboratories [Art68; Cho71] heterostructures of high crystalline quality with very sharp boundaries between different materials grown on top of each another can be produced. Epitaxial growth of the heterostructure can take place when a molecular beam hits a heated substrate mounted in the ultra-high vacuum growth chamber. The molecular beams are provided by heated effu-

Figure 3.2: *(a) Growth scheme of sample B. Growth takes place along the [001] direction. (b) Simplified asymmetric band edge profile resulting from the single-sided silicon δ-doping realized in sample B.*

sion cells containing ultra-clean amounts of the materials, which should be incorporated in the heterostructure. The stoichiometry of the resulting crystal can be influenced by the relative fluxes of the different elements, which in turn can be adjusted by the temperature of the individual effusion cells. Shutters in front of the effusion cells 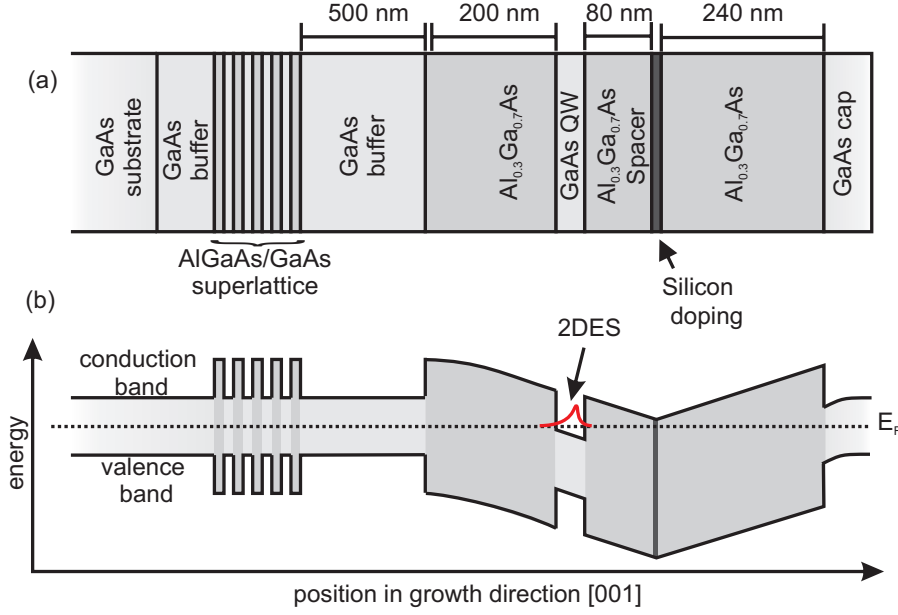are used to quickly interrupt the molecular beams in order to achieve, ideally, atomically sharp transitions between different stoichiometries inside the grown heterostructure. A scheme of an MBE machine including a rotating sample holder for an improved uniformity of the thicknesses of the epitaxially grown layers [Cho81] is shown in Fig. 3.1. To achieve highest sample qualities, the unintended incorporation of defect atoms has to be avoided. Therefore, besides using ultra-clean materials in the effusion cells, growth takes place in an ultra-high vacuum supported by cryogenic cooling shields to freeze out any unintended atoms remaining in the chamber. Under optimized conditions and the use of growth schemes as discussed in Sec. 3.1.2, two-dimensional electron gases with a mobility up to $30 \cdot 10^6 \, \text{cm}^2/\text{Vs}$ can be achieved [Uma09].

3.1   Sample structure

Two completely different sample structures were used in this work. For the experiments on the inplane spin dephasing anisotropy (see Sec. 2.2.7 and Chap. 5), samples with a single-sided δ-doped growth scheme were used, which will be discussed in Sec. 3.1.1. The experiments on coherent spin dynamics as well as on the spin dephasing anisotropy in (110)-grown samples (see Secs. 2.2.7, 2.2.8 and Chap. 6) require a more complex growth scheme, being elucidated afterwards in Sec. 3.1.2.

3.1.1   Single-sided δ-doped heterostructures

In this work four samples with an asymmetric band edge profile were investigated, having an active region consisting of a GaAs quantum well, separated by an 80 nm wide

#	sample number	growth axis	width (nm)	density n (10^{11} cm^{-2})	mobility μ (10^6 cm^2/Vs)	Fermi temp. T_F (K)
A	D080627C	[001]	10	1.96	0.54	81
B	D080627B	[001]	15	2.23	1.64	92
C	C060306A	[001]	20	2.1	1.6	87
D	C030504A	[001]	25	2.1	2.2	87
B'	D080627B	[001]	15	0.8 - 2.7	$-^1$	$-^1$

Table 3.1: *Parameters of the single-sided δ-doped asymmetric heterostructures. On sample B' a semi-transparent NiCr gate was fabricated.*

Al$_{0.3}$Ga$_{0.7}$As spacer layer from a Si-δ-doping layer. The parameter varied in this sample series was the quantum well width, whereas the asymmetry of the band edge profile was kept constant. The intention was to change the relative strength of the Rashba and Dresselhaus contributions by changing the Dresselhaus parameter β. As it was discussed in Sec. 2.2.2 and experimentally demonstrated [Ley07b],

$$\beta \propto \langle k_{001}^2 \rangle \propto \frac{\pi^2}{d^2} \tag{3.1}$$

depends on the expectation value of the squared quantized electron wave vector $\langle k_{001}^2 \rangle$, and can therefore be tuned by the width d of the quantum well. The constant thickness of the spacer layer and a constant doping density provides a constant asymmetry of the quantum wells, as was shown in measurements using magnetogyrotropic photogalvanic effects [Lec09].

The main parts of the growth structure of the four investigated samples shall be discussed using the example of sample B. In Fig. 3.2 schemes of the growth structure (panel (a)), as well as the resulting band edge profile (panel (b)) of sample B, are shown. First, an epitaxial GaAs buffer layer was grown on the [001]-oriented substrates, followed by a superlattice of 200 periods of 7 nm of Al$_{0.3}$Ga$_{0.7}$As and 3 nm of GaAs. The function of the superlattice is to provide a smooth and clean surface free of defects for the growth of the main part of the sample. On top of the superlattice, a second GaAs buffer layer is grown before producing a 200 nm thick layer of Al$_{0.3}$Ga$_{0.7}$As. This layer is the lower barrier of the 15 nm wide GaAs quantum well, which is separated by an 80 nm wide Al$_{0.3}$Ga$_{0.7}$As barrier from a Silicon (Si) δ-doping layer with a sheet density of about $2 \cdot 10^{12}$ cm^{-2}. Here, the doping layer is grown after the QW to prevent segregation [Hua88; Liu93] of Si dopant atoms into the QW. A part of the excess electrons in the highly doped layer can tunnel into the GaAs quantum well, where the Fermi energy lies inside the first conduction band, leading to the formation of a 2DES. The δ-doping layer is covered with 240 nm of Al$_{0.3}$Ga$_{0.7}$As and a thin 10 nm thick GaAs capping to prevent the AlGaAs layer from oxidation. The carrier density n, as well as the electron mobility μ of the 2DES, were determined in magneto-transport measurements at liquid helium temperature, and are listed in Tab. 3.1. In this table also the carrier densities and the mobilities of the samples A, C and D are included, which have different widths of the GaAs quantum well. The increase of the electron mobility with an increasing quantum well width d is a result of the reduced influence of scattering at the GaAs/AlGaAs boundary for wider quantum wells. In addition, the penetration of the electron wave function into the low-mobility barrier material is reduced for lower confinement energies and hence higher electron mobilities μ are possible. The latter argument is also of great importance for the complex growth structures presented in the following section.

---

[1] not determined for this sample.

In Tab. 3.1 also sample B' is listed, which is a piece of the same waver, from which sample B was taken from. On sample B' a semi-transparent NiCr gate was fabricated, as will be discussed in more detail in Sec. 3.2.2.

For the sake of completeness it should be noted that the growth structure of the samples C and D slightly deviates from that of samples A and B; the GaAs buffer following the first superlattice and the 200 nm thick $Al_{0.3}Ga_{0.7}As$ layer is replaced by a second superlattice with 20 periods of 20 nm of $Al_{0.3}Ga_{0.7}As$ and 6.2 nm of GaAs. However, an influence of this difference on the experimental results shown in Chap. 5 could not be detected.

3.1.2   Double-sided δ-doped high-mobility heterostructures

Since the production of the earliest MBE grown samples, there have been huge efforts in the development of high-mobility 2DESs embedded in GaAs-based heterostructures, where nowadays electron mobilities up to $30 \cdot 10^6 \, cm^2/Vs$ can be reached [Uma09]. What follows is a short discussion about how a growth structure can be optimized in order to allow for very high mobilities[2] μ.
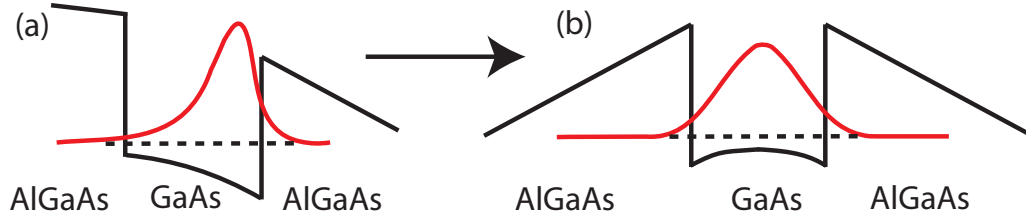

Figure 3.3: *Scattering of electrons at the GaAs/AlGaAs interface and the penetration of the electron wave function into the low-mobility material AlGaAs can be reduced by using symmetric (b) instead of asymmetric (a) growth and doping profiles.*

Starting from high-mobility remotely doped systems, the next important step to improve the electron mobility is the usage of symmetric instead of asymmetric growth profiles, as depicted in Fig. 3.3. In symmetrically grown and doped systems the wave function is centered in the GaAs quantum well, in contrast to an asymmetric band edge profile, where the wave function is shifted towards one of the GaAs/$Al_xGa_{1-x}As$ interfaces. With this approach, the scattering of the electrons due to interface roughness, as well as the penetration of the electron wave function into the low-mobility material $Al_xGa_{1-x}As$[3], can be reduced. In addition to this, the aluminum content in the barriers surrounding the GaAs quantum well can be optimized as well: to increase the mobility in $Al_xGa_{1-x}As$, the aluminum content x in the barriers should be kept as small as possible. On the other side, a small aluminum content x leads to a decrease of the band gap of $Al_xGa_{1-x}As$, resulting in lower walls of the quantum well and a larger penetration depth of the electron wave function into the barrier. Optimizing the aluminum fraction x in combination with the quantum well width d leads, in the case of this work, to $Al_xGa_{1-x}As$ barriers with a fraction $x = 0.25$ and a relatively large quantum well width $d = 30$ nm.

The mobility of double-sided doped symmetric structures can be further enhanced. This goal can be reached by depositing a large fraction of the doping atoms farther away from the 2DES, in order to reduce remote impurity scattering by the doping atoms. As shown in Fig. 3.4, two δ-doping layers on each side of the quantum well can

---

[2]Helpful discussions with the sample grower Dr. D. Schuh are gratefully acknowledged [Sch10].

[3]The mobility in $Al_xGa_{1-x}As$ is reduced, in consequence of so-called alloy scattering.
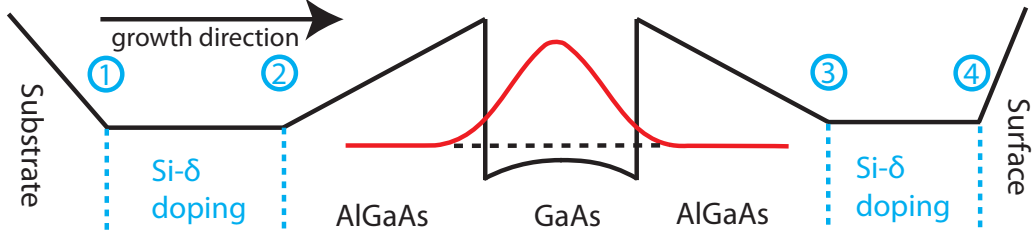
Figure 3.4: *Simplified band edge profile of a growth scheme including four doping layers. The layers 1 and 4 provide flat band conditions while the layers 2 and 3 provide the carriers for the 2DES.*

be deposited for this purpose. The layers 1 and 4 with a relatively high sheet density of dopants provide flat band conditions, whereas the layers 2 and 3 with a lower sheet density of dopants provide the carriers for the 2DES. The doping layers 2, 3 and 4 are deposited as δ-doping layers because electron scattering is reduced using this geometry. The doping layer 1 in the investigated samples is realized as a bulk doping layer for historical and technical reasons [Sch10] without any known drawback for the mobility.

For a further increase of the electron mobility, an approach introduced by Baba et al. [Bab83] can be used, who were the first to propose the separation of the doping atoms from Al-containing layers. With this the formation of so-called DX centers[4] can be avoided. This approach was perfected, and so-called short-period superlattice (SPSL) δ-doping layers were developed with which the highest mobilities reported so far could be achieved [Uma09].
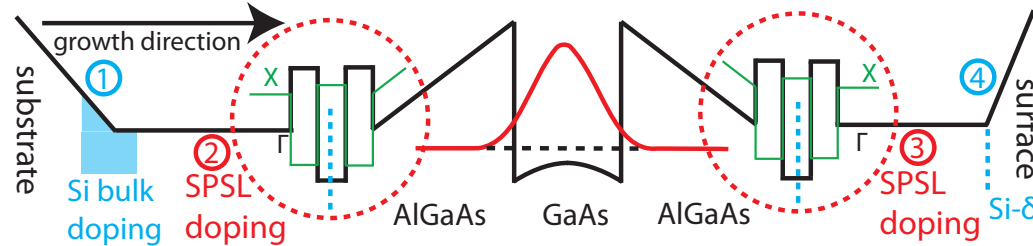

Figure 3.5: *Simplified band edge profile of a growth scheme including four doping layers. The layers 1 (bulk doping layer) and 4 (δ-doping layer) provide flat band conditions while the layers 2 and 3 (realized as SPSL doping layers) provide the carriers for the 2DES.*

The concept of SPSL doping layers consists of δ-doped thin GaAs layers, which are part of a GaAs/AlAs superlattice having just a few periods. As discussed in [Uma09], the donor electrons are confined and quantized in the doping layer and allow, therefore, a better charge transfer to the 2DES. In addition, the widths of the GaAs and the AlAs layer can be adjusted to form a type II superlattice [Guh98]. There, the ground state in the AlAs layers (which can then be found in the X-band) is lower than the quantized ground state in the thin GaAs layers between the AlAs barriers. Therefore, a fraction of

---

[4]DX centers, reviewed in Ref. [Moo90], are deep donor levels in many III-V semiconductors. In $Al_xGa_{1-x}As$, they control the conductivity for $x > 0.22$. Due to the large binding energy on the order of 200 meV, the donor electron occupies the DX level at low temperatures. By illumination with light, the DX center can be ionized and the donor electron is transferred into the conduction band, leading to a photoinduced increase of the conductivity. Because of low transfer rates between the conduction band and the DX center, the electron remains in the conduction band for a long time (minutes to days), after the illumination is turned of again. This is well-known as persistent photoconductivity (PPC). DX centers were also shown to act as scattering centers for the electrons and influence the electron mobility inside the quantum well [Buk94].

the donor electrons moves to the X band in the AlAs layers, where they can effectively screen the electric fields generated by the ionized donors [Rös10]. A second effect of the electron transfer to the X band is that these electrons normally do not contribute to the transport properties of the sample, because of the higher effective mass in the X band. A scheme of the resulting band edge profile using a simplified SPSL approach including just one δ-doped GaAs layer is shown in Fig. 3.5.

#	sample number	growth axis	width (nm)	density n $(10^{11}\mathrm{cm}^{-2})$	mobility μ $(10^6\ \mathrm{cm^2/Vs})$	τ_p (ps)	τ_{ee} (ps)
E	D081022A	[001]	30	2.97	14.8	563	88
F	D081205A	[110]	30	3.4	5.1	194	130
G	D081104B	[110]	30	2.7	2.1	83	77

Table 3.2: *Parameters of the double-sided δ-doped high-mobility heterostructures.*

In this work several samples, which make use of the SPSL concept and show, therefore, high electron mobilities (up to about $15\cdot10^6\ \mathrm{cm^2/Vs}$) are investigated. Here, also different substrates, oriented along the [001] or the [110] crystallographic direction, were used, leading to crystal growth along the respective axis. In Tab. 3.2, some parameters of the investigated samples are shown. The carrier density n, as well as the electron mobility μ, were determined using magneto-transport measurements at a sample temperature of 1.5 K. The transport scattering time τ_p was calculated directly from the mobility, whereas the electron-electron scattering time τ_{ee} was calculated for a temperature of 4.5 K, following Refs. [Gla02; Gla03; Gla04b].
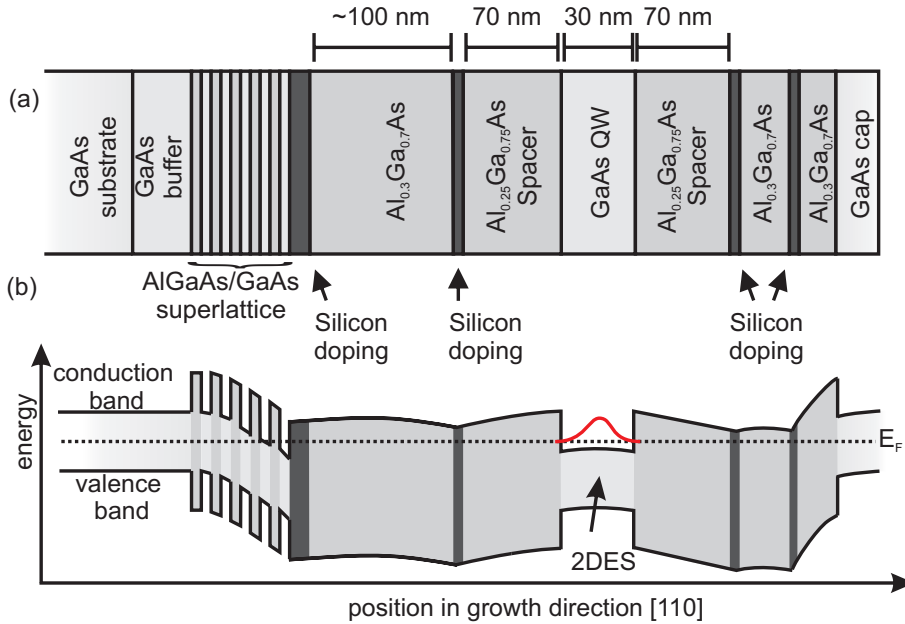
Figure 3.6: *(a) Growth scheme of the high-mobility sample G, which is grown along the [110] direction. (b) Simplified, highly symmetric band edge profile of the double-sided Si-doped heterostructure realized in sample G. The 2DES resides in the 30 nm wide GaAs quantum well. (Adapted from [Gri12])*

The particular growth scheme relevant for this work shall now be briefly discussed using the example of sample G (see Tab. 3.2), which is depicted together with a sketch of the resulting band edge profile in Fig. 3.6. For sample G, a (110)-oriented substrate was used, on which for the same reasons as already discussed (Sec. 3.1.1) first an epitaxial

GaAs buffer layer and a GaAs/AlGaAs superlattice were grown. The superlattice is followed by a bulk Silicon doping layer and an $Al_{0.3}Ga_{0.7}As$ layer. The aluminum fraction $x = 0.3$ in this layer is decreased slowly to $x = 0.25$ during its growth. Then a SPSL-type doping layer was grown, consisting of a 2 nm wide, δ-doped GaAs channel surrounded by 2 nm thick AlAs barriers. The active region of the sample is a 30 nm wide GaAs quantum well, having a 70 nm thick $Al_{0.25}Ga_{0.75}As$ spacer layer with a reduced Al fraction on each side. Next, the second SPSL-type doping layer is grown; it is followed by a 20 nm thick AlGaAs layer in which the aluminum fraction is driven back to the initial value of $x = 0.3$. The main part of the growth structure is completed with the fourth doping layer, which is realized as a standard δ-doping layer in $Al_{0.3}Ga_{0.7}As$. Finally, a 30 nm thick $Al_{0.3}Ga_{0.7}As$ layer and a thin GaAs capping is produced in order to prevent the Al-containing layers from oxidation. The sheet density of Si atoms is about $2 \cdot 10^{11} \, cm^{-2}$ at doping layer 1, $2 \cdot 10^{12} \, cm^{-2}$ at the doping layers 2 and 3, and $3.4 \cdot 10^{12} \, cm^{-2}$ at doping layer 4. These values were calculated from calibrated[5] Si fluxes and the exposure time for each layer.

In the (001)-grown sample E, the Si atoms predominantly replace Ga atoms and act as donors. In contrast, Si shows in general an amphoteric behavior if growth takes place on the (110) surface: depending on the growth conditions, the dopant atoms occupy either sites of the Ga or As sublattice, where they act as donors or acceptors, respectively [Sch93; Xu99]. Therefore, the growth conditions of samples F and G were adjusted by the sample growers as best as possible in order to achieve mainly n-type doping. Anyway, in the doping layers of the investigated samples F and G, most likely, a certain amount of Si still is incorporated on As sites [Sch12]. This leads to the compensation of a part of the desired donor electrons by holes, provided by the acceptors. Resulting from this, a lower number of electrons can be transferred to the QW, leading to a lower carrier density n of the 2DES. Differences in the behavior of the samples F and G regarding the sample temperature or under optical gating may be attributed to the amphotericity of Si on (110) surfaces, as will be discussed in detail in Sec. 6.2.3 and in App. A.

3.2 Sample preparation

3.2.1 Fabrication of optically thin samples

In this work, as will be discussed in detail in Sec. 4.1, all-optical measurement techniques were used for the investigation of spin dynamics. It is important for the results shown in Sec. 6.1 to achieve temperatures as low as possible during the measurement. Therefore, heat input into the sample must be reduced. One possible heat source is the absorption of laser power in the sample substrate, which has, in the samples presented in Sec. 3.1, a lower bandgap than the confined electron system inside the quantum well structure. In order to avoid this source of heat during the measurements, the GaAs substrate was removed in the following way: after cleaning a 5 by 5 mm sized piece of the sample and a C-cut sapphire wedge substrate by sonication in purest acetone, the sample was glued onto the sapphire substrate with an optical adhesive. The adhesive was cured by exposing it for about 10 min to ultraviolet light. The next step is to mechanically remove a large part of the substrate by grinding it down to about 50-100 microns using a SiC 1200 grit abrasive paper, which was wetted with purified water. To compensate

---

[5]For the calibration of the Si fluxes uniformly doped bulk samples with a layer thickness of $1 \, \mu m$ and a growth time of 1 h are produced, what corresponds to about 1 monolayer per second. The resulting doping concentration corresponding to the adjusted constant Si flux is measured by standard Hall measurements. From this, the number of Si atoms per square unit built in the crystal per second can be determined. For the delta doping layers the Si shutter is opened for a certain time; this time in combination with the determined Si flux gives the number of deposited Si atoms per square unit.

for the wedge angle of the sapphire substrate during the grinding process, a second sapphire wedge substrate is glued to its backside rotated by 180° using mounting wax. This stack of the sample and the second sapphire wedge substrate is finally mounted to the grinding unit. The remaining thickness of the sample was repeatedly controlled during the grinding process using a micrometer measuring gauge. After the desired remaining thickness is reached, the sample is unglued from the second sapphire plate by heating the complete stack to a temperature where the mounting wax becomes liquid and allows a separation. With a cleaning step, as discussed above, the mechanical part of substrate removal is completed.
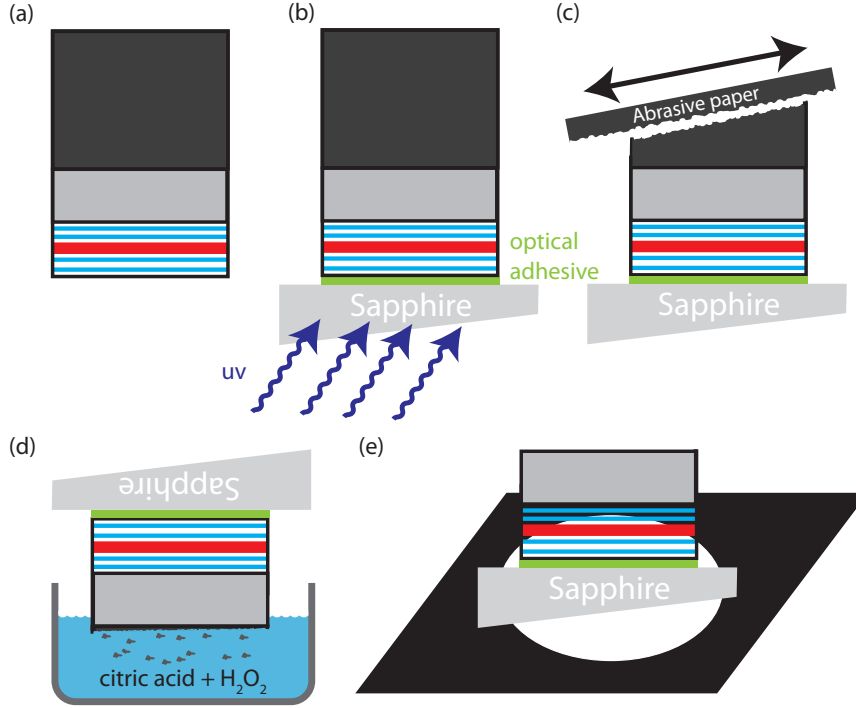

Figure 3.7: *Fabrication scheme of optically thin samples. The MBE grown sample (a) is glued to a sapphire wedge substrate using an optical adhesive (b). After the removal of the substrate (c, d), the remaining sample stack is mounted to an aluminum sample holder (e) and can be used for transmission experiments.*

The mechanical part is followed by a wet-chemical step, in which the remaining GaAs substrate is selectively etched away in a solution of citric acid and hydrogen peroxide. The etching solution is fabricated by solving 30.2 g of citric acid monohydrate in 25 ml of purest water; 10 ml of hydrogen peroxide with a concentration of 30 volume percent are added. The etch rate of this solution in GaAs is about 20 μm per hour with a selectivity of 1:100 at room temperature [DeS92]. The high selectivity leads to a drastic slowdown of the etching process if an Al-containing layer is reached; this is the case at the AlGaAs/GaAs superlattice, which works, therefore, as an etch stop. If the sample is etched down to the atomically flat superlattice, the appearence of the surface changes from matt gray to silvery, and the sample can be taken out of the etching solution. To remove residual amounts of the mounting wax, the sample is cleaned in boiling acetone and finally glued into an aluminum sample holder using Fixogum. A picture of a completely processed optically thin sample can be seen in panel (a) of Fig. 3.8.

It should be noted here that the thinned layer can be strained to some degree, caused by the different thermal expansion coefficients of the sapphire wedge substrate and the GaAs/AlGaAs heterostructure layer. Also, a reduction of the mobility, as well as
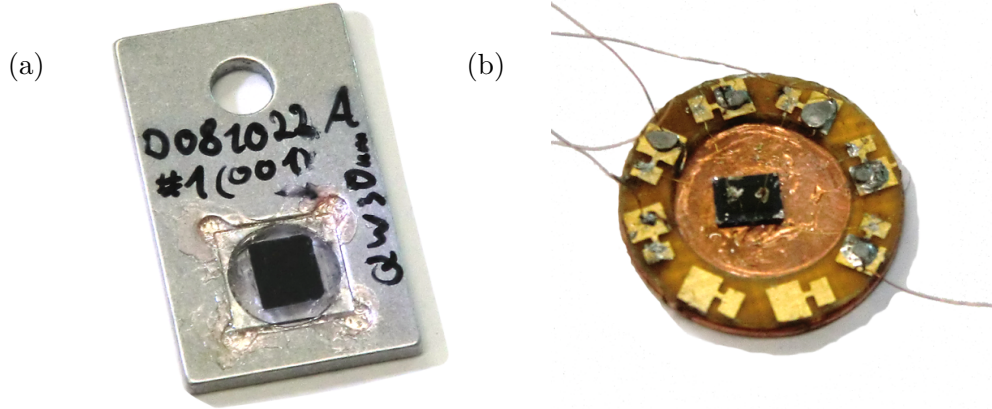
Figure 3.8: *(a) Thinned sample, mounted into an aluminum sample holder. (b) Sample with a semi-transparent top gate, mounted on a copper plate. Thin Au wires (hardly visible) connect the 2DES and gate contacts with the contact pads on the sample holder.*

changes in the carrier density, can be expected or can be observed, respectively. This seems to be particularly the case for samples with the complex growth scheme shown in Sec. 3.1.2.

3.2.2 Fabrication of semi-transparent gates

The built-in electric field in samples A-D presented in Sec. 3.1.1 determines the strength of the Rashba contribution to the SO field, and, hence, influences the spin dephasing anisotropy discussed in Sec. 2.2.7. By means of an applied gate voltage between a top gate and the 2DES, the built-in electric field, the SO field and the carrier density can be varied simultaneously, allowing for a tuning of the spin dephasing anisotropy to some degree, see Sec. 5.3. In order to retain optical access to the 2DES even if a metallic top gate is deposited, semi-transparent gates were used in this work, which provided both good electrical properties as well as a transmission coefficient on the order of about 80 percent.

The fabrication process of a semi-transparent gate begins with a cleaning step as described in Sec. 3.2.1. This can be skipped if the sample is as perfectly clean as it comes out of the MBE machine. Next, the electric contacts to the 2DES are fabricated. Therefore, a small scratch is made in each corner of the sample surface using a diamond tip scratcher. With a clean soldering rod, a small amount of Indium (In) is deposited on top of the scratches, which is then alloyed into the crystal by heating the sample under forming gas atmosphere within 60 s to 350° C and keeping it for an additional 60 s at this temperature. After cooling out, an Ohmic contact between the In drop at the scratch and the 2DES is formed.

After the electric contacts to the 2DES are realized, the borders of the sample are masked using sticky tape in order to define the gate area. Then, the sample is mounted in a high vacuum evaporation chamber, where an about 6 nm thick layer of a nickel/chromium (NiCr) alloy is deposited on the uncovered part of the sample surface, yielding a transmission of about 80 percent. After the removal of the sticky tape and, if necessary, the adhesive residue by help of a cotton bud and acetone, thin gold wires are soldered to the In contacts. Then, the sample is transferred to a separately prepared sample holder, where it is fixed using heat-conductive paste. The thin gold wires are soldered to contact pads on the sample holder. Prior to this, to each contact pad an enamelled copper wire should be soldered having a plug-in IC Pin on the other end,

which can be connected to a contact terminal in the cryostat (for details see Sec. 4.5). Finally, the ends of two thin gold wires are fixed with conductive silver to the semi-transparent gate and to the contact pads. At the end, the quality of the contacts can be checked by measuring the resistances between the single contacts.

For this work, a gate was fabricated on a piece of the same waver from which sample B was taken. In the following, this gated sample will be denoted as sample B'. Using a multimeter, resistances of 30 kΩ between the 2DES contacts and about 400 kΩ between the two gate contacts were determined at room temperature. The I-V characteristics of the gate and the 2DES show a non-linear diode-like behavior, as will be shown in Sec. 5.3. The differential resistance $R = \partial U/\partial I$ between the 2DES and the NiCr gate at $T = 4$ K is on the order of about 300 kΩ in the voltage range $-1\,\text{V} < U < 5\,\text{V}$.

Chapter 4

Measurement techniques and experimental setup

In this chapter the experimental techniques used for the determination of spin and carrier dynamics, as well as for sample characterization, will be discussed.

4.1 Time-resolved Faraday/Kerr rotation

The all-optical time-resolved Faraday or Kerr rotation (TRFR/TRKR) technique is a widely used method to investigate spin dynamics on timescales from 100 fs up to several nanoseconds [Aws85; Bau94]. Based on the Faraday or the magneto-optic Kerr effect [Far46; Ber99], the evolution of an optically generated spin ensemble can be mapped via the rotation of the polarization plane of a linearly polarized probe laser pulse, which is either transmitted through (Faraday geometry) or reflected (Kerr geometry) by a magnetized sample. The time resolution is achieved by means of an adjustable time delay between the circularly polarized pump pulse, which provides the spin polarization in the sample, and the linearly polarized probe pulse. The rotation angle Θ of the polarization plane (in the case of the Kerr effect also the ellipticity) is analyzed using a balanced bridge detector.
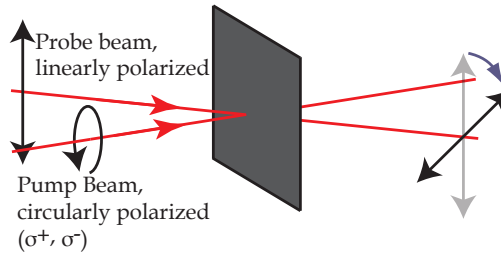
Figure 4.1: *Illustration of the principle of TRFR measurements. The polarization axis of the linearly polarized probe pulse is rotated due to the magnetization, generated by the circularly polarized pump pulse.*

In a balanced bridge detector, a Wollaston prism divides the incident light beam into two weakly divergent beams with polarizations oriented perpendicular to each other. Both beams are focussed on photodiodes, which are connected to an electronic amplifier,

where the intensity difference between the two beams is analyzed. A $\lambda/2$-waveplate in front of the Wollaston prism can be used to rotate the main axis of the incident (elliptic) light in a way to adjust the intensity difference to zero if no spin polarization is present in the sample; this is the case without any pump pulse, for example. Suitable for the use of a lock-in detection scheme, this technique allows for the precise measurement of very small rotation angles Θ with a resolution of about 100 nrad in the particular setup, which was used for this work.

In the TRFR/TRKR measurements performed for this work, the beam of a mode-locked Ti:sapphire laser tuned to a wavelength slightly above the Fermi energy is split into a pump and a probe beam (see Fig. 4.2). The pump beam is circularly polarized by a quarter waveplate, whereas the probe beam remains linearly polarized. Both beams are aligned parallel to each other and are focussed by an achromatic lens with a focal length[1] $f = 31$ cm to a small spot with a spot diameter of about 80 microns on the sample. Usually, the pump pulse is oriented parallel to the sample normal, whereas the probe pulse has an incident angle of about 6°. Due to the optical selection rules (see
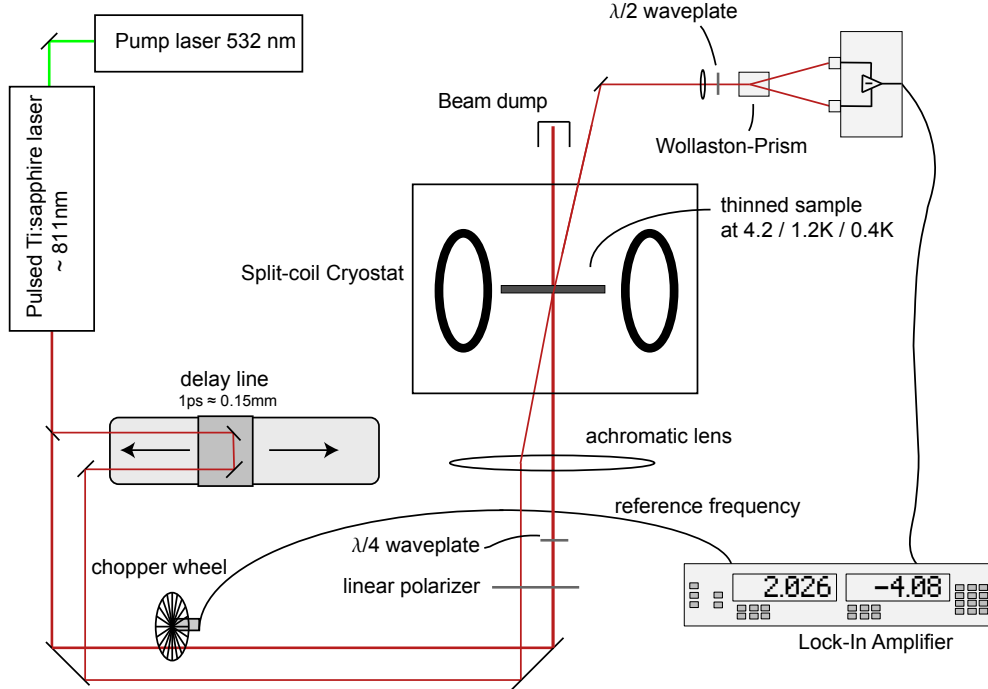
Figure 4.2: *Typical setup for a TRFR measurement, including a pulsed laser system, a delay line, polarization optics, an achromatic lens as well as the detection unit with an lock-in amplifier.*

Sec. 2.2.3), the pump pulse creates an ensemble of spin-polarized electrons, whereas the probe beam is affected by the magnetization of the electron ensemble via the Faraday or Kerr effect, as illustrated in Fig. 4.1. The reflected or transmitted probe pulse, having also an angle of about 6° to the sample normal, can be separated from the pump pulse, and is coupled into an optical bridge detector as discussed above. There, the rotation angle Θ of the linear polarization is analyzed. The time delay Δt of the pump and the probe pulse is provided by a $l = 30$ cm long mechanical delay line, which allows for time delays Δt between -180 ps and 1.8 ns. The pump beam was modulated in amplitude for the purpose of the lock-in measurement, using an optical chopper wheel.

---

[1]In some experiments an achromatic lens with a focal length of $f = 21$ cm was used, yielding a spot diameter of about 50 μm.

To eliminate spin-independent contributions to the measurement signal, each measurement is done for both circular polarizations σ^+/σ^- of the pump beam. The spin-dependent part of the measurement signal is expected to change its sign when the circular polarization is changed from σ^+ to σ^-. Thus, the spin signal can be extracted by subtracting the σ^+-data from the σ^--data. This is shown in panel (a) of Fig. 4.3. Fitting the TRFR/TRKR data with the appropriate fitting function for the particu-
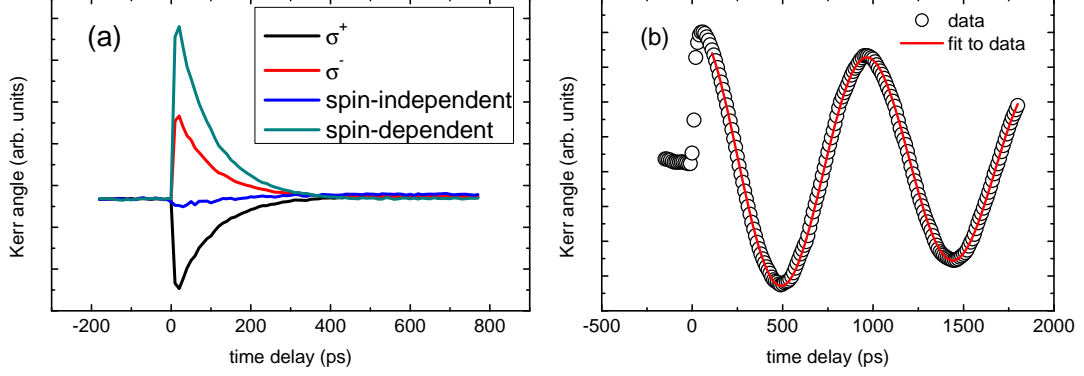

Figure 4.3: *(a) Typical TRFR/TRKR trace of an exponentially damped spin ensemble. Shown are the two traces for excitation with σ^+/σ^- light and their sum and difference, respectively. The difference is proportional to the spin polarization in the sample, whereas the sum is proportional to spin-independent phenomena. (b) The oscillating TRKR signal (open circles) in the case of an applied external magnetic field B is proportional to the out-of-plane component $s_z(t)$ of the spin ensemble, and can be fitted with an exponentially damped cosine function (red line).*

lar system (see Secs. 2.2.4, 2.2.7 and 2.2.8) allows for the determination of important spin dephasing parameters, like the spin dephasing times $T_{xx,yy,zz}$ as well as the electron g factor. Due to the fact that the Faraday/Kerr angle Θ is only sensitive to the out-of-plane component $s_z(t)$ of the spin polarization for near-normal incidence, a typical TRFR/TRKR signal shows damped oscillations (see panel (b) of Fig. 4.3) if the spin ensemble is forced to undergo a precession about a fixed near-inplane axis. This leads in the case of isotropic spin dephasing to exponentially damped oscillations with the Larmor frequency $\Omega_L = g\mu_B B/\hbar$, from which the electron g factor can be directly determined.

4.2 Resonant spin amplification technique

The length of the delay line used for the TRFR/TRKR technique, presented in Sec. 4.1, limits the window, in which the dynamics of the spin polarization can be observed directly, to about 2 ns in the case of this work. For more precise measurements of long spin dephasing times, the resonant spin amplification (RSA) technique [Kik98; Kik99] is favorable, which is a variation of the TRFR/TRKR technique and which has been succesfully applied to systems of different dimensionality [Kik99; Ast08; Yug09; Kor10].

If the spin dephasing times are on the order of the repetition period T_{rep} of the pulsed laser, the spin ensembles generated by subsequent laser pulses can interfere with one another. If a small external magnetic field $\boldsymbol{B}$ is applied, the interference of the precessing spin ensembles resulting in a modulation of the Kerr/Faraday angle can be measured for a fixed time delay between pump and probe pulses as a function of the magnetic field $\boldsymbol{B}$. For magnetic fields $\boldsymbol{B}$ leading to Larmor frequencies
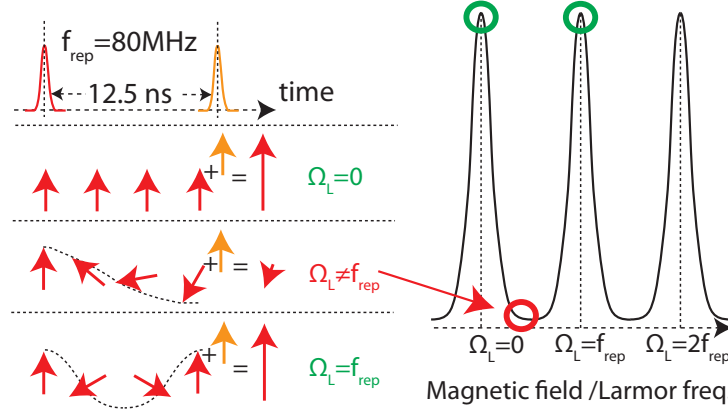
$$\Omega_L = g\mu_B B/\hbar = mf_{rep} \tag{4.1}$$

Figure 4.4: *Scheme of the build-up of the RSA signal. Subsequent pulses interfere with one another. Depending on the Larmor frequency Ω_L, the interference is constructive or destructive, leading to the characteristic multi-peak shape.*

matching multiples $m f_{rep}$ of the laser repetition frequency f_{rep}, the polarization of the spin ensemble is resonantly amplified. In contrast, Larmor frequencies Ω_L, which do not fullfill condition (4.1), lead to destructive interference of the spin ensembles generated by subsequent pulses and in general to a low overall polarization of the total spin ensemble. A scheme of the build-up process of the RSA signal is depicted in Fig. 4.4.

The experimental setup for a RSA measurement is very similar to a TRKR measurement, as shown in Fig. 4.2. However, the significant difference is that the delay line is *fixed* at a certain time delay and an additional magnetic field has to be available, which is in the case of this work provided by an electromagnet or superconducting coils inside a split-coil cryostat system (see also Sec. 4.5). The time delay Δt between the pump and the probe pulse is usually adjusted to a small negative value. Thus, the probe pulse arrives *before* the pump pulse or nearly one laser repetition period T_{rep} after the previous pump pulse. The laser repetition period T_{rep} of the pulsed Ti:sapphire laser used in this work is about 12.5 ns, which exceeds by far the carrier thermalization and recombination times of the investigated systems.

The expected and well-known multi-peak shape of RSA traces in the case of isotropic spin dephasing is shown in the left panel of Fig. 4.5. The distance of the peaks is mainly related to the electron g factor, whereas the full width at half maximum (FWHM) of the peaks reflects the spin dephasing time. Qualitatively, narrow peaks can be observed in systems with a long spin dephasing time; systems with a short spin dephasing time are characterized by peaks with a large FWHM. In the case of strongly anisotropic spin dephasing in symmetric (110)-grown 2DESs (see Sec. 2.2.7), one expects a different shape of the RSA signal, as shown in the right panel of Fig. 4.5. As already discussed [Gri12], and will be shown later in this section, the growth-axis spin dephasing time T_{zz} is correlated with the FWHM of the zero-field RSA peak. In contrast, the FWHM of the RSA peaks at finite magnetic field values is related to the in-plane spin dephasing time T_{yy}. Here, again the coordinate system $x||[1\bar{1}0]$, $y||[00\bar{1}]$ and $z||[110]$ will be used and the magnetic field is assumed to point along the x direction.

For a quantitative extraction of the spin dephasing times as well as the electron g factor from the RSA traces, a comparison of the measurement data with an appropriate theoretical model is neccessary. Here, in particular a model function for RSA traces, measured on slightly asymmetric (110)-grown heterostructures, shall be discussed, because it is of major importance for the results shown in Sec. 6.2. Following Refs. [Gla08; Gla10a], the expected shape of a RSA trace can be derived in dependence of the applied magnetic field B and the constant time delay Δt between pump and probe pulse. Since
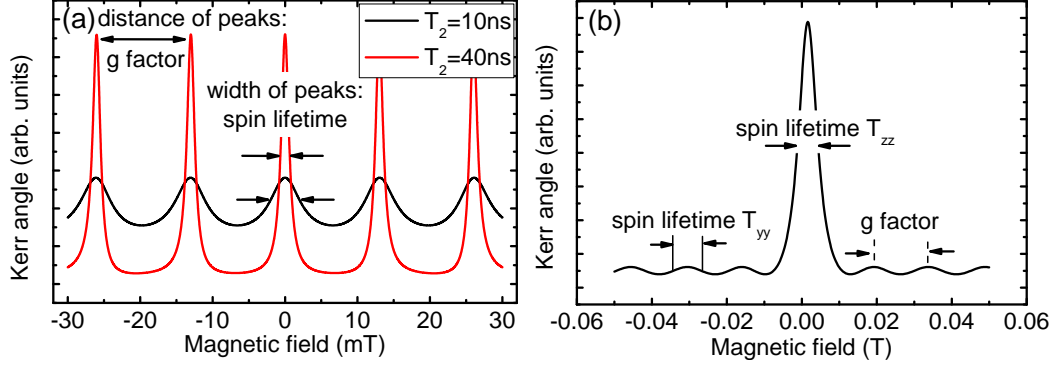
Figure 4.5: *(a) Typical shape of a RSA trace in the case of isotropic spin dephasing. The width of the peaks is connected with the spin dephasing time: an increase of the spin dephasing time leads to a smaller width of the peaks. (b) In the case of anisotropic spin dephasing in (110)-grown samples a different shape of the RSA signal can be expected. A characteristic feature is the narrow peak at $B = 0$, connected with the long out-of-plane SDT T_{zz}. Peaks of a larger width at non-zero magnetic fields are an indication for a shorter in-plane SDT.*

a sequence of many pulses contributes to the RSA signal, one has to build the sum over the spin polarizations $s_z(\Delta t + mT_{rep})$, generated by many subsequent pulses. Usually the number of pulses in the experiment is very large, and so one can approximate the resulting spin polarization $s_z(B, \Delta t)$ as a sum over an infinite sequence of pulses:

$$s_z(B, \Delta t) = \sum_{m=1}^{\infty} s_z(B, \Delta t + mT_{rep}) \tag{4.2}$$

The geometric series in Eq. (4.2) can be rewritten in a more compact way [Gla08]:

$$s_z(B, \Delta t) = \frac{s_0}{2} e^{-(T_{rep} + \Delta t)/\overline{T}} \frac{e^{T_{rep}/\overline{T}} C\left[\tilde{\Omega}(T_{rep} + \Delta t)\right] - C\left(\tilde{\Omega}\Delta t\right)}{\cosh\left(T_{rep}/\overline{T}\right) - \cos\left(\tilde{\Omega}T_{rep}\right)}. \tag{4.3}$$

Here, s_0 is the spin polarization generated by a single pulse and $\overline{T}^{-1} = (\Gamma_{yy} + \Gamma_{zz})/2$ is the average spin relaxation rate. The Γ_{ij} are the components of the spin relaxation rates tensor for the slightly asymmetric (110)-grown system (see Eq. (2.54)). The function C reads

$$C(\zeta) = \cos\zeta + \left[(\Gamma_{yy} - \Gamma_{zz})/2\tilde{\Omega}\right]\sin\zeta. \tag{4.4}$$

For the electron spin precession frequency in the considered case one gets

$$\tilde{\Omega} = \sqrt{(g\mu_B B/\hbar)^2 - \Gamma_{yy}^2/4}, \tag{4.5}$$

where g is the electron g factor and B is the external applied magnetic field. Due to the special properties and the nondiagonal spin relaxation rates tensor in the case of slightly asymmetric (110)-grown heterostructures, it is important to remember the relation $T_{zz} \approx 2/\Gamma_{zz}$; for details see Ref. [Tar09]. By using the model for $s_z(B, \Delta t)$, shown in Eqs. (4.3) - (4.5), it was possible to extract the spin dephasing times T_{zz} and T_{yy} as well as the electron g factor. Experimental results on this will be shown in detail in Sec. 6.2.

It should be noted that Eq. (4.3) was derived under the assumption that spin dephasing of the z component is governed by a regular Rashba contribution to the SO
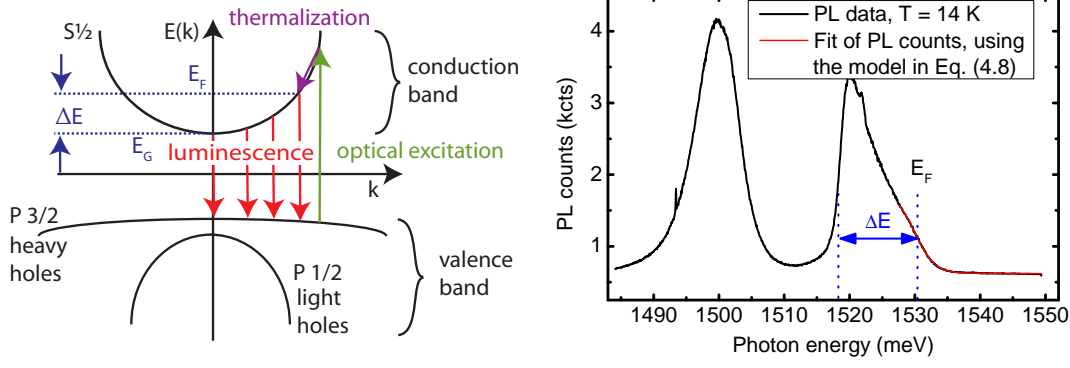
Figure 4.6: *The spectral width ΔE of the PL peak is related to the energy spectrum of the electrons in the conduction band: $\Delta E = E_F - E_G$. The peak at about 1.5 eV can most likely be attributed to carbon impurities [Str81].*

field. If, in contrast, random Rashba fields [She03; Gla10c; Gla10b] determine the spin dephasing of the z component, one had

$$\tilde{\Omega} = \sqrt{(g\mu_B B/\hbar)^2 - (\Gamma_{yy} - \Gamma_{zz})^2/4}$$ (4.6)

for the electron spin precession frequency and $T_{zz} = 1/\Gamma_{zz}$.

4.3 Photoluminescence spectroscopy

In many cases spin dynamics is closely connected to the dynamics of the charge carriers and the fundamental properties of the system under investigation. As discussed in Secs. 2.2.4 and 2.2.8, the strongly temperature-dependent microscopic scattering time τ massively influences spin dephasing via the EY and the DP mechanism. The latter also depends via $\mathbf{\Omega}(\mathbf{k}_F)$ (see Eq. 2.44) strongly on the highest occupied electron wave vector $\mathbf{k}_F$, and hence on the carrier density n of the 2DES, which determines the Fermi energy E_F and the Fermi wave vector $\mathbf{k}_F$. As a common experimental technique, photoluminescence (PL) and photoluminescence excitation (PLE) experiments allow for the characterization of a 2DES in its basic parameters, like the carrier density n, the temperature T_e of the electron system as well as the absolute and relative spectral positions of emission and absorption lines.

In PL measurements in 2DESs, electron-hole pairs are generated by above-bandgap excitation, then thermalize by intra-subband scattering events, and relax towards the band extrema of the conduction and the valence band. In doped systems they can recombine under energy and momentum conservation, and emit photons having energies between the bandgap energy E_G and the Fermi energy E_F, where the highest occupied electron state can be found, which can contribute to photoluminescence. A scheme of a PL process, as well as a typical PL trace having a shark-fin like shape[2], is shown in Fig. 4.6. Due to the large effective mass of the heavy-hole valence band, the spectral width ΔE of a PL line is determined mainly by the conduction band dispersion. From the resulting PL linewidth $\Delta E = E_F - E_G$ and with the constant density of states in a 2DES the carrier density of the 2DES can be estimated to

$$n = \frac{E_F m^*}{\pi\hbar^2} = \frac{\Delta E[\text{meV}]}{3.57}10^{11}\text{ cm}^{-2},$$ (4.7)

---

[2]The second peak at about 1.5 eV visible in the right panel of Fig. 4.6 most likely can be attributed to carbon impurities [Str81].
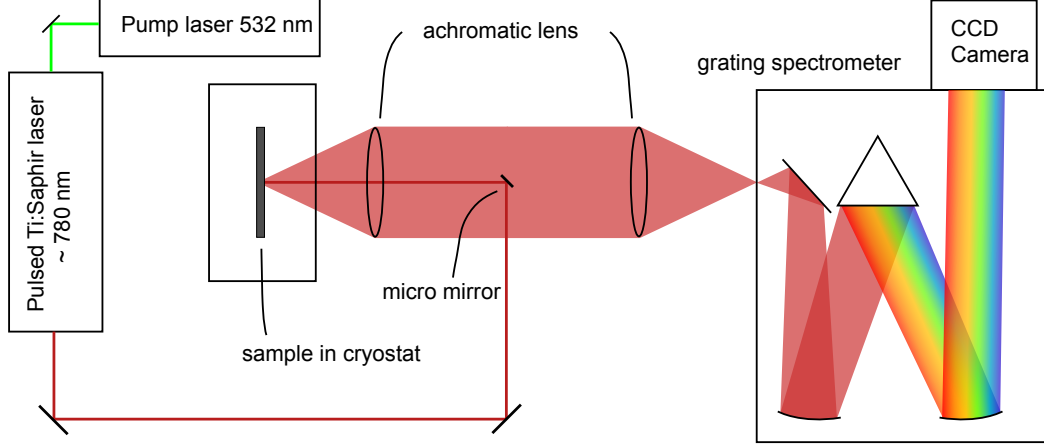
Figure 4.7: *Measurement setup for a photoluminescence measurement. The emitted PL light is focussed by achromatic lenses on the entry slit of a grating spectrometer.*

where $m^* = 0.067m_0$ is the effective mass [Sti69; Sti71; Law71] for a conduction band electron in GaAs. This method allows for the all-optical determination of the carrier density within some error bars, also under the conditions of optical gating (cf. Sec. 2.1.3). In the case of very low carrier densities, where the electron-hole Coulomb interaction is not screened sufficiently [Kle85a; Shi95], excitons are formed and the method is no longer applicable.

As mentioned, in addition to the estimation of the carrier density n, the determination of the temperature T_e of the electron system during the photoluminescence lifetime τ_{PL} is possible as a consequence of the Fermi-Dirac statistics of the electrons. Due to the finite width of the step of the Fermi-Dirac distribution function

$$f(\epsilon, T) = \frac{1}{1 + e^{\frac{\epsilon - E_F}{k_B T}}} \tag{4.8}$$

at the Fermi energy E_F, the carrier density n is smeared out for $T_e > 0$ in an interval $E_F \pm k_B T_e$ around E_F. During the recombination process, the Fermi-Dirac distribution of carriers in the k-space translates into an energy distribution around the high-energy tail of the PL, which thus can be approximated with a Fermi-Dirac function. From a fit with the function in Eq. (4.8), the Fermi energy E_F, as well as the temperature T_e of the electron system, can be determined. They are related to the spectral width $\delta E \propto k_B T_e$ and the position of the high-energy tail of the PL.

A typical setup for PL measurements is shown in Fig. 4.7. For this work the beam of a mode-locked Ti:sapphire laser with a pulse length of about 1 ps was focussed on the sample using an achromatic lens. In this case, the laser wavelength was tuned to about 780 nm, which is clearly above the bandgap of the 2DESs in the investigated quantum wells and below the bandgap of the surrounding barriers in order to avoid optical gating effects (see Sec. 2.1.3). The excited photoluminescence light was coupled into a grating spectrometer using a second achromatic lens, where the light is spectrally resolved and detected with a Peltier-cooled CCD camera.

The use of a streak camera system instead of the CCD camera allows also for a temporal resolution of the photoluminescence, if a pulsed laser is used for the excitation. From the time-resolved PL (TRPL) traces obtained this way, the PL decay time τ_{PL} can be determined [Rya84].

A variation of the PL technique is the photoluminescence excitation spectroscopy (PLE). Here, PL spectra are taken for different wavelengths λ_{ex} of the laser light used

for excitation of the PL. The amplitude of the PL spectra depends on the absorption of the 2DES, which changes with λ_{ex}. Therefore, the dependence of the PL amplitude on the excitation wavelength yields information about the absorption of the 2DES. A typical PLE spectrum is depicted in Fig. 6.1.

4.4   Time-resolved differential transmission spectroscopy

The photocarrier recombination time τ_{PL} is the timescale on which the radiative carrier recombination process, discussed in Sec. 4.3, occurs. To determine τ_{PL}, besides TRPL also the so-called time-resolved differential transmission (TRDT) spectroscopy can be used, making use of the change of the absorption induced by the generation of photoexcited carriers [Sha77; Sha79; Sch96]. During the lifetime of the optically excited carriers, the absorption of a laser, tuned resonantly to the absorption edge of a 2DES, is reduced as a consequence of the nonequilibrium occupation of initial and final states. By tuning the time delay between a linearly polarized pump pulse, which creates the excess carriers, and an also linearly polarized probe pulse, which is used to detect the relative change of the transmission, the recombination time τ_{PL} can be determined under the conditions of resonant excitation, similar to the case of TRFR/TRKR measurements (see Sec. 4.1).

4.5   Low-temperature setup

All the experimental results presented in Chaps. 5 and 6 were obtained at low temperatures $0.4\ \text{K} < T < 150\ \text{K}$, using three different cryostat systems. The measurements on the in-plane spin dephasing anisotropy presented in Chap. 5 were performed in an Oxford Microstat HiRes II (Pillar version) continuous-flow (cf) cryostat, where nominal sample temperatures between 4 K and room temperature can be achieved. In this cryostat, the sample is mounted on the cold finger using a thin film of vacuum grease and is exposed to vacuum. Thus, the thermal contact between the sample and the cold finger is crucial for the resulting sample temperature during measurement. A bad thermal contact can lead to an elevated sample temperature, exceeding the nominal sample temperature by a nearly uncontrollable value[3]. In addition, due to the certain distance between the heat sensor (located near the base of the cold finger) and the sample (on top of the cold finger), the sample temperature in general seems to exceed the nominal temperature by about 5-10 K. In this setup, an in-plane magnetic field B up to 400 mT is provided by a home-built electromagnet.

For measurements at lower temperatures, an Oxford Spectromag split-coil cryostat with an ^{3}He insert was available, in which temperatures down to 0.4 K and magnetic fields of up to 11 T can be achieved. The magnetic field orientation can be chosen either perpendicular (Faraday geometry) or parallel (Voigt geometry) to the sample plane. The experimental results on coherent spin dynamics, presented in Sec. 6.1, were obtained in this cryostat system, as well as a part of the measurements on anisotropic spin dynamics shown in Secs. 6.2.3 and 6.2.4.

For temperature-dependent PL measurements without applied magnetic field, a Janis ST-100 cf optical cryostat was used. Here, lower sample temperatures than in the Oxford Microstat HiRes II (Pillar version) cf cryostat could be achieved.

---

[3]In principle, PL measurements could be performed, from which one could estimate the sample temperature.

Chapter 5

Spin dynamics in two-dimensional electron systems with asymmetric band edge profile

In this chapter, experimental results on the spin dephasing anisotropy in (001)-grown GaAs/AlGaAs quantum wells with an asymmetric band edge profile (see Sec. 3.1.1) are presented. First, the well width dependence of this anisotropy is discussed in Sec. 5.1. It will be shown that the Dresselhaus parameter β in the samples A-D changes in agreement with the theoretical expectation and decreases with an increasing quantum well width d. Afterwards, a dependence of the spin dephasing anisotropy (i.e., the ratio β/α) on the sample temperature will be demonstrated in Sec. 5.2. Finally, in Sec. 5.3 the observed change of the spin dephasing anisotropy as a consequence of electrostatically gating sample B' will be presented, followed by a discussion of the dependence of spin dynamics on the excitation intensity and the degree of initial spin polarization (Sec. 5.4).

The spin dephasing anisotropy presented in this chapter was investigated using the TRKR technique, see Sec. 4.1. In order to determine the out-of-plane spin dephasing time $T_{[001]}$ as well as the anisotropic in-plane spin dephasing times $T_{[110]}$ and $T_{[1\bar{1}0]}$, the optically generated spin ensemble pointing initially out-of-plane has to be rotated into the sample plane. For this purpose, TRKR traces were taken with a magnetic field $\boldsymbol{B}$, applied parallel to the crystallographic axis $[1\bar{1}0]$ or $[110]$. If the magnetic field is applied along the $[110]$ direction, the spin ensemble precesses towards the $[1\bar{1}0]$ direction, as it is schematically shown in Fig. 5.1. The average spin dephasing time (see also Eq. 2.52)

$$\overline{T_{B||[110]}} = 2 \left(\frac{1}{T_{[001]}} + \frac{1}{T_{[1\bar{1}0]}} \right)^{-1} \tag{5.1}$$

in this case has contributions from the out-of-plane SDT $T_{[001]}$ and the in-plane SDT $T_{[1\bar{1}0]}$. In contrast, if the magnetic field $\boldsymbol{B}$ is parallel to the $[1\bar{1}0]$ direction, the optically excited spin ensemble rotates towards the $[110]$ direction, and one gets for the average spin dephasing time

$$\overline{T_{B||[1\bar{1}0]}} = 2 \left(\frac{1}{T_{[001]}} + \frac{1}{T_{[110]}} \right)^{-1}. \tag{5.2}$$

In the case of anisotropic spin dephasing with $T_{[110]} \neq T_{[1\bar{1}0]}$, different values of the average spin dephasing times $\overline{T_{B||[1\bar{1}0]}}$ and $\overline{T_{B||[110]}}$ can be expected. The two TRKR traces shown in Fig. 5.2, with obviously different spin dephasing times, were obtained on
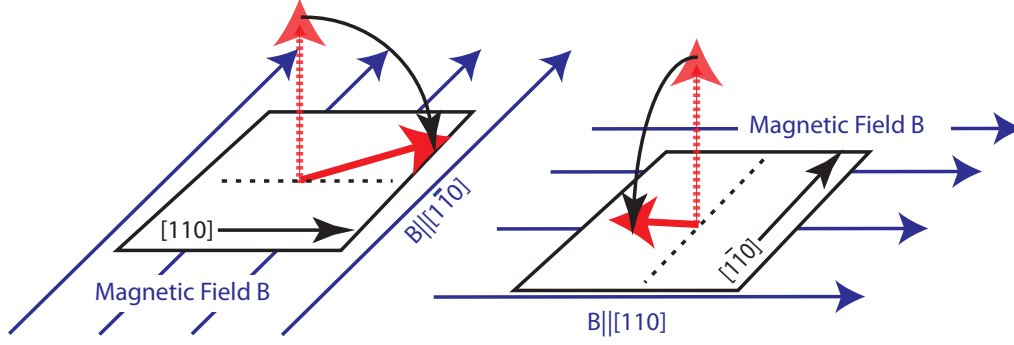
47

Figure 5.1: *The optically excited spin ensemble precesses in the external applied magnetic field **B**. Depending on the orientation of the magnetic field relative to the crystallographic axis, the spin ensemble rotates towards the [110] or the [1$\bar{1}$0] crystallographic direction.*
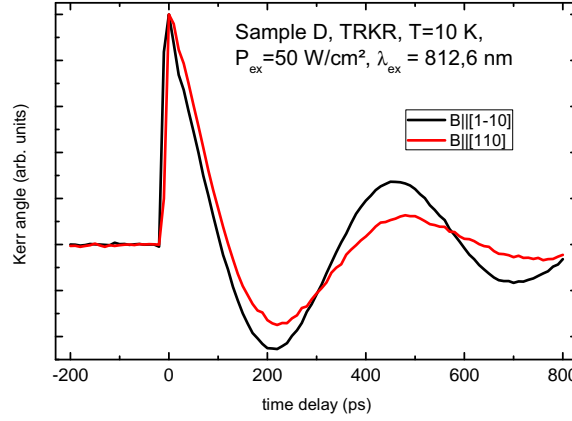

Figure 5.2: *Normalized TRKR traces, measured on Sample D at a nominal sample temperature of 10 K with a magnetic field of B = 400 mT applied. The average spin dephasing time $\overline{T}$ is obviously longer if the magnetic field **B** is applied along the [1$\bar{1}$0] direction.*

sample D at a temperature of $10\,\mathrm{K}$ with a magnetic field $B = 400\,\mathrm{mT}$, applied parallel to the [110] and the [1$\bar{1}$0] crystallographic axis. In the experimental setup used for this work, the orientation of the magnetic field, produced by a heavy electromagnet, could not be changed easily. Therefore, the alignment of the magnetic field **B** parallel to the respective crystallographic axis had to be realized via the sample orientation in the cryostat. Unfortunately, there was also no possibility to rotate the sample within the cryostat during one cooling cycle.

However, two different approaches could be used to obtain the desired TRKR data with the magnetic field pointing along the particular crystallographic directions: as depicted in panel (a) of Fig. 5.3, the first approach was to mount two sample pieces on the cold finger of the cryostat at the same time, rotated to each other by an angle of 90°. This allows for the measurement of $\overline{T_{B||[1\bar{1}0]}}$ and $\overline{T_{B||[110]}}$ within the same cooling cycle, but not at the same position. This may cause some error resulting from unavoidable sample inhomogeneities. In the second approach (see panel (b) of Fig. 5.3), just one piece of the sample was mounted in the cryostat. This piece was rotated by 90° degree after the first measurement series with the magnetic field applied along a certain direction was completed, and the cryostat was warmed up. In a second cooling cycle, the remaining
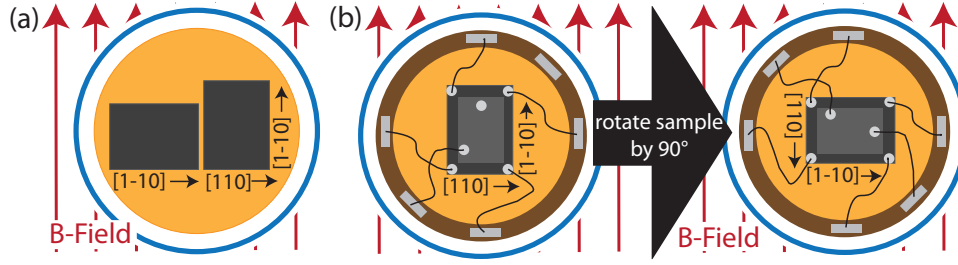
Figure 5.3: *Approaches to determine the spin dephasing anisotropy: (a) two pieces of the sample are mounted on the coldfinger of the cryostat at the same time. (b) Just one sample is mounted on the cold finger. The sample is rotated after the first measurement run. Here, two cooling cycles are needed.*

measurement series could be performed. The second approach principally allows the measurement on nearly the same sample position, but not within the same cooling cycle. Moreover, this may lead to some error caused by a change of the experimental conditions between the first and the second cooling cycle. Here, it is particularly important to mention the high relevance of the thermal contact between the cold finger of the cryostat and the sample, as was already discussed in Sec. 4.5. This is of major importance in systems showing a strong temperature dependence of spin dynamics, as it will be discussed in detail in Sec. 5.2 for the investigated samples.

Both approaches were used within this work. However, it is the first approach with two pieces of the sample in the cryostat, which was mainly used. By the usage of a motorized x-y translation stage, the two measurement positions on the two samples could be approached repeatedly with sufficient precision. As an exception, the measurements performed on the gated sample B' presented in Sec. 5.3 were done using the second approach. The reason for this is that inside the cryostat there would not have been enough space for two gated samples.

Usually, for each orientation of the magnetic field, a series of TRKR measurements was performed with different values $0\,\mathrm{mT} \leq |B| \leq 400\,\mathrm{mT}$ of the magnetic field B. In Fig. 5.4, the results of such a measurement series on sample D are shown. In the case of $B = 0\,\mathrm{mT}$, the optically generated spin ensemble does not precess and remains oriented along the [001] direction. In this case an exponential decay of the spin ensemble takes place with the SDT $T_{[001]}$, which, of course, should be the same for $B||[110] \to 0$ and $B||[1\bar{1}0] \to 0$. It should be noted that the condition

$$T_{[001]}\big|_{B||[110]\to 0} \stackrel{!}{=} T_{[001]}\big|_{B||[1\bar{1}0]\to 0} \tag{5.3}$$

was always used to make sure that the two measurement series with $B||[1\bar{1}0]$ and $B||[110]$ were performed under comparable experimental conditions. If no significant difference was observed, the measurements with finite magnetic field were started. Otherwise, a different sample position should be chosen, where the condition (5.3) is fullfilled. In the case of a bad thermal contact, the sample had to be remounted.

Under optimized experimental conditions, a typical measurement series yields results as shown in Fig. 5.4. There, the average SDTs $\overline{T_{B||[1\bar{1}0]}}$ and $\overline{T_{B||[110]}}$ are plotted, determined from TRKR traces taken on sample D at a nominal sample temperature of $T = 10\,\mathrm{K}$ for the particular values and orientations of the magnetic field $\boldsymbol{B}$. At $B = 0\,\mathrm{mT}$, the obtained values coincide, being a proof for comparable experimental conditions in the two measurement series with $B||[1\bar{1}0]$ and $B||[110]$. In contrast, the determined average SDTs $\overline{T_{B||[1\bar{1}0]}}$ and $\overline{T_{B||[110]}}$ for $|B| > 0\,\mathrm{mT}$ are apparently quite different from each other. This is an unambiguous indication for the presence of a strong in-plane SDA in the investigated sample D.
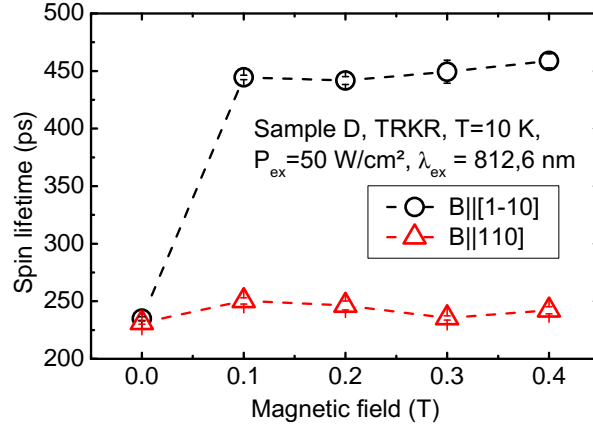
Figure 5.4: *Average spin dephasing times measured on sample D with 25 nm well width for magnetic field orientations along the [110] and [1̄10] direction. The sample temperature was 10 K. The dashed lines are drawn in support of a better recognition.*

From the average spin dephasing times, the corresponding in-plane spin dephasing times $T_{[110]}$ and $T_{[1\bar{1}0]}$ can be calculated, using the Eqs. (5.1) and (5.2). Furthermore, as it was shown in Refs. [Ave99; Ave06], from $T_{[110]}$ and $T_{[1\bar{1}0]}$ the ratio[1]

$$\left|\frac{\beta}{\alpha}\right| = \frac{\sqrt{T_{[110]}} + \sqrt{T_{[1\bar{1}0]}}}{\sqrt{T_{[110]}} - \sqrt{T_{[1\bar{1}0]}}} \qquad (5.4)$$

can be calculated, which is a measure for the relative strength of the Rashba and the Dresselhaus contribution to the SO field. The data points shown in Fig. 5.4 yield[2] $T_{[110]} \approx 50\,\text{ns}$ and $T_{[1\bar{1}0]} = 317 \pm 10\,\text{ps}$, leading to a value of $|\beta/\alpha| \approx 1.2$.

From the TRKR traces obtained in a finite magnetic field $\boldsymbol{B}$, also the components g_{xx}, g_{yy} and g_{xy} of the electron g factor tensor $\hat{\boldsymbol{g}}$ can be determined, using the coordinate system $x||[100]$, $y||[010]$ and $z||[001]$. For this purpose, the Larmor frequency $\Omega_L = g\mu_B B/\hbar$ for different orientations of the magnetic field $\boldsymbol{B}$ is extracted from the measurement data[3] (see, e.g., Fig. 5.2) by a fit using the model presented in Eqs. (2.51) and (2.52). By a linear fit of the magnetic field dependence of Ω_L, the g factor component along the corresponding magnetic field direction can be extracted, as shown in Fig. 5.5. In this work usually the values $g_{[110]}$ and $g_{[1\bar{1}0]}$ were extracted, from which both, g_{xx} as well as the off-diagonal components $g_{xy} = g_{yx}$ of the $\hat{\boldsymbol{g}}$ factor tensor, can be calculated. The in-plane g factor depends on the angle ϕ between the magnetic field and the [100] direction as

$$g(\phi) = -\sqrt{g_{xx}^2 + g_{xy}^2 + 2g_{xx}g_{xy}\sin 2\phi}, \qquad (5.5)$$

---

[1]It was noted in Ref. [Ave06], that the right hand side of Eq. (5.4) yields either the ratio $|\alpha/\beta|$ or its reciprocal value $|\beta/\alpha|$. In this work presumably the ratio $|\beta/\alpha|$ was observed; this will be discussed in detail in Sec. 5.3.

[2]In the case of a ratio $|\beta/\alpha| \approx 1$, the determination of $T_{[110]}$ is no longer possible with high precision, using the presented method. This problem and possible solutions will be discussed in more detail in Sec. 5.2.2.

[3]It should be noted that the sign of the Larmor frequency Ω_L in the common TRKR setup is not directly accessible. If it should be determined from the experiment, a more sophisticated approach is neccesary [Yan10]. By a comparison with the literature [Yug07] and own experiments [Lec11], the values of the g factor can be expected to be negative in the investigated samples A-G, and a minus sign is added by hand to the determined absolute values of the g factor components.
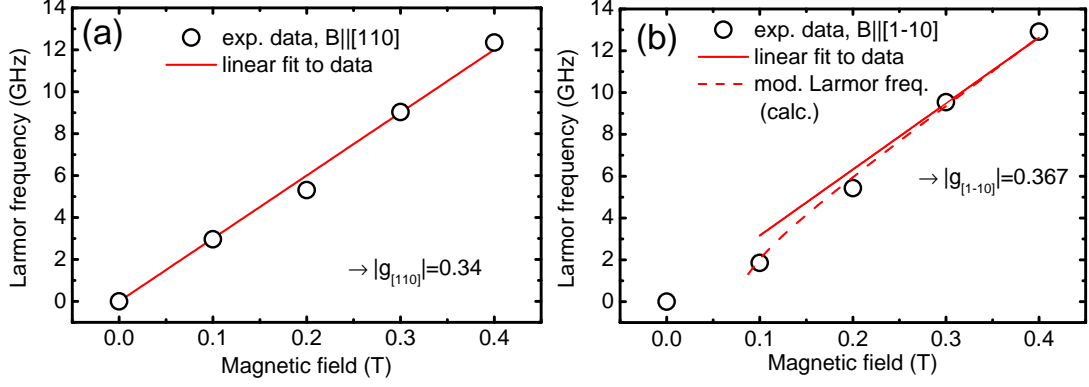
Figure 5.5: *Larmor frequency determined from TRKR traces measured on sample D at a temperature of 10 K. With the magnetic field $\boldsymbol{B}$ applied along the $[1 \pm 10]$ direction, the electron g factor can be determined by a linear fit to (a) $|g_{[110]}| = 0.34$ and (b) $|g_{[1\bar{1}0]}| = 0.367$, respectively. In the case of $\boldsymbol{B}||[1\bar{1}0]$, the Larmor frequency is reduced at the lowest magnetic field values. Resulting from different SDTs $T_{[001]}$ and $T_{[110]}$, this is in agreement with the expectation: the dashed line represents calculated values of the modified Larmor frequency $\tilde{\Omega}$ (see, Eq. (2.52)).*

which was discussed in detail in Refs. [Kal93; Eld11]. From this,

$$g_{xx} = \frac{g_{[110]} + g_{[1\bar{1}0]}}{2} \tag{5.6}$$

and

$$g_{xy} = \frac{g_{[110]} - g_{[1\bar{1}0]}}{2}, \tag{5.7}$$

can be easily determined, where $\phi = \pm 45°$ for $\boldsymbol{B}||[1\pm10]$. In sample D, at a temperature $T = 10\,\mathrm{K}$, values of $g_{[110]} = -0.34$ and $g_{[1\bar{1}0]} = -0.367$ could be determined as shown in Fig. 5.5, yielding $g_{xx} = -0.354$ and $g_{xy} = 0.013$. In the case of $\boldsymbol{B}||[1\bar{1}0]$, the Larmor frequency is reduced at the lowest magnetic field values. This results from different SDTs $T_{[001]}$ and $T_{[110]}$ and is in agreement with the expectation. The dashed line in panel (b) of Fig. 5.5 represents calculated values of the modified Larmor frequency $\tilde{\Omega}$ (see, Eq. (2.52)).

In the following, the dependence of spin dynamics in the investigated samples A-D on different parameters like the quantum well width d (Sec. 5.1), the sample temperature T (Sec. 5.2), the carrier density n (Sec. 5.3) and the excitation intensity I_{ex} (Sec. 5.4) will be discussed.

5.1 Dependence of spin dynamics on the well width

In DP spin dynamics, the spin dephasing time T_2^* is given by (see Sec. 2.2.6)

$$\frac{1}{T_2^*} = \Omega^2(\boldsymbol{k}_F)\tau, \tag{5.8}$$

where τ is the microscopic scattering time and

$$\boldsymbol{\Omega} = \boldsymbol{\Omega}_{SIA,\,2D} + \boldsymbol{\Omega}_{D,\,2D,\,001} = \frac{\alpha}{\hbar} \begin{pmatrix} k_{010} \\ -k_{100} \\ 0 \end{pmatrix} + \frac{\beta}{\hbar} \begin{pmatrix} -k_{100} \\ k_{010} \\ 0 \end{pmatrix} \tag{5.9}$$

the effective SO field, having both, Rashba and Dresselhaus contributions. Due to the dependence of $\beta = \gamma \left(\frac{\pi}{d}\right)^2$ on the QW width d, a variation of d results in a change of the SO field Ω. This, in consequence of Eq. 5.8, leads to a change of the spin dephasing time T_2^*.

A change of the effective SO field Ω influences the in-plane and the out-of-plane components of the spin relaxation tensor $\hat{\Gamma}$ differently. First, in Sec. 5.1.1 the focus should be on the dependence of the growth axis SDT $T_{[001]}$. Secondly, the experimental results on the dependence of the in-plane spin dephasing anisotropy on the QW width d will be presented (Sec. 5.1.2). Finally, dependencies of the g factor on the quantum well width d and the asymmetry of the QW will be discussed in Sec. 5.1.3.

5.1.1   Dependence of the growth-axis SDT $T_{[001]}$ on the well width
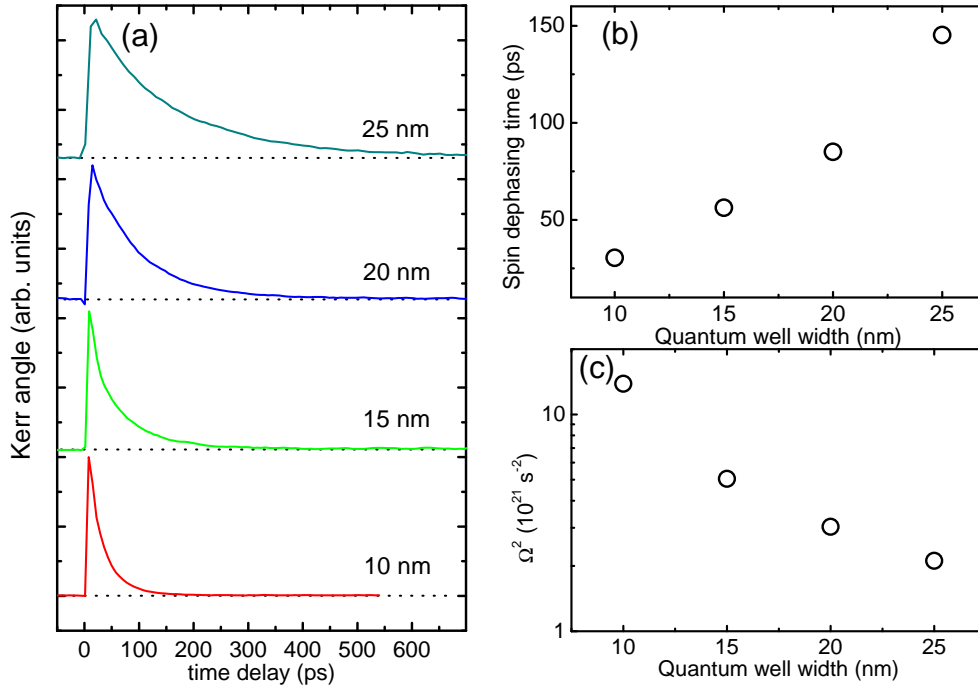

Figure 5.6: *(a) Zero-field TRKR traces of samples A-D at $T = 4\,K$. (b) Zero-field spin dephasing time $T_{[001]}$, plotted against the QW width. (c) Expected SO field Ω^2 as a function of the QW width.*

The out-of-plane spin dephasing rate $1/T_{[001]} = \Gamma_{[001]} = C(\alpha^2 + \beta^2)$ with the parameter C, depending on the scattering time τ [Ave99], is expected to increase strongly with α and β. Because α is intentionally kept constant in the investigated samples, predominantly a change of the parameter $\beta \propto \gamma \left(\frac{\pi}{d}\right)^2$ leads to a change of $\Gamma_{[001]} = 1/T_{[001]}$. In Fig. 5.6 (a) zero-field TRKR traces of the four investigated samples A-D at a temperature of 4 K and an excitation intensity of $50\,\mathrm{W/cm^2}$ are shown, from which the growth-axis SDT $T_{[001]}$ can be extracted (panel (b)). The extracted SDTs $T_{[001]}$ show a strong increase from 30 ps in sample A ($d = 10\,\mathrm{nm}$) to about 150 ps in sample D, with the $d = 25\,\mathrm{nm}$ wide QW. The strong increase of $T_{[001]}$ for increasing QW width d can be well understood. This behavior is a consequence of the decrease of the Dresselhaus SO field Ω_D, according to $\Omega_D \propto \gamma d^{-2}$.

For a quantitative analysis of the dependence of $T_{[001]}$ on the QW width d, the dependence of the Dresselhaus spin splitting constant[4] $\gamma = \gamma(E_c)$ on the QW width d and

---

[4]Apparently, γ is *not* a constant. However, in order to retain the common terminology, γ will still

the confinement energy E_c has to be taken into account as well. As was shown by Winkler [Win03], the value of γ decreases if the confinement energy E_c increases[5]. Unfortunately, there is very little experimental data on this basic constant available, regarding the literature for GaAs/AlGaAs QWs. In addition, the presented values of γ for a certain confinement energy E_c show some spread. For $E_c \approx 10\,\mathrm{meV}$ values for $|\gamma|$ ranging from $16.5 \pm 3\,\mathrm{eV\mathring{A}^3}$ [Jus95] to $11 \pm 1\,\mathrm{eV\mathring{A}^3}$ [Ley07b] were reported. Studer et al. [Stu10] determined also the sign of γ and got values in the range $-5 < \gamma < -8\,\mathrm{eV\mathring{A}^3}$ for $d = 15\,\mathrm{nm}$ wide QWs (which corresponds to $E_c \approx 25\,\mathrm{meV}$). Koralek et al. [Kor09] estimated a value of $|\gamma| = 5.0\,\mathrm{eV\mathring{A}^3}$ from measurements on a series of QWs with $7\,\mathrm{nm} < d < 15\,\mathrm{nm}$, using transient spin grating spectroscopy.

In order to proceed with the quantitative analysis of $T_{[001]}$, values of γ for the investigated samples A-D were carefully estimated on the basis of the available data [Jus95; Ley07b; Stu10; Eld11]. In addition, a value of $\gamma \approx 16\,\mathrm{eV\mathring{A}^3}$ could be determined from sample E ($E_c \approx 6\,\mathrm{meV}$), as will be shown in detail in Sec. 6.1.2. Panel (b) of Fig. 5.7 shows the values for γ, which are used for the calculation of the SO field Ω. The values of Ω^2 calculated this way are shown in panel (c) of Fig. 5.6. Here, already the ratio β/α of Dresselhaus and Rashba contributions to the SO field is considered in each sample. However, this will be discussed in detail in Sec. 5.1.2.
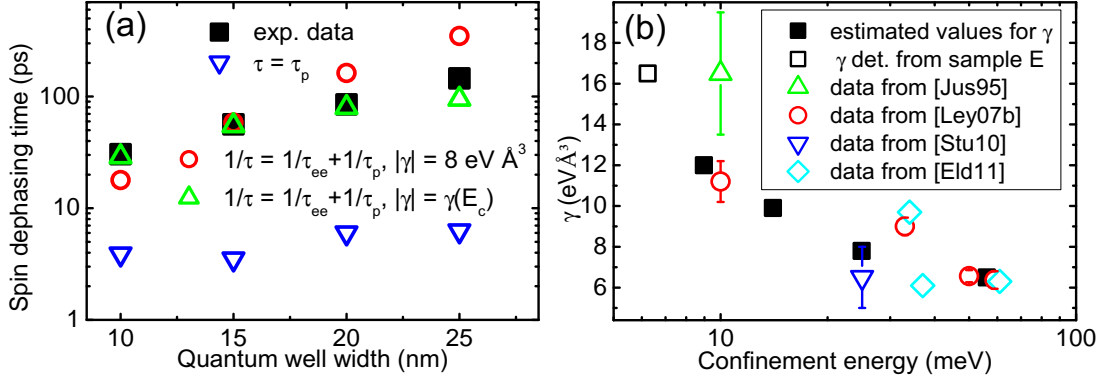

Figure 5.7: *(a) Zero-field SDT $T_{[001]}$ extracted from the experimental data (black squares) and calculated values, taking different scattering processes into account. The best agreement can be achieved if ee scattering processes are taken into account (red circles) and if in addition the dependence of the Dresselhaus constant γ on the confinement energy is considered (green triangles). Momentum scattering processes, only, do not lead to an appropriate description (blue triangles). (b) Used values for γ in dependence of the confinement energy (full symbols), estimated from Refs. [Jus95; Ley07b; Stu10; Eld11] (open symbols). The open square represents the value of γ, determined from sample E (see Sec. 6.1.2 for details).*

From the obtained values of Ω^2, the expected SDT $T_{[001]}$ can be calculated, taking into account different contributions to the microscopic scattering time τ. For the calculation of $T_{[001]}$, the expression in Eq. (5.8) for the DP SDT in the motional narrowing regime was used. Comparing the resulting values with the experimentally determined SDT $T_{[001]}$, the limiting scattering mechanism, dominating the microscopic scattering time τ, can be inferred. If τ is taken to be equal to the momentum scattering time τ_p (see Tab. 3.1), known from magneto-transport measurements, the calculated values for $T_{[001]}$ are

---

be denoted as spin splitting *constant*.

[5]The dependence of γ on the confinement energy is mainly governed by confinement energy dependent offsets between subbands in the conduction, as well as in the valence band. To a lesser extent, also the penetration of the wave function into the barrier material has an influence on the value of γ. There, the value of $|\gamma|$ is lower [Win03].

clearly lower than in the experiment (blue triangles in panel (a) of Fig. 5.7). This is a clear indication that τ_p is not the most relevant scattering time in this case.

If in addition contributions of the strongly temperature dependent ee scattering processes to the microscopic scattering time τ are taken into account, the calculated SDTs are found to be in good agreement with the experimental values[6]. The contribution $1/\tau_{ee}$ of ee collisions to the microscopic scattering rate

$$1/\tau = 1/\tau_p + 1/\tau_{ee} \tag{5.10}$$

were calculated using Eq. (2.10) and a reasonable value of $T = 15\,\mathrm{K}$ for the temperature of the electron system (green triangles in Fig. 5.7). From PL measurements (see Sec. 4.3) at a nominal sample temperature of $T = 4\,\mathrm{K}$ it could be inferred that the electron temperature is about $15\,\mathrm{K}$ under the used experimental conditions. The elevated temperature of the electron system being higher than the lattice temperature is a well-known result of optical pumping [Rya84][7].

To point out the relevance of the dependence of the spin splitting constant γ on the confinement energy E_c, the theoretically expected SDT $T_{[001]}$ was also calculated under the assumption of a fixed $|\gamma| = 8\,\mathrm{eV\mathring{A}^3}$ (red circles in panel (a) of Fig. 5.7). The agreement of experimental and calculated values is clearly reduced, underlining the importance of the dependence of γ on the confinement energy E_c. Here, it should be noted again that the numerical results shown in Fig. 5.7 are based on a careful, but rough estimation of γ. This was necessary due to the small amount of experimental data available concerning this important constant.

In conclusion, the expected dependence of the SDT $T_{[001]}$ on the QW width d could be verified. The determined values of $T_{[001]}$ get larger when the QW width d is increased. This can be well-described due to the decrease of the Dresselhaus parameter $\beta \propto \gamma(E_c)d^{-2}$, if, in addition, the dependence of the Dresselhaus spin splitting constant $\gamma(E_c)$ on the confinement energy E_c is considered. Further, the microscopic scattering time τ could be shown to be dominated by the ee scattering time τ_{ee} under the particular experimental conditions. The good agreement between the experimental and the theoretically expected values for $T_{[001]}$ can only be achieved, considering the contribution τ_{ee} from ee collisions to the microscopic scattering time τ .

5.1.2   Dependence of the in-plane spin dephasing anisotropy on the well width

Similarly as in the case of the growth-axis SDT $T_{[001]}$, the confinement length d also influences the in-plane SDTs T_{xx} and T_{yy}. In systems having an asymmetric band edge profile, the interference of the Rashba and the Dresselhaus contribution to the SO field $\boldsymbol{\Omega}$ in Eq. (5.9) can lead to a strong in-plane spin dephasing anisotropy, as discussed in detail in Sec. 2.2.7. By a variation of the QW width d, and hence the Dresselhaus parameter $\beta = \gamma\left(\frac{\pi}{d}\right)^2$, the important ratio β/α can be tuned in a controlled way, if the strength of the Rashba contribution is kept constant. In the investigated samples A-D, the Rashba contribution to the SO field results from an asymmetric, single-sided δ-doping profile. The spacer width, as well as the dopant concentration, are kept constant in order to provide a constant strength of the Rashba field throughout the sample series.

---

[6]The little mismatch of the experimental and the calculated value of the SDTs in the case of sample D $(d = 25\,\mathrm{nm})$ can most likely be attributed to a slightly higher sample temperature as in the case of samples A-C. Also a small deviation $\Delta d = d_r - d \approx 2\,\mathrm{nm}$ of the real QW width d_r from the nominal value d could explain the deviation.

[7]In addition, it was found out that the sample temperature in the continuous-flow cryostat used is always slightly higher than the nominal temperature. This is due to technical reasons (see, for details, Sec. 4.5).
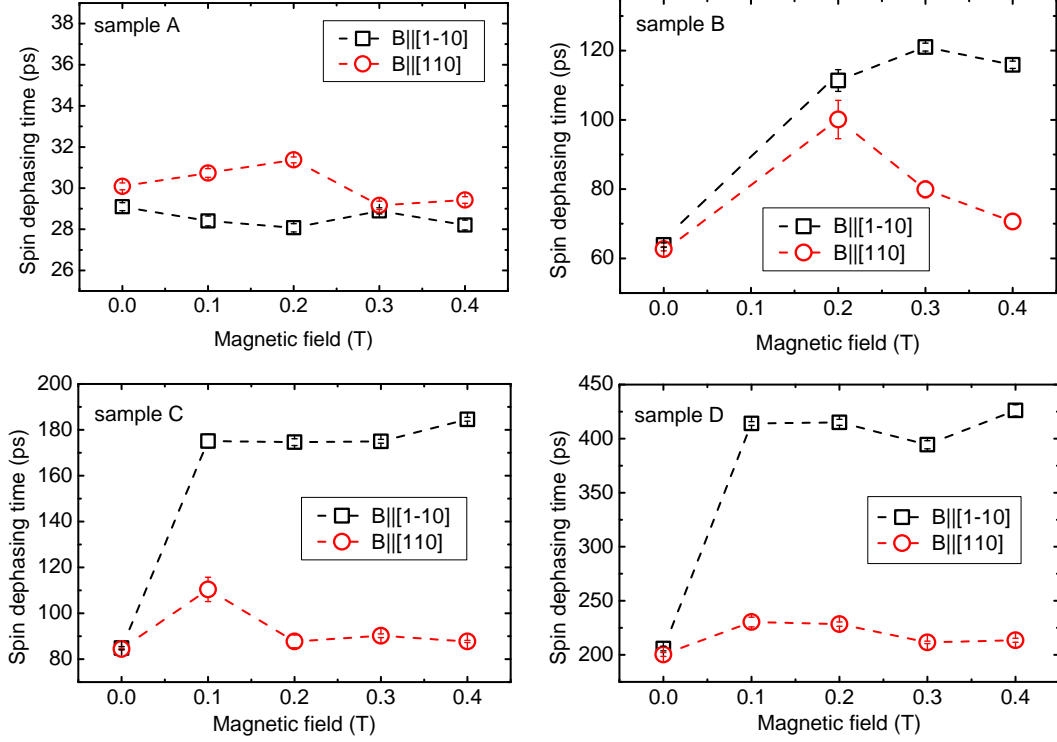
Figure 5.8: *Spin dephasing times extracted from TRKR measurements at a temperature of $T = 4\,K$ with the magnetic field applied along the $[110]$ and the $[1\bar{1}0]$ direction. The spin dephasing anisotropy is clearly visible in samples B-D. In sample A no spin dephasing anisotropy could be detected. The dashed lines are drawn in support of a better recognition.*

For the observation of the in-plane spin dephasing anisotropy, a series of TRKR measurements were performed with the magnetic field $\boldsymbol{B}$ applied along the $[110]$ and the $[1\bar{1}0]$ direction. The magnetic field forces the optically generated spin ensemble, pointing initially out-of-plane, to precess into the sample plane. There, it experiences a contribution from the in-plane spin dephasing time, resulting in the average spin dephasing time

$$\frac{1}{\overline{T}} = \frac{1}{2}\left(\frac{1}{T_{[001]}} + \frac{1}{T_{[1(\pm 1)0]}}\right), \tag{5.11}$$

as discussed in Sec. 2.2.7. In Fig. 5.8, the extracted average spin dephasing times are shown for the magnetic field $\boldsymbol{B}$ applied along the $[110]$ and the $[1\bar{1}0]$ direction. The spin dephasing times in samples B-D show a clear dependence on the orientation of the applied magnetic field. If the spin ensemble is rotated into the $[110]$ crystallographic direction due to a magnetic field $\boldsymbol{B}||[1\bar{1}0]$, the average spin dephasing time is about twice as long as if the magnetic field is oriented parallel to the perpendicular $[110]$ direction, or, without a magnetic field. This means in consequence of Eq. (5.11) that a strong in-plane spin dephasing anisotropy with $T_{[110]} \gg T_{[1\bar{1}0]}, T_{[001]}$ could be observed in the samples B-D. This anisotropy is a clear hint that in the samples B-D the ratio β/α, defined in Eq. (5.4), is close to 1.

The extraction of the ratio β/α from the measurement data can be done after calculating $T_{[110]}$ and $T_{[1\bar{1}0]}$ from the average spin dephasing times $\overline{T_{B||[1\bar{1}0]}}$ and $\overline{T_{B||[110]}}$. For sample B the ratio $\beta/\alpha \approx 2.4$ was found, whereas the ratio in sample C is about 1.4, in good agreement with earlier measurements on this sample [Sti07b]. For a value of β/α closer to 1, as it most likely could be observed in sample D, the errors in the deter-
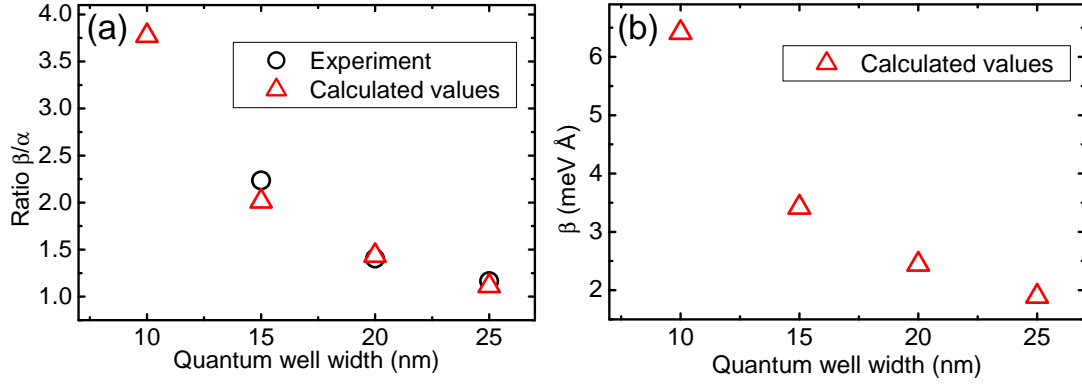
Figure 5.9: *(a) Experimentally determined values of the ratio β/α in samples B-D at a sample temperature of $T = 4\,K$ (black circles). The red triangles show the expected dependence of the ratio, assuming $\alpha = 1.7\,meV\mathring{A}$, and using the calculated values for β, shown in panel (b).*

mination of the nearly diverging in-plane SDT $T_{[110]}$ get relatively large. The average SDT $\overline{T_{B||[1\bar{1}0]}}$ is about a factor of 2 higher than $\overline{T_{B||[110]}}$ or $T_{[001]}$, meaning that the in-plane SDT $T_{[110]}$ would be infinite. Thus, uncertainties in the determination of $\overline{T_{B||[1\bar{1}0]}}$, $\overline{T_{B||[110]}}$ and $T_{[001]}$ lead to huge error bars for the determined SDT $T_{[110]}$. Therefore, the value $\beta/\alpha = 1.2$, determined for sample D, has a limited precision.

In panel (a) of Fig. 5.9, the experimentally determined values of the ratio β/α are plotted against the QW width d. As it can be seen, the ratio β/α decreases with increasing QW width d. This can be understood by looking on the well width dependence of the Dresselhaus parameter β, which was calculated (see panel (b) of Fig. 5.9) considering the dependence of the Dresselhaus constant γ on the confinement energy E_c [Win03; Ley07b; Eld11], as discussed in Sec. 5.1.1. Here, the estimated values for γ, shown in Fig. 5.7, were used again. In the sample series A-D with fixed Rashba parameter α, the expected decrease of the Dresselhaus parameter β also leads to an observable decrease of the ratio β/α if the QW width d is increased. For comparison, the red triangles in panel (a) of Fig. 5.9 represent the calculated value of β/α, assuming a value of $\alpha = 1.7\,meV\mathring{A}$. This value of α could also be reproduced in band structure calculations using the simulation software nextnano[3] developed at the Walter Schottky Institute in Munich (for details, see App. B).

In contrast to what was shown for samples B-D, in sample A no spin dephasing anisotropy could be detected. The reason for this is the relatively short spin dephasing time $T_{[001]}$, and the small absolute value of the electron g factor, determined to be about $g = -0.15$ in a comparable sample [Lec11]. Due to this, a higher magnetic field than available in the used setup would be necessary to rotate the spin ensemble into the sample plane within the spin lifetime in order to create a significant contribution of the in-plane SDTs $T_{[110]}$ and $T_{[1\bar{1}0]}$. On the other hand, due to the narrow width of the QW in sample A, and in consequence of the strong Dresselhaus field, it can be expected (see panel (a) of Fig. 5.9) that β and α are quite different. Therefore, just a weakly developed spin dephasing anisotropy is expected in this case.

5.1.3   Change of the g factor tensor components with the well width d

As pointed out in Sec. 2.2.5, the SO coupling in semiconductors strongly affects the electron g factor, leading in certain cases also to anisotropies of the g factor tensor $\hat{g}$, with non-zero off-diagonal elements g_{xy}. In particular, the asymmetric bandprofile of sam-

ples A-D in combination with the symmetry of the Dresselhaus SO field (see Sec. 2.2.2 for details) is expected to lead to an in-plane g factor anisotropy, as it was discussed theoretically [Kal93] and observed [Eld11] in recent experiments. In Ref. [Eld11] quantum structures with an opposite band gradient in the valence and the conduction band were investigated. In the present work, in contrast, the dependence of the g factor tensor components in samples having different quantum well widths and thus different strengths of the Dresselhaus field can be studied, while the Rashba field is intentionally fixed to $\alpha \approx 1.7 \, \mathrm{meV\AA}$ throughout the sample series.
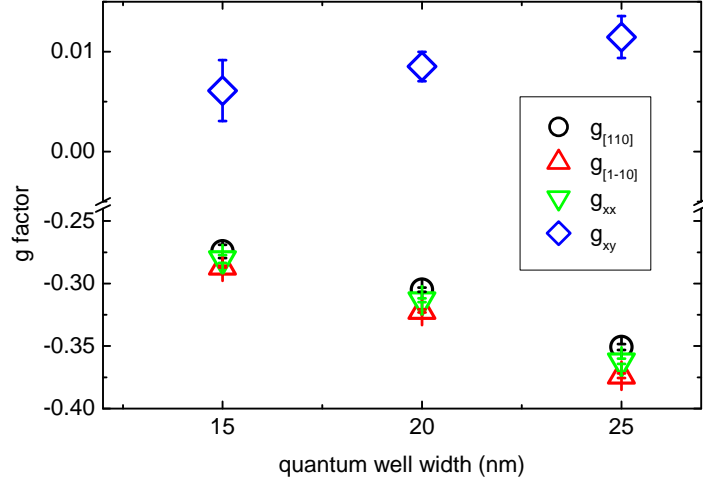

Figure 5.10: *Components of the g factor tensor $\hat{g}$. $g_{[110]}$ (black circles) and $g_{[1\bar{1}0]}$ (red triangles) are experimentally values determined from TRKR measurements at $T = 10\,K$, from which the diagonal element g_{xx} (green triangles), as well as the off-diagonal elements $g_{xy} = g_{yx}$ (blue rhombs), can be calculated.*

In Fig. 5.10, the in-plane components $g_{[110]}$ (black circles) and $g_{[1\bar{1}0]}$ (red triangles) of the g factor tensor are shown for the samples B-D, determined from TRKR measurements with the magnetic field applied along the [110] and [1$\bar{1}$0] direction. From this, the values of g_{xx} (green triangles) and g_{xy} (blue rhombs) were calculated, using the expressions in Eqs. (5.6) and (5.7), respectively. The data shown in Fig. 5.10 clearly shows the previously observed decrease [Yug07; Lec11] of g_{xx} for an increase of the quantum well width d. The penetration depth of the electron wave function into the AlGaAs barrier with a g factor of $g = 0.5$ increases for more narrow QWs, leading to an increase of the average g factor of the electrons, see Fig. 5.11. In addition, the non-parabolicity of the conduction band affects the g factor as well, if higher k values of the conduction band get occupied as a result of the larger confinement energy in more narrow QWs.

Furthermore, non-zero off-diagonal elements g_{xy} can be observed for samples B-D, which is in agreement with theoretical predictions [Kal93] and experimental findings [Eld11; Nef11]. Moreover, an increase of the off-diagonal component g_{xy} with increasing QW width can be observed, as can be seen in Fig. 5.10. It was shown theoretically[Kal93] that

$$g_{xy} = \frac{2\gamma e}{\hbar^3 c \mu_B} \left[\langle p_z^2 \rangle z - \langle p_z^2 z \rangle \right] \tag{5.12}$$

depends on the Dresselhaus constant γ and the built-in electric field E_z, determining the strength of the Rashba-type SO field. Since the Rashba field is fixed throughout the sample series, the well width dependence of g_{xy} can be assigned to the dependence of the Dresselhaus spin splitting constant γ on the confinement energy, which was shown earlier.

5.2   Dependence of spin dynamics on the sample temperature

After it was shown that the QW width d is an important parameter for spin dynamics, the influence of the sample temperature T on spin dynamics should be discussed. A temperature dependence of the DP spin dephasing time

$$\frac{1}{T_2^*} = \Omega^2(\boldsymbol{k}_F)\tau \tag{5.13}$$

can either be introduced by a change of the SO field $\Omega(\boldsymbol{k}_F)$ with temperature, or by a temperature dependence of the microscopic scattering time τ. The latter has temperature dependent contributions from momentum scattering processes due to thermally activated phonons (see, e.g. [Ash03]), and the strongly temperature dependent ee collisions, see Eq. (2.10). The resulting temperature dependence of the microscopic scattering time τ has a dramatic influence on the SDTs. This will be discussed in particular for $T_{[001]}$ in Sec. 5.2.1 for the investigated samples A-D. The results can be compared to what was reported earlier [Ley07a] for 2DESs with a lower electron mobility μ.

Besides a temperature dependent influence of τ on the SDT, the SO field $\Omega(\boldsymbol{k}_F)$ can be affected by the temperature as well. This can either be due to a change of the Fermi wave vector $k_F = \sqrt{2\pi n}$ as a result of a temperature-dependent variation of the carrier density n, or a change of the prefactors α and β in Eq. (5.9). For example, the temperature dependent transfer processes of donor electrons from the doping layer into the QW can lead to a change of the band edge profile, and hence to a change of the Rashba contribution Ω_R to the SO field. This will be discussed later in Sec. 6.2.2 also for the case of dsd high-mobility 2DESs. In 2DES with an asymmetric band edge profile, where the Dresselhaus and Rashba contributions to the SO field interfere with each other, a different temperature dependence of Ω_D and Ω_R would lead to a temperature-dependent change of the ratio β/α. As it will be discussed in detail in Sec. 5.2.2, this strongly affects the in-plane spin dephasing anisotropy.

5.2.1   Dependence of the growth-axis SDT $T_{[001]}$ on the sample temperature

For the determination of the temperature dependence of the growth-axis SDT $T_{[001]}$, zero-field TRKR traces were taken on samples A-D at different sample temperatures T ranging from nominally $4\,\mathrm{K}$ up to $130\,\mathrm{K}$ for sample B. The excitation intensity I_{ex} was fixed to $50\,\mathrm{W/cm^2}$. Throughout the sample series, an increase of the growth axis SDT $T_{[001]}$ with an increasing sample temperature is observable. However, between 80 and $90\,\mathrm{K}$ a maximum is reached (see panel (a) of Fig. 5.12). In this temperature range, the Fermi temperatures $T_F = E_F/k_B$ of the 2DESs under investigation are
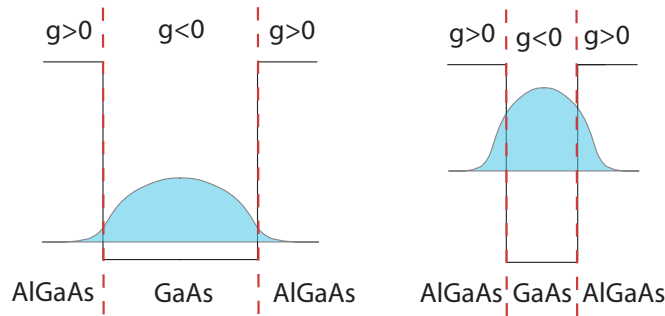

Figure 5.11: *Scheme of the position of the lowest conduction subband in QWs of different widths. The penetration depth of the electrons wave function into the AlGaAs barrier, having a different g factor, is higher for narrow QWs.*
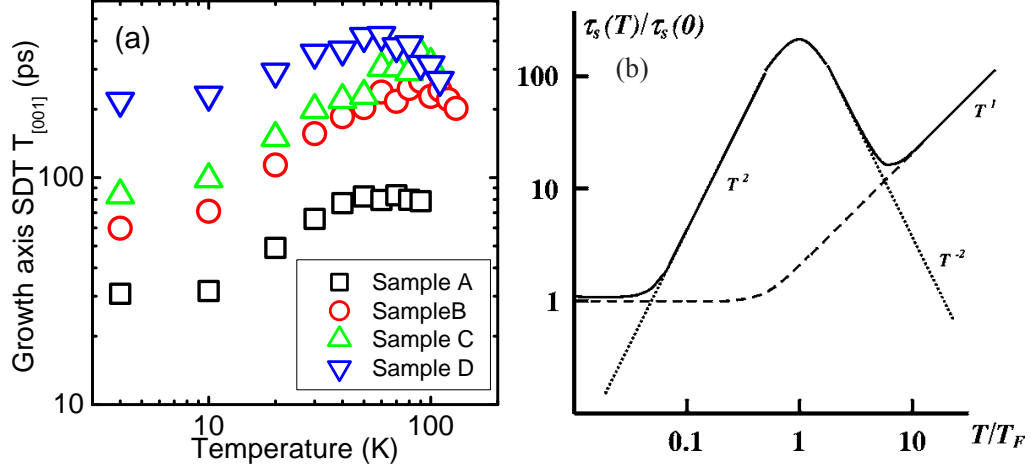
Figure 5.12: *(a) Growth axis SDTs obtained from TRKR measurements on samples A-D. (b) Expected dependence of the SDT on T/T_F (taken from [Ley07a]).*

expected to be. T_F is the temperature at which the width $\delta E = k_B T$ of the Fermi-Dirac distribution function is on the order of the Fermi energy E_F, leading to a crossover from a system of degenerate electrons to the non-degenerate state[8]. Calculating T_F from the carrier density n, which was determined from magneto-transport measurements at 4 K, yields the values shown in Tab. 3.1 in Sec. 3.1.1, ranging from about 80 to 90 K for the investigated samples A-D. If the temperature dependence of the experimentally determined growth-axis SDT $T_{[001]}$ is compared to the theory discussed in Refs. [Ley07a] and [Gla04b], the experimentally observed increase of $T_{[001]}$ can be attributed to an increase of the ee scattering rate. In contrast to the prediction of a T^2 dependence for temperatures T below T_F (see Fig. 5.12(b)), a nearly linear dependence of $T_{[001]}$ in this temperature range was observed in this work. Having a closer look on Fig. 4 of Ref. [Ley07a], the determined growth axis SDTs do not show a simple T^2 dependence as well. A possible reason for this could be the temperature dependence of both, the Rashba and the Dresselhaus parameters α and β: the Dresselhaus spin splitting constant $\gamma \propto 1/\sqrt{E_G}$ can be expected to change with the temperature, due to a dependence on the temperature-dependent band gap energy E_G [Var67]. For the Rashba contribution, a temperature dependence of α was already reported [Eld08]. Therefore, the increase of the resulting SO field $\boldsymbol{\Omega}$ with temperature could compensate the decrease of the microscopic scattering time ($\propto T^{-2}$) to some degree. This would result in a temperature dependence of $T_{[001]} \propto T^{2-\epsilon}$, where $\epsilon > 0$ describes the temperature dependence of the SO field $\boldsymbol{\Omega}^2 \propto T^\epsilon$.

---

[8]The occupation of electron states is described by the step-like Fermi-Dirac distribution function, see Eq. (4.8). In the case of a degenerate electron gas, the width $\delta E = k_B T$ of the step at the Fermi edge is small compared to the Fermi energy E_F of the electron gas. In the limit of a completely degenerate electron gas (T=0), all states in the momentum space are fully occupied up to the Fermi energy E_F. In contrast, states, having a higher energy $E > E_F$, are completely unoccupied. At higher temperatures $T > T_F$, or in the case of a low carrier concentration n, the Fermi-Dirac distribution can be approximated by the classical Maxwell-Boltzmann distribution function $f(\epsilon, T) \propto \exp(-\epsilon/k_B T)$. An electron system is denoted as non-degenerate, if the fermionic carriers obey to Maxwell-Boltzmann statistics.
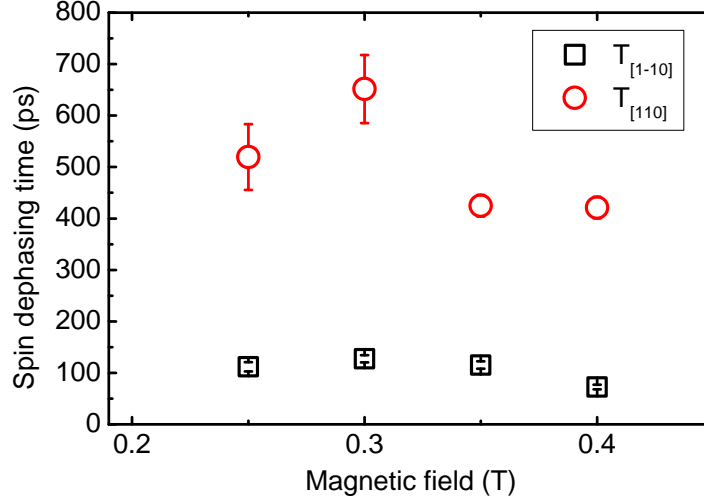
Figure 5.13: *In-plane SDTs $T_{[110]}$ and $T_{[1\bar{1}0]}$ of sample B at a nominal sample temperature of 4 K, determined by a fit using the model in Eq. (2.51).*

5.2.2   Dependence of the in-plane spin dephasing anisotropy on the sample temperature

The in-plane spin dephasing anisotropy, which was shown in Sec. 5.1.2 for samples B-D, having a different QW width d, was also studied in dependence of the sample temperature T. For each temperature, therefore, sets of TRKR traces were taken. Fitting this data with Eq. (2.51) allows for the determination of the SDTs $T_{[110]}$, $T_{[1\bar{1}0]}$ and $T_{[001]}$ as well as the elements of the electron g factor tensor $\hat{g}$. The extraction of these values was done as follows: First, the TRKR trace without a magnetic field applied was fitted with a simple exponentially decaying function, yielding the out-of-plane SDT $T_{[001]}$. Keeping this value fixed, the values of $T_{[1\pm10]}$, as well as the g factor along the corresponding crystallographic direction, was determined by a fit of the data taken at $|B| > 0$ mT, using the model in Eq. (2.51). Fig. 5.13 shows the extracted values for both in-plane SDTs of sample B at a nominal temperature of 4 K for different values of the applied magnetic field $\boldsymbol{B}$.

As in Sec. 5.1.2, the ratio β/α should be calculated from $T_{[110]}$ and $T_{[1\bar{1}0]}$ for every temperature step, being a measure for the spin dephasing anisotropy. The values of $T_{[110]}$ and $T_{[1\bar{1}0]}$ extracted from the TRKR traces show a certain spread, as can be seen from the data presented in Fig. 5.13. Hence, for the determination of β/α the mean values of $T_{[1\pm10]}$ were calculated from the datapoints[9] at $B = 0.3$ T, $B = 0.35$ T and $B = 0.4$ T. The resulting ratios β/α, determined on sample B, are shown in Fig. 5.14 for temperatures ranging from $T = 4$ K up to $T = 130$ K. Within a certain error, an increase of β/α can be observed in this temperature range.

A similar behavior can also be observed in samples C and D, as it is presented in Fig. 5.15. Beyond a sample temperature of $T \approx 90$ K, the ratio β/α reaches relatively high values and spin dephasing is nearly isotropic. In contrast, in those two samples spin dephasing is strongly anisotropic at low temperatures. In sample C, the calculated values of β/α get very close to 1 from $T = 10$ K to $T = 30$ K, whereas in sample D values close to 1 were found between $T = 4$ K and $T = 80$ K. The values close to 1 result from extremely long SDTs $T_{[110]}$ extracted from the corresponding TRKR traces. Obviously, an extremely long SDT determined from the relatively short time window, being accessible in a TRKR measurement, is subject to a huge error. Having a closer

---

[9]In the case of sample D, the magnetic field values were $B = 0.2$ T, $B = 0.3$ T and $B = 0.4$ T.
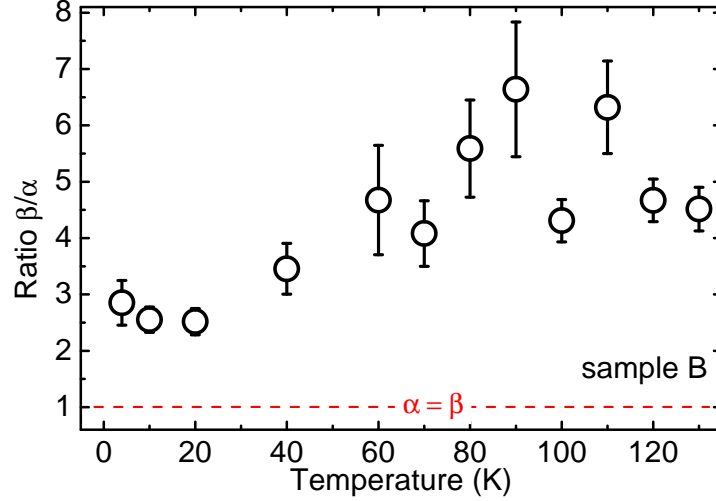
Figure 5.14: *Observed change of the spin dephasing anisotropy: the ratio β/α increases with increasing temperature.*

look at Eqs. (2.51), (2.52) and (5.2), it can be seen that for extremely long SDTs $T_{[110]} \gg T_{[001]}$ spin dynamics is no longer significantly influenced by the precise value of $T_{[110]}$. If, in particular, the in-plane spin dephasing rate $\Gamma_{[110]}$ becomes as small as the error $\Delta\Gamma_{[001]} = \Delta(1/T_{[001]})$ of the out-of-plane spin dephasing rate $\Gamma_{[001]}$, the value of $T_{[110]}$ is in principle completely undetermined.

Facing this problem, the two limiting cases of the used measurement method should be emphasized: The ratio β/α cannot be determined with precision, if the spin dephasing anisotropy is too *weak*, i.e., if the in-plane SDTs $T_{[110]}$ and $T_{[1\bar{1}0]}$ are equal within their error. In contrast, if the in-plane spin dephasing anisotropy is too *strong*, $T_{[110]}$ cannot be determined with precision. In consequence, it cannot be determined how close the ratio of β/α is to 1.

To get around this problem, a different approach could be used for future experiments. In this work, in-plane SDTs were only determined for two angles $\phi = \pm45°$ between the magnetic field and the [100] crystallographic axis. In order to achieve a higher precision in the determination of the ratio β/α, measurements for additional values of ϕ could be performed, as it was done in the literature, e.g., in Ref. [Lar08]. From data points obtained for different angles ϕ, having a finite in-plane SDT T_{ϕ}, the determination of the ratio β/α should be possible with a higher accuracy, using the expression

$$\frac{1}{2}\left[\Gamma_{[001]} + \Gamma_{\phi}\right] = \frac{3C\beta^2}{4}\left[1 + \left(\frac{\alpha}{\beta}\right)^2 + \frac{2\alpha}{3\beta}\sin(2\phi)\right]. \tag{5.14}$$

Eq. (5.14) was presented by Eldridge *et al.* [Eld11] on the basis of calculations by Averkiev *et al.* [Ave99].

Keeping in mind the limitations of the measurement method used in this work, the obtained results on the low temperature dependence of the observed spin dephasing anisotropy in the samples C and D should be discussed. As can be seen from Fig. 5.15, both samples show a ratio of β/α very close to 1 in a certain temperature range. Data points without error bars reflect situations as described above with $T_{[110]} \gg T_{[001]}$, where $\Delta T_{[110]} \approx T_{[110]}$ is valid for the uncertainty $\Delta T_{[110]}$ of $T_{[110]}$. Nevertheless, the relation $T_{[110]} \gg T_{[001]} \approx T_{[1\bar{1}0]}$ still holds, suggesting that β/α is close to 1. This can be taken as a hint that especially in sample D a regime with $\alpha \approx \beta$ is accessible in a wide temperature range. Unfortunately, a more precise determination of the values β/α is
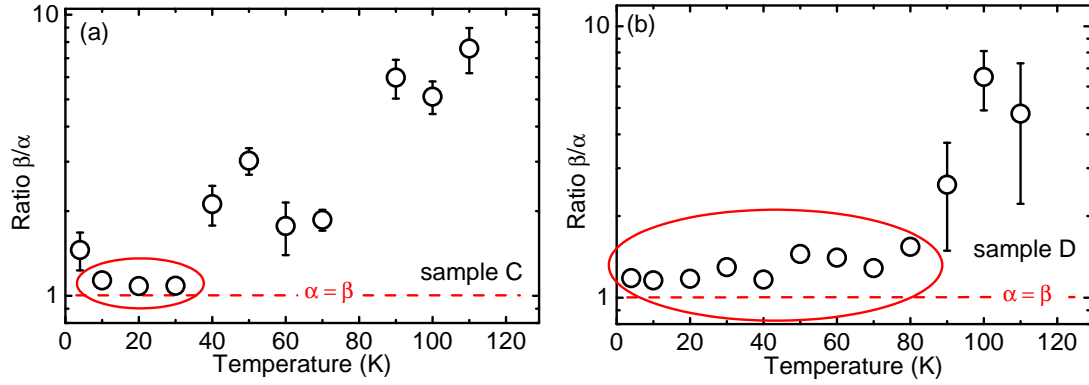
Figure 5.15: *Experimentally observed dependence of the spin dephasing anisotropy on the sample temperature in (a) sample C and (b) sample D. The ratio β/α increases with increasing temperature. The values inside the red ellipses having no error bars reflect the limitation of the measurement method and cannot be given with precision. Hence, they must not be over-interpreted.*

not possible with the applied method. Hence, the values without error bars, marked by the red ellipses, must not be over-interpreted.

In summary, a temperature dependence of the ratio β/α has been experimentally observed in samples B-D. From this, a different temperature dependence of the Rashba and the Dresselhaus parameter $\alpha(T)$ and $\beta(T)$ can be inferred. However, the origin of this different temperature dependence could not be identified unambiguously. For this, a more precise determination of β/α and a detailed study of the temperature dependence of the band edge profile of the 2DES, as well as the carrier density n would have been necessary. Moreover, the applied measurement method allows just the determination of the ratio[10] $|\beta/\alpha|$. The independent determination of $\alpha(T)$ and $\beta(T)$ maybe could be done in future experiments, using magnetogyrotropic photogalvanic effects [Gan04; Lec09; Lec11]. Here, a separation of the SIA and BIA contributions to the SO field is possible.

5.3 Dependence of spin dynamics on the carrier density

In order to investigate how the SDTs, as well as the spin dephasing anisotropy, can be influenced by the application of an external gate voltage, a series of TRKR measurements was performed on a piece of sample B. On this piece, denoted as B', a semi-transparent NiCr gate was fabricated, following the recipe presented in Sec. 3.2.2. First, in order to find the gate voltage range, in which the sample can be operated without suffering damage, the I-V characteristics of the sample were determined. As depicted in panel (a) of Fig. 5.16, the I-V characteristics has a diode-like shape. If the sample is negatively biased, the absolute value of the current $|I|$ through the sample stack strongly increases, and exceeds $|I| > 100\,\mu\text{A}$ at $U_G = -2\,\text{V}$. In contrast, the current clearly shows a slower increase for positive biases. As a consequence, the gate voltage range for TRKR measurements was restricted to gate voltages $U_G > -1.5\,\text{V}$ in order to avoid high currents, which may lead to some sample damage.

The sample was further characterized using PL measurements. As can be seen from panel (b) of Fig. 5.16, the FWHM of the PL traces strongly depends on the applied gate voltage. It has been already mentioned (see Sec. 4.3) that the spectral width ΔE of the PL is directly related to the carrier density n of a 2DES. Thus, the increasing

---

[10]Or $|\alpha/\beta|$, as was already noted. For details, see Ref. [Ave06].
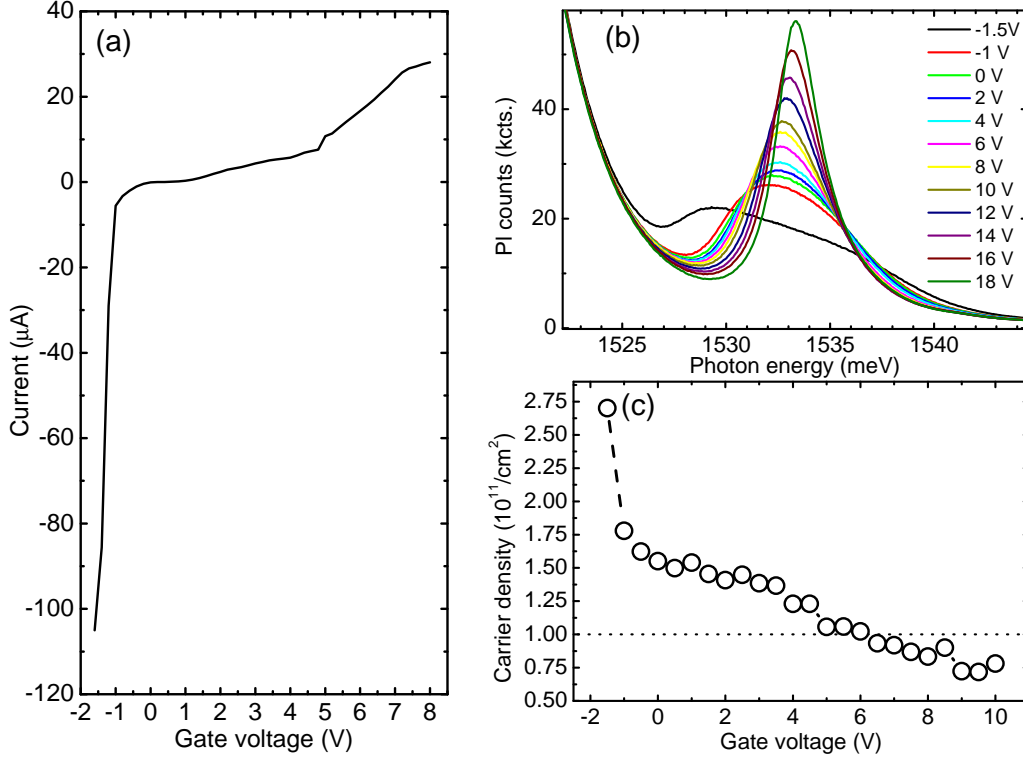
Figure 5.16: *(a) The I-V characteristics of sample B' show a diode-type behavior. (b) PL traces of sample B' for different applied gate voltages. (c) Carrier density inside the QW extracted from the PL data shown in panel (b). The data shown in panels (a) and (b) were taken at a nominal sample temperature of $T = 4$ K. The dotted line in panel (c) marks the carrier density region, in which the transition to the excitonic regime occurs. The dashed line is drawn in support of a better recognition.*

spectral width ΔE for negative gate voltages can be interpreted as an increase of the carrier density n. A positive bias leads to a depletion of the 2DES, connected with more narrow PL peaks. At higher gate voltages, a smooth transition to a very narrow excitonic lineshape can be observed in the PL traces. Using Eq. (4.7), the carrier density of the 2DES can be estimated for every gate voltage from the spectral width of the PL. Panel (c) of Fig. 5.16 shows the carrier density n obtained in this way. At an increasing positive bias, the carrier density n is reduced, whereas an increase of n can be observed for negative applied voltages. For gate voltages $U_G > +5$ V the carrier density n falls below $1 \cdot 10^{11}$ cm^{-2}. Below this carrier concentration, a transition between free electrons and the excitonic regime takes place [Kle85a; Shi95]. This work focusses on spin dynamics of free electrons; therefore, the upper limit of the applied gate voltages was fixed at $U_{max} = 5$ V. At this gate voltage and the corresponding carrier density, the system is likely to consist mainly of free electrons. Combined with the lower limit of the gate voltage resulting from the diode breakdown voltage, spin dynamics of free electrons can be studied for gate voltages -1.5 V $< U_G < +5$ V in sample B'.

The dependence of the carrier density n on the applied external gate voltage U_G, shown in panel (c) of Fig. 5.16, can be qualitatively understood by analyzing a simplified band edge profile of sample B', as shown in Fig. 5.17. A positive applied gate voltage shifts the conduction band upwards, and thus leads to a depletion of the 2DES. At the same time, the band bending in the QW region can be expected to be reduced. In contrast, for negative gate voltages the carrier density n increases. Consequently, also the band bending increases, which directly determines the strength of the Rashba
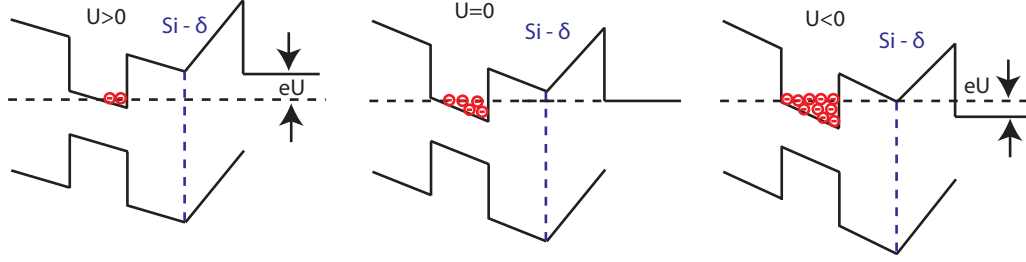
Figure 5.17: *Simplified picture of the band edge profile of sample B' in the presence of an external applied gate voltage U_G. The carrier density n, as well as the band bending inside the QW, changes in dependence of U_G.*

contribution to the SO field.

Of high importance is the fact that both, the carrier density *and* the band bending are affected by the applied gate voltage. The carrier density n determines the Fermi wavevector $k_F = \sqrt{2\pi n}$ and thereby the amplitude $\Omega(k_F)$ of the SO field, which affects the SDT as

$$\frac{1}{T_2} \propto \Omega^2(\boldsymbol{k}_F)\tau, \tag{5.15}$$

for details see Sec. 2.2.6. Besides the SO field, also the two contributions τ_p and τ_{ee} of the microscopic scattering time τ are affected by a change of the carrier density n: the electron mobility μ is reduced for lower n, leading to a shorter transport scattering time τ_p (see, e.g. [Rös10]). In addition, for a decreasing carrier density n, also the ee scattering time τ_{ee} is reduced, as can be deduced from Eq. (2.10).

In conclusion, the zero-field SDT $T_{[001]}$ can be expected to show a clear dependence on the applied gate voltage U_G. In panel (a) of Fig. 5.18, the experimentally observed
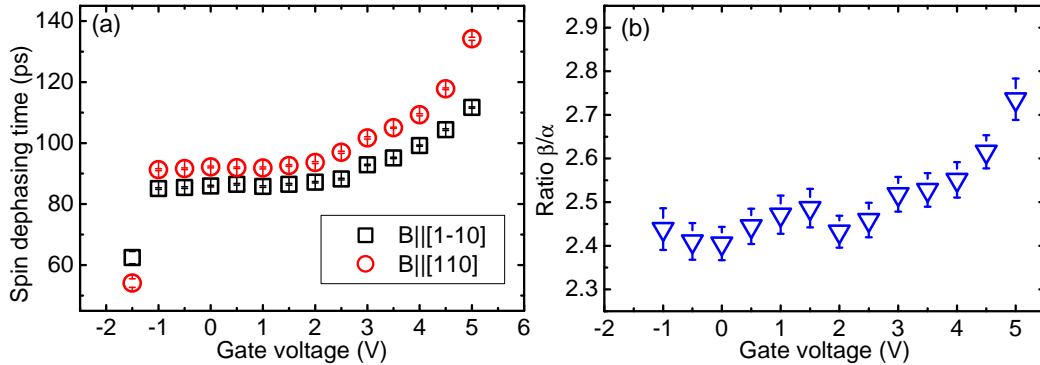

Figure 5.18: *(a) Zero-field SDT $T_{[001]}$ and (b) ratio β/α in dependence of the applied gate voltage U_G determined by TRKR measurements at a sample temperature of $T = 4\,K$.*

dependence of the zero-field SDT $T_{[001]}$ can be seen. $T_{[001]}$ clearly shows an increase in the interval $-1.5\,\text{V} < U_G < 5\,\text{V}$, in which the carrier density is reduced from about $2.75 \cdot 10^{11}\,\text{cm}^{-2}$ to about $1 \cdot 10^{11}\,\text{cm}^{-2}$ (see panel (c) of Fig. 5.16). Therefore, the experimentally observed dependence of $T_{[001]}$ on the applied gate voltage U_G is qualitatively in agreement with the expectation, based on the framework of DP spin dephasing, as discussed above. A quantitative analysis of the gate voltage dependence of $T_{[001]}$ is not part of this work.

Of particular interest in this work is the in-plane SDA, generated by the interference of the Dresselhaus and the Rashba contribution to the SO field. As stated above, an

applied gate voltage U_G results, besides the influence on the carrier density, also in a change of the band bending and the electric field E_z, present in the QW region. As depicted in Fig. 5.17, the band bending, and hence the built-in electric field E_z is reduced for a positive bias $U_G > 0$, which leads to a depletion of the 2DES. In contrast, E_z increases for negative gate voltages U_G, leading to an increase of the carrier density n inside the QW. E_z directly affects the Rashba contribution $\Omega_{SIA,2D}$ (see Eq. (2.24)) to the SO field, leaving the Dresselhaus contribution unchanged. Due to this, a change of the ratio β/α with U_G can be expected, manifesting itself in a dependence of the in-plane SDA on the externally applied gate voltage U_G.

In the same way as discussed in Secs. 5.1.2 and 5.2.2, the ratio β/α can be determined for a set of gate voltages U_G from the in-plane SDA. For this reason, series of TRKR measurements were performed with the external magnetic field applied along the [110] and [1$\bar{1}$0] crystallographic direction. The relevant in-plane SDTs $T_{[110]}$ and $T_{[1\bar{1}0]}$ were extracted by fitting the model shown in Eq. (2.51) to the data[11]. From these values, the ratio β/α can be calculated, using Eq. (5.4). Panel (b) of Fig. 5.18 shows the determined values for a nominal sample temperature of $T = 4$ K. In the investigated gate voltage range, a slight increase of β/α for an increasing value of U_G can be observed. This can be attributed to a decrease of the Rashba parameter $\alpha = 2\alpha_R E_z$: a higher positive gate voltage results in a lower band bending, and hence in a lower electric field E_z, leading to a smaller value of α. In contrast, the Dresselhaus parameter $\beta = \gamma \left(\frac{\pi}{d}\right)^2$ is not affected. Therefore, the variation of the ratio β/α is determined by the gate voltage dependence of the Rashba parameter α.
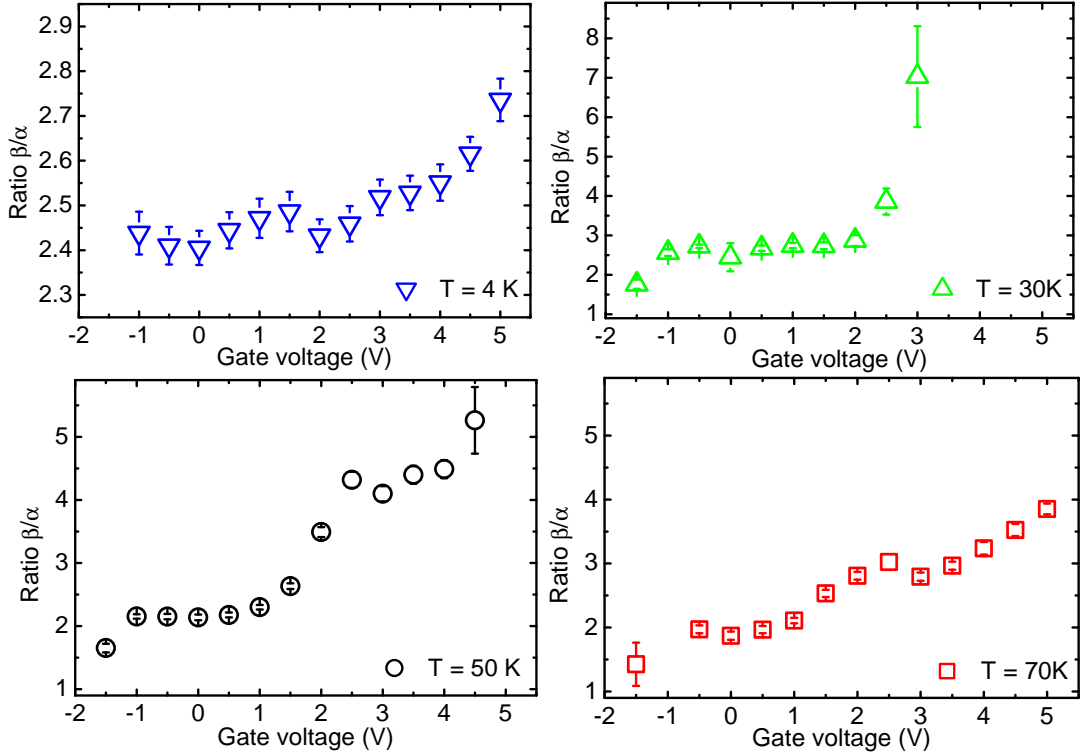
Figure 5.19: *Dependence of the ratio β/α on an applied gate voltage. The gate voltage dependence is shown for sample temperatures of 4, 30, 50 and 70 K.*

---

[11]It should be noted that in the case of sample B' the TRKR signal showed an additional contribution, which could be identified via the electron g factor of $g_{sub.} = -0.44$ as spin dynamics in the nominally undoped GaAs substrate. Therefore, an additional term $s_{0,sub.} \exp^{-t/T_{sub.}} \cos\left(g_{sub.}\mu_B B/\hbar t\right)$ describing this bulk spin dynamics contribution was added to the fitting function.

The gate voltage dependence of the ratio β/α was determined for sample temperatures $T = 30$, 50 and 70 K, as well. Similar to what was observed at $T = 4$ K, the ratio β/α increases with the gate voltage U_G. Interestingly, the change of β/α in the investigated voltage range is much larger at elevated temperatures: as can be seen from the data shown in Fig. 5.19, the extracted values of β/α at $T = 50$ K range from 1.6 up to about 5. In contrast, at $T = 4$ K just a small variation $\Delta(\beta/\alpha) \approx 0.3$ was observed. The reason for this behavior as well as a qualitative understanding still lacks. One more open question can be found in the apparent deviation of the determined ratio β/α in the unbiased sample B' from the corresponding value in sample B without the NiCr gate for temperatures $T \geq 30$ K. A reason for the significant deviation could not be identified unambiguously. One possible explanation for this could be that the NiCr gate has a considerable influence on the temperature dependence of the band edge profile in sample B'. Thus, samples B and B' might no longer be comparable at elevated temperatures.

In conclusion, the qualitative dependence of the in-plane SDA (which is connected to the ratio β/α) on the external applied gate voltage was demonstrated for sample B'. It could be shown that the gate voltage can be used to tune the ratio β/α in sample B' within a certain range, which was found to be small at $T = 4$ K. In addition, the dependence of the SDT $T_{[001]}$ on the applied gate voltage was presented: the gate-voltage-induced change of the carrier density n strongly affects the SDTs in the sample. This was displayed using the example of $T_{[001]}$. It should be noted that a change of the SDT depending on the gate voltage may generate some additional problems for possible realizations of the SFET proposed by Datta et al. [Dat90].

5.4 Dependence of spin dynamics on the excitation intensity

In this section, the dependence of the out-of-plane SDT $T_{[001]}$ on the excitation intensity I_{ex}, and the degree of initial spin polarization (DISP) of the 2DES will be presented. As was experimentally shown by Stich et al. [Sti07a; Sti07c], the initial spin polarization present in a 2DES has a strong influence on the spin dephasing properties. The experiments shown in Refs. [Sti07a; Sti07c] were performed on a piece of the same wafer sample C was taken from. Here it will be discussed, whether the dependence on the initial spin polarization is also observable in samples A and B[12].

As pointed out in Sec. 2.2.3, the DISP P (see Eq. (2.29)) in a 2DES after optical excitation depends on the density n_{opt} and the degree of spin polarization of the optically excited carriers as well as on the resident carrier density n of the 2DES. Therefore, the DISP P of the 2DES is affected by both, a change of the intensity I_{ex} of the exciting laser pulses determining the optically excited carrier density n_{opt}, as well as a change of the degree of circular polarization of the laser light, which governs the degree of spin polarization of the optically generated carriers.

In the experiments presented in this section, the excitation intensity I_{ex} was varied, while the degree of circular polarization of the pump beam was kept constant. A series of TRKR measurements was performed with $2\,\mathrm{W/cm^2} < I_{ex} < 1000\,\mathrm{W/cm^2}$ without an applied magnetic field, from which $T_{[001]}$ was determined by an exponential fit. Panel (a) of Fig. 5.20 shows the experimentally determined dependence of $T_{[001]}$ on the excitation intensity. In the applied excitation intensity range, a strong increase of $T_{[001]}$ is visible. The most probable reasons for this strong increase could be a pump-induced heating of the sample, the increase of the DISP, or both of them.

In order to check the influence of pump-induced heating, PL measurements were performed for a set of excitation intensities I_{ex}, from which the pump-induced change of the electron temperature T_e of the 2DES could be extracted. The relevant temperature

---

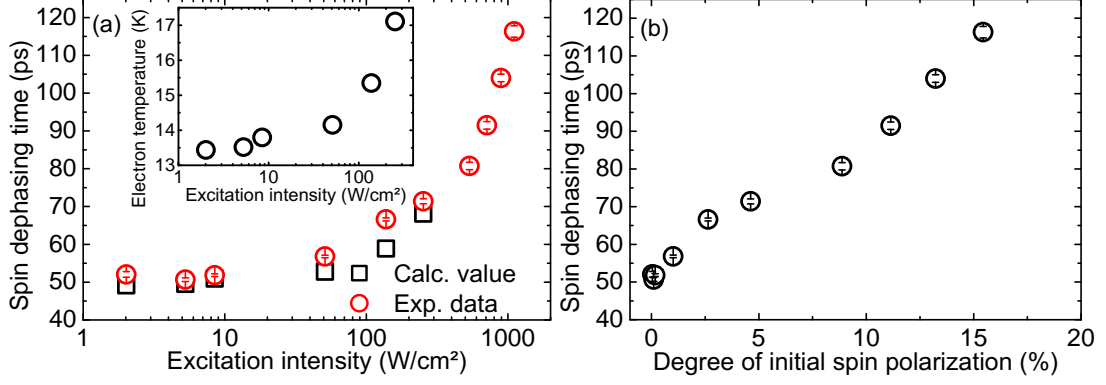[12]For sample D, such measurements were not performed.

Figure 5.20: *(a) Experimentally determined SDT $T_{[001]}$ (red circles) in sample B and calculated values (black squares), taking into account the change of the electron temperature T_e plotted against the excitation intensity. (b) Experimentally determined SDT $T_{[001]}$ determined by TRKR measurements on sample B plotted against the calculated value of the DISP of the 2DES.*

T_e was determined from the high-energy tail of the PL, as discussed in Sec. 4.3. As can be seen in the inset in panel (a) of Fig. 5.20, an increase of the excitation intensity I_{ex} leads to an increase of the electron temperature T_e of the 2DES in sample B. In consequence, the strongly temperature dependent ee scattering time τ_{ee} (see Eq. (2.10)) and hence the microscopic scattering time τ will decrease. Therefore, from Eq. (5.8) one can expect an increase of the SDT $T_{[001]}$ for higher excitation intensities I_{ex}. The black squares in panel (a) of Fig. 5.20 represent calculated values of $T_{[001]}$, taking into account the available values[13] of T_e for the particular excitation intensities. Comparing these values to the experimental data, it can be deduced that the observed increase of $T_{[001]}$ is correlated most likely with the pump-induced heating of the 2DES.

In contrast, panel (b) of Fig. 5.20 shows the dependence of $T_{[001]}$ in sample B with respect to the calculated value of the DISP P. The nearly linear increase of $T_{[001]}$ with P is clearly visible. However, from the presented data it cannot be unambiguously shown, that the increase of $T_{[001]}$ is only governed by the increase of the DISP. For this reason, a measurement series as presented in Refs. [Sti07a; Sti07c] with a varied degree of circular polarization of the pump beam would be suitable, where the total intensity of the pump beam, and hence the pump-induced heating could be kept constant.

However, the situation looks different in sample A: here, the experimentally determined SDTs $T_{[001]}$ deviate from the calculated values, taking into account only the influence of pump-induced heating. As it is shown in panel (a) of Fig. 5.21, only for the lowest excitation intensities I_{ex} the calculated values describe the experimental data very well. For higher excitation intensities, the experimentally determined SDT drastically exceeds the calculated value. One reason for this deviation could be that the temperature T_e of the electron system determined from PL measurements in this case is quite different from the temperature T_e under the conditions of TRKR measurements, at least for higher excitation intensities. If $T_{[001]}$ is plotted against the calculated value of the DISP P (see panel (b) of Fig. 5.21), a nearly linear increase of $T_{[001]}$ with the increasing DISP P can be observed. This behavior of the 2DES in the more narrow QW

---

[13]It should be noted, that the experimental conditions in TRKR and PL measurements are quite different: While the laser wavelength is tuned resonantly to the absorption edge of the 2DES in TRKR experiments, in PL measurements a significantly shorter wavelength is used for excitation. Due to the different excess energies of the optically generated electron-hole pairs, the resulting electron temperature T_e in these two cases may be different under the conditions present in TRKR and PL measurements.
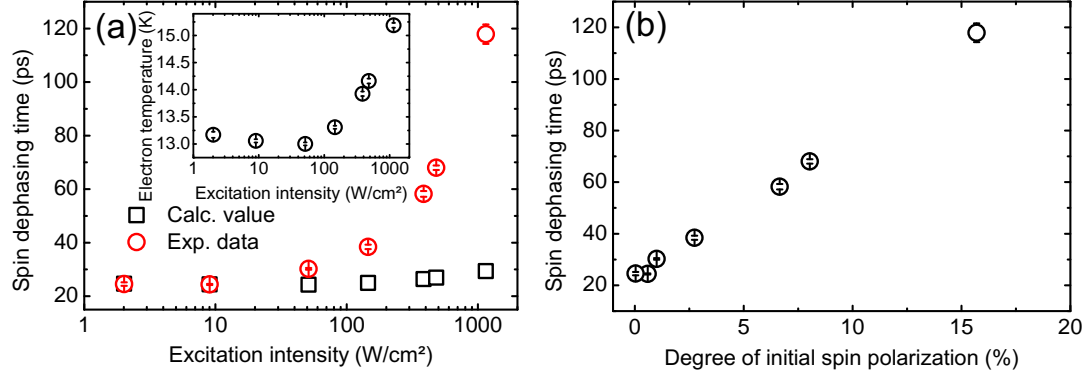
Figure 5.21: *(a) Experimentally determined SDT $T_{[001]}$ (red circles) in sample A and calculated values (black squares), taking into account the change of the electron temperature T_e plotted against the excitation intensity (depicted in the inset). (b) Experimentally determined SDT $T_{[001]}$ determined by TRKR measurements on sample A plotted against the calculated value of the DISP of the 2DES.*

of sample A is similar to what could be observed in sample B. As it was discussed above for sample B, in future experiments the total intensity of the pump beam should be kept constant, what would allow for a clear separation of the influence of an increasing DISP and pump-induced heating of the 2DES. Otherwise, the contribution of both effects on the SDT $T_{[001]}$ cannot be determined unambiguously.

In conclusion, a strong dependence of $T_{[001]}$ on the excitation intensity I_{ex} has been proven. This may be related to the pump-induced heating of the 2DES, which could be observed in some PL measurements, or to the increase of the degree of initial spin polarization of the 2DES. Unfortunately, the available measurement data did not allow for a clear separation of these two relevant contributions, which can affect the SDT $T_{[001]}$.

Chapter 6

Spin dynamics in high-mobility two-dimensional electron systems with a symmetric band edge profile

In this chapter the focus will be on spin dynamics in symmetrically grown and doped QWs, as presented in Sec. 3.1.2.

In samples grown along the [001] crystallographic direction, the highly symmetric band edge profile allows for highest mobilities and, consequently, for extremely long microscopic scattering times τ at very low temperatures $T < 4$ K. Under these conditions, the weak scattering regime of the DP mechanism is accessible, and coherent spin dynamics can be observed. The first part of this chapter deals with coherent oscillations of an optically excited spin ensemble. Even without an applied external magnetic field, the spin ensemble will be shown to precess about the SO field $\boldsymbol{\Omega}_D(\boldsymbol{k})$. If a magnetic field perpendicular to the sample plane is applied, the electrons fulfill a cyclotron motion, while the spin precesses about the SO field. This leads to a characteristic change of the beating pattern, and the cyclotron effect on coherent spin precession can be observed [Gri09].

The second part of this chapter treats spin dynamics in 2DESs embedded in (110)-grown heterostructures with a highly symmetric band edge profile. As discussed in Sec. 2.2.7, in such structures a strong spin dephasing anisotropy of in-plane and out-of-plane oriented spins can be expected. The observation of strongly anisotropic spin dephasing will be presented in Sec. 6.2.1, followed by a discussion of the temperature dependence of this anisotropy (see also [Gri12]). Finally, it will be shown that extremely long SDTs up to about 250 ns can be observed in sample G under conditions of optical gating (see Sec. 2.1.3). This will be related to a drastic reduction of the 2D carrier density n, which can be mapped by PL measurements (see Sec. 4.3).

6.1 Coherent spin dynamics in (001)-grown 2DESs

6.1.1 Zero-field coherent spin precession

Due to the high mobility $\mu = 14.8 \cdot 10^6$ cm^2/Vs of the 2DES in sample E at low temperatures, the electrons can move ballistically over distances on the order of a few microns without being scattered. Under such conditions, the weak scattering regime of the
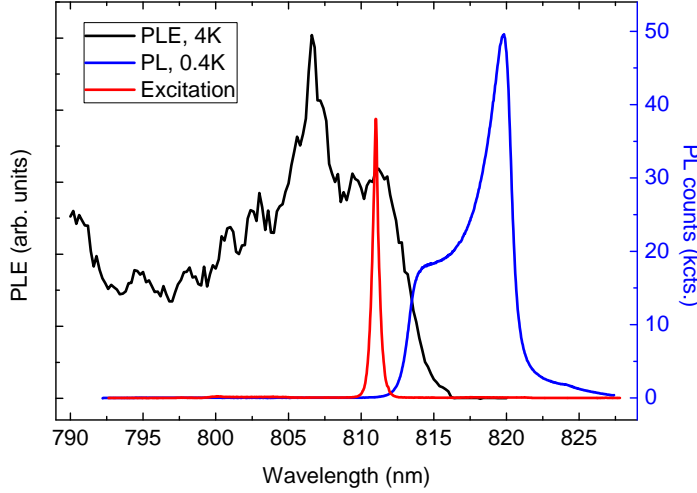
69

Figure 6.1: *Spectral position of the pump laser with respect to the PL and PLE signal of the sample. The laser is tuned to a wavelength slightly above the Fermi energy of the 2DES, where the PLE signal shows a local maximum.*

DP mechanism (see Sec. 2.2.6) is accessible, where coherent oscillations of an optically generated spin ensemble about the SO field can be observed [Ley07b; Sti07c; Gri09].

In this work, coherent spin dynamics in the weak scattering regime of the DP mechanism were studied on sample E. In order to achieve lowest temperatures, the heat input into the sample had to be kept as small as possible. For the purpose of a reduced absorption of laser power in the sample substrate, an optically thin piece of sample E was fabricated using the recipe presented in Sec. 3.2.1. This sample was initially characterized using PL and PLE measurements (see Sec. 4.3). Fig. 6.1 shows the PL trace obtained from sample E at a temperature of $T = 0.4$ K, where the sample was illuminated with 780 nm light from a pulsed Ti:sapphire laser. It also depicts a PLE measurement performed by Dr. Michael Hirmer at a sample temperature of 4 K, which clearly shows the inset of absorption in the vicinity of the Fermi edge of the sample. For wavelengths λ_{ex} longer than 815 nm, the 2DES is nearly transparent, while a maximum of the absorption appears at about 811 nm, as can be seen in Fig. 6.1. In order to generate a significant spin polarization in the 2DES, the wavelength λ_{ex} of the laser, used in the TRFR measurements presented later in this section, was tuned to this maximum value of the absorption, slightly above the Fermi energy of the 2DES. There, in addition to the high absorption of the 2DES, the wavelength-dependent Verdet constant[1] $V(\lambda)$ has a higher value than directly at the Fermi edge, where $V(\lambda)$ changes its sign, resulting in a vanishing Faraday angle $\Theta \propto V(\lambda) = 0$. In the case of sample E, a maximum of the Faraday signal could be detected at a spectral position $\lambda_{ex} = 811$ nm of the exciting laser. The spectral position of the laser relative to the PL and the PLE signal of the sample can be seen in Fig. 6.1.

After the pre-characterization, spin dynamics in sample E were revealed at a sample temperature of $T = 4.5$ K, using TRFR measurements. As shown in panel (a) of Fig. 6.2, the TRFR trace shows an oscillatory behavior even without an external magnetic field applied and is damped out after about 63 ps. The oscillations of the signal can be attributed to a coherent precession of the total spin ensemble about the Dresselhaus SO field $\boldsymbol{\Omega}_D(\boldsymbol{k})$: while the electrons move through the crystal with a wave vector $\boldsymbol{k}$, the electron spins precesses about the k-dependent SO field $\boldsymbol{\Omega}_D(\boldsymbol{k})$. Due to the long

---

[1]The typical dependence of the Faraday/Kerr angle on the photon energy of the probe beam is, e.g., depicted in [Fur07].
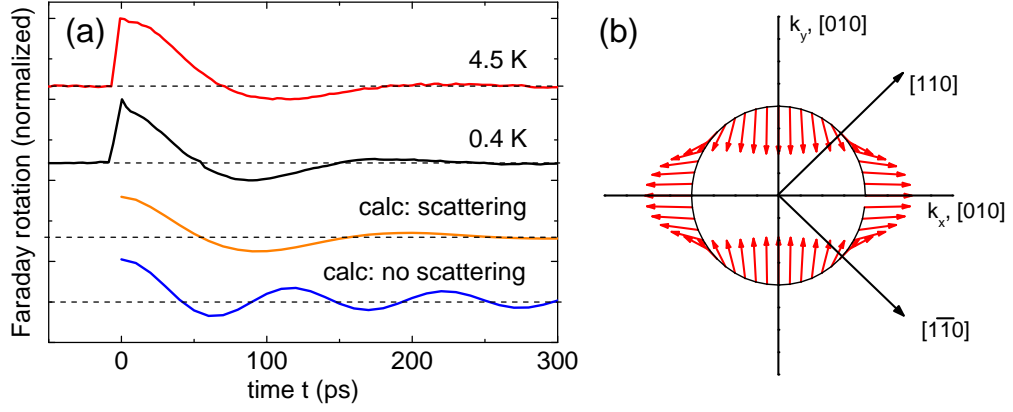
Figure 6.2: *(a) Zerofield TRFR traces of sample E, obtained at sample temperatures of $T = 4\,K$ and $T = 0.4\,K$ using an excitation intensity $I_{ex} \approx 50\,W/cm^2$. Also shown are two calculated traces: the orange curve was calculated taking into account ee scattering events, whereas damping in the blue curve is only due to momentum scattering events and the anisotropy of the Dresselhaus SO field. (b) Symmetry of the Dresselhaus-type SO field, present in sample E.*

microscopic scattering time τ, present in the sample at low temperatures, the single electron spin can precess a number $\Omega_D(\boldsymbol{k})\tau \geq 1$ of revolutions, before the electron is scattered. After a scattering event, spin precession is about the new SO field $\boldsymbol{\Omega}_D(\boldsymbol{k'})$, depending on the electron wave vector $\boldsymbol{k'}$ of the scattered electron. In the present
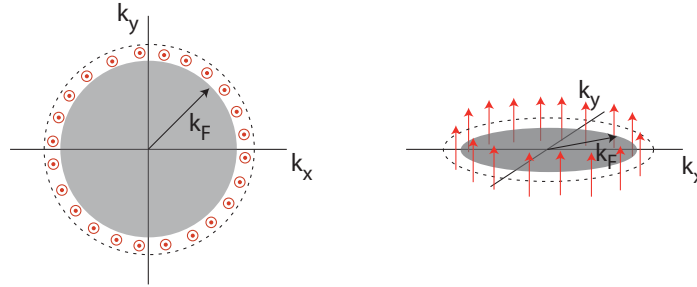

Figure 6.3: *In an n-doped system, excess carriers can be created optically around the Fermi disc. There, they have a wave vector with $|\boldsymbol{k}| = k_F$. The optically excited spins are initially oriented out of plane.*

experiment not only the evolution of a single spin is measured, but the evolution of an optically generated spin ensemble. Due to optical excitation of e-h pairs in an n-doped system, the generated carriers are equally distributed around the Fermi circle, as it is depicted in Fig. 6.3. There, they have a wave vector with $|\boldsymbol{k}| = k_F$. In the case of the k-linear Dresselhaus term (see Eq. (2.21)), every single spin of the optically generated spin ensemble experiences the *same* absolute value $\Omega_D(k_F)$ of the SO field. For this reason, a *coherent* precession of the optically excited spin ensemble can be observed experimentally.

The oscillatory behavior is expected as well if, in addition, the cubic terms in the Dresselhaus SO field (see Eq. (2.20)) are taken into account. This is necessary for sample E, where the relation $\langle k_{001}^2 \rangle \gg k_{010,100}^2$ is no longer valid, due to the large QW width d and the relatively high doping level. Considering the cubic Dresselhaus terms, the absolute value $\Omega(\boldsymbol{k}_F)$ of the SO field around the Fermi circle is no longer constant,

but depends on the direction in the k-space. This leads via different spin precession frequencies of different spin subsets, located at different positions in the k-space, to a faster dephasing of the total spin ensemble.

Compared to the extremely long momentum scattering time $\tau_p \approx 560$ ps, determined from magneto-transport measurements, the coherent oscillations of the spin ensemble are damped out very fast: fitting an exponential damped cosine to the TRFR data shown in Fig. 6.2, a dephasing time of $T_2^* \approx 63$ ps could be determined at $T = 4.5$ K. If the sample was cooled down to $T = 0.4$ K, T_2^* increases to 74 ps, which is also significantly shorter than the value determined for τ_p.

The fast decay of the spin beats cannot exclusively be attributed to contributions of the cubic Dresselhaus term: the blue curve in panel (a) of Fig. 6.2, calculated under the assumption that momentum scattering, as well as the anisotropy of the Dresselhaus SO field $\Omega_D(k_F)$, is relevant for the damping of the zero-field oscillations, shows a significantly weaker damping than the experimentally observed data. In contrast, if in addition contributions of the ee scattering rate $1/\tau_{ee}$ to the microscopic scattering rate $1/\tau$ are taken into account, the calculation is in good agreement with the experimental observation (orange curve in panel (a) of Fig. 6.2). For the calculation it was assumed that the 2DES is overheated due to optical pumping. Therefore, a reasonable temperature of the electron system of about 4 K at a lattice temperature of 0.4 K was used for the calculation.
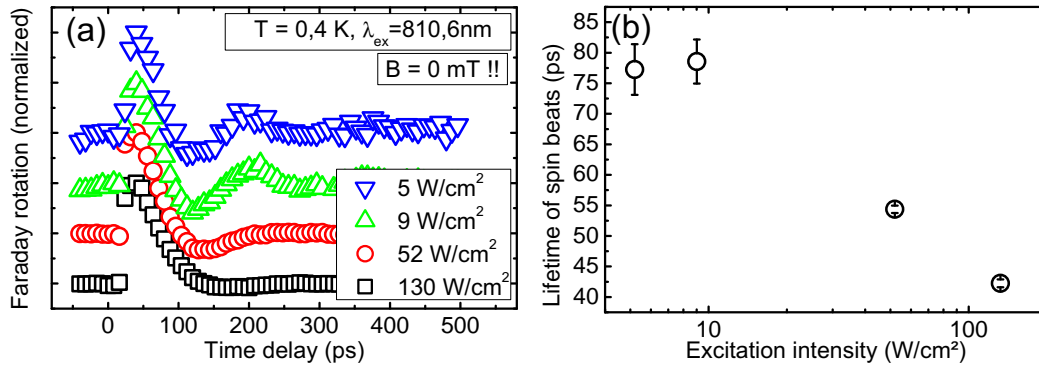

Figure 6.4: (a) Zero-field TRFR traces taken at $T = 0.4$ K, using different excitation intensities I_{ex}. (b) Lifetimes of the spin beats extracted by fitting an exponentially damped cosine function to the TRFR data shown in (a).

For the purpose of checking the dependence of the decay time T_2^* of the spin beats on the temperature T_e of the electron system, the excitation intensity I_{ex} was reduced in order to reduce the energy input into the 2DES. As it can be clearly seen from the TRFR traces in panel (a) of Fig. 6.4, more oscillations become visible for a reduced excitation intensity I_{ex}. Fitting an exponentially damped cosine to this data yields the lifetime of the spin beats shown in panel (b) of Fig. 6.4. The increase of the decay time T_2^* can be attributed to an increased ee scattering time τ_{ee} in consequence of a reduced temperature T_e of the 2DES: from PL measurements performed at a sample temperature of $T = 0.4$ K (see panel (a) of Fig. 6.5), the temperature T_e of the 2DES could be determined by fitting the high-energy tail of the PL with the Fermi-Dirac function (see Eq. (4.8)). The spectral width δE of the high-energy tail of the PL decreases for lower excitation intensities, as can be seen from panel (b) of Fig. 6.5. Because $\delta E \propto k_B T_e$ is proportional to the temperature T_e of the 2DES, a decrease of the electron temperature can directly be observed. The obtained values[2] for T_e are shown in panel (c) of Fig. 6.5,

---

[2] It should be noted that the excitation conditions in PL and TRFR measurements are quite different:
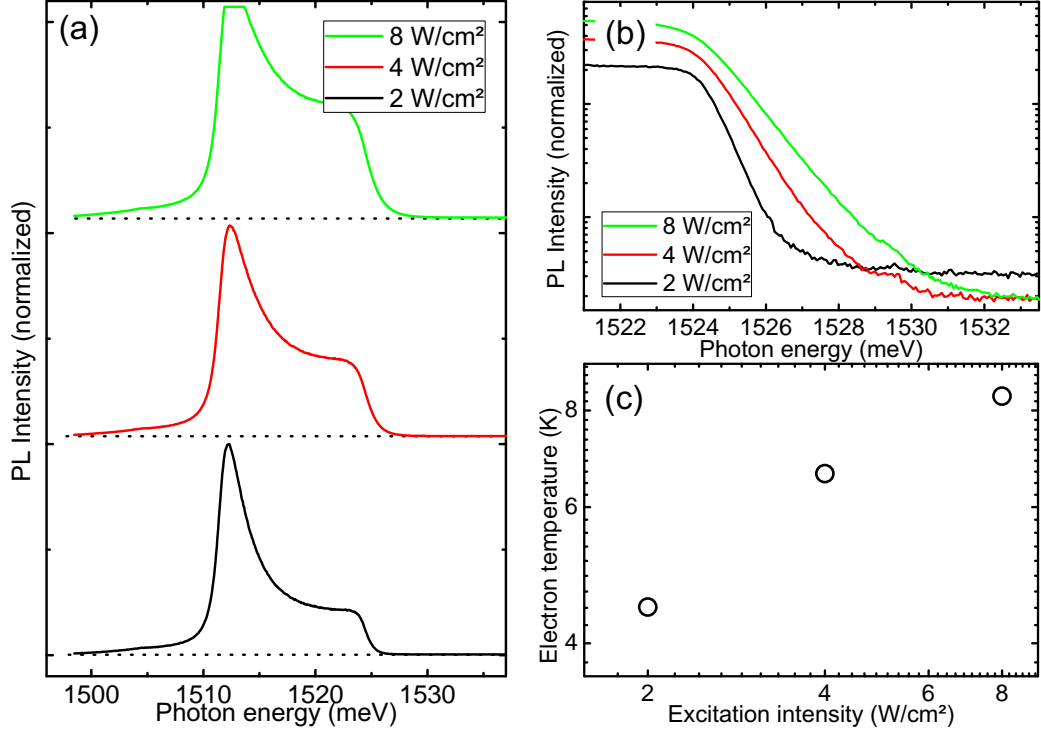
Figure 6.5: *(a) PL traces of sample E taken at $T = 0.4\,K$ at different excitation intensities I_{ex}. The traces are shifted for clarity. (b) High-energy tail of the PL traces shown in panel (a). By fitting the high-energy edge with the Fermi-Dirac function, the electron temperature of the 2DES can be determined. The corresponding values are shown in panel (c).*

ranging from about 4 K to about 8 K for $2\,\mathrm{W/cm}^2 < I_{ex} < 8\,\mathrm{W/cm}^2$. In consequence of Eq. (2.10), an increase of T_e is expected to result in a decrease of the ee scattering time τ_{ee}. In a system where the microscopic scattering time τ is limited by the ee scattering time τ_{ee}, a decrease of τ can be expected for a higher temperature T_e of the 2DES. In the weak scattering regime of the DP mechanism, the decay time of the oscillatory signal is expected to be proportional to the microscopic scattering time τ (see Eq. (2.45)), which is consistent with the experimental observation.

In conclusion of this section, zero-field coherent oscillations of the spin ensemble could be observed at temperatures of $T < 4\,\mathrm{K}$. It was discussed that damping of the spin beats occurs faster than it would be expected from the extremely long momentum scattering time $\tau_p \approx 560\,\mathrm{ps}$. The comparatively rapid decay of the zero-field coherent oscillations was attributed to electron-electron scattering processes, being most likely the relevant scattering process under the experimental conditions: the observed increase of the decay time T_2^* of the zero-field oscillations for a reduced excitation intensity I_{ex} is in agreement with the expectation for the behavior of the ee scattering time τ_e with respect to the lowered temperature of the 2DES.

---

in TRFR measurements, the laser wavelength λ is tuned slightly above the Fermi energy, whereas in PL measurements the excitation is off-resonant with an excess energy of about 60 meV. Thus, due to the non-resonant excitation, the 2DES temperature T_e determined from PL measurements can be higher than T_e under the conditions of resonant excitation during TRFR measurements.

6.1.2 Cyclotron effect on coherent spin precession

After the optically generated spin ensemble was shown to fulfill coherent oscillations about the Dresselhaus-type SO field, in this section the influence of a weak external magnetic field, oriented perpendicular to the sample plane, on the coherent dynamics will be discussed.

If a magnetic field $\boldsymbol{B} = (0, 0, B)$ is applied perpendicular to the sample plane, the ballistically moving electrons are forced on cyclotron orbits in real space. As depicted in Fig. 6.6, the cyclotron motion in real space is connected with a motion of the electron in k-space: the optically generated electron, starting at a wave vector with $|\boldsymbol{k}| \approx k_F$ near to the Fermi surface, moves around the Fermi disc with the cyclotron frequency $\omega_c = eB/m^*$. In contrast to the cyclotron motion in real space, where the radius of the cyclotron orbit depends on the magnetic field, the "radius" of the cyclotron "orbit" in k-space remains constant. Thus, an increase of the external magnetic field leads to a faster rotation of the electron in k-space, while the absolute value of the wave vector $\boldsymbol{k}$ is conserved in the absence of scattering.
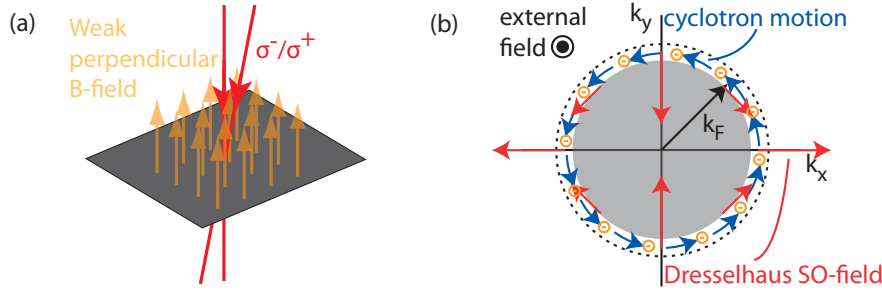

Figure 6.6: *(a) Orientation of the sample plane relative to the external applied magnetic field. (b) The weak magnetic field perpendicular to the sample plane forces the electrons to move on cyclotron orbits. Similar to the cyclotron motion in real space, there is also cylcotron motion in k-space, which is depicted here. During the cyclotron motion, the electron spins experience the Dresselhaus SO field.*

A very important consequence of the cyclotron motion of the electron in k-space is the *continuous* change of the SO field, felt by the single electron spin: without an external magnetic field, the direction and the amplitude of the SO field felt by a single electron spin is constant as long as the electron does not experience scattering. In stark contrast, *within* a perpendicular magnetic field the electrons wave vector $\boldsymbol{k}$ and the corresponding SO field $\boldsymbol{\Omega}(\boldsymbol{k})$ are *continuously* changing with the cyclotron frequency ω_c. Therefore, the single electron spin precesses no longer about a constant, but a rapidly changing SO field[3].

Similarly as it was discussed in Sec. 6.1.1 for the zero-field case, an ensemble of electron spins, equally distributed around the Fermi circle, can be expected to show a coherent behavior, also and in particular within an applied magnetic field: the cyclotron motion leads to an averaging of the absolute value[4] of the SO field acting on the single electron spins. In consequence, the temporal evolution of the out-of-plane spin component of any single electron spin is nearly independent of the corresponding initial position of the

---

[3]As mentioned in Sec. 2.2.8, spin precession about the weak external magnetic field $\boldsymbol{B}$ can be neglected because of $\omega_L \ll \Omega(\boldsymbol{k})$.

[4]The linear contribution of the Dresselhaus field Ω_D (see Eq. (2.61)) results in an isotropic strength $|\boldsymbol{\Omega}_D(\boldsymbol{k}_F)| = \Omega_D(k_F)$ of the SO field, acting on electrons located at the Fermi circle. Contributions to $\boldsymbol{\Omega}_D$ being cubic in $\boldsymbol{k}$ introduce an anisotropy of the amplitude of the SO field. However, the cyclotron rotation of the electrons in the k-space leads to an averaging of the SO field acting on a single electron spin.
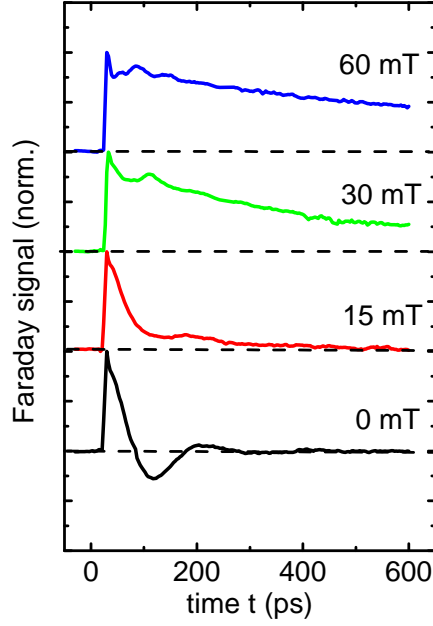
Figure 6.7: *TRFR traces taken at $T = 0.4$ K on sample E in weak perpendicular magnetic fields. A drastic change of the signal is clearly visible.*

optically generated electron in k-space. Because the all-optical TRFR measurements are only sensitive on the out-of-plane component of the spin polarization, this allows for the observation of coherent dynamics of the optically generated spin ensemble.

In contrast to previous works [Sih04; Fuk08], where spin dynamics in *large* perpendicular magnetic fields have been discussed, in the present work the case of *weak* perpendicular magnetic fields B will be presented. In this classical case, the spacing $\Delta E_L = \hbar\omega_c = \frac{\hbar e B}{m^*}$ of the Landau levels is small[5] compared to the thermal energy $E_T = k_B T$ and the spectral width ΔE_λ of the laser pulses used for the generation of spin-polarized electron-hole pairs. Thus, for the magnetic fields applied in this work, the width ($\propto E_T$) of the Landau levels exceeds their spacing ($\propto E_L$), and the electron density of states can be treated as constant.

The dramatic consequences of a weak perpendicular magnetic field on coherent spin dynamics can be seen in Fig. 6.7. There are two main features visible in the experimentally obtained TRFR traces, which were taken at $T = 0.4$ K: the frequency of the spin beats is getting higher with increasing amplitude of the magnetic field. In addition, a long-lived tail (see also panel (a) of Fig. 6.8) of the spin polarization appears after the spin beats are damped out, and the TRFR traces do not longer cross the zero-line for magnetic fields $|B| > 10$ mT. For a quantitative analysis, as it is shown in panel (a) of Fig. 6.8, the TRFR data were fitted with the theoretical model presented in Eq. (2.64). The determined dependencies of the effective spin beats frequency Ω_{eff}, the spin beats amplitude $\mathcal{B}$ and the lifetime τ_s of the long tail can be seen in panels (b)-(d) of Fig. 6.8. Whereas both, Ω_{eff} and τ_s, show an increase with the applied magnetic field, the amplitude $\mathcal{B}$ of the observable spin beats reduces drastically.

The experimental results obtained this way can be explained on the basis of the kinetic equation approach, presented in Sec. 2.2.8. First, the focus should be on the spin beats

---

[5]The Landau level spacing is $\Delta E_L \approx 0.1$ meV for the largest magnetic field applied ($B = 60$ mT). Assuming a slightly overheated electron system and $T_e \approx 4$ K, the thermal energy E_T is about 0.34 meV. The spectral width of the pulsed laser (pulse length ≈ 1 ps) is about 0.7 meV. Therefore, one has $\Delta E_\lambda > E_T > \Delta E_L$.
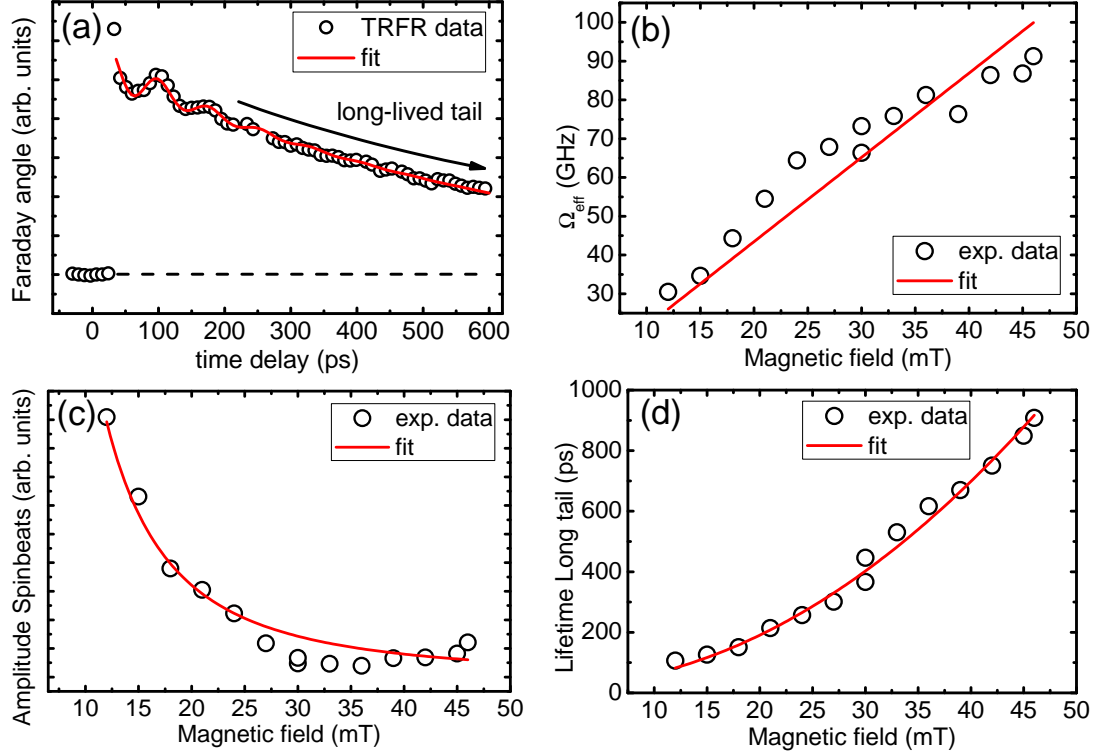
Figure 6.8: *(a) TRKR trace taken on sample E in a 36 mT perpendicular magnetic field at a sample temperature T = 0.4 K. The fast oscillations superimposed on the long-lived, exponentially decaying tail are clearly visible. The red line is a fit to the experimental data. (b) Angular frequency Ω_{eff} of the spin beats. (c) Amplitude of the spin beats and (d) lifetime of the long-lived tail. The red lines in panels (b)-(d) show a fit to the data, according to the model presented in Sec. 2.2.8.*

frequency Ω_{eff}, which is expected to depend as

$$\Omega_{eff} = \sqrt{\left(\frac{eB}{m^*}\right)^2 + \Omega_{k_F}^2} \tag{6.1}$$

on the applied magnetic field B. The increase of the spin beats frequency is a consequence of the cyclotron rotation of the SO field, and can be understood with the help of the following simple picture: the single electron spin is created at a certain time with wave vector $\boldsymbol{k}_0$, and starts to process about the SO field $\boldsymbol{\Omega}(\boldsymbol{k}_0)$. Without a magnetic field applied, precession of the single electron spin takes place in the constant SO field with precession frequency $|\boldsymbol{\Omega}(\boldsymbol{k}_0)|$. In a weak perpendicular magnetic field $\boldsymbol{B} = (0, 0, B)$, the electron wave vector $\boldsymbol{k}$ rotates in k-space, resulting in a time-dependent SO field $\boldsymbol{\Omega}(\boldsymbol{k})$, acting on the electron spin. Seen from the perspective of the rest frame of the electron, the SO field seems to rotate with the cyclotron frequency ω_c. Thus, the axis of spin precession is continuously changed, while the electron spin is precessing about the SO field. In particular, after a time interval $\Delta t = \pi/\omega_c$, when one has $\boldsymbol{k}(\Delta t) = -\boldsymbol{k}_0$, the SO field $\boldsymbol{\Omega}(\boldsymbol{k})$ felt by the electron spin has changed its sign and reads $-\boldsymbol{\Omega}(\boldsymbol{k}_0)$. Apparently, the precession direction becomes inverted after a time interval $\Delta t \propto \omega_c^{-1}$. This means that the electron spin cannot longer fulfill complete precession cycles. Furthermore, the electron spin can process just by a certain small angle $\varphi = \Omega(k)\Delta t \propto \Omega(k)\omega_c^{-1}$, until the precession direction is inverted. After this, spin precession takes place in the opposite direction, resulting in a minimum of the spin beat signal. This proves that the frequency

of the fast spin beats is given by an interplay of the SO field $\boldsymbol{\Omega}(\boldsymbol{k})$ and the cyclotron frequency ω_c: the SO fields, leading to precession of the single electron spin, are rapidly changed with the cyclotron frequency $\omega_c = eB/m^*$. Thus, the applied magnetic field $\boldsymbol{B}$ controls the periods in which the spin precesses into the sample plane or in the opposite direction. Due to the faster cyclotron motion at a higher magnetic field, the switching between "spin precesses into the sample plane" and "spin precesses out of the sample plane" occurs faster. This simple picture allows for the understanding of the increase of the spin beats frequency with increasing magnetic field.

When higher magnetic fields have been applied, a strong increase of the spin beats frequency could be observed experimentally. In panel (b) of Fig. 6.8 a fit of the experimentally determined values of Ω_{eff} according to Eq. (6.1) is shown. From this fit, which shows good agreement of the experimental data and the theoretical model, the effective mass m^* of the electrons can be determined as well. This will be discussed later.

Considering again the simple picture given above, the reduction of the spin beat amplitude

$$\mathcal{B} = \frac{\Omega_{k_F}^2}{\left(\frac{eB}{m^*}\right)^2 + \Omega_{k_F}^2} \tag{6.2}$$

with increasing magnetic field $\boldsymbol{B}$ can be understood as well: the spin precession frequency is determined by the strength of the SO field $\boldsymbol{\Omega}(\boldsymbol{k})$, whereas the angle φ, about which the electron spin precesses, is depending on $\boldsymbol{\Omega}(\boldsymbol{k})$ and the time interval Δt in which precession can occur about a certain SO field. For a higher magnetic field, the time $\Delta t = \pi/\omega_c$ is shorter and in consequence the precession angle φ, about which the electron spin can precess before the precession direction is changed, is smaller. Therefore, the modulation depth of the exponentially decaying spin signal is lower for higher fields. This was also observed in the experiment, as can be seen from panel (c) of Fig. 6.8, where the amplitude of the spin beats is plotted with respect to the applied magnetic field. A fit (red line in panel (c) of Fig. 6.8) of the data according to the model shown in Eq. (6.2) illustrates the good agreement between the theoretical model and the experimental observations.

The second main feature, visible in the TRFR data shown in Fig. 6.7, should be discussed as well: the long-lived tail of the optically generated spin polarization. The lifetime τ_s of this long-lived component in the TRFR signal drastically exceeds the microscopic scattering time τ. This is in stark contrast to the lifetime of the spin beats, which are damped out on a timescale τ_b, being proportional to τ. Panel (d) of Fig. 6.8 shows the values of τ_s determined from a fit of the measured TRFR traces with the model shown in Eq. (2.64).

The appearance of the long-lived tail with lifetime $\tau_s \gg \tau$ is a consequence of the rotation of the SO field $\boldsymbol{\Omega}(\boldsymbol{k})$, acting on the electron spin, which results from the cyclotron rotation of the electron wave vector $\boldsymbol{k}$. This condition is similar to what can be found in the motional narrowing regime of the DP mechanism, where spin dephasing is suppressed due to a rapid change of the SO field governed by scattering events. In the case of a weak perpendicular magnetic field in a very clean sample at low temperatures, the cyclotron motion of the electrons predominantly leads to a continuous and rapid change of the $\boldsymbol{k}$ vector and hence the SO field $\boldsymbol{\Omega}(\boldsymbol{k})$, instead of frequent, random scattering events. Thus, at $\Omega(\boldsymbol{k}) \ll \omega_c$, spin precession about the SO field $\Omega(\boldsymbol{k})$ is much slower than the variation of the SO field $\Omega(\boldsymbol{k})$, resulting from the cyclotron motion of the electrons. This is the same situation as in the motional narrowing regime, where long spin dephasing times can be observed.

After the dramatic effect of a weak perpendicular magnetic field on coherent dynamics of an optically excited spin ensemble was shown for a fixed excitation intensity $I_{ex} =$

44 W/cm², the effect of a reduced excitation intensity I_{ex} on spin dynamics will now
be presented. As it was already discussed in Secs. 5.4 and 6.1.1, the temperature T_e of
a 2DES can exceed the lattice temperature T in consequence of pump-induced heating.
Due to the strong temperature dependence of the ee scattering time τ_{ee}, a reduced
excitation intensity leading to a lower temperature T_e of a 2DES should lead to an
increase of the ee scattering time τ_{ee}, and hence to a longer microscopic scattering time
τ. As can be seen from Eqs. (2.65) and (2.67), both, the decay times τ_s and τ_b, depend
on the microscopic scattering time τ. Therefore, a reduction of the electron temperature
T_e due to a reduced pump intensity I_{ex} can be expected to have a significant effect on
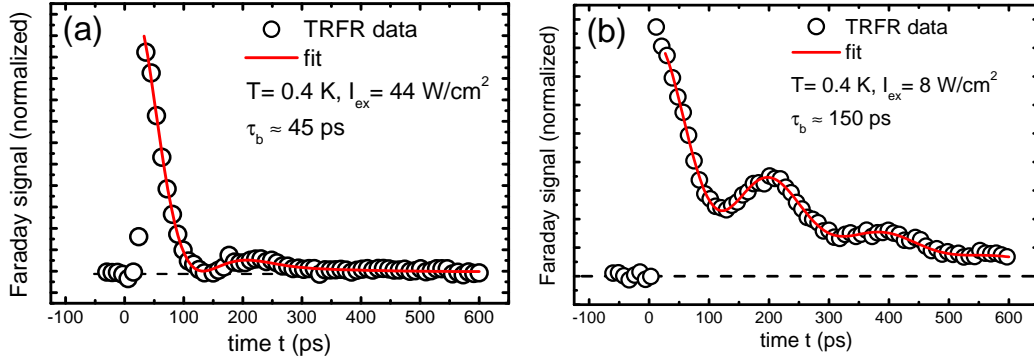coherent spin dynamics.

Figure 6.9: *TRFR traces taken at a sample temperature $T = 0.4$ K at an excitation
intensity I_{ex} of (a) 44 W/cm² and (b) 8 W/cm². The spin beats apparently live longer
at a reduced excitation intensity I_{ex}. A magnetic field of $B = 12\,mT$ was applied per-
pendicular to the sample plane.*

In order to investigate the dependence of spin dynamics on the excitation intensity,
a series of TRFR measurements at $T = 0.4$ K with different excitation intensities
2 W/cm² $< I_{ex} <$ 44 W/cm² were performed. As can be seen from the TRFR traces
shown in Fig. 6.9, the lifetime τ_b of the spin beats increases from $\tau_b \approx 45$ ps to $\tau_b \approx 150$ ps
if the excitation intensity I_{ex} is reduced from $I_{ex} = 44$ W/cm² to $I_{ex} = 8$ W/cm². A
detailed overview of the resulting values of τ_s and τ_b is given in Fig. 6.10. In panel (a)
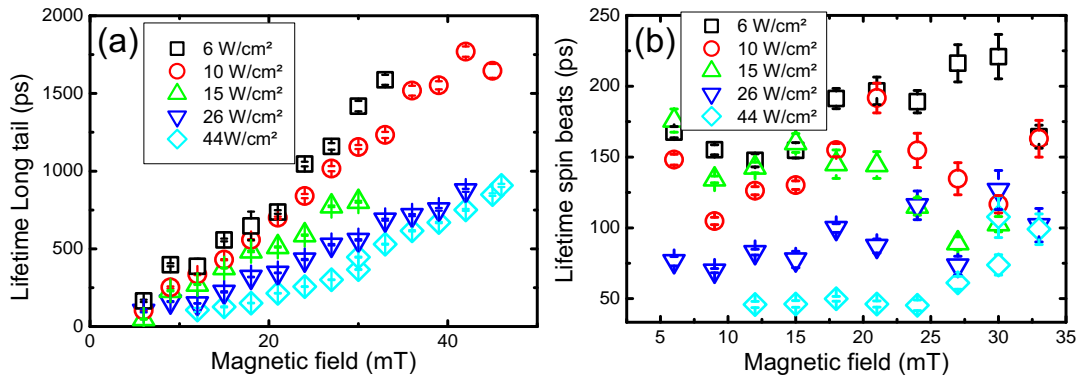
Figure 6.10: *(a) Values for the lifetime τ_s of the long tail of the spin polarization,
determined from the TRFR data by a fit with the model in Eq. (2.64). The obtained
values τ_s for a certain magnetic field value are higher if the excitation intensity I_{ex} is
reduced. (b) Lifetime τ_b of the spin beats, determined from the TRFR data by a fit with
the model in Eq. (2.64). Even though the determined values show some spread, it can
be seen that the spin beats live longer for a reduced excitation intensity I_{ex}.*

the lifetime τ_s of the long-lived tail of the TRFR traces is plotted against the applied magnetic field for different excitation intensities I_{ex}. It can be seen clearly that for a certain magnetic field value $|\boldsymbol{B}|$, the decay time τ_s increases for a reduced excitation intensity. In panel (b) of Fig. 6.10, the determined values of the lifetime τ_b of the spin beats are plotted. Here, some spread in the experimental data is visible. However, a clear tendency is visible: long lifetimes of the spin beats can be found for low excitation intensities and vice versa. Having a look on the linear dependencies of $\tau_s \propto \tau$ (c.f. Eq. (2.65)) and $\tau_b \propto \tau$ (c.f. Eq. (2.67)) on the microscopic scattering time τ, one can deduce from Fig. 6.10 that a reduction of the excitation intensity I_{ex} leads to an increase of τ: both τ_s and τ_b show an increase if I_{ex} is reduced. For example, at $B = 20$ mT, τ_s increases by a factor of about 3 if I_{ex} is reduced from 44 W/cm^2 to about 10 W/cm^2. The corresponding values of the lifetime τ_b of the spin beats increase as well, in this case by a factor 3. Therefore, the observed behavior of τ_s and τ_b can be attributed to the increase of the microscopic scattering time τ by a factor of about 3. This increase of τ most likely is governed by a decrease of the temperature T_e of the 2DES, resulting from the lower heat input at lower excitation intensities I_{ex}. A change of T_e leads to a variation of the ee scattering time τ_{ee} (see Eq. (2.10)), which seems to limit τ in the presented experiments.

Using the expression in Eq. (2.67), the microscopic scattering time τ can be calculated from the lifetime τ_b of the spin beats. The values obtained for τ this way are shown in panel (a) of Fig. 6.11, and range between 20 ps and about 100 ps. If these
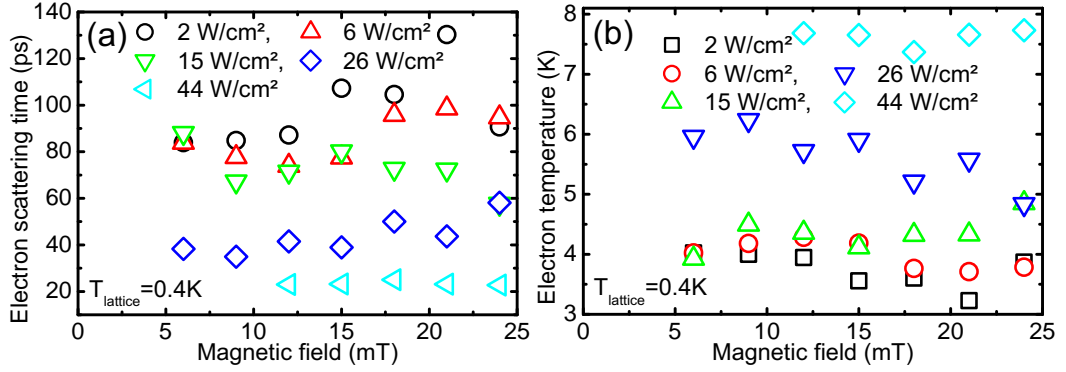

Figure 6.11: *(a) ee scattering time calculated from the decay time τ_b of the spin beats, using the assumption $\tau_p \gg \tau_{ee}$. (b) Calculated temperature T_e of the 2DES, using the values from (a) and the model in Eq. (2.10).*

values are compared to the momentum scattering time $\tau_p \approx 500$ ps, determined from magneto-transport measurements on the unprocessed sample, it can be concluded that the microscopic scattering time is limited by the shorter ee scattering time τ_{ee}. Therefore, the experimentally observed microscopic scattering rate

$$\frac{1}{\tau} = \frac{1}{\tau_p} + \frac{1}{\tau_{ee}} \overset{\tau_p \gg \tau_{ee}, \tau}{\approx} \frac{1}{\tau_{ee}} \tag{6.3}$$

is approximately equal to the ee scattering rate τ_{ee}^{-1}. For this reason, the y-axis in Fig. 6.11 is labeled as electron scattering time. The relation $\tau \approx \tau_{ee}$ is true at least for higher excitation intensities $I_{ex} \geq 15$ W/cm^2. At lower excitation intensities, a saturation-like behavior of the scattering time τ can be observed. This can be taken as a hint for either a reduced momentum scattering time τ_p in the thinned sample, or a saturation of the lowest experimentally achievable electron temperature T_e: after the removal of the sample substrate, the band edge profile in the active region most likely has changed a bit. Additionally, some strain may be introduced into the structure

due to different heat expansion coefficients of the sapphire wedge substrate and the remaining heterostructure stack. Thus, a reduced mobility $\mu' < \mu$, and hence a shorter momentum scattering time $\tau'_p < \tau_p$ would be reasonable. In contrast, the saturation of the microscopic scattering time τ at about 100 ps can be also explained by a lowest experimentally achievable electron temperature. There are some reasons for this: First, not only the pump pulses used for the generation of spin polarization, but also the probe pulses used for the detection of the spin polarization can introduce some heat into the 2DES. A reduction of the probe beam intensity I_{probe} to below 10 W/cm^2 could result in a lower temperature of the 2DES, but would also lead to a loss of signal and an unacceptable signal-to-noise-ratio. Secondly, cooling of the 2DES was shown to be very inefficient at low temperatures T_e of the electron system [Dan89]. The lowest achieved electron temperature T_e in sample E could be found in the temperature range $3\,\text{K} < T_e < 8\,\text{K}$, as can be seen in panel (b) of Fig. 6.11. Here, the temperatures T_e of the 2DES were calculated from the values of the ee scattering time τ_{ee} shown in panel (a) of Fig. 6.11, using the expression in Eq. (2.10).

In conclusion, the saturation of the experimentally determined microscopic scattering time τ, at values of about 100 ps, is most likely governed by the electron scattering time τ_{ee} in a slightly overheated 2DES. However, a reduction of the mobility μ to a lower value μ' in the thinned sample cannot be excluded.

Even if the electron mobility μ' in the thinned sample was not measured in magneto-transport measurements, the determined microscopic scattering time $\tau \approx 100$ ps yields a lower limit of $\mu' > 3 \cdot 10^6 \text{cm}^2/\text{Vs}$. Thus, the observation of coherent spin oscillations about the SO field within an additional weak magnetic field allows in principle for an all-optical determination of the mobility μ of a 2DES, or at least for the determination of a lower limit of μ.
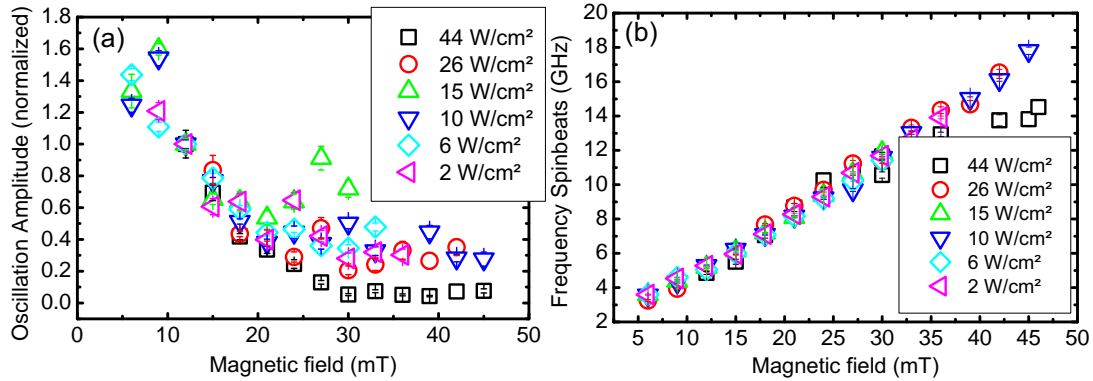

Figure 6.12: *(a) Amplitude $\mathcal{B}$ and (b) frequency $\Omega_{eff}/2\pi$ of the spin beats for different excitation intensities I_{ex}. These two quantities show no dependence on the excitation intensity connected with the microscopic scattering time τ, what is in agreement with Eqs. (2.66) and (6.1).*

In stark contrast to the presented features of the spin signal depending on the microscopic scattering time τ, the amplitude $\mathcal{B}$ of the spin beats, as well as the spin beats frequency Ω_{eff}, are independent of τ, as it is apparently visible in Fig. 6.12. This is in agreement with Eqs. (2.66) and (6.1), which illustrate that both the amplitude $\mathcal{B}$, as well as the frequency Ω_{eff} of the spin beats, are expected to be independent of the microscopic scattering time τ. Therefore, a change of the excitation intensity I_{ex}, having a strong influence on τ, leaves $\mathcal{B}$ and Ω_{eff} unchanged.

Moreover, with the presented experimental technique it is also possible to determine the effective mass m^* of the spin-polarized electrons. In contrast to the commonly used

methods for the determination of the effective mass, like cyclotron resonance or the usage of the de Haas-van Alphen effect (see, e.g. [Ash03]), where usually high magnetic fields must be applied, very weak magnetic fields are sufficient[6] here. The effective mass m^* of the electrons determines the cyclotron frequency $\omega_c = eB/m^*$, which enters the effective spin precession frequency

$$\Omega_{eff} = \sqrt{\left(\frac{eB}{m^*}\right)^2 + \Omega_{k_F}^2}. \qquad (6.4)$$

Therefore, by fitting the experimental data with the expression shown in Eq. (6.4), the effective mass m^* can be determined from the magnetic field dependence of Ω_{eff}. A fit of the values of Ω_{eff} experimentally obtained at $T = 0.4$ K and an excitation intensity $I_{ex} = 6$ W/cm^2 (see Fig. 6.13) leads to an effective mass $m^* = 0.076m_0$. This value slightly deviates from the literature value [Sti69; Sti71; Law71] for GaAs of $m^* = 0.067m_0$. The reason for this could be found most likely in the non-parabolicity of the conduction band: the optically generated spin polarized electrons are located at the Fermi circle. Due to the resident carrier concentration $n \approx 3 \cdot 10^{11}$cm^{-2}, the Fermi energy can be found at about 11 meV above the bottom of the first quantized electron subband in the QW. The corresponding Fermi wave vector is about $k_F \approx 0.014$ Å^{-1}. For this wave vector an effective mass $m^* \approx 0.072m_0$ could be determined from a nextnano^3 simulation of the band structure of sample E. For this, the $E(k)$ dispersion of the first conduction band was calculated, using the 8×8 $k \cdot p$ method. Panel (b) of Fig. 6.13 depicts the dependence of the effective mass m^* on the in-plane momentum, which was determined from the simulated energy dispersion $E(k)$ (not shown). Although the experimental value cannot be reproduced precisely in the calculation, the calculation underlines the importance of the nonparabolicity of the conduction band: the effective mass of electrons located near to the Fermi edge of the 2DES in sample E clearly exceeds the literature value of $m^* = 0.067m_0$ [Sti69; Sti71; Law71]. Therefore, the experimentally observed value $m^* = 0.076m_0$ can in part be explained by the nonparabolicity of the conduction band.
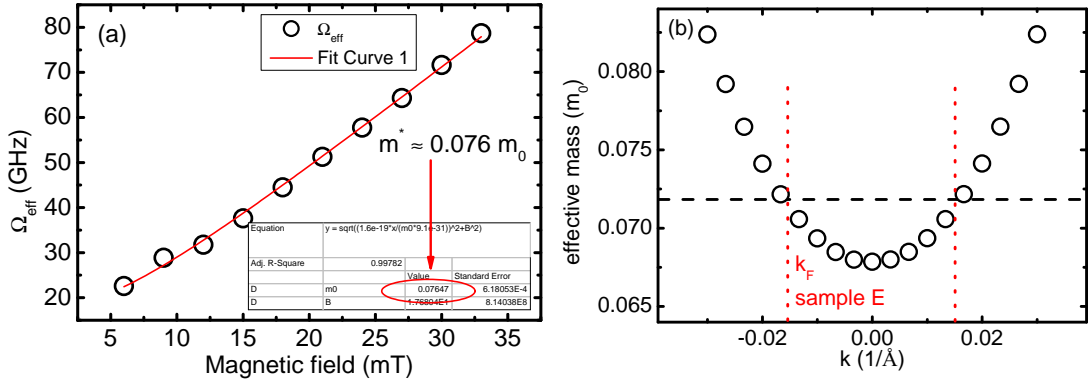

Figure 6.13: *Fitting the frequency Ω_{eff} of the spin beats with the expression in Eq. (6.1) allows for the determination of the effective mass m^*. Here, data points determined from a measurement at $T = 0.4$ K and an excitation intensity $I_{ex} = 6$ W/cm^2 are shown, leading to an effective electron mass of $m^* = 0.076m_0$. (b) Dependence of the effective mass on the in-plane electron wave vector $\bm{k}$, calculated from a nextnano^3 simulation.*

---

[6]It is only very recently, that the effective mass can also be determined directly, without a magnetic field using the angle-resolved photo emission spectroscopy (ARPES) technique, reviewed for example in [Lee09].

In addition to the effective mass, the value of the Dresselhaus spin splitting constant γ in sample E can be determined from the frequency of the coherent oscillations of the spin ensemble. For this purpose, a Larmor frequency $\Omega_{eff} = |\mathbf{\Omega}(\mathbf{k}_F)| \approx 20\,\mathrm{GHz}$ could be extrapolated for zero magnetic field. From the determined oscillation frequency[7] of $|\mathbf{\Omega}_D(\mathbf{k}_F)| \approx 20\,\mathrm{GHz}$ a value of

$$\gamma = \frac{\hbar|\mathbf{\Omega}_D(\mathbf{k}_F)|}{|k_F|\left(\left(\frac{\pi}{d}\right)^2 - \frac{k_F^2}{4}\right)} \approx 16\,\mathrm{eV\mathring{A}}^3 \tag{6.5}$$

could be calculated for the 2DES residing in the $d = 30\,\mathrm{nm}$ wide QW of sample E, also considering the cubic contributions to the Dresselhaus SOF[8]. Here, the absolute value of the Fermi wave vector $|k_F| = \sqrt{2\pi n}$ was calculated from the carrier density $n = 2.97 \times 10^{11}\,\mathrm{cm}^{-2}$, as listed in Tab. 3.2. The determined value, corresponding to a confinement energy of about $6\,\mathrm{meV}$, was already shown in Fig. 5.7. There, it fills the gap between bulk GaAs (no confinement, $\gamma = 27.58\,\mathrm{eV\mathring{A}}^3$ [Win03]) and the previously determined value $\gamma \approx 11.5\,\mathrm{eV\mathring{A}}^3$ [Ley07b] in a $20\,\mathrm{nm}$ wide QW ($E_c \approx 10.2\,\mathrm{meV}$).

In conclusion of this section, coherent zero-field oscillations could be observed in sample E at a temperature $T = 0.4$ K. They were shown to be damped out mainly due to ee scattering events. This is due to the fact that the momentum scattering time τ_p exceeds the ee scattering time τ_{ee} in the 2DES, which is slightly overheated in consequence of optical pumping. Further it was shown that spin dynamics are drastically affected by a weak perpendicular magnetic field, which forces the electrons to move on cyclotron orbits. The appearing features, namely the fast spin beats, as well as the long-lived tail were shown to be in agreement with a theoretical model based on a kinetic equation approach. It was discussed that the presented experiments allow for the direct determination of the microscopic scattering time τ, which is most likely limited by ee scattering processes in the case of this work. Finally, it was shown that this method gives directly access to the effective mass m^* of the electrons. However, the experimentally observed value $m^* = 0.076m_0$ deviates from the literature value $m^* = 0.067m_0$ [Sti69; Sti71; Law71] for GaAs. This in part can be explained by the nonparabolicity of the conduction band, what was confirmed by nextnano[3] simulation of the bandstructure of sample E. Finally, from the frequency of the spin beats, the value of the Dresselhaus spin splitting constant γ could be determined for a low confinement energy of about $6\,\mathrm{meV}$.

6.2 Extended spin dephasing times in (110)-grown 2DESs

After the discussion of coherent spin dynamics in the (001)-grown sample E at a temperature $T = 0.4$ K, the observation of anisotropic spin dynamics (see Sec. 2.2.7) in the (110)-grown samples F and G will now be presented. The discussion in this section follows in parts the description in Refs. [Gri11; Gri12], where some of the experimental results have been already published. In Sec. 6.2.1 it will be shown that a strong spin dephasing anisotropy can be observed in TRKR and RSA measurements on both samples. The observed temperature dependence of the SDA in sample G will be elucidated in Sec. 6.2.2. After this, a strong dependence of the spin dephasing times on weak above-barrier illumination will be shown in Sec. 6.2.3. Finally, the long SDTs achievable under the conditions of optical gating, leading to a significant polarization of the nuclear spin system, are presented in Sec. 6.2.4.

---

[7]Due to the high symmetry of the band edge profile in sample E, the Rashba contribution to the SO field $\mathbf{\Omega}_R$ is negligibly small. Thus, the SO field can be taken to be equal to the Dresselhaus SO field, and one has $|\mathbf{\Omega}(\mathbf{k}_F)| \approx |\mathbf{\Omega}_D(\mathbf{k}_F)|$.

[8]In Eq. (6.5), $\beta = \gamma\langle k_z^2 \rangle$ was replaced by $\beta = \gamma(\langle k_z^2 \rangle - k_F^2/4)$, following Ref. [Gan04].
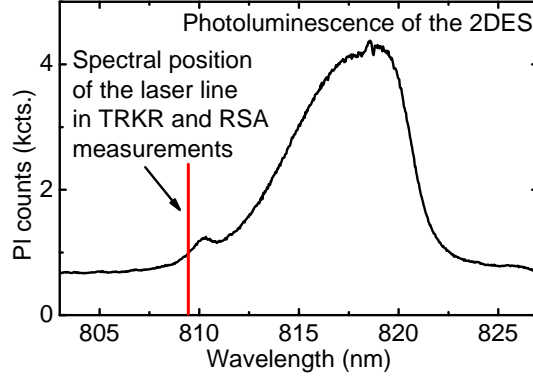
Figure 6.14: *PL of sample G at a nominal temperature of* 28 *K. The red line marks the spectral position of the laser line in the TRKR and RSA measurements.*

6.2.1 Spin dephasing anisotropy in symmetric (110)-grown 2DESs

As discussed in Sec. 2.2.7, spin dephasing is expected to be anisotropic in (110)-grown 2DESs, having a highly symmetric band edge profile. In order to investigate the SDA in samples F and G, both, TRKR as well as RSA measurements, were performed, while the samples were mounted on the cold finger of a continuous-flow cryostat (see Sec. 4.5). In order to pre-characterize the sample and determine the 2DES temperature T_e, PL measurements were performed as well. An analysis of the spectral width ΔE and the high-energy tail of the PL yields a carrier density of $n \approx 3.2 \cdot 10^{11}$ cm^2, and an electron temperature of about 35 K at a nominal sample temperature of 26 K. The laser wavelength is tuned to a value of $\lambda_{ex} = 809.4$ nm in order to excite electrons near-resonantly from the valence band into unoccupied states of the conduction band, slightly above the Fermi energy. Fig. 6.14 illustrates the relative spectral position of the laser line in the later shown TRKR and RSA measurements and the PL.

In TRKR measurements at a temperature of $T = 26$ K and an excitation intensity of about 8 W/cm^2, a relatively long out-of-plane SDT T_{zz} was observed on sample G. In panel (a) of Fig. 6.15, a TRKR trace without a magnetic field applied can be seen, which clearly shows a very slow decay of the optically generated spin ensemble in the accessible time window[9] of about 2 ns. In order to also determine the in-plane SDT T_{yy}, a sufficiently high magnetic field $\boldsymbol{B} = (B, 0, 0)$ is applied parallel to the sample plane along the x-direction, leading to a modified precession frequency $\tilde{\Omega} = \sqrt{\Omega_L^2 - \frac{\Gamma_{yy}^2}{4}}$ (see Sec. 2.2.7). By this, the optically generated spin ensemble, pointing initially out-of-plane, is forced to precess into the sample plane, where it experiences contributions of the shorter in-plane SDT T_{yy}. It was discussed in Sec. 2.2.7 that in this case the optically generated spin ensemble rotates and decays monoexponentially as

$$s_z(t) = s_0 e^{-t/\overline{T}} \left[\cos \tilde{\Omega} t + \frac{\Gamma_{xx} - \Gamma_{zz}}{2\tilde{\Omega}} \sin \tilde{\Omega} t \right]. \qquad (6.6)$$

For the average decay time $\overline{T}$ one has $\overline{T} = 2/(\Gamma_{zz} + \Gamma_{xx})$. This means that the average spin dephasing *rate* $1/\overline{T} = (\Gamma_{zz} + \Gamma_{xx})/2$ is the average of the spin dephasing rates[10] Γ_{zz} (along the [110] direction) and Γ_{yy} (along the in-plane direction [00$\overline{1}$]). In contrast to the slow decay of the spin polarization in the case of B=0, in panel (b) of Fig. 6.15 the case

---

[9]The accessible time window in the TRFR/TRKR measurements presented in this work is defined by the length $l = 30$ cm of the available delay line. See, for details, Sec. 4.1.

[10]It should be noted that in the case of a slightly asymmetric (110)-grown QW, the out-of-plane SDT T_{zz} is related to Γ_{zz} via $T_{zz} = \frac{2}{\Gamma_{zz}}$, due to the effect of off-diagonal elements in the spin relaxation rates tensor [Tar09].
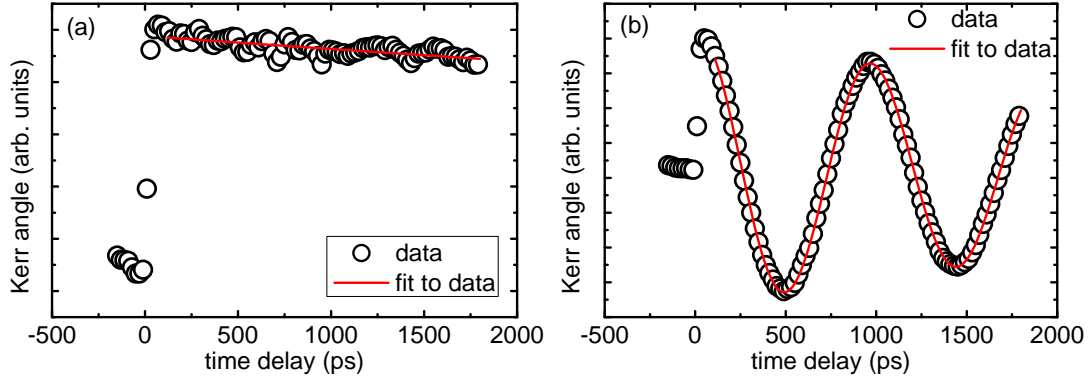
Figure 6.15: *Observation of long spin dephasing times in TRKR measurements at $T = 26\,K$ without magnetic field (a) and with a magnetic field of $200\,mT$ applied parallel to the sample plane (b). The excitation intensity was $I_{ex} = 8\ W/cm^2$, the laser wavelength was tuned to $809.4\ nm$, as it is illustrated in Fig. 6.14.*

of $B = 200$ mT is shown, where an average SDT of $\overline{T} = 4$ ns could be extracted from the oscillating TRKR trace. For the determination of T_{zz} using a single exponential fit, attention has to be paid to the remaining spin polarization before the arrival of the pump pulse, as can be seen from Fig. 6.16. Here, the two TRKR traces shown in Fig. 6.15 are plotted in one diagramm, without adding any additional offset. The amplitude of the zero-field TRKR signal (red line) at a negative time delay Δt (i. e. before the arrival of the pump pulse) corresponds to the cumulated spin polarization created by the previous pump pulses. Taking this into account, T_{zz} can be determined to be about 80 ± 10 ns. This value, together with the value $\overline{T}(200$ mT$)= 4$ ns of the average SDT in the presence of an applied in-plane magnetic field of 200 mT, leads to $T_{yy} \approx 2$ ns. This value is apparently much shorter than the out-of-plane SDT T_{zz}, which verifies the presence of a spin dephasing anisotropy in sample G.

In order to assure oneself that the observed TRKR signal stems from the 2DES residing in the 30 nm wide QW, a look on the electron g factor is helpful. The absolute value of g could be determined to be $|g| = 0.370 \pm 0.003$, by performing a series of TRKR measurements in different magnetic fields. This value is in agreement with experimental data taken on comparable samples [Lec11] and expectations from theory [Yug07]. In contrast, a possible contribution to the TRKR signal from the GaAs wafer substrate would show a different g factor of -0.44 under the applied measurement conditions [Oes95]. Therefore, it can be concluded that the slowly decaying spin signal has its origin indeed in the 2DES.

As discussed above, TRKR measurements can be principally used to demonstrate the existence of a SDA in the (110)-grown sample G. However, the determined SDT of $T_{zz} \approx 80$ ns drastically exceeds the time window of about 2 ns, which can be directly observed with the available delay line. Therefore, the determined value for T_{zz} is object to some error. For a more precise determination of the SDTs T_{zz} and T_{yy}, RSA measurements (see Sec. 4.2) were performed under the same conditions as in the TRKR experiments. An RSA trace taken at a temperature of $T = 26$ K and a corresponding fit using the expression in Eq. (4.3) is shown in panel (b) of Fig. 6.17. The obtained RSA trace shows the shape expected for the case of anisotropic spin dephasing in (110)-oriented 2DESs quite well, for comparison see Fig. 6.17(a). For a quantitative analysis of the spin dephasing parameters, the experimental data was compared with the model shown in Eq. (4.3) by adjusting[11] the spin dephasing rates Γ_{zz} and Γ_{yy}, the amplitude s_0 and

---

[11]Due to the complicated fitting function, the parameters had to be adjusted carefully by hand.
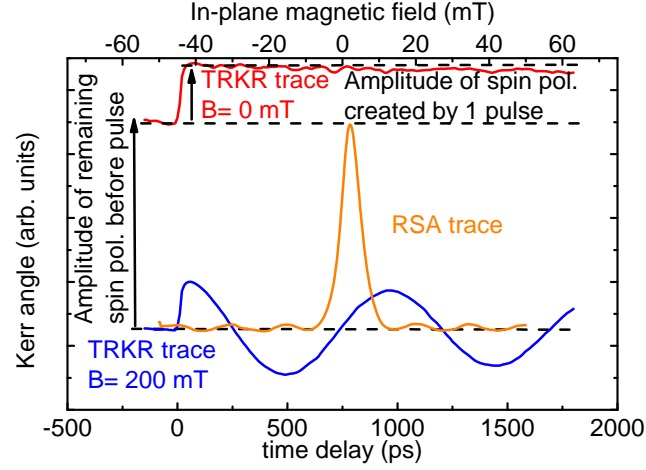
Figure 6.16: *TRKR traces from Fig. 6.15, taken at $B = 0$ (red line) and $B = 200$ mT (blue line). The non-zero Kerr signal of the zero-field TRKR trace at negative time delay $\Delta t < 0$ corresponds to the cumulated, remaining spin polarization of the previous pump pulses. The signal amplitude created by a single pump pulse is significantly lower. In the case of $B = 200$ mT, the spin ensemble is damped out on a shorter timescale. Thus, nearly no TRKR signal is visible at $\Delta t < 0$. Also depicted is an RSA trace taken at a fixed time delay $\Delta t = -50$ ps under the same experimental conditions as the TRKR traces ($I_{ex} = 8$ W/cm^2, $\lambda_{ex} = 809.4$ nm). For the negative time delay $\Delta t = -50$ ps, the coincidence of the TRKR and RSA signal levels at $B = 0$ and for $|B| > 0$ can be seen quite well.*
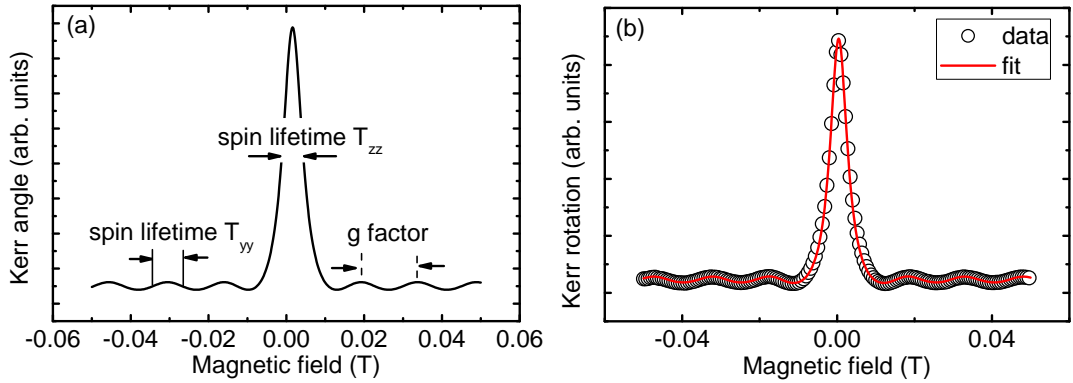

Figure 6.17: *(a) Expected shape of an RSA trace in the case of anisotropic spin dephasing. (b) RSA trace taken on sample G under similar experimental conditions as in Fig. 6.15. The excitation intensity was 8 W/cm^2 and the laser wavelength was tuned to 809.4 nm. These are the same values as in the time-resolved measurements shown in Fig. 6.15. The red line is a fit to the data using the expression in Eq. (4.3). The extracted SDTs are $T_{zz} = 2/\Gamma_{zz} \approx 60$ ns and $T_{yy} = 2.2$ ns; the determined absolute value of the g factor is 0.367 ± 0.002.*

the g factor. As mentioned in Sec. 4.2, the time delay between pump and probe pulses was fixed to $\Delta t = -50$ ps in all the RSA measurements presented in this work. The best agreement of the experimental data shown in panel (b) of Fig. 6.17 and the model could be achieved for an out-of-plane SDT $T_{zz} = 2/\Gamma_{zz} \approx 60$ ns and $T_{yy} = 2.2$ ns for the in-plane SDT. The determined value for the SDT T_{yy} is in good agreement with the results of the time-resolved measurements shown above. The observed difference in the T_{zz} values can be attributed to the fact that TRKR measurements become imprecise[12] if the spin lifetime becomes longer than the time window that can be directly observed with the delay line used.

From the RSA trace, the absolute value $|g| = 0.367 \pm 0.002$ of the electron g factor could be extracted as well. This value matches the value determined from the TRKR measurements within some small tolerance. As discussed above for the time-resolved measurement, this ensures that the obtained signal has its origin in the high-mobility 2DES, residing in the 30 nm wide QW.

Assuming that the SDTs T_{zz} and T_{yy} are limited by the DP mechanism, the relative strength of the (out-of-plane) Dresselhaus and the (in-plane) Rashba contribution to the SO field can be calculated by combining the terms shown in Eq. (2.55). From this the expression

$$\frac{\beta}{\alpha} = \sqrt{\frac{2\Gamma_{yy}}{\Gamma_{zz}} - 1} = \sqrt{\frac{T_{zz}}{T_{yy}} - 1} \qquad (6.7)$$

can be derived, being a measure for the symmetry of the band edge profile: in the case of an highly symmetric band edge profile with a vanishingly small Rashba contribution α, the ratio β/α is expected to reach high values. The values $T_{zz} \approx 60$ ns and $T_{yy} = 2.2$ ns yield a ratio $\beta/\alpha \approx 5.1$. This clearly shows the dominance of the Dresselhaus-type SO field in sample G at a temperature of 26 K.

In conclusion, it was shown that besides different other techniques, the RSA technique is a convenient tool for the investigation of anisotropic spin dynamics in (110)-grown 2DES. In stark contrast to TRKR and Hanle-type measurements [Ast08; Völ11], all the relevant parameters can be extracted individually from a single RSA trace: in TRKR measurements, subsequent measurement runs have to be performed in order to determine the out-of-plane SDT T_{zz} (B=0 mT) and the in-plane SDT, where the spin ensemble is rotated in the sample plane by an applied magnetic field $|B| > 0$ mT. The measurement run with the magnetic field applied allows also for the determination of the g factor. This is in contrast to Hanle-type measurements, from which the g factor cannot be obained at all. Furthermore, the in Hanle-type measurements determined spin dephasing time is the square root of a product of T_{zz} and T_{yy}, which does not allow for the independent determination of the in-plane and the out-of-plane component.

Automatic fitting routines failed because of the complexity of the model shown in Eq. (4.3).

[12]In the case of SDTs exceeding the time window directly accessible with the delay line used and the laser repetition period T_{rep}, the zero-field TRKR traces nearly have the shape of a step function, as it is illustrated in Fig. 6.16. The obtained TRKR traces have both, a small slope and a small curvature, which does not allow for a precise determination of T_{zz}. Moreover, the recombination of spin-polarized photoexcited carriers can affect the TRKR traces in the accessible time window. The optically generated holes recombine within the minority carrier lifetime τ_{PL} with electrons. In sample G, τ_{PL} could be determined from TRPL measurements (see, Fig. 6.25). The recombination of a hole with a spin-polarized electron leads to a loss of spin polarization, which results in a decrease of the TRKR signal. In consequence, the decay of the observed TRKR traces in the first few hundred ps (corresponding to the minority carrier lifetime τ_{PL}) in general has contributions of both, regular spin dephasing as well as the recombination of spin-polarized electrons. However, for the applied low excitation intensity of $I_{ex} = 8\,\mathrm{W/cm^2}$ and the corresponding low degree of initial spin polarization of the 2DES (see also Sec. 2.2.3), the carrier recombination can be expected to have a minor influence on the TRKR traces shown in Figs. 6.15 and 6.16. In this case, it is more likely (by a factor of n/n_{opt}) that an optically generated nonequilibrium hole recombines with an unpolarized resident electron, because the resident carrier density n is much larger than the density n_{opt} of the optically generated spin-polarized electrons.
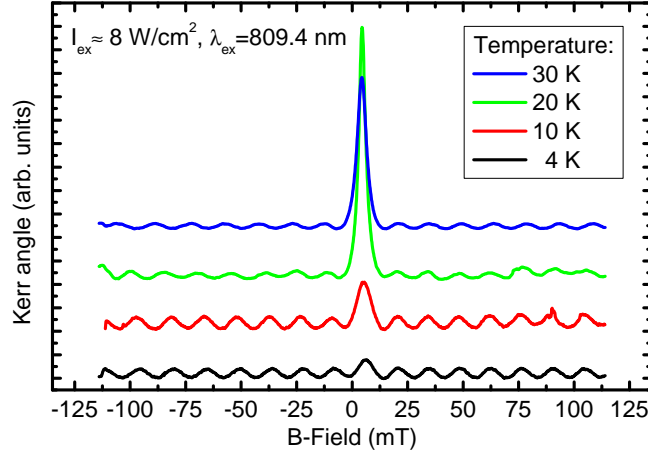
Figure 6.18: *RSA spectra taken at sample temperatures from $T = 4$ K up to $T = 30$ K. The drastic change of the RSA signal and particularly the change of the signal amplitude at $B = 0$ is clearly visible.*

6.2.2 Temperature dependence of the spin dephasing anisotropy

After the RSA technique was shown to be suitable for the investigation of anisotropic spin dynamics in (110)-grown 2DES, the temperature dependence of the spin dephasing anisotropy will be elucidated in this section. RSA measurements performed at lower sample temperatures revealed a strong temperature dependence of the spin dephasing anisotropy, manifesting itself in a drastic change of the RSA signal. As can be seen in Fig. 6.18, in particular the amplitude and the FWHM of the central RSA peak at zero magnetic field changes. This is an indication for a change of the out-of-plane SDT T_{zz}, which is connected with the FWHM of the central peak. In contrast, the shapes of the peaks at finite magnetic fields remain nearly unchanged, indicating a weak temperature dependence of the in-plane SDT T_{yy}. In order to investigate this strong temperature dependence in detail, a series of RSA measurements with small temperature steps of 2 K was performed. As discussed in Sec. 6.2.1, the SDTs T_{zz} and T_{yy} were determined by a comparison of the experimental data and the model in Eq. (4.3). This requires that the spin dephasing rates Γ_{zz} and Γ_{yy}, the signal amplitude s_0 and the electron g factor are adjusted by hand. The values extracted this way from the experimental data are presented in panel (a) of Fig. 6.19. Apparently, the out-of-plane SDT T_{zz} shows a strong increase with temperature over more than one order of magnitude. At about $T = 26$ K a maximum with $T_{zz} \approx 100$ ns is reached if an excitation intensity of about 120 W/cm² is used. A further increase of the temperature leads to a decrease of T_{zz}. However, the determined values still exceed the previously reported ones [Mül08] for temperatures up to 50 K. In stark contrast to the behavior of the out-of-plane SDT, the in-plane SDT T_{yy} remains nearly constant at a value of about 2 ns in the observed temperature range. The different temperature dependence of T_{zz} and T_{yy} also leads to a strong temperature dependence of the ratio β/α, being a measure for the symmetry of the band edge profile near to the 2DES. Panel (b) of Fig. 6.19 shows the values calculated from the SDTs shown in panel (a), using Eq. (6.7). At low temperatures, the Rashba and Dresselhaus contributions to the SO field are found to be comparable, whereas for $T > 25$ K the Rashba contribution is of less importance. From this it can be concluded that the band edge profile in the active region of sample G is quite symmetric for $T > 25$ K, whereas at low temperatures a significant asymmetry in the band edge profile is present, leading to a comparatively large Rashba contribution with $\alpha \approx \beta$. Therefore, the values for β/α shown in Fig. 6.19 are a first hint for a temperature dependence of the symmetry
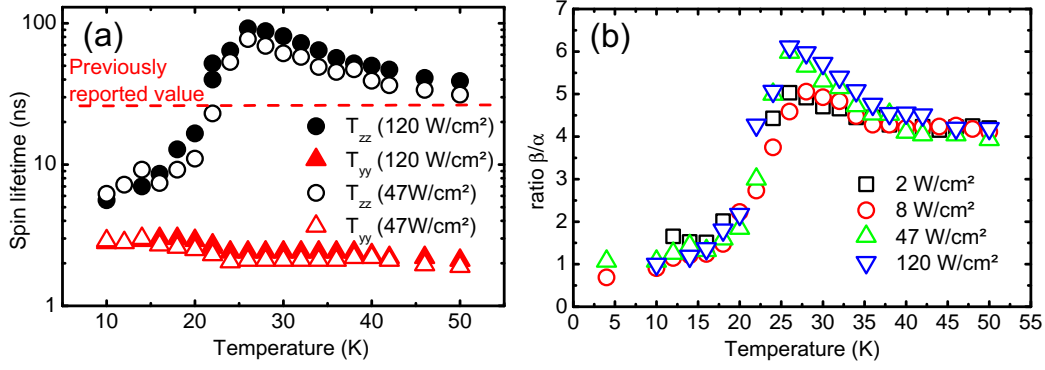
Figure 6.19: *(a) In-plane and out-of-plane SDTs T_{yy} and T_{zz} extracted from RSA traces taken on sample G with an excitation intensity of $I_{ex} = 47$ W/cm^2 and $I_{ex} = 120$ W/cm^2, respectively. The out-of-plane SDT T_{zz} is strongly temperature-dependent, having a sharp maximum at about 26 K. T_{zz} in sample G reaches values up to about 100 ns, which clearly exceed the values reported in Ref. [Mül08]. (b) Ratio β/α determined from the SDTs T_{yy} and T_{zz} shown in panel (a). The change of β/α can most likely be attributed to a change of the symmetry of the band edge profile.*

of the band edge profile.

The reason for the quite different temperature dependence of the in-plane and the out-of-plane SDT can most likely be attributed to a strong temperature dependence of the carrier density n for 4 K $< T <$ 25 K. PL measurements performed in the same temperature range revealed a strong increase of the spectral width ΔE of the PL of the 2DES, which indicates an increase of the carrier density $n \propto \Delta E$ (see, Eq. (4.7)). Panel (a) of Fig. 6.20 shows exemplary PL traces, taken at different temperatures 5 K $< T <$ 70 K. Whereas the spectral width ΔE of the PL trace taken at $T = 4$ K is comparatively small, a significant increase of ΔE occurs when the sample is heated up to about 30 K. For a quantitative analysis, the spectral width $\Delta E = E_F - E_G$ of the PL traces was extracted by fitting the high-energy tail of the PL with a Fermi-Dirac function, which yields the Fermi energy E_F. The band gap energy E_G was determined from the position of the steep low-energy edge of the PL, as depicted in panel (b) of Fig. 6.20. From the spectral width ΔE, the carrier density n of the 2DES can be directly calculated, using Eq. (4.7). As it is shown in panel (d) of Fig. 6.20, the extracted values of n show a strong increase in the observed temperature range: from about $1.5 \cdot 10^{11}$ cm^{-2} to a value exceeding $3 \cdot 10^{11}$ cm^{-2}. The increase of the spectral width ΔE of the PL with temperature, which is connected to the carrier density n, can be clearly seen in panel (c) of Fig. 6.20: the spectral width ΔE of the PL increases rapidly in the temperature range 4 K $< T <$ 25 K. This is connected with a redshift of the low-energy tail and an increase of the Fermi energy E_F. The blueshift of E_F can be attributed to an higher symmetry of the band edge profile, whereas the redshift of the low energy edge is most likely governed by band gap renormalization processes [Kle85b] resulting from the increase of the carrier density n of the 2DES. In addition, PL from the second subband can be observed for $T > 25$ K. This is due to the large carrier density n at this temperature, connected with a Fermi energy E_F just slightly below the second conduction subband[13]. Due to the spectral width $\delta E = k_B T$ of the Fermi step, a finite occupation of the second subband is possible, leading to the observed PL signal. Furthermore, the data shown in panel (c) of Fig. 6.20 illustrates the strong temperature dependence of the PL peak attributed to carbon impurities [Str81]: whereas the PL amplitudes of the 2DES and the

---

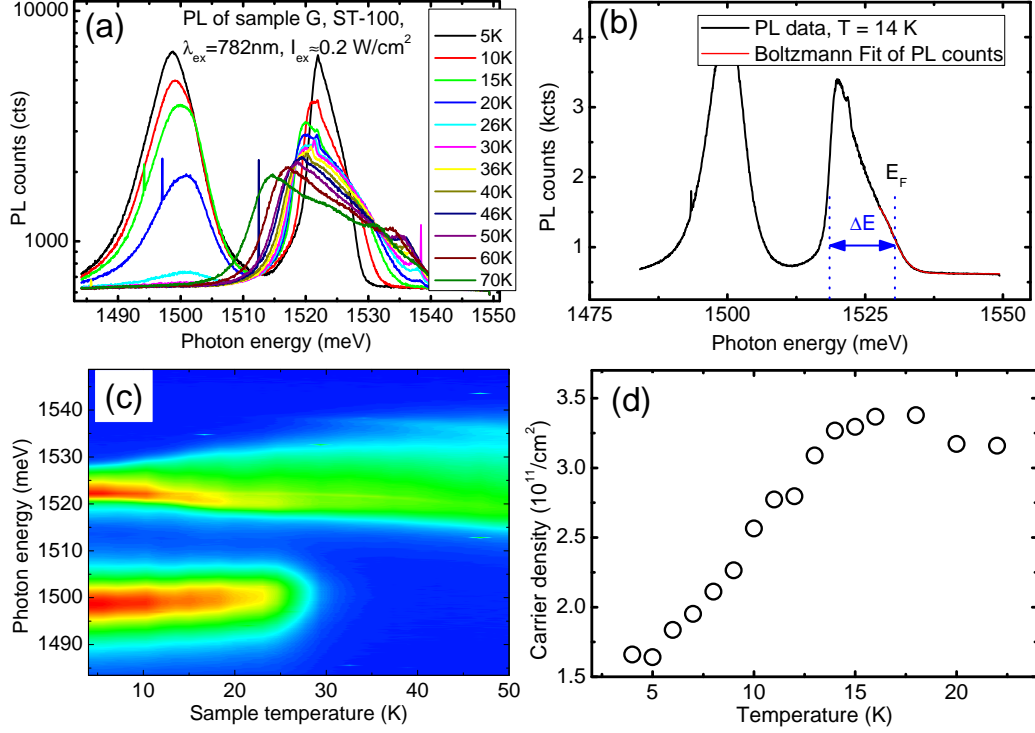[13]From nextnano^3 simulations an inter-subband spacing of 13 meV can be expected for the particular 30 nm wide QW in sample G.

Figure 6.20: *(a) PL traces taken at sample temperatures 5 K < T < 70 K. With increasing temperature, the FWHM of the 2DES PL peak increases as well. (b) The spectral width ΔE is connected with the carrier density n (see, Sec. 4.3). (c) Dependence of the PL signal on the temperature; the intensity is color-coded with an logarithmic scale. (d) Carrier density n, extracted from the spectral width of the PL traces using Eq. (4.7).*

carbon impurities are comparable at low temperatures $T < 15$ K, the part in the signal attributed to the carbon impurities vanishes completely between 20 K and 30 K. This observed decay of the carbon impurity PL amplitude with temperature is in agreement with earlier observations [Teh88; Teh90], where a model for the temperature dependence was discussed as well.

After the carrier density n in sample G was shown to be strongly temperature-dependent for 4 K < T < 25 K, the consequences on the SDTs T_{yy} and T_{zz} and the SDA will be discussed, focussing first on T_{yy}. The in-plane SDT $T_{yy} = (\Omega_D^2(k_F)\tau)^{-1}$ is governed by the microscopic scattering time τ and the Dresselhaus SO field

$$\mathbf{\Omega}_D^{(110)}(\mathbf{k}) = \frac{\gamma}{\hbar} \left[0, 0, k_x(\langle k_z^2 \rangle - (k_x^2 - 2k_y^2)) \right], \qquad (6.8)$$

having linear and cubic contributions of the wave vector $\mathbf{k}$. An increase of the carrier density n, connected via $k_F = \sqrt{2\pi n}$ with the wave vector k_F of the highest occupied electron state, leads to an increase of Ω_D. Due to the observed increase of the carrier density n with the sample temperature (see, Fig. 6.20(d)), the SDT T_{yy} would be expected to decrease with temperature. However, the increase of the SO field Ω_D is compensated by a decrease of the strongly temperature-dependent ee scattering time τ_{ee} (see, Eq. (2.10)) contributing to the microscopic scattering time τ. Thus, the in-plane SDT T_{yy} remains nearly unchanged in the observed temperature range 5 K < T < 50 K, as presented in panel (a) of Fig. 6.19. In contrast, the out-of-plane SDT T_{zz} is not limited by the Dresselhaus SO field Ω_D. As it was discussed [Gri12], two main reasons for the limited values of T_{zz} at low temperatures have to be considered. First, some
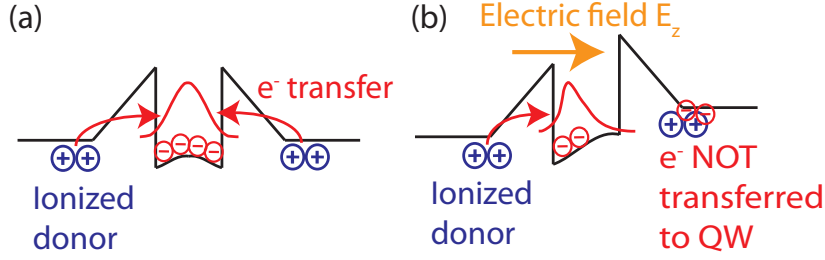
Figure 6.21: *(a) In a dsd heterostructure, electrons are transferred symmetrically from both sides into the QW from the doping layers, leaving back ionized donor atoms in the doping layers. The band edge profile remains symmetric. (b) If the electron transfer is not symmetric for some reason, the band edge profile becomes asymmetric and a built-in electric field E_z appears.*

"frozen asymmetry" in the band edge profile may result in a Rashba SO field Ω_R governed by an electron density δn located to the left or to the right of the 2DES (see panel (b) of Fig. 6.21). Such an asymmetric electron density δn may exist due to an incomplete transfer process of donor electrons from one of the doping layers on both sides of the QW. The electrons not transferred to the QW may be trapped either in the X band of the AlAs surrounding the doping layer, or somewhere in the spacer layer between the QW and the remote doping. The asymmetric electron density δn was discussed [Gri12] to result in a built-in electric field[14] $E_z = e\delta n/\kappa$, and hence in a regular Rashba SO field with $\alpha = 2\alpha_R e\delta n/\kappa$, where κ is the dielectric constant and $\alpha_R = 5$ eÅ^2 the Rashba coefficient for GaAs [Win03]. It was shown in panel (b) of Fig. 6.19 that at low temperatures the Rashba SO field is comparable to the Dresselhaus SO field, i.e., that $\alpha \approx \beta = \gamma \left(\frac{\pi}{d}\right)^2$. Therefore, the required asymmetric carrier density

$$\delta n = \frac{\gamma \pi^2 \kappa}{2\alpha_R e d^2} \tag{6.9}$$

can be estimated to be on the order of 1×10^{11} cm^{-2}. This value is comparable to the observed change in the carrier density, as can be seen in panel (d) of Fig. 6.20.

A second reason for the observed short out-of-plane SDT T_{zz} and the reduced SDA at low temperatures could be spin dephasing caused by spatially fluctuating electric fields of the ionized donor atoms. Under the assumption that these fluctuations are not fully screened by charge carriers residing in the X valley of the AlAs layers [Gla10b], random Rashba fields lead to spin dephasing with a rate [She03]

$$\Gamma_{zz} = \frac{16\pi}{\hbar^3} \frac{m^* e^2 \alpha_R^2 n_d k_F}{\kappa^2 R_d}. \tag{6.10}$$

Here, $R_d \approx 85$ nm is the distance of the ionized donors from the center of the 2DES, and n_d is the donor density on each side of the QW. A calculation of the SDT T_{zz} using the nominal donor concentration $n_d \approx 2 \times 10^{12}$ cm^{-2} (see also Sec. 3.1.2) yields values on the order of a few nanoseconds. Therefore, it is hard to distinguish whether random or regular Rashba fields dominate spin dephasing at low temperatures. The experimentally observed reduction of the carrier density after cooling the sample from $T \approx 30$ K to $T \approx 4$ K connected with a redshift of the PL are strong hints that a certain electron density δn at low temperatures is trapped somewhere outside the 30 nm wide QW. If the carrier density δn can be found on one side of the QW, the resulting band

---

[14]Here, the simple model of a plate capacitor is used, where the electric field E is defined by the *charge* density $e\delta n$ divided by the dielectric constant κ.

bending causes the appearance of a regular Rashba field and a reduced transition energy observable in PL measurements. However, some influence of random Rashba fields at low temperatures cannot be excluded. At higher temperatures, the asymmetry of the band edge profile vanishes due to a redistribution of the carriers between the SPSL-type donor layers and the 2DES. In consequence, the regular Rashba field disappears. A similar temperature behavior can also be expected for random Rashba fields limiting spin dephasing: for higher temperatures, the charge redistribution as discussed above may switch on the screening of the random Rashba field [Rös10]. In consequence, spin dephasing times on the order of 50 to 100 ns become observable.

In conclusion, the observed temperature dependence of the SDTs in sample G was attributed to a temperature-dependent change of the carrier density n. The in-plane SDT $T_{yy} \propto (\Omega_D^2 \tau)^{-1}$, governed by the Dresselhaus SO field Ω_D, remains nearly constant due to the counteracting changes of the microscopic scattering time τ and the carrier density n. Whereas a higher temperature leads to a decrease of τ, the increasing carrier density n results in a larger Ω_D. In contrast, the out-of-plane component T_{zz} is sensitive to in-plane Rashba-type contributions of the SO field. Without much doubt, the varying carrier density n is also connected to a change of the symmetry of the band edge profile and the corresponding Rashba field Ω_R. At low temperatures, Rashba fields caused by the most likely quite asymmetric band edge profile or random fluctuations of the donor potentials strongly limit the out-of-plane SDT T_{zz}. At higher temperatures $T > 25$ K, where the band edge profile is highly symmetric and/or the random Rashba fields are efficiently screened, very long SDTs T_{zz} on the order of 50 to 100 ns were observed.

A nearly similar behavior of the in-plane and the out-of-plane SDT could be observed in TRKR measurements taken on sample F. In these measurements, T_{zz} and T_{yy} show an increase with temperature, until they reach a maximum[15] at about $T \approx 40$ K (T_{zz}) and $T \approx 80$ K (T_{yy}), respectively (see, Fig. 6.22). The determined values of T_{yy} are lower compared to the corresponding values in sample F. This is in agreement with the expectation: due to the higher carrier density n in sample F, larger SO fields are involved, leading to a lower SDT T_{yy}. It is most likely that for the same reason the out-of-plane SDT T_{zz} has its maximum also at a lower value of about 30 ns. Fig. 6.22 includes values of the ratio β/α as well, which are a measure for the symmetry of the band edge profile. Using the formula in Eq. (6.7), the presented values of β/α were calculated from the corresponding SDTs T_{zz} and T_{yy}, and show a very weak temperature dependence within the investigated temperature range 4 K$< T <$160 K. The high value of $\beta/\alpha > 4$ is an indication for the high symmetry of the band edge profile in the active region of sample F. In addition, it can be deduced from the presented data that the symmetry of the band edge profile in sample F is nearly independent from the temperature, which is in stark contrast to the behavior of sample G (c.f. Fig. 6.19). The reason for this may be found in slightly different growth parameters: the nominal concentration n_d of dopants was increased in sample F; in addition, the growth temperature was reduced during the deposition of the Si donor atoms in order to reduce the number Si_{As} of Si atoms built in the crystal on As sites [Xu99], where they act as acceptors and lead to unintended holes in the doping layers[16]. The combination of these two changes leads to a higher doping efficiency, which becomes visible due to the resulting higher carrier concentration n in the 2DES. Finally it should be noted that in consequence of the precise control of

---

[15]It should be noted that the temperature T, where the SDTs reach their maximum values, is not in coincidence with the Fermi temperature of $T_F \approx 140$ K of the 2DES, which corresponds to the carrier density of $n = 3.4 \times 10^{11}$ cm^{-2} in sample F (see, Tab. 3.2). This is in stark contrast to what was shown in Sec. 5.2.1 for the out-of-plane SDT in the (001)-grown samples A-D with an asymmetric band edge profile. However, the reason for this different behavior is not clear, yet.

[16]Holes present in the doping layer compensate donor electrons, which thus can not be transferred into the 2DES. Hence, the doping efficiency is drastically reduced.
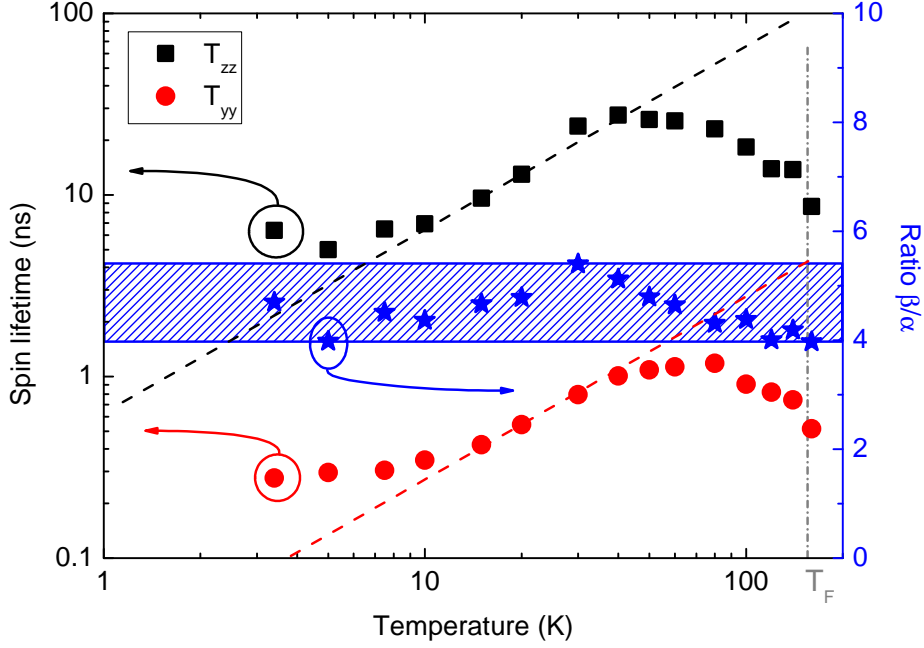
Figure 6.22: *SDTs T_{zz} and T_{yy} determined from TRKR measurements on sample F. The extracted SDTs show an increase with temperature until they reach a maximum at about $T \approx 40\,K$ (T_{zz}) and $T \approx 80\,K$ (T_{yy}), respectively. The dashed lines have slope 1, for reference. The blue stars mark the ratio β/α calculated from T_{zz} and T_{yy} using the formula in Eq. (6.7). The grey line marks the Fermi temperature of $T_F \approx 140\,K$ of sample F, corresponding to a carrier density of $n = 3.4 \times 10^{11}\,cm^{-2}$ (see, Tab. 3.2).*

the band edge profile and the growth parameters, the mobility μ in sample F exceeds $5 \times 10^6\,cm^2/Vs$. This value, clearly exceeding the mobility $\mu \approx 2 \times 10^6\,cm^2/Vs$ of sample G, has been the highest mobility achieved in (110)-grown heterostructures so far [Sch12].

For a deeper understanding of the temperature dependence of the carrier density, as well as the symmetry of the band edge profile, more measurements would be necessary. Facing the complex growth structure of the presented samples and the particular problem of the amphotericity of the dopant atoms on {110} facets, a simple explanation for the different behavior observed in samples F and G cannot be given, so far.

6.2.3   Dramatic increase of spin dephasing times caused by optical gating

After the observation of long SDTs T_{zz} on the order of 50-100 ns was discussed in the previous section, the strong influence of illuminating sample G with weak above-barrier light will now be presented. The SDTs T_{zz} and T_{yy} will be shown to dramatically increase under the conditions of optical gating (see Sec. 2.1.3), reaching values T_{zz} on the order of about 150-200 ns.

As emphasized several times in this work, the DP spin dephasing rate Γ depends on the strength of the SO field $|\Omega(k_F)|$ at the Fermi wave vector and the microscopic scattering rate τ as

$$\Gamma = \frac{1}{T_2} = \Omega(k_F)^2 \tau. \tag{6.11}$$

Therefore, a change of the Fermi wave vector $k_F = \sqrt{2\pi n}$, connected to a change of the carrier density n, is expected to have a strong influence on the SDT observable in the 2DES. Moreover, in a system where the ee scattering time τ_{ee} limits the microscopic
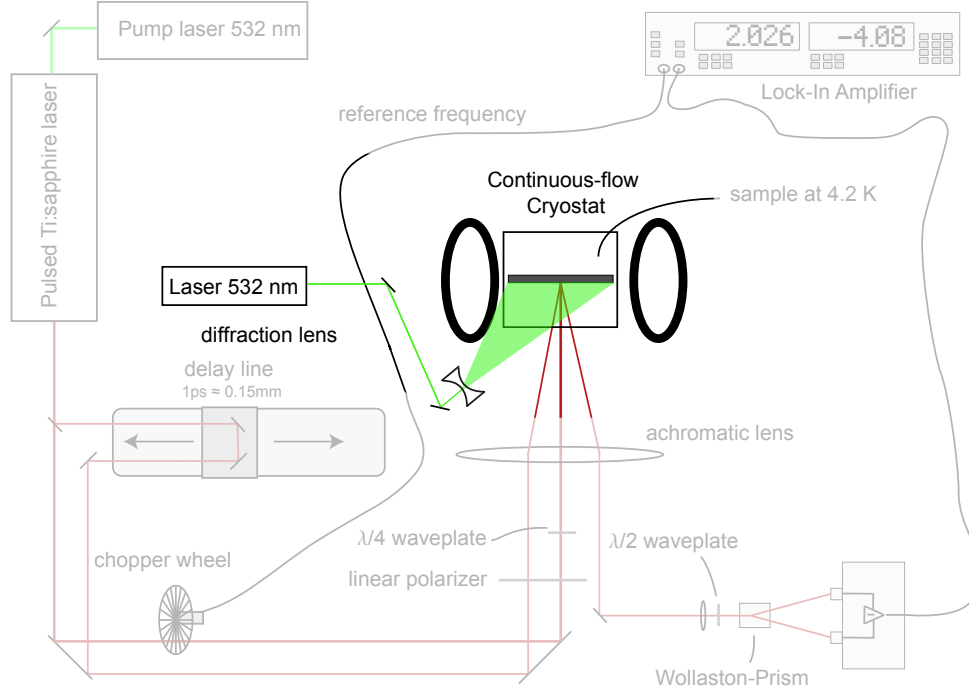
Figure 6.23: *Experimental setup used for the RSA measurements with above-barrier illumination. Here, in addition to the setup presented in Fig. 4.2, the whole sample is illuminated by a defocussed beam of a green 532 nm DPSS laser.*

scattering time τ, the dependence of τ_{ee} on the carrier density $n \propto E_F$ affects the SDT as well, see Eq. (2.10).

The carrier density n of a 2DES, residing in a symmetrically grown and doped heterostructure, can be tuned all-optically using the optical gating technique (see Sec. 2.1.3). In the experiments presented in this section, the above-barrier illumination is provided by a beam of a frequency-doubled diode-pumped solid state (DPSS) laser, hitting the sample under oblique incidence (see Fig. 6.23). The photon energy $E_{Phot} \approx 2.3$ eV of the 532 nm continuous wave laser beam exceeds the band gap energy $E_G \approx 1.83$ eV of the $Al_{0.25}Ga_{0.75}As$ barrier (c.f. Eq. (2.3)), surrounding the 30 nm wide QW[17]. In order to provide an illumination intensity being homogeneous on the length scale of the laserspot ($2r \approx 50~\mu$m) of the pulsed Ti:sapphire laser used for the RSA measurements, the laser beam of the green DPSS laser was defocussed using a $f = -40$ mm diffraction lens. The resulting diameter of the green laser beam at the sample was about 1 cm, and, therefore, exceeding the sample size. The power of the above-barrier illumination could be varied by a continuously tunable neutral density filter wheel and was adjusted to logarithmically increasing values $P_{532~nm}$ by help of a power meter. The corresponding intensity of the green laser beam at the sample surface can be roughly estimated to be $I_{532~nm} \approx P_{532~nm}/1$ cm^2.

The effect of weak above-barrier illumination on the PL of sample G can directly be seen in panel (a) of Fig. 6.24: the spectral width of the photoluminescence line decreases for a more intense above-barrier illumination. The illumination intensity $I_{532nm} \approx 400~\mu$W/cm^2 required for a reduction of the carrier density to a steady-state value of $n_s \approx n_0/2$ (c.f. Eq. 2.11) is extremely small on this sample. For comparison, the average

---

[17]For comparison, in some experiments a 635 nm laser diode ($E_{Phot} \approx 1.95$ eV) was used for the above-barrier illumination, resulting in a similar behavior as in the case of the green 532 nm laser.
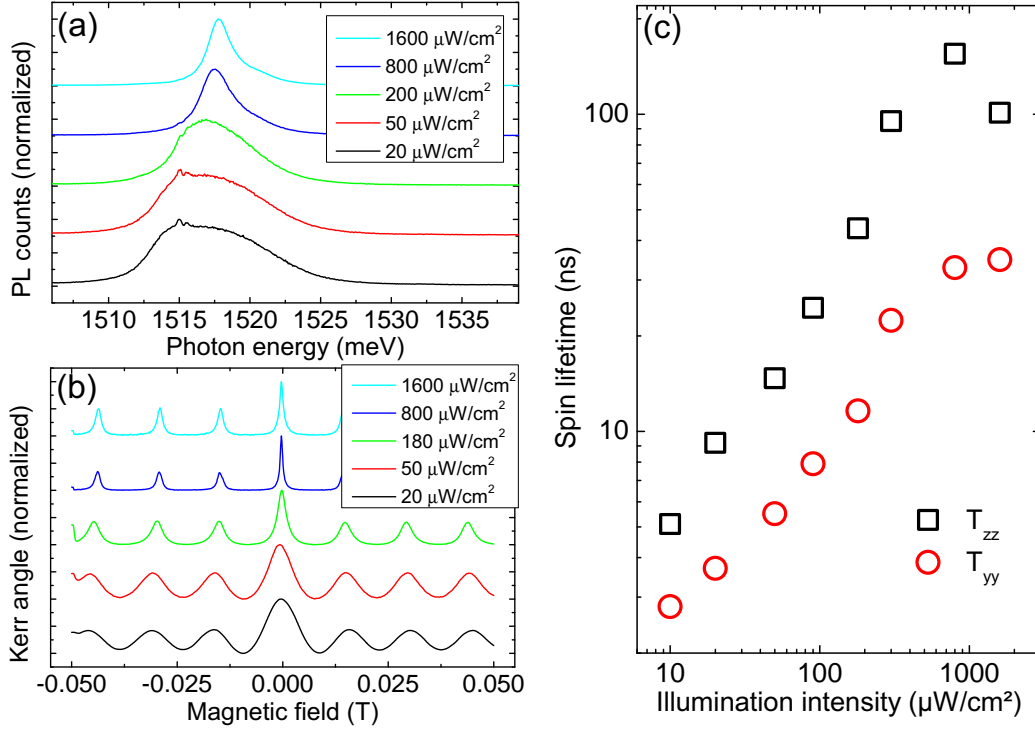
Figure 6.24: *(a) PL traces of sample G at $T = 4$ K under the conditions of optical gating using a 532 nm cw DPSS laser. The FWHM of the PL peak decreases with increasing above-barrier illumination intensity $I_{532\text{nm}}$. (b) RSA traces taken under the conditions of optical gating for different intensities $I_{532\text{nm}}$ at a sample temperature of $T = 4$ K. (c) Spin dephasing times T_{zz} and T_{yy} extracted from the RSA traces using Eqs. (4.3)-(4.5).*

excitation intensity of the Ti:sapphire laser used for the TRKR/RSA measurements is about $I_{ex} \approx 8$ W/cm^2, which exceeds $I_{532\text{nm}}$ by orders of magnitude. Nevertheless, even a very low intensity of above-barrier light has a dramatic effect on the RSA signal, as it is shown in panel (b) of Fig. 6.24. The line width of the RSA peaks significantly decrease if $I_{532\text{nm}}$ is increased. As discussed in Sec. 4.2, the FWHM of the RSA peaks is connected with the anisotropic SDTs T_{zz} and T_{yy}. A comparison of the experimental RSA data with the model in Eq. (4.3), adjusting the values of the SDTs T_{zz} and T_{yy}, the g factor and the amplitude s_0, yields the values of T_{zz} and T_{yy} shown in panel (c) of Fig. 6.24. Here, a strong increase of both, the in-plane as well as the out-of-plane SDT, with the amount of above-barrier light is visible. Both, T_{zz} and T_{yy}, increase more than about one order of magnitude in the observed range of $I_{532\text{nm}}$, reaching maximum values of $T_{zz} \approx 150$ ns and $T_{yy} \approx 35$ ns. For the highest intensity $I_{532\text{nm}} \approx 1600$ μW/cm^2, the value of T_{zz} drops to about 100 ns. The reason for this may be found in the presence of optically generated holes, leading to BAP spin dephasing (see Sec. 2.2.6). The holes injected by the optical gating process (see Sec. 2.1.3) into the valence band states of the QW exist there for a timespan on the order of the minority carrier lifetime $\tau_{PL} \approx 375$ ps, which was determined from TRPL measurements (see Fig. 6.25). The hole concentration p inside the QW can be taken to depend linearly on the illumination intensity $I_{532\text{nm}}$. Therefore, the BAP spin dephasing rate $1/\tau_{BAP} \propto p$ (see Eq. (2.47)) increases with $I_{532\text{nm}}$ and may exceed the DP dephasing rate Γ_{zz} for a certain value of $I_{532\text{nm}}$. In addition, also the hyperfine mechanism (see Sec. 2.2.6) could contribute to spin dephasing in this case, where the 2DES is strongly depleted.

Interestingly, both, T_{zz} and T_{yy}, show the same dependence on $I_{532\text{nm}}$, which is in
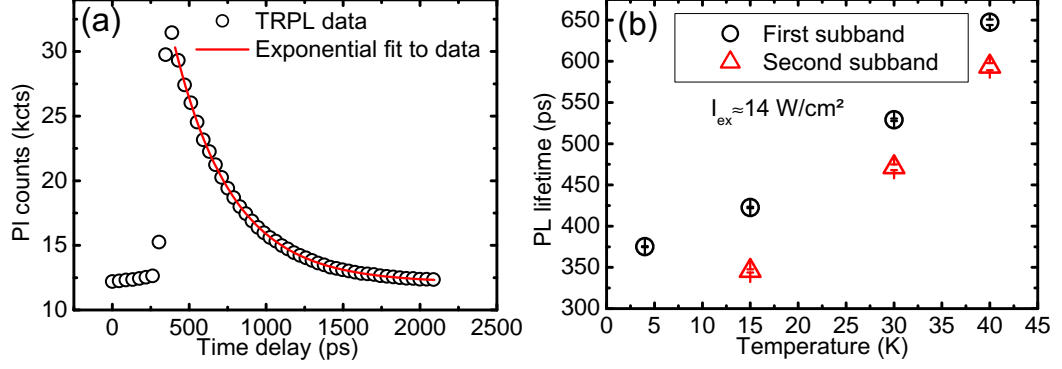
Figure 6.25: *(a) TRPL trace taken on sample G at a sample temperature of $T = 4$ K, using an excitation intensity $I_{ex} \approx 15$ W/cm². (b) Extracted PL lifetimes τ_{PL} of the first and the second conduction subband.*

stark contrast to the behavior of T_{zz} and T_{yy} on the sample temperature, as discussed in the previous section. The uniform behavior of T_{zz} and T_{yy} in this case is a clear indication that both SDTs are governed by one single spin dephasing mechanism, the DP mechanism. Because in the DP mechanism the SDTs

$$\frac{2}{T_{zz}} = \Omega_R^2(\mathbf{k}_F)\tau, \quad \frac{1}{T_{yy}} = \Omega_D^2(\mathbf{k}_F)\tau \tag{6.12}$$

are limited by the strength of the SO fields $\Omega_{D/R}$ and the microscopic scattering time τ, the consequences of above-barrier illumination on those two quantities have to be considered: First, a reduction of the carrier density $n \propto k_F^2$ due to optical gating leads to lower SO fields $\Omega_{D/R}(k_F)$. Because both, the Dresselhaus as well as the Rashba contribution to the SO field, are linear in k, a change of the Fermi wave vector $k_F = \sqrt{2\pi n}$ equally affects $\Omega_D(k_F)$ and $\Omega_R(k_F)$. Secondly, a change of the carrier density n affects both contributions to the microscopic scattering time τ. The momentum scattering time τ_p and the ee scattering time τ_{ee} decrease if the carrier density n is reduced. In consequence, the SDTs T_{zz} and T_{yy} are similarly affected by a change of the SO fields as well as the reduced microscopic scattering time τ. Therefore, the observed similar behavior of T_{zz} and T_{yy} can be taken as a strong hint, that both T_{zz} and T_{yy} are limited by the DP mechanism under the conditions present during the measurements at a nominal sample temperature of $T = 4$ K.

In order to relate the above-barrier illumination intensity I_{532nm} to the steady-state carrier density n_s of the 2DES, PL measurements were performed. From the spectral width of the obtained PL traces the carrier density n could be extracted using the expression in Eq. (4.7). The carrier densities n_s resulting from PL measurements at different temperatures are shown in panel (a) of Fig. 6.26. A decrease of the carrier density n_s with increasing I_{532nm} is clearly visible. Subsequent to these PL measurements, RSA measurements were performed under the same experimental conditions[18]. Thus, the SDTs T_{zz} and T_{yy}, extracted from an RSA trace measured at a certain value I_{532nm} of the above-barrier light, could be related to the carrier density n_s corresponding to I_{532nm}. Values of T_{zz} and T_{yy} resulting from such a measurement series can be seen in panel (b) of Fig. 6.26. The determined values of the SDTs show an increase if the steady-state carrier density n_s of the 2DES is reduced. The increase of the in-plane SDT T_{yy} can be attributed to the decrease of both, the Dresselhaus SO field Ω_D as well as the microscopic scattering rate τ, as discussed above. From the data points given in panel (b), the dependence of the SDTs of both the carrier density n, as well as the

---

[18]Of course, the laser wavelength had to be tuned from $\lambda_{PL} = 780$ nm to $\lambda_{RSA} = 809.1$ nm.
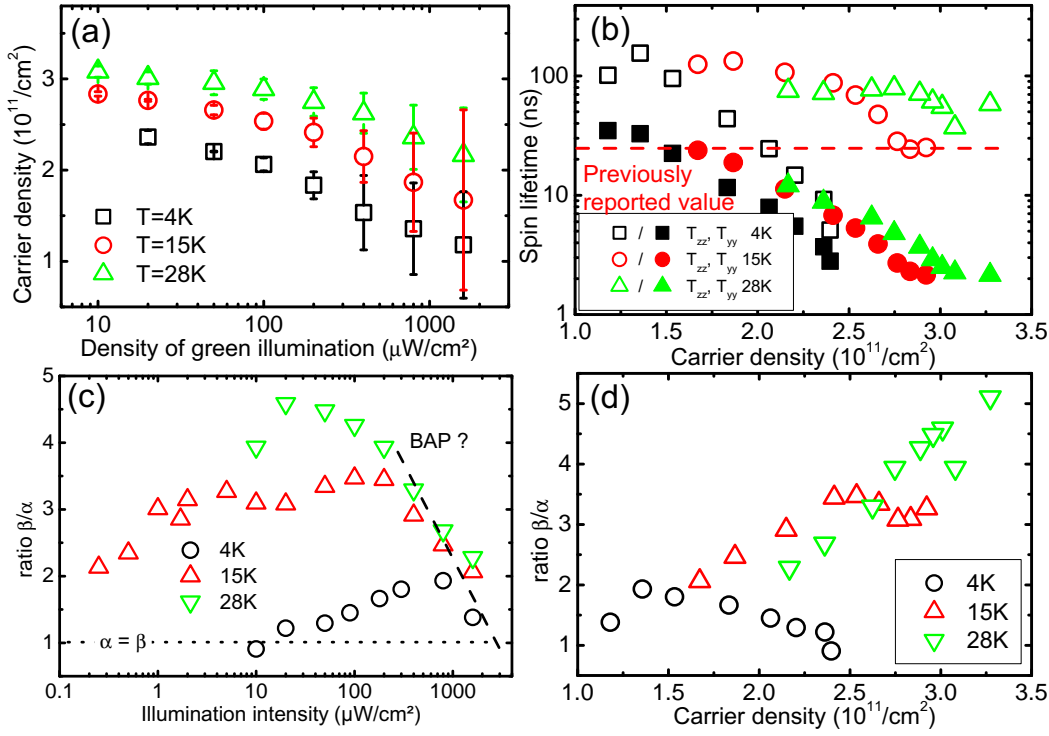
Figure 6.26: (a) Carrier density n of sample G extracted from the spectral width of PL traces. The carrier density was optically controlled using a defocussed green laser beam. (b) T_{zz} and T_{yy} extracted from RSA traces taken on sample G under the conditions of optical gating. The excitation intensity I_{ex} was about 8 W/cm^2. The carrier densities n corresponding to the illumination intensities I_{532nm} were extracted from the data shown in panel (a). The red line marks the value for T_{zz} previously reported in [Mül08]. (c) Ratio β/α determined from the values T_{zz} and T_{yy}, using Eq. (6.7). The ratio seems to drop for higher illumination intensities independent of the sample temperature. (d) Ratio β/α plotted against the carrier density n.

strongly temperature-dependent microscopic scattering time τ, can be seen quite well: for a fixed carrier density n, the observed SDTs T_{yy} are longer at higher temperatures T. This is in agreement with the expectation for the strongly temperature-dependent microscopic scattering time τ (see Eq. (2.10)).

In contrast, the values of T_{zz} are found to behave differently from T_{yy}. At a sample temperature of $T = 28$ K, the out-of-plane SDT T_{zz} saturates at a value $T_{zz} \approx 75$ ns. This can be seen from the data points shown in panel (b) of Fig. 6.26. Moreover, the absolute increase of T_{zz} is apparently smaller compared to the strong increase observed at a sample temperature of 4 K, where T_{zz} increases about one order of magnitude. At lower temperatures, even a decrease of the SDT becomes visible for the lowest carrier densities n, corresponding to the highest illumination intensities I_{532nm}. The behavior of T_{zz} on the illumination intensity I_{532nm} can be attributed most likely to an interplay of a change of the symmetry of the band edge profile, induced by optical gating, as well as a second, not DP-type contribution to spin dephasing. As it can be seen in panel (c) of Fig. 6.26, the symmetry of the band edge profile, expressed in the ratio β/α, first shows an increase until it drops rapidly to very low values. The reason for the increase of β/α and the corresponding increase of the symmetry of the band edge profile most likely could be found in a redistribution of carriers between the 2DES and the doping layers on both sides of the QW. Following the Lambert-Beer absorption law (see, e.g. [Ber99]), the intensity $I_{532\,nm}(z) \propto \exp(-\alpha' z)$ of above-barrier photons drops
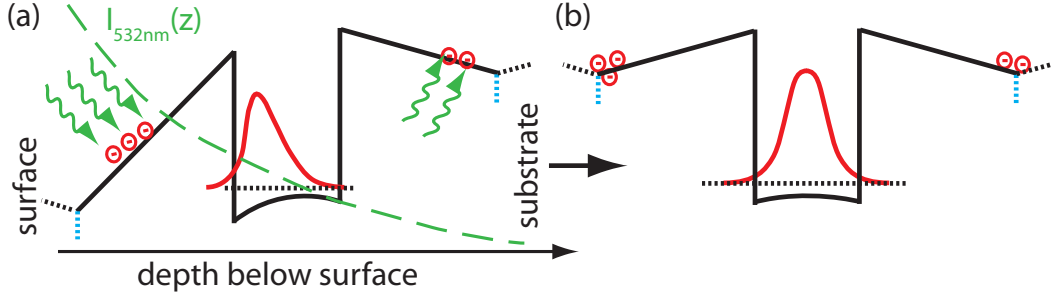
Figure 6.27: (a) The intensity $I_{532\,nm}$ of the above-barrier illumination drops exponentially for an increasing depth below the sample surface. In consequence, the numbers of electron-hole pairs created in the barriers to the left and to the right of the QW are different. (b) The asymmetric electron transfer from the 2DES towards the doping layers results in a symmetrization of an initially tilted band edge profile.

exponentially with increasing distance z from the surface. α' is the absorption constant. In consequence, the numbers of electron-hole pairs created in the barriers to the left and to the right of the QW are different, leading in effect to an asymmetric electron transfer from the 2DES towards the doping layers. This is schematically depicted in Fig. 6.27. Due to the asymmetric electron transfer, the symmetry of the band edge profile is expected to change: the conduction band edge at the doping layer, which is closer to the surface, is lifted more than at the position of the doping layer on the opposite side of the QW. Experimentally, an increase of the ratio β/α for an increasing illumination intensity with above-barrier light was observed. Thus, the change of the symmetry of the band edge profile, induced by the above-barrier illumination, compensates the initial asymmetry, which is most likely present at $T < 20$ K (see Sec. 6.2.2). From this it can be inferred that the band edge profile of sample G without additional illumination is tilted as depicted in panel (a) of Fig. 6.27.

For higher illumination intensities I_{532nm} the ratio β/α drops rapidly, nearly independent of the sample temperature. The reason for this may be found most likely in the increasing influence of the BAP mechanism resulting from the increasing steady-state hole density p, present in the QW in consequence of optical gating. If the BAP spin dephasing rate $1/\tau_{BAP} \propto p$ becomes higher than the DP dephasing rate Γ_{zz}, the out-of-plane SDT is no more limited by the DP mechanism. Nevertheless, the determined ratio β/α would decrease towards a final value of about 1, corresponding to a case without spin dephasing anisotropy[19] and equal spin dephasing rates $\Gamma_{zz} = \Gamma_{yy}$.

The same behavior could also be found in RSA measurements on sample G, performed in the split-coil cryostat system, where sample temperatures down to $T = 0.4$ K can be achieved. Panel (a) of Fig. 6.28 shows the dependence of the spin dephasing rates Γ_{zz} and Γ_{yy}, extracted from RSA measurements, at a sample temperature of 1.1 K. After the decrease of the dephasing rates of about one order of magnitude and a minimum rate of $\Gamma_{zz} \approx 9$ MHz at an illumination intensity of $I_{532nm} \approx 100\ \mu W/cm^2$, Γ_{zz} and Γ_{yy} show an increase and become equal for $I_{532nm} > 400\ \mu W/cm^2$. Interestingly, in this case Γ_{zz} can even become slightly larger than Γ_{yy}. The reason for this is not completely clear. One possible reason for the case $\Gamma_{zz} > \Gamma_{yy}$ could be the temporally inhomogeneous hole density $p(\Delta t)$: $p(\Delta t)$ has a maximum when the pump pulse hits the sample, i.e., for small positive Δt. At the same time, the optically generated spin ensemble is oriented perpendicular to the sample plane, experiencing the dephasing rate $\Gamma_{zz} \approx \Gamma_{BAP}$. Because the hole concentration p for small times Δt after the arrival of

---

[19]In contrast to the DP mechanism, the BAP mechanism leads in general to isotropic spin dephasing.
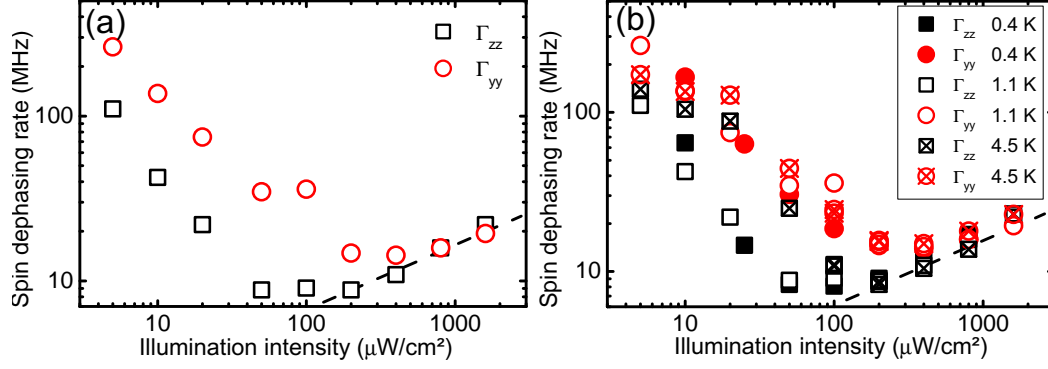
Figure 6.28: *(a) Spin dephasing rates Γ_{zz} and Γ_{yy} extracted from RSA measurements on sample G at a temperature of 1.1 K. The out-of-plane dephasing rate Γ_{zz} shows a minimum at $I_{532\mathrm{nm}} \approx 100\ \mu W/cm^2$. For $I_{532\mathrm{nm}} > 400\ \mu W/cm^2$ the rates Γ_{zz} and Γ_{yy} become nearly equal. (b) The dependence of Γ_{zz} and Γ_{yy} on $I_{532\mathrm{nm}}$ is nearly independent of the sample temperature. The dashed black lines are drawn in support of a better recognition.*
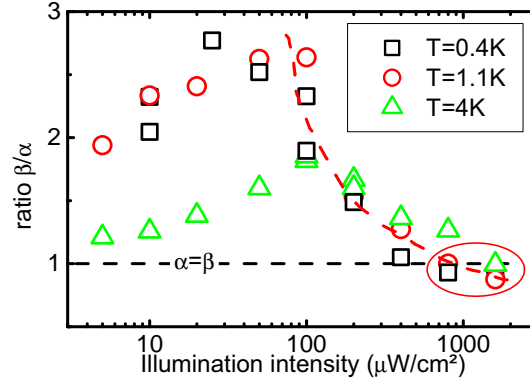

Figure 6.29: *Ratio β/α calculated from the low temperature data shown in Fig. 6.28. At high illumination intensities $I_{532\mathrm{nm}}$ the ratio drops quickly for all temperatures. This may be related to the BAP mechanism. The dashed red line is drawn in support of a better recognition, whereas the dashed black line points out the case of isotropic spin dephasing ($\alpha = \beta$).*

the pump pulse is higher, the corresponding BAP dephasing rate Γ_{BAP} can be expected to be higher as well. In contrast, due to the weak magnetic fields applied and the small Larmor frequencies, all of the holes excited by the pump pulses have finished their recombination processes, until the electron spin ensemble is precessed into the sample plane. Therefore, the in-plane component Γ_{yy} of the spin relaxation rates tensor $\hat{\Gamma}$ corresponds to a smaller BAP dephasing rate $\Gamma'_{BAP} < \Gamma_{BAP}$ resulting from a lower hole density p.

The transition from the regime of anisotropic DP spin dephasing to the regime with equal rates Γ_{zz} and Γ_{yy} can also be seen in Fig. 6.29. In the case of equal rates, the ratio β/α is expected to be 1, what is marked with the dashed black line in Fig. 6.29. Values of β/α smaller than one correspond to situations where $\Gamma_{zz} > \Gamma_{yy}$, as discussed above.

As can be seen from the data presented in Fig. 6.28, very small spin dephasing rates $\Gamma_{zz} \approx 8$ MHz can be achieved in sample G at low temperatures corresponding to ultra-long spin dephasing times T_{zz}. The highest values for T_{zz} were found in measurements at a nominal sample temperature of $T = 0.4$ K under additional illumination with green
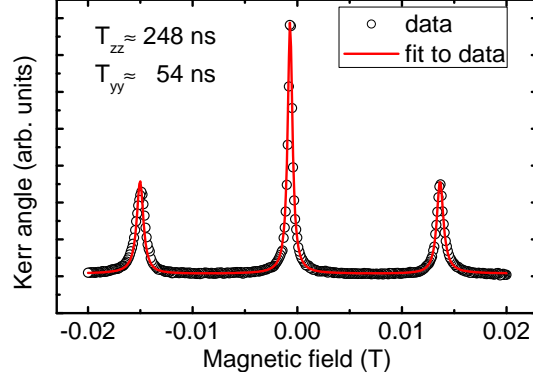
Figure 6.30: *RSA data taken at $T = 0.4$ K and an illumination intensity $I_{532\mathrm{nm}} \approx 100\ \mu W/cm^2$. The red line is a fit to the experimental data using the model in Eq. (4.3). The fit yields $T_{zz} \approx 248$ ns and $T_{yy} \approx 54$ ns. The excitation intensity I_{ex} of the pulsed near-infrared Ti:sapphire laser was about 8 W/cm^2.*

laser light. Fig. 6.30 shows an RSA trace, taken at $T = 0.4$ K and $I_{532\mathrm{nm}} \approx 100\ \mu\mathrm{W/cm^2}$, and a corresponding fit, from which the longest observed SDTs $T_{zz} \approx 248$ ns and $T_{yy} \approx 54$ ns could be extracted. The extracted value for T_{zz} exceeds the previously reported values [Mül08] for SDTs in GaAs-based 2DESs by one order of magnitude. Even the in-plane SDT $T_{yy} \approx 54$ ns is twice as long as the former record value.

It is hard to distinguish whether the SDT of 248 ns is limited by the DP mechanism, or the BAP mechanism resulting from the amount of holes present in the QW due to optical gating. For higher illumination intensities $I_{532\mathrm{nm}}$, however, spin dynamics seem to be governed by the BAP mechanism[20], whereas for lower intensities the DP mechanism seems to limit the anisotropic SDTs T_{zz} and T_{yy}.
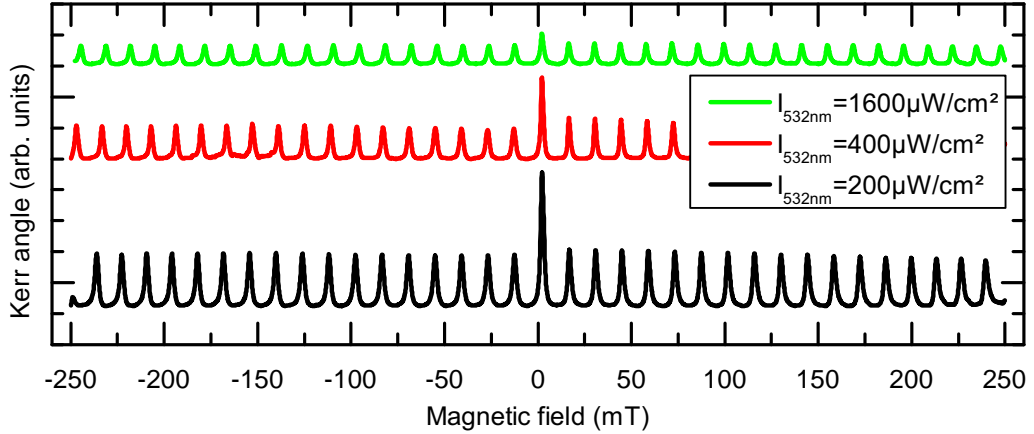

Figure 6.31: *RSA spectra (not normalized) taken at $T = 3.4$ K under the conditions of optical gating. The amplitude of the RSA peaks does not decay, even for the highest excitation intensity $I_{532\mathrm{nm}} \approx 1600\ \mu W/cm^2$, applied in the experiments.*

---

[20]Due to the lack of a full theoretical understanding in terms of a formula for the BAP spin dephasing rate for two-dimensional systems, just a rough estimate of Γ_{BAP} is possible. The steady-state hole density p in the QW, resulting from optical gating can be estimated the same way as it was presented for electrons in Sec. 2.2.3. Considering also the carrier recombination time $\tau_{PL} \approx 500$ ps, the hole concentration at $I_{532\mathrm{nm}} \approx 1000\ \mu\mathrm{W/cm^2}$ can be estimated to be about $p \approx 10^6\mathrm{cm^{-2}}$, what corresponds to about 25 holes inside the probe laser spot. Under this assumption Γ_{BAP} can be estimated to be on the order of about 10 MHz, the same order of magnitude as observed in the experiment.

Finally, it should be noted that in RSA experiments in higher magnetic fields no decrease of the peak amplitude with increasing magnetic field could be observed (see Fig. 6.31). This is true, even for the highest excitation intensity $I_{532\text{nm}} \approx 1600 \ \mu\text{W/cm}^2$ sample G was exposed to, corresponding to the lowest carrier density n. The constant amplitude of the RSA peaks for $|B| > 0$ mT is a clear indication for a very small g factor inhomogeneity in the investigated sample [Gla08]. This is in stark contrast to what can be found in systems with localized carriers [Yug09; Kor10], where the g factor inhomogeneity leads to a decay of the amplitude of the RSA peaks with increasing magnetic field strength. From the absence of a g factor inhomogeneity, one can infer that even at the lowest carrier density n, the electrons are delocalized. Thus, the observed long and anisotropic SDTs T_{zz} and T_{yy} are dephasing times of free electrons, localization effects can be ruled out.

6.2.4 Evidence for efficient dynamical nuclear polarization

Two regimes, where long SDTs $T_{yy,zz}$ could be observed, were discussed in Secs. 6.2.2 and 6.2.3. In these cases, a build-up of a large electron spin polarization s_0 is possible due to the long SDTs T_{yy} and T_{zz}, being on the order of the laser repetition period T_{rep}. Due to the hyperfine interaction, a transfer of spin polarization from the electron system to the nuclear spin system can be expected [Dya74]. This is denoted [Abr59] as dynamic nuclear polarization (DNP), and was observed in several experiments on n-doped GaAs bulk samples [Kik00; Hua12], 2DES embedded in QWs grown along the [001] [Mal00a] or the [110] crystallographic direction [Sal01a; Sal01b], or QD systems [Kha03; Che11]. Also in this work, some influence of the interaction between the 2DES and the system of the lattice nuclei was observable under certain conditions, where the electron spin polarization reaches high values. This case can be found in particular at low temperatures $T < 4$ K, where T_{yy} and T_{zz} can clearly exceed the laser repetition period under the conditions of optical gating. The constructive interference of spin ensembles generated by subsequent laser pulses leads to a high polarization of the electron spin system at magnetic field values, corresponding to the positions of the RSA maxima. Moreover, a high electron spin polarization can be created by the usage of a high excitation intensity I_{ex} at higher temperatures as well. In the following it will be shown how RSA traces are affected by the influence of spin polarized lattice nuclei. A rough estimation of the achieved degree of nuclear polarization will be given as well.

First, the influence of the nuclear spin system on electron spin dynamics at a sample temperature of $T = 3.4$ K and high excitation intensities $110 \ \text{W/cm}^2 < I_{ex} < 300 \ \text{W/cm}^2$ will be discussed. The initial spin polarization of the electron system is controlled via the degree of circular polarization of the pump pulse, while the total number of electron-hole pairs, created by a single pump pulse, is kept constant. The circular polarization of the pump beam was varied via the orientation of the $\lambda/4$ wave plate with respect to the optical axis of the linear polarizer in the TRKR/RSA setup (see Fig. 4.2). The obtained RSA traces (see panel (a) of Fig. 6.32) show a strong dependence on the initial spin polarization of the 2DES: for a small degree of circular polarization, corresponding to a small spin polarization s_0 present in the sample, the RSA trace has the usual shape. In contrast, for increasing circular polarization, the shape of the RSA trace significantly changes. The RSA beats are strongly damped and finally vanish until at a certain magnetic field value around $B = 0$, the signal reappears. When positive magnetic fields $B > 0$ are reached, the RSA signal is damped anew. This drastic influence on the RSA signal can be suppressed, if the helicity of the pump beam is modulated from σ^+ to σ^- at a frequency of 19 Hz. This is realized experimentally by mounting a liquid crystal retarder (LCR) before the $\lambda/4$ wave plate, which rotates the linear polarization axis of the laser light hitting the $\lambda/4$ wave plate by $0°$ or $90°$,
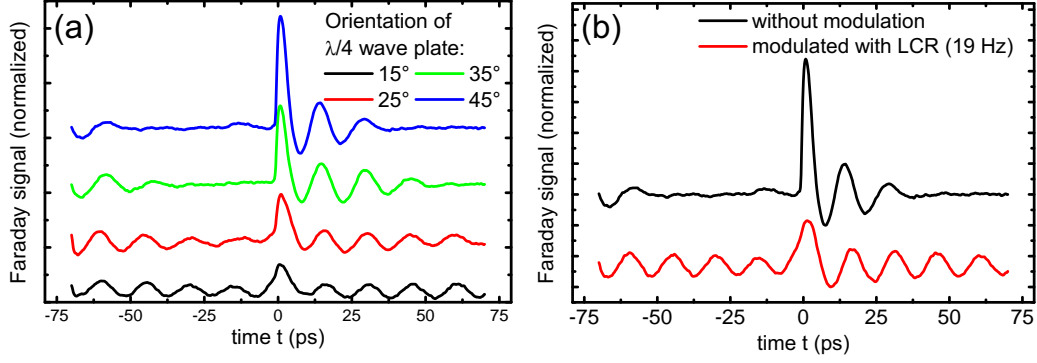
Figure 6.32: *(a) RSA traces taken on sample G at $T = 3.4$ K and a high excitation intensity $I_{ex} \approx 300$ W/cm^2. The degree of circular polarization of the pump beam was varied via the orientation of the $\lambda/4$ wave plate. For increasing circular polarization, the RSA shape changes drastically. (b) By modulating the helicity of the pump beam by the use of an liquid crystal retarder (LCR) with a frequency of 19 Hz, the signal change can be significantly suppressed.*

depending on the voltage applied to the LCR. Panel (b) of Fig. 6.32 shows two RSA traces with and without a modulation of the helicity of the pump beam, taken under comparable experimental conditions. Apparently, the modulation of the helicity with a frequency of 19 Hz leads to a strong suppression of the effect, which leads to the deformation of the RSA signal in the case of a constant helicity of the pump beam[21]. The low frequency being necessary for a suppression of the underlying effect gives information about the relevant time scale $t > 0.05$ s. Thus, electron spin dynamics in this case is affected by the helicity of light on the timescale of seconds, which is the usual timescale for processes based on the weak hyperfine interaction. Therefore, the observed effect responsible for deforming the RSA spectra in Fig. 6.32, can most likely be attributed to a DNP process (see Sec. 2.3.2). In the case of a highly polarized electron system, a significant transfer of spin polarization from the electron spin system to the nuclear spin system can be inferred, leading to the build-up of an induced nuclear magnetic field B_n. In the general case, where B_n and the external magnetic field B are not parallel, complex dynamics of the electron spin system coupled to the nuclear spin system can be expected. If the polarization of the electron spin system is low, resulting from a low circular degree of circular polarization (black line in Fig. 6.32(a)) of the inciding pump beam or a modulation of its helicity (red line in Fig. 6.32(b)), the induced nuclear magnetic field B_n is weak. This leads to a small coupling between the electron spin ensemble and the system of the lattice nuclei, resulting in nearly undisturbed electron spin dynamics.

In order to find more evidence that a DNP process causes the change of the RSA signal, further measurements were performed. In RSA measurements under the conditions of optical gating ($I_{532nm} \approx 200$ μW/cm^2), a dependence of the RSA signal on the sweep rate of the magnetic field B could be observed, which is presented in Fig. 6.33. In the case of fast sweeping with a rate of about 1.4 mT/s, RSA peaks are visible, damped on the magnetic field scale. Similar to what is depicted in Fig. 6.32, the amplitude of the RSA peaks decreases for increasing the magnetic field. The measurement run started at an initial value of $B = -70$ mT. At $B \approx 0$ mT, the amplitude of the RSA signal

---

[21]The remaining asymmetry observable in the RSA trace with modulated helicity most likely results from properties of the used LCR. The switching times $t_{1\to2}$ and $t_{2\to1}$ between the two used states of the LCR are not equal, leading in effect to slightly different time intervals $t_{\sigma+}$ and $t_{\sigma-}$ in which the sample is exposed to σ^+ and σ^- light.
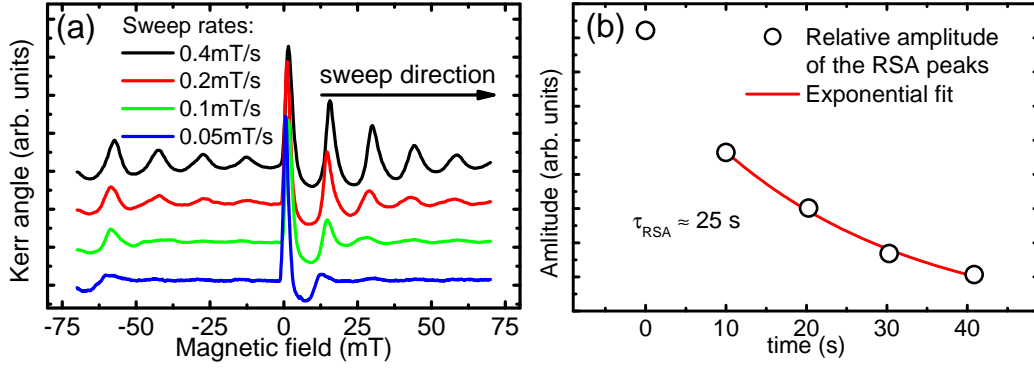
Figure 6.33: *(a) RSA traces taken on sample G at $T = 3.4$ K under the conditions of optical gating $I_{532\text{nm}} \approx 200\ \mu W/cm^2$, and a relative high excitation intensity $I_{ex} \approx 110\ W/cm^2$. The obtained RSA traces clearly depend on the sweep rate of the magnetic field. The sweep direction was from negative to positive magnetic fields, as indicated by the arrow. (b) Decay of the amplitudes of the RSA peaks for $B > 0$, evaluated for the RSA trace with the fastest sweep rate. The extracted decay time τ_{RSA} is approximately 25 s.*

rapidly increases, and begins to decrease anew. This behavior is also visible for the slower sweep rates. Here, the RSA maxima are strongly damped on the magnetic field scale and just a few peaks occur until a constant signal is observed. In the case of the slowest sweep rate just one significant peak can be observed. The data presented in Fig. 6.33 shows that the modification of the RSA signal is not related to the magnetic field scale, but rather to the laboratory timescale. From the RSA trace with the fastest sweep rate, the decay time τ_{RSA} of the amplitude $s(B)$ of the RSA peaks at positive magnetic fields could be determined. Therefore, the amplitude $s(B)$ of the RSA peaks at $B > 0$ was related to the laboratory time passed by since $B = 0$. A monoexponential fit yields the decay time $\tau_{RSA} \approx 25$ s. Thus, in the case of the fastest sweep rate, the duration of a single measurement run (≈ 100 s) is comparable to the timescale on which the RSA signal vanishes. This is in stark contrast to the case of the slowest sweep rate. Here, the duration of the measurement is about 15 minutes, and thereby about a factor of 10 longer than in the measurement with the highest sweep rate. In this case, the sweep rate of the magnetic field seems to be lower than the rate on which the RSA signal is affected. In consequence, the obtained RSA signal maps the transient states, which the electron spin ensemble passes through while DNP takes place and the induced Overhauser field B_n changes. Due to the lack of an appropriate model, a quantitative analysis of the RSA traces presented in Fig. 6.33 has not been possible so far.

In a further measurement series, the influence of the angle between the sample normal and the external applied magnetic field was investigated. For this purpose, a piece of sample G was mounted in the split-coil cryostat system (see Sec. 4.5), where the sample could be rotated about an axis perpendicular to the sample normal and the magnetic field direction; the angle α between the sample normal and the magnetic field direction was adjusted to small values $-1° < \alpha < 1°$. Despite the small adjusted angle, a significant change of the RSA spectra was observable at a temperature of $T = 1.1$ K when the sample was additionally illuminated with weak above-barrier light ($I_{532\text{nm}} \approx 100\ \mu W/cm^2$). As it can be seen in Fig. 6.34 (a), the RSA peak positions for $|\alpha| = 1°$ are shifted by small magnetic field values ΔB relative to the position of the RSA spectra taken at $\alpha = 0°$. Extracting the shift ΔB of the peaks relative to the position where they are expected, the values shown in panel (b) of Fig. 6.34 are yielded. Prior to the start of all measurement runs, the sample was in the dark, resulting
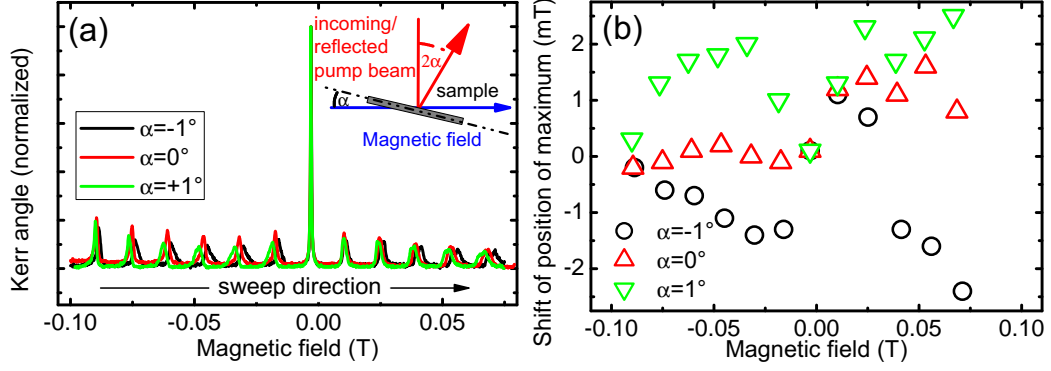
Figure 6.34: *(a) RSA traces taken on sample G at $T = 1.1$ K under the conditions of optical gating $I_{532\mathrm{nm}} \approx 100~\mu W/cm^2$, and a low excitation intensity $I_{ex} \approx 8~W/cm^2$. The sample normal was at a small angle α to the magnetic field direction. (b) Shift ΔB of the positions of the RSA maxima relative to their expected positions. The shift can be attributed to an induced Overhauser field B_n generated by an efficient dynamical nuclear polarization process.*

in a shift $\Delta B \approx 0$ mT shortly after exposing the sample to the green illumination. Before the sample is exposed to the above-barrier light, the conditions of long SDTs T_{yy} and T_{zz} have not been fulfilled. Thus, the electron SDTs are short, resulting in a low electron spin polarization. In consequence, no transfer of spin polarization to the nuclear spin system can occur. Therefore, the nuclear spin system can be taken to be initially unpolarized. When the sample is exposed to the weak above-barrier light, the condition of long SDTs T_{yy} and T_{zz} is established, leading to a build-up of nuclear spin polarization. However, shortly after the start of the measurement run one still has $\Delta B \approx 0$ mT. After the build-up of the induced Overhauser field B_n, values of $|\Delta B|$ up to ≈ 2.5 mT could be extracted from the RSA traces. This corresponds to a nuclear spin polarization, which was roughly estimated (for details, see, App. C) to be on the order of about 5 %, taking into account the geometry of the setup (see Fig. C.1). A more precise analysis and determination of the degree of nuclear spin polarization has to include additional details, for example the shape of the electron envelope function leading to a spatial inhomogeneous polarization of the nuclei [Ţif11].

In conclusion, the interaction between a highly polarized electron spin system and the system of the lattice nuclei could be observed in RSA measurements in a temperature range from 1.1 K$< T <$3.4 K on sample G, when long SDTs T_{yy} and T_{zz} were established in the 2DES by means of optical gating. Due to the demonstrated dependencies of the observed effects on the angle between the sample normal and the magnetic field, the sweep rate and the initial spin polarization of the 2DES, there is strong evidence for an efficient DNP process. The tunability of the SDTs T_{yy} and T_{zz}, as well as the carrier density n, will allow a detailed study of the coupling of the electron spin system and the system of the lattice nuclei even at different temperatures.

Chapter 7

Summary

In conclusion of this work, spin dynamics in two-dimensional high-mobility electron systems was studied in dependence of various parameters. The varied parameters were the confinement length d, the sample temperature T, the carrier density n as well as the excitation intensity I_{ex}. The investigation of samples grown along different crystallographic directions allowed the observation of strong spin dephasing anisotropies, resulting from the symmetry properties of the involved SO fields. Applying classical magnetic fields perpendicular to the sample plane of the ultra-high mobility sample E allowed for the observation of the cyclotron effect on coherent spin precession.

The dependence of spin dynamics on the confinement length d was studied in 2DESs having an asymmetric band profile. A strong increase of the out-of-plane SDT T_{zz} with increasing QW width d could be shown. This was attributed to the dependence of the Dresselhaus parameter $\beta = \gamma \left(\frac{\pi}{d}\right)^2$ on d. In addition, the importance of the dependence of the Dresselhaus spin splitting constant $\gamma(E_c)$ on the confinement energy E_c was discussed. The experimentally observed spin dephasing times could be reproduced in calculations, assuming a reasonable temperature $T_e = 15\,\mathrm{K}$ of the slightly overheaten electron systems. Under these experimental conditions, the microscopic scattering rate $1/\tau$ is significantly influenced by contributions of electron-electron scattering processes. This could be inferred from the good agreement of the experimental and the calculated values, which can only be achieved, if the ee scattering processes are taken into account. In addition, the dependence of the in-plane spin dephasing anisotropy on the confinement length d could be mapped. A decrease of the ratio β/α for an increasing d could be shown experimentally in samples B-D, what is (for a fixed value of α) in agreement with the theoretical expectation. The lowest value of the ratio $\beta/\alpha \approx 1.2$ could be detected on sample D at a nominal sample temperature of $T = 10\,\mathrm{K}$. Moreover, some components of the g factor tensor $\hat{\boldsymbol{g}}$ could be determined. The diagonal elements g_{xx} showed the well-known dependence [Yug07] on the confinement energy E_c, whereas an increase of the off-diagonal elements could be observed for an increasing QW width d.

Moreover, spin dynamics in samples A-D was studied at different sample temperatures T. Experimentally, the previously reported [Ley07a] strong increase of the out-of-plane SDT $T_{[001]}$ with T could be reproduced, showing a maximum in a temperature range, which corresponds to the Fermi temperature T_F of the corresponding 2DES. In measurements on the in-plane spin dephasing anisotropy, resulting from the interference of the Rashba and the Dresselhaus contributions, an increase of the ratio β/α with the sample temperature T could be observed in samples B-D. From this, a different temperature behavior of the Rashba and the Dresselhaus parameters $\alpha(T)$ and $\beta(T)$ could be inferred.

However, a full understanding of the experimentally observed behavior is still lacking. In addition, the limitations of the precision of the presented measurement method was discussed in the context of the temperature dependent measurements, where ratios of β/α close to 1 could be observed.

The dependence of spin dynamics on the carrier density n was studied in measurements on sample B', having a semi-transparent NiCr gate. Both, the out-of-plane SDT $T_{[001]}$ as well as the in-plane spin dephasing anisotropy, were found to be affected by the applied gate voltages U_G. The experimentally observed effect of U_G on the in-plane SDA was small at a temperature $T = 4\,\mathrm{K}$, whereas a significant change of the ratio β/α was observable at temperatures $30\,\mathrm{K} < T < 70\,\mathrm{K}$. In TRKR measurements on samples A-C with varied excitation intensity I_{ex}, a strong dependence of the spin dephasing time $T_{[001]}$ on I_{ex} could be observed. However, it could not be determined unambiguously, whether the observed dependence results mainly from an increasing degree of initial spin polarization [Sti07a] or whether it has to be attributed to a pump-induced heating of the 2DES.

In experiments on ultra-high-mobility samples with a symmetric band edge profile, grown along the [001] crystallographic direction, coherent spin dynamics could be observed. Coherent oscillations of an optically generated spin ensembles about the Dresselhaus-type SO field could be observed experimentally, even without an external magnetic field applied. Damping of the zero-field oscillations could be mainly ascribed to electron collisions. In addition, contributions to the Dresselhaus SO field being cubic in k were identified to be of a certain relevance for damping of the coherent spin oscillations.

The application of a small external magnetic field perpendicular to the sample plane was demonstrated to have a dramatic effect on coherent spin dynamics: the frequency of the spin beats strongly increases, and a long-lived tail of the spin polarization appears. This experimentally observed cyclotron effect on coherent spin precession was found to be in agreement with a theoretical model, based on a kinetic equation approach. From TRFR measurements in a finite magnetic field, the microscopic scattering time τ can be determined, as well as the effective mass of the electrons, located near to the Fermi edge of the 2DES. The effective mass of the electrons was found to slightly exceed the literature value for GaAs of $m^* = 0.067m_0$, which was attributed (at least in part) to the nonparabolicity of the conduction band. The nonparabolicity of the conduction band could be reproduced in a nextnano[3] simulation of the bandstructure of sample E. Moreover, the analysis of the spin beats frequency $|\Omega_D(k_F)|$ allowed the determination of the Dresselhaus spin splitting constant γ for a small confinement energy $E_c \approx 6\,\mathrm{meV}$.

In high-mobility samples with a symmetric band edge profile, grown along the [110] crystallographic direction, extended spin dephasing times and a strong spin dephasing anisotropy for in-plane and out-of-plane oriented spins could be experimentally observed. The long out-of-plane SDT T_{zz} result from a supression of the DP spin dephasing mechanism for spins oriented along the [110] direction: due to the special symmetry of $\boldsymbol{\Omega}_D^{(110)}(\boldsymbol{k})$ in (110)-grown 2DESs, spin dephasing of growth-axis oriented spins caused by the Dresselhaus SOF is supressed. In addition, in consequence of the highly symmetric band edge profile the Rashba contribution Ω_R to the SOF is nearly vanishing. Thus, extremely long electron spin dephasing times up about $100\,\mathrm{ns}$ could be determined in sample G from RSA measurements. The RSA technique was proven as a convenient tool for the determination of long and anisotropic spin dephasing times, even in (110)-grown 2DES. Using this experimental technique, a strong temperature dependence of the anisotropy in sample G could be mapped. The reason for the obverved dependence on the lattice temperature was attributed to Rashba fields, resulting from a temperature dependent asymmetry of the band edge profile. As a second possible reason, random

Rashba fields were discussed, caused by inefficiently screened ionized remote donor atoms.

A dramatic increase of the spin dephasing times T_{zz} and T_{yy} could be observed in experiments, where the sample was additionally illuminated with above-barrier light. The decrease of the carrier density n, resulting from optical gating, could be monitored via PL measurements. The strong increase of the SDTs was attributed to the lowered carrier density n, and the in consequence smaller values of the SOFs $\mathbf{\Omega}_D^{(110)}(k_F)$ and $\Omega_R(k_F)$ at the Fermi edge, which are limiting the SDTs in the DP mechanism. At low temperatures of $T < 4\,\mathrm{K}$, extremely low spin dephasing rates $\Gamma zz \approx 8\,\mathrm{MHz}$ could be observed under the conditions of optical gating, corresponding to a SDT $T_{zz} \approx 248\,\mathrm{ns}$. This value exceeds the previously observed values [Mül08] by about one order of magnitude. The reduction of the SDTs at high intensities of the above-barrier illumination was attributed to the BAP spin dephasing mechanism.

Strong evidence for an efficient dynamical nuclear polarization process was found in RSA measurements under the conditions of optical gating, where extremely long electron SDTs can be observed. The shape of the RSA spectra was demonstrated to be deformed in dependence of the helicity of the incident pump pulses. Moreover, the relevant timescale (on the order of seconds) could be identified, on which the RSA signal is affected. From measurements, where the sample was slightly tilted with repect to the external magnetic field, the Overhauser shift of the RSA peaks could be extracted. The corresponding degree of nuclear spin polarization was estimated to be on the order of about 5%.

Bibliography

[Abr59]   M. Abraham, M. A. H. McCausland, and F. N. H. Robinson, *Dynamic Nuclear Polarization*, Phys. Rev. Lett. **2**, 449 (June 1959). (Cit. on pp. 26, 100).

[Abr61]   A. Abragam. *The principles of nuclear magnetism.* Ed. by J. Birman, S. F. Edwards, R. H. Friend, C. H. Llewellyn Smith, M. Rees, D. Sherrington, and G. Veneziano. Vol. 32. The international series of monographs on physics. Oxford, Clarendon Press, 1961. Chap. 6, 159 (cit. on pp. 21, 26).

[Ada85]   S. Adachi, *GaAs, AlAs, and $Al_x Ga_{1-x} As$@B: Material parameters for use in research and device applications*, J. Appl. Phys. **58**, 1 (Aug. 1985). (Cit. on p. 5).

[And62]   R. Anderson, *Experiments on Ge-GaAs heterojunctions*, Solid-State Electronics **5**, 341 (Sept. 1962). (Cit. on pp. 6, 7).

[Aro83]   A. G. Aronov, G. E. Pikus, and A. N. Titkov, *Spin relaxation of conduction electrons in p-type Ill-V compounds*, Sov. Phys. JETP **57**, 680 (Mar. 1983). (Cit. on p. 21).

[Art68]   J. R. Arthur Jr., *Interaction of Ga and As_2 Molecular Beams with GaAs Surfaces*, J. Appl. Phys. **39**, 4032 (July 1968). (Cit. on p. 29).

[Ash03]   N. W. Ashcroft. *Solid State Physics.* Thomson Press (India) Ltd, 2003. ISBN: 8131500527 (cit. on pp. 5, 8, 25, 58, 81).

[Asp86]   D. E. Aspnes, S. M. Kelso, R. A. Logan, and R. Bhat, *Optical properties of $Al_x Ga_{1-x} As$*, J. Appl. Phys. **60**, 754 (July 1986). (Cit. on p. 6).

[Ast08]   G. V. Astakhov, M. M. Glazov, D. R. Yakovlev, E. A. Zhukov, W. Ossau, L. W. Molenkamp, and M. Bayer, *Time-resolved and continuous-wave optical spin pumping of semiconductor quantum wells*, Semiconductor Science and Technology **23**, 114001 (2008). (Cit. on pp. 41, 86).

[Ave06]   N. S. Averkiev, L. E. Golub, A. S. Gurevich, V. P. Evtikhiev, V. P. Kochereshko, A. V. Platonov, A. S. Shkolnik, and Y. P. Efimov, *Spin-relaxation anisotropy in asymmetrical (001) $Al_x Ga_{1-x} As$ quantum wells from Hanle-effect measurements: Relative strengths of Rashba and Dresselhaus spin-orbit coupling*, Physical Review B **74**, 033305 (2006). (Cit. on pp. 1, 3, 14, 21, 23, 50, 62).

[Ave99]   N. S. Averkiev and L. E. Golub, *Giant spin relaxation anisotropy in zinc-blende heterostructures*, Phys. Rev. B **60**, 15582 (Dec. 1999). (Cit. on pp. 1, 21, 23, 50, 52, 61).

[Aws85]   D. D. Awschalom, J. M. Halbout, S. von Molnar, T. Siegrist, and F. Holtz-berg, *Dynamic Spin Organization in Dilute Magnetic Systems*, Phys. Rev. Lett. **55**, 1128 (Sept. 1985). (Cit. on pp. 2, 39).

[BA91]   S. Bar-Ad and I. Bar-Joseph, *Absorption quantum beats of magnetoexcitons in GaAs heterostructures*, Phys. Rev. Lett. **66**, 2491 (May 1991). (Cit. on p. 17).

[Bab83]   T. Baba, T. Mizutani, and M. Ogawa, *Elimination of Persistent Photocon-ductivity and Improvement in Si Activation Coefficient by Al Spatial Sepa-ration from Ga and Si in Al-Ga-As:Si Solid System - a Novel Short Period AlAs/n-GaAs Superlattice*, Jpn. J. Appl. Phys. **22**, 627 (Oct. 1983). (Cit. on p. 33).

[Bal11]   A. Balocchi, Q. H. Duong, P. Renucci, B. L. Liu, C. Fontaine, T. Amand, D. Lagarde, and X. Marie, *Full Electrical Control of the Electron Spin Relax-ation in GaAs Quantum Wells*, Phys. Rev. Lett. **107**, 136604 (Sept. 2011). (Cit. on p. 14).

[Bar48]   J. Bardeen and W. H. Brattain, *The Transistor, A Semi-Conductor Triode*, Phys. Rev. **74**, 230 (July 1948). (Cit. on p. 1).

[Bas08]   I. Baskin, B. M. Ashkinadze, E. Cohen, and L. N. Pfeiffer, *Mechanism of microwave-induced photoluminescence modulation and optically detected res-onances due to a two-dimensional electron gas in a heterostructure*, Phys. Rev. B **78**, 195318 (Nov. 2008). (Cit. on p. 9).

[Bau83]   R. S. Bauer, P. Zurcher, and H. W. Sang Jr., *Inequality of semiconductor heterojunction conduction-band-edge discontinuity and electron affinity dif-ference*, Appl. Phys. Lett. **43**, 663 (Oct. 1983). (Cit. on p. 6).

[Bau94]   J. J. Baumberg, D. D. Awschalom, N. Samarth, H. Luo, and J. K. Furdyna, *Spin beats and dynamical magnetization in quantum structures*, Phys. Rev. Lett. **72**, 717 (Jan. 1994). (Cit. on pp. 2, 17, 39).

[Ber06]   B. A. Bernevig, J. Orenstein, and S.-C. Zhang, *Exact SU(2) Symmetry and Persistent Spin Helix in a Spin-Orbit Coupled System*, Phys. Rev. Lett. **97**, 236601 (Dec. 2006). (Cit. on p. 22).

[Ber99]   L. Bergmann and C. Schaefer. *Optics of waves and particles.* de Gruyter, 1999. ISBN: 3110143186 (cit. on pp. 39, 96).

[Bir75]   G. L. Bir, A. G. Aronov, and G. E. Pikus, *Spin relaxation of electrons due to scattering by holes*, Sov. Phys. JETP **42**, 705 (Nov. 1975). (Cit. on p. 20).

[Blo46]   F. Bloch, *Nuclear Induction*, Phys. Rev. **70**, 460 (Oct. 1946). (Cit. on p. 16).

[Bra02]   M. A. Brand, A. Malinowski, O. Z. Karimov, P. A. Marsden, R. T. Harley, A. J. Shields, D. Sanvitto, D. A. Ritchie, and M. Y. Simmons, *Precession and Motional Slowing of Spin Evolution in a High Mobility Two-Dimensional Electron Gas*, Phys. Rev. Lett. **89**, 236601 (Nov. 2002). (Cit. on pp. 2, 3, 20, 25).

[Bro04]   F. X. Bronold, A. Saxena, and D. L. Smith, *Semiclassical kinetic theory of electron spin relaxation in semiconductors*, Phys. Rev. B **70**, 245210 (Dec. 2004). (Cit. on p. 16).

[Buk94]   E. Buks, M. Heiblum, Y. Levinson, and H. Shtrikman, *Scattering of a two-dimensional electron gas by a correlated system of ionized donors*, Semicon-ductor Science and Technology **9**, 2031 (1994). (Cit. on p. 33).

[Byc84a]   Y. A. Bychkov and E. I. Rashba, *Oscillatory effects and the magnetic susceptibility of carriers in inversion layers*, J. Phys. C: Solid State **17**, 6039 (1984). (Cit. on p. 13).

[Byc84b]   Y. A. Bychkov and E. I. Rashba, *Properties of a 2D electron gas with lifted spectral degeneracy*, JETP Lett. **39**, 78 (Jan. 1984). (Cit. on p. 13).

[Car99]   A. J. C. Cardoso, F. Qu, and P. C. Morais, *Optical control of the two-dimensional electron-gas density in single asymmetric quantum wells: Magnetic-field effect*, Phys. Rev. B **60**, 4501 (Aug. 1999). (Cit. on p. 11).

[Cha86]   A. Chaves, A. Penna, J. Worlock, G. Weimann, and W. Schlapp, *Optical control of two-dimensional electron density in a single asymmetric quantum well*, Surface Science **170**, 618 (Apr. 1986). (Cit. on pp. 10, 11).

[Che11]   R. V. Cherbunin, K. Flisinski, I. Y. Gerlovin, I. V. Ignatiev, M. S. Kuznetsova, M. Y. Petrov, D. R. Yakovlev, D. Reuter, A. D. Wieck, and M. Bayer, *Resonant nuclear spin pumping in (In,Ga)As quantum dots*, Phys. Rev. B **84**, 041304 (July 2011). (Cit. on p. 100).

[Cho71]   A. Y. Cho, *GaAs Epitaxy by a Molecular Beam Method: Observations of Surface Structure on the (001) Face*, J. Appl. Phys. **42**, 2074 (Apr. 1971). (Cit. on pp. 1, 29).

[Cho81]   A. Y. Cho and K. Y. Cheng, *Growth of extremely uniform layers by rotating substrate holder with molecular beam epitaxy for applications to electro-optic and microwave devices*, Appl. Phys. Lett. **38**, 360 (Mar. 1981). (Cit. on pp. 1, 29, 30).

[Cio09]   M. Ciorga, A. Einwanger, U. Wurstbauer, D. Schuh, W. Wegscheider, and D. Weiss, *Electrical spin injection and detection in lateral all-semiconductor devices*, Phys. Rev. B **79**, 165321 (Apr. 2009). (Cit. on p. 15).

[Coi04]   W. A. Coish and D. Loss, *Hyperfine interaction in a quantum dot: Non-Markovian electron spin dynamics*, Phys. Rev. B **70**, 195340 (Nov. 2004). (Cit. on p. 21).

[Con35]   E. U. Condon and G. H. Shortley. *The Theory of Atomic Spectra*. Cambridge University Press, 1935, 441. ISBN: 0521092094 (cit. on p. 12).

[Cro05a]   S. A. Crooker and D. L. Smith, *Imaging Spin Flows in Semiconductors Subject to Electric, Magnetic, and Strain Fields*, Phys. Rev. Lett. **94**, 236601 (June 2005). (Cit. on p. 18).

[Cro05b]   S. A. Crooker, M. Furis, X. Lou, C. Adelmann, D. L. Smith, C. J. Palmstrøm, and P. A. Crowell, *Imaging Spin Transport in Lateral Ferromagnet/Semiconductor Structures*, Science **309**, 2191 (2005). (Cit. on p. 14).

[Dam91]   T. C. Damen, L. Via, J. E. Cunningham, J. Shah, and L. J. Sham, *Subpicosecond spin relaxation dynamics of excitons and free carriers in GaAs quantum wells*, Phys. Rev. Lett. **67**, 3432 (Dec. 1991). (Cit. on p. 20).

[Dan89]   M. Daniels, B. Ridley, and M. Emeny, *Hot electron energy relaxation via acoustic phonon emission in $GaAs/Al_{0.24}Ga_{0.76}As$ single and multiple quantum wells*, Solid-State Electronics **32**, 1207 (Dec. 1989). (Cit. on p. 80).

[Dat90]   S. Datta and B. Das, *Electronic analog of the electro-optic modulator*, Appl. Phys. Lett. **56**, 665 (Feb. 1990). (Cit. on pp. 2, 66).

[DeS92]   G. C. DeSalvo, W. F. Tseng, and J. Comas, *Etch Rates and Selectivities of Citric Acid/Hydrogen Peroxide on GaAs, $Al_{0.3}G_{0.7}As$, $In_{0.2}Ga_{0.8}As$, $In_{0.53}Ga_{0.47}As$, $In_{0.52}Al_{0.48}As$, and InP*, J. Electrochem. Soc. **139**, 831 (Mar. 1992). (Cit. on p. 36).

[DiV95]   D. P. DiVincenzo, *Quantum Computation*, Science **270**, 255 (1995). (Cit. on p. 2).

[DiV97]   D. P. DiVincenzo. "TOPICS IN QUANTUM COMPUTERS". In: *Mesoscopic electron transport [proceedings of the NATO Advanced Study Institute on Mesoscopic Electron Transport, Curaçao, Netherlands Antilles, 25 June - 5 July 1996]*. Ed. by L. L. Sohn, L. P. Kouwenhoven, and G. Schön. Vol. 345. Nato ASI series. Kluwer Acad. Publ., 1997, 657 (cit. on p. 2).

[Din78]   R. Dingle, H. L. Stormer, A. C. Gossard, and W. Wiegmann, *Electron mobilities in modulation-doped semiconductor heterojunction superlattices*, Appl. Phys. Lett. **33**, 665 (Oct. 1978). (Cit. on p. 1).

[Dir28]   P. A. M. Dirac, *The Quantum Theory of the Electron*, Proceedings of the Royal Society of London. Series A **117**, 610 (Feb. 1928). (Cit. on pp. 1, 12).

[Dre55]   G. Dresselhaus, *Spin-Orbit Coupling Effects in Zinc Blende Structures*, Phys. Rev. **100**, 580 (Oct. 1955). (Cit. on p. 12).

[Dru00]   P. Drude, *Zur Elektronentheorie der Metalle*, Annalen der Physik **306**, 566 (1900). (Cit. on p. 11).

[Dru81]   T. J. Drummond, H. Morkoç, K. Hess, and A. Y. Cho, *Experimental and theoretical electron mobility of modulation doped $Al_xGa_{1-x}As/GaAs$ heterostructures grown by molecular beam epitaxy*, J. Appl. Phys. **52**, 5231 (Aug. 1981). (Cit. on p. 7).

[Dya71a]   M. I. Dyakonov and V. I. Perel, *Spin Orientation of electrons associated with the interband absorption of light in semiconductors*, Sov. Phys. JETP **33**, 1053 (1971). (Cit. on pp. 1, 12, 18, 19).

[Dya71b]   M. I. Dyakonov and V. I. Perel, *Spin relaxation of conduction electrons in noncentrosymmetric semiconductors*, Sov. Phys. Solid State **13**, 3023 (1971). (Cit. on pp. 1, 18).

[Dya73]   M. I. Dyakonov and V. Perel, *Hyperfine Interaction in Optical Orientation of Electrons in Semiconductors*, Sov. Phys. JETP **36**, 995 (May 1973). (Cit. on p. 21).

[Dya74]   M. I. Dyakonov and V. Perel, *Optical orientation in a system of electrons and lattice nuclei in semiconductors. Theory*, Sov. Phys. JETP **38**, 177 (Jan. 1974). (Cit. on pp. 21, 100).

[Dya84]   M. I. Dyakonov and V. I. Perel. "Theory of optical orientation of electrons and nuclei in semiconductors". In: *Optical Orientation, Modern Problems in Condensed Matter Science*. Ed. by F. Meier and B. P. Zakharchenya. Vol. 8. North-Holland, Amsterdam, 1984. Chap. 2, 11 (cit. on pp. 15, 27).

[Dya86]   M. I. Dyakonov and V. Kachorovskii, *Spin relaxation of two-dimensional electrons in noncentrosymmetric semiconductors*, Sov. Phys. Semicond. **20**, 110 (Jan. 1986). (Cit. on pp. 1, 12, 13, 23).

[Dzh02]   R. I. Dzhioev, V. L. Korenev, I. A. Merkulov, B. P. Zakharchenya, D. Gammon, A. L. Efros, and D. S. Katzer, *Manipulation of the Spin Memory of Electrons in n-GaAs*, Phys. Rev. Lett. **88**, 256801 (June 2002). (Cit. on p. 28).

[Döh04]   S. Döhrmann, D. Hägele, J. Rudolph, M. Bichler, D. Schuh, and M. Oestreich, *Anomalous Spin Dephasing in (110) GaAs Quantum Wells: Anisotropy and Intersubband Effects*, Phys. Rev. Lett. **93**, 147405 (Sept. 2004). (Cit. on pp. 2, 20).

[Ein05]   A. Einstein, *Zur Elektrodynamik bewegter Körper*, Annalen der Physik **322**, 891 (1905). (Cit. on p. 1).

[Ein16]   A. Einstein, *Die Grundlage der allgemeinen Relativitätstheorie*, Annalen der Physik **354**, 769 (1916). (Cit. on p. 1).

[Eld08]   P. S. Eldridge, W. J. H. Leyland, P. G. Lagoudakis, O. Z. Karimov, M. Henini, D. Taylor, R. T. Phillips, and R. T. Harley, *All-optical measurement of Rashba coefficient in quantum wells*, Physical Review B **77**, 125344 (2008). (Cit. on p. 59).

[Eld11]   P. S. Eldridge, J. Hübner, S. Oertel, R. T. Harley, M. Henini, and M. Oestreich, *Spin-orbit fields in asymmetric (001)-oriented GaAs/Al$_x$Ga$_{1-x}$As quantum wells*, Phys. Rev. B **83**, 041301 (Jan. 2011). (Cit. on pp. 3, 14, 17, 51, 53, 56, 57, 61, 129).

[Ell54]   R. J. Elliott, *Theory of the Effect of Spin-Orbit Coupling on Magnetic Resonance in Some Semiconductors*, Phys. Rev. **96**, 266 (Oct. 1954). (Cit. on pp. 12, 17, 18).

[Esi86]   S. Esipov and I. Levinson, *Electron temperature in a two-dimensional gas: Energy losses to optical phonons*, JETP **63**, 191 (Jan. 1986). (Cit. on p. 9).

[Far46]   M. Faraday, *Experimental Researches in Electricity. Nineteenth Series*, Philosophical Transactions of the Royal Society of London **136**, 1 (1846). (Cit. on pp. 2, 39).

[Fer30]   E. Fermi, *Über die magnetischen Momente der Atomkerne*, Zeitschrift für Physik A Hadrons and Nuclei **60**, 320 (1930). (Cit. on pp. 21, 26).

[Fle84]   V. Fleisher and I. A. Merkulov. "Optical orientation of the coupled electron-nuclear spin system of a semiconductor". In: *Optical Orientation, Modern Problems in Condensed Matter Science*. Ed. by F. Meier and B. P. Zakharchenya. Vol. 8. North-Holland, Amsterdam, 1984. Chap. 5, 173 (cit. on p. 27).

[Fuk08]   D. Fukuoka, T. Yamazaki, N. Tanaka, K. Oto, K. Muro, Y. Hirayama, N. Kumada, and H. Yamaguchi, *Spin dynamics of two-dimensional electrons in a quantum Hall system probed by time-resolved Kerr rotation spectroscopy*, Physical Review B **78**, 041304 (2008). (Cit. on p. 75).

[Fur07]   M. Furis, D. L. Smith, S. Kos, E. S. Garlid, K. S. M. Reddy, C. J. Palmstrøm, P. A. Crowell, and S. A. Crooker, *Local Hanle-effect studies of spin drift and diffusion in n:GaAs epilayers and spin-transport devices*, New Journal of Physics **9**, 347 (2007). (Cit. on p. 70).

[Gan04]   S. D. Ganichev, V. V. Bel'kov, L. E. Golub, E. L. Ivchenko, P. Schneider, S. Giglberger, J. Eroms, J. De Boeck, G. Borghs, W. Wegscheider, D. Weiss, and W. Prettl, *Experimental Separation of Rashba and Dresselhaus Spin Splittings in Semiconductor Quantum Wells*, Phys. Rev. Lett. **92**, 256601 (June 2004). (Cit. on pp. 1, 14, 62, 82).

[Gla02]   M. M. Glazov and E. L. Ivchenko, *Precession Spin Relaxation Mechanism Caused by Frequent Electron-Electron Collisions*, JETP Lett. **75**, 403 (Mar. 2002). (Cit. on p. 34).

[Gla03]   M. M. Glazov, *Mechanism of the D'yakonov-Perel' spin relaxation in frequent electron-electron collisions in a quantum well with a finite width*, Physics of the Solid State **45**, 1162 (June 2003). (Cit. on pp. 9, 34).

[Gla04a]   M. M. Glazov, *Magnetic field effects on spin relaxation in heterostructures*, Phys. Rev. B **70**, 195314 (Nov. 2004). (Cit. on p. 25).

[Gla04b]   M. M. Glazov and E. L. Ivchenko, *Effect of Electron-Electron Interaction on Spin Relaxation of Charge Carriers in Semiconductors*, JETP **99**, 1279 (2004). (Cit. on pp. 9, 34, 59).

[Gla05]   M. M. Glazov and E. Y. Sherman, *Nonexponential spin relaxation in magnetic fields in quantum wells with random spin-orbit coupling*, Phys. Rev. B **71**, 241312 (June 2005). (Cit. on p. 24).

[Gla07]   M. M. Glazov, *Effect of structure anisotropy on low temperature spin dynamics in quantum wells*, Solid State Communications **142**, 531 (2007). (Cit. on p. 25).

[Gla08]   M. M. Glazov and E. Ivchenko, *Resonant spin amplification in nanostructures with anisotropic spin relaxation and spread of the electronic g factor*, Semiconductors **42**, 951 (Aug. 2008). (Cit. on pp. 23, 42, 43, 100).

[Gla10a]   M. M. Glazov, *Spin beats and resonant spin amplification in (110)-grown quantum wells*, private communication (2010). (Cit. on pp. 23, 42).

[Gla10b]   M. M. Glazov, M. A. Semina, and E. Y. Sherman, *Spin relaxation in multiple (110) quantum wells*, Phys. Rev. B **81**, 115332 (Mar. 2010). (Cit. on pp. 24, 44, 90).

[Gla10c]   M. Glazov, E. Sherman, and V. Dugaev, *Two-dimensional electron gas with spin-orbit coupling disorder*, Physica E: Low-dimensional Systems and Nanostructures **42**, 2157 (July 2010). (Cit. on pp. 24, 44).

[Gri09]   M. Griesbeck, M. M. Glazov, T. Korn, E. Y. Sherman, D. Waller, C. Reichl, D. Schuh, W. Wegscheider, and C. Schüller, *Cyclotron effect on coherent spin precession of two-dimensional electrons*, Phys. Rev. B **80**, 241314 (Dec. 2009). (Cit. on pp. 2, 9, 20, 25, 69, 70).

[Gri11]   M. Griesbeck, M. Glazov, E. Sherman, T. Korn, D. Schuh, W. Wegscheider, and C. Schüller, *Anisotropic spin dephasing in a (110)-grown high-mobility GaAs/AlGaAs quantum well measured by resonant spin amplification technique*, Proceedings of SPIE **8100**, 810015 (2011). (Cit. on pp. 23, 82).

[Gri12]   M. Griesbeck, M. M. Glazov, E. Y. Sherman, D. Schuh, W. Wegscheider, C. Schüller, and T. Korn, *Strongly anisotropic spin relaxation revealed by resonant spin amplification in (110) GaAs quantum wells*, Phys. Rev. B **85**, 085313 (Feb. 2012). (Cit. on pp. 2, 34, 42, 69, 82, 89, 90).

[Guh98]   S. Guha, Q. Cai, M. Chandrasekhar, H. R. Chandrasekhar, H. Kim, A. D. Alvarenga, R. Vogelgesang, A. K. Ramdas, and M. R. Melloch, *Photoluminescence of short-period GaAs/AlAs superlattices: A hydrostatic pressure and temperature study*, Phys. Rev. B **58**, 7222 (Sept. 1998). (Cit. on p. 33).

[Has97]   T. Hassenkam, S. Pedersen, K. Baklanov, A. Kristensen, C. B. Sorensen, P. E. Lindelof, F. G. Pikus, and G. E. Pikus, *Spin splitting and weak localization in (110) GaAs/Al$_x$Ga$_{1-x}$As quantum wells*, Phys. Rev. B **55**, 9298 (Apr. 1997). (Cit. on pp. 13, 23).

[Heb94]   A. P. Heberle, W. W. Rühle, and K. Ploog, *Quantum beats of electron Larmor precession in GaAs wells*, Phys. Rev. Lett. **72**, 3887 (June 1994). (Cit. on p. 17).

[Hei25]   W. Heisenberg, *Über quantentheoretische Umdeutung kinematischer und mechanischer Beziehungen.* Zeitschrift für Physik A Hadrons and Nuclei **33**, 879 (1925). (Cit. on p. 1).

[Hil02]   D. J. Hilton and C. L. Tang, *Optical Orientation and Femtosecond Relaxation of Spin-Polarized Holes in GaAs*, Phys. Rev. Lett. **89**, 146601 (Sept. 2002). (Cit. on p. 20).

[Hua12]   J. Huang, Y. S. Chen, A. Ludwig, D. Reuter, A. D. Wieck, and G. Bacher, *Electron-nuclei spin coupling in GaAs–Free versus localized electrons*, Appl. Phys. Lett. **100**, 132103 (Mar. 2012). (Cit. on pp. 27, 100).

[Hua88]   S. Huant, M. Grynberg, G. Martinez, B. Etienne, B. Lambert, and A. Regreny, *Magnetooptical studies of shallow donors in selectively doped GaAs/-GaAlAs multiple quantum wells*, Solid State Communications **65**, 1467 (Mar. 1988). (Cit. on p. 31).

[Hüb11]   J. Hübner, S. Kunz, S. Oertel, D. Schuh, M. Pochwalstroka, H. T. Duc, J. Förstner, T. Meier, and M. Oestreich, *Electron g-factor anisotropy in symmetric (110)-oriented GaAs quantum wells*, Phys. Rev. B **84**, 041301 (July 2011). (Cit. on p. 17).

[Jun96]   T. Jungwirth and A. H. MacDonald, *Electron-electron interactions and two-dimensional–two-dimensional tunneling*, Phys. Rev. B **53**, 7403 (Mar. 1996). (Cit. on p. 9).

[Jus95]   B. Jusserand, D. Richards, G. Allan, C. Priester, and B. Etienne, *Spin orientation at semiconductor heterointerfaces*, Phys. Rev. B **51**, 4707 (Feb. 1995). (Cit. on p. 53).

[Kal93]   V. K. Kalevich and V. L. Korenev, *Electron g-factor anisotropy in asymmetric GaAs/AlGaAs quantum well*, JETP Lett. **57**, 571 (May 1993). (Cit. on pp. 17, 51, 57).

[Kat04]   Y. K. Kato, R. C. Myers, A. C. Gossard, and D. D. Awschalom, *Observation of the Spin Hall Effect in Semiconductors*, Science **306**, 1910 (Dec. 2004). (Cit. on p. 15).

[Kes90]   H. W. van Kesteren, E. C. Cosman, W. A. J. A. van der Poel, and C. T. Foxon, *Fine structure of excitons in type-II GaAs/AlAs quantum wells*, Phys. Rev. B **41**, 5283 (Mar. 1990). (Cit. on p. 17).

[Kha01]   A. V. Khaetskii and Y. V. Nazarov, *Spin-flip transitions between Zeeman sublevels in semiconductor quantum dots*, Phys. Rev. B **64**, 125316 (Sept. 2001). (Cit. on p. 21).

[Kha03]   A. Khaetskii, D. Loss, and L. Glazman, *Electron spin evolution induced by interaction with nuclei in a quantum dot*, Phys. Rev. B **67**, 195329 (May 2003). (Cit. on pp. 21, 100).

[Kik00]   J. M. Kikkawa and D. D. Awschalom, *All-Optical Magnetic Resonance in Semiconductors*, Science **287**, 473 (Jan. 2000). (Cit. on pp. 26, 27, 100).

[Kik98]   J. M. Kikkawa and D. D Awschalom, *Resonant Spin Amplification in n-Type GaAs*, Phys. Rev. Lett. **80**, 4313 (May 1998). (Cit. on pp. 3, 41).

[Kik99]   J. M. Kikkawa and D. D. Awschalom, *Lateral drag of spin coherence in gallium arsenide*, Nature **397**, 139 (Jan. 1999). (Cit. on pp. 3, 41).

[Kim92]   D.-S. Kim, J. Shah, J. E. Cunningham, T. C. Damen, S. Schmitt-Rink, and W. Schäfer, *Carrier-carrier scattering in a degenerate electron system: Strong inhibition of scattering near the Fermi edge*, Phys. Rev. Lett. **68**, 2838 (May 1992). (Cit. on p. 9).

[Kle85a]   D. A. Kleinman, *Theory of excitons in semiconductor quantum wells containing degenerate electrons or holes*, Phys. Rev. B **32**, 3766 (Sept. 1985). (Cit. on pp. 45, 63).

[Kle85b] D. A. Kleinman and R. C. Miller, *Band-gap renormalization in semiconductor quantum wells containing carriers*, Phys. Rev. B **32**, 2266 (Aug. 1985). (Cit. on p. 88).

[Kli80]   K. v. Klitzing, G. Dorda, and M. Pepper, *New Method for High-Accuracy Determination of the Fine-Structure Constant Based on Quantized Hall Resistance*, Phys. Rev. Lett. **45**, 494 (Aug. 1980). (Cit. on pp. 1, 11).

[Kni49]   W. D. Knight, *Nuclear Magnetic Resonance Shift in Metals*, Phys. Rev. **76**, 1259 (Oct. 1949). (Cit. on p. 27).

[Kog02]   T. Koga, J. Nitta, T. Akazaki, and H. Takayanagi, *Rashba Spin-Orbit Coupling Probed by the Weak Antilocalization Analysis in InAlAs/InGaAs/-InAlAs Quantum Wells as a Function of Quantum Well Asymmetry*, Phys. Rev. Lett. **89**, 046801 (July 2002). (Cit. on p. 1).

[Koo09]   H. C. Koo, J. H. Kwon, J. Eom, J. Chang, S. H. Han, and M. Johnson, *Control of Spin Precession in a Spin-Injected Field Effect Transistor*, Science **325**, 1515 (Sept. 2009). (Cit. on pp. 2, 15).

[Kor09]   J. D. Koralek, C. P. Weber, J. Orenstein, B. A. Bernevig, S.-C. Zhang, S. Mack, and D. D. Awschalom, *Emergence of the persistent spin helix in semiconductor quantum wells*, Nature **458**, 610 (Apr. 2009). (Cit. on pp. 22, 53).

[Kor10]   T. Korn, M. Kugler, M. Griesbeck, R. Schulz, A. Wagner, M. Hirmer, C. Gerl, D. Schuh, W. Wegscheider, and C. Schüller, *Engineering ultralong spin coherence in two-dimensional hole systems at low temperatures*, New Journal of Physics **12**, 043003 (2010). (Cit. on pp. 41, 100).

[Kuk89]   I. V. Kukushkin, K. von Klitzing, K. Ploog, V. E. Kirpichev, and B. N. Shepel, *Reduction of the electron density in GaAs-$Al_x Ga_{1-x}As$ single heterojunctions by continuous photoexcitation*, Phys. Rev. B **40**, 4179 (Aug. 1989). (Cit. on p. 10).

[Kun12]   Y. Kunihashi, M. Kohda, H. Sanada, H. Gotoh, T. Sogawa, and J. Nitta, *Proposal of spin complementary field effect transistor*, Appl. Phys. Lett. **100**, 113502 (Mar. 2012). (Cit. on p. 22).

[Köl12]   D. Kölbl, D. M. Zumbühl, A. Fuhrer, G. Salis, and S. F. Alvarado, *Breakdown of the Korringa Law of Nuclear Spin Relaxation in Metallic GaAs*, Phys. Rev. Lett. **109**, 086601 (Aug. 2012). (Cit. on p. 26).

[Lam68]   G. Lampel, *Nuclear Dynamic Polarization by Optical Electronic Saturation and Optical Pumping in Semiconductors*, Phys. Rev. Lett. **20**, 491 (Mar. 1968). (Cit. on pp. 21, 26).

[Lan81]   L. D. Landau and E. M. Lifshitz. *Quantum Mechanics Non-Relativistic Theory.* 3rd ed. Vol. 3. Butterworth Heinemann, 1981 (cit. on pp. 6, 17).

[Lar08]   A. V. Larionov and L. E. Golub, *Electric-field control of spin-orbit splittings in GaAs/$Al_x Ga_{1-x}As$ coupled quantum wells*, Phys. Rev. B **78**, 033302 (July 2008). (Cit. on pp. 14, 61).

[Law71]   P. Lawaetz, *Valence-Band Parameters in Cubic Semiconductors*, Phys. Rev. B **4**, 3460 (Nov. 1971). (Cit. on pp. 45, 81, 82).

[Lec09]   V. Lechner, L. E. Golub, P. Olbrich, S. Stachel, D. Schuh, W. Wegscheider, V. V. Bel'kov, and S. D. Ganichev, *Tuning of structure inversion asymmetry by the delta-doping position in (001)-grown GaAs quantum wells*, Appl. Phys. Lett. **94**, 242109 (June 2009). (Cit. on pp. 14, 31, 62).

[Lec11]   V. Lechner, L. E. Golub, F. Lomakina, V. V. Bel'kov, P. Olbrich, S. Stachel, I. Caspers, M. Griesbeck, M. Kugler, M. J. Hirmer, T. Korn, C. Schüller, D. Schuh, W. Wegscheider, and S. D. Ganichev, *Spin and orbital mechanisms of the magnetogyrotropic photogalvanic effects in GaAs/$Al_xGa_{1-x}As$ quantum well structures*, Phys. Rev. B **83**, 155313 (Apr. 2011). (Cit. on pp. 17, 50, 56, 57, 62, 84).

[Lee09]   W. S. Lee, I. M. Vishik, D. H. Lu, and Z.-X. Shen, *A brief update of angle-resolved photoemission spectroscopy on a correlated electron system*, Journal of Physics: Condensed Matter **21**, 164217 (2009). (Cit. on p. 81).

[Lev99]   M. Levinshtein, M. Shur, and S. Rumyantsev, eds. *Handbook series on Semiconductor Parameters*. Vol. 2. World Scientific, 1999 (cit. on pp. 5–7, 132).

[Ley07a] W. J. H. Leyland, G. H. John, R. T. Harley, M. M. Glazov, E. L. Ivchenko, D. A. Ritchie, I. Farrer, A. J. Shields, and M. Henini, *Enhanced spin-relaxation time due to electron-electron scattering in semiconductor quantum wells*, Phys. Rev. B **75**, 165309 (Apr. 2007). (Cit. on pp. 9, 58, 59, 105).

[Ley07b] W. J. H. Leyland, R. T. Harley, M. Henini, A. J. Shields, I. Farrer, and D. A. Ritchie, *Oscillatory Dyakonov-Perel spin dynamics in two-dimensional electron gases*, Phys. Rev. B **76**, 195305 (2007). (Cit. on pp. 2, 3, 20, 25, 31, 53, 56, 70, 82).

[Lit08]   K. L. Litvinenko, L. Nikzad, C. R. Pidgeon, J. Allam, L. F. Cohen, T. Ashley, M. Emeny, W. Zawadzki, and B. N. Murdin, *Temperature dependence of the electron Landé g factor in InSb and GaAs*, Phys. Rev. B **77**, 033204 (Jan. 2008). (Cit. on p. 17).

[Liu93]   H. C. Liu, Z. R. Wasilewski, M. Buchanan, and H. Chu, *Segregation of Si delta doping in GaAs-AlGaAs quantum wells and the cause of the asymmetry in the current-voltage characteristics of intersubband infrared detectors*, Appl. Phys. Lett. **63**, 761 (Aug. 1993). (Cit. on p. 31).

[Loi12]   S. Loibl, *Optische Kontrolle der Ladungsträgerdichte hochbeweglicher zweidimensionaler Elektronensysteme*, grad. thesis, Regensburg university (Sept. 2012). (Cit. on pp. 127, 128).

[Mal00a] A. Malinowski and R. Harley, *Dynamic nuclear Overhauser shifts in Larmor beats from a quantum well*, Solid State Communications **114**, 419 (Apr. 2000). (Cit. on pp. 26, 28, 100).

[Mal00b] A. Malinowski, R. S. Britton, T. Grevatt, R. T. Harley, D. A. Ritchie, and M. Y. Simmons, *Spin relaxation in GaAs/$Al_xGa_{1-x}As$ quantum wells*, Phys. Rev. B **62**, 13034 (Nov. 2000). (Cit. on p. 3).

[Mar83]   V. A. Marushchak, M. Stepanova, and A. Titkov, *Spin relaxation of conduction electrons in moderately doped gallium arsenide crystals*, Sov. Phys. Solid State **25**, 2035 (1983). (Cit. on p. 12).

[Mei07]   L. Meier, G. Salis, I. Shorubalko, E. Gini, S. Schon, and K. Ensslin, *Measurement of Rashba and Dresselhaus spin-orbit magnetic fields*, Nat. Phys. **3**, 650 (Sept. 2007). (Cit. on p. 14).

[Mei84]   F. Meier and B. P. Zakharchenya, eds. *Optical Orientation*. Vol. 8. Modern Problems in Condensed Matter Science. North-Holland, Amsterdam, 1984 (cit. on p. 2).

[Mim80]   T. Mimura, S. Hiyamizu, T. Fujii, and K. Nanbu, *A New Field-Effect Transistor with Selectively Doped GaAs/n-$Al_xGa_{1-x}As$ Heterojunctions*, Japanese Journal of Applied Physics **19**, 225 (1980). (Cit. on p. 1).

[Moo90]   P. M. Mooney, *Deep donor levels (DX centers) in III-V semiconductors*, J. Appl. Phys. **67**, 1 (Feb. 1990). (Cit. on p. 33).

[Mül08]   G. M. Müller, M. Römer, D. Schuh, W. Wegscheider, J. Hübner, and M. Oestreich, *Spin Noise Spectroscopy in GaAs (110) Quantum Wells: Access to Intrinsic Spin Lifetimes and Equilibrium Electron Dynamics*, Phys. Rev. Lett. **101**, 206601 (Nov. 2008). (Cit. on pp. 2, 3, 20, 87, 88, 96, 99, 107).

[Nef11]   Y. A. Nefyodov, A. V. Shchepetilnikov, I. V. Kukushkin, W. Dietsche, and S. Schmult, *Electron g-factor anisotropy in $GaAs/Al_{1-x}Ga_xAs$ quantum wells of different symmetry*, Phys. Rev. B **84**, 233302 (Dec. 2011). (Cit. on pp. 17, 57).

[Nit97]   J. Nitta, T. Akazaki, H. Takayanagi, and T. Enoki, *Gate Control of Spin-Orbit Interaction in an Inverted $In_{0.53}Ga_{0.47}As/In_{0.52}Al_{0.48}As$ Heterostructure*, Phys. Rev. Lett. **78**, 1335 (Feb. 1997). (Cit. on p. 1).

[Odo06]   B. Odom, D. Hanneke, B. D'Urso, and G. Gabrielse, *New Measurement of the Electron Magnetic Moment Using a One-Electron Quantum Cyclotron*, Phys. Rev. Lett. **97**, 030801 (July 2006). (Cit. on p. 17).

[Oes95]   M. Oestreich and W. W. Rühle, *Temperature Dependence of the Electron Landé g Factor in GaAs*, Phys. Rev. Lett. **74**, 2315 (Mar. 1995). (Cit. on pp. 17, 84).

[Oes96]   M. Oestreich, S. Hallstein, A. P. Heberle, K. Eberl, E. Bauser, and W. W. Rühle, *Temperature and density dependence of the electron Landé g factor in semiconductors*, Phys. Rev. B **53**, 7911 (Mar. 1996). (Cit. on p. 17).

[Ohn99]   Y. Ohno, R. Terauchi, T. Adachi, F. Matsukura, and H. Ohno, *Spin Relaxation in GaAs(110) Quantum Wells*, Phys. Rev. Lett. **83**, 4196 (Nov. 1999). (Cit. on p. 3).

[Ove53]   A. W. Overhauser, *Polarization of Nuclei in Metals*, Phys. Rev. **92**, 411 (Oct. 1953). (Cit. on p. 27).

[Pag77]   D. Paget, G. Lampel, B. Sapoval, and V. I. Safarov, *Low field electron-nuclear spin coupling in gallium arsenide under optical pumping conditions*, Phys. Rev. B **15**, 5780 (June 1977). (Cit. on pp. 27, 28).

[Pag84]   D. Paget and V. Berkovits. "Optical investigation of hyperfine coupling between electronic and nuclear spins". In: *Optical Orientation, Modern Problems in Condensed Matter Science*. Ed. by F. Meier and B. P. Zakharchenya. Vol. 8. North-Holland, Amsterdam, 1984. Chap. 9, 381 (cit. on p. 27).

[Pet05]   J. R. Petta, A. C. Johnson, J. M. Taylor, E. A. Laird, A. Yacoby, M. D. Lukin, C. M. Marcus, M. P. Hanson, and A. C. Gossard, *Coherent Manipulation of Coupled Electron Spins in Semiconductor Quantum Dots*, Science **309**, 2180 (Sept. 2005). (Cit. on p. 21).

[Pik84]   G. E. Pikus and A. N. Titkov. "Spin relaxation under optical orientation in semiconductors". In: *Optical Orientation, Modern Problems in Condensed Matter Science*. Ed. by F. Meier and B. P. Zakharchenya. Vol. 8. North-Holland, Amsterdam, 1984. Chap. 3, 73 (cit. on p. 20).

[Pla01]   M. Planck, *Ueber das Gesetz der Energieverteilung im Normalspectrum*, Annalen der Physik **309**, 553 (1901). (Cit. on p. 1).

[Ras06]   E. I. Rashba, *Spin-orbit coupling and spin transport*, Physica E: Low-dimensional Systems and Nanostructures **34**, 31 (Aug. 2006). (Cit. on pp. 1, 12).

[Ras60]   E. I. Rashba, *Properties of semiconductors with an extremum loop. 1. Cyclotron and combinational resonance in a magnetic field perpendicular to the plane of the loop*, Sov. Phys. Solid State **2**, 1224 (1960). (Cit. on p. 13).

[Rid91]   B. K. Ridley, *Hot electrons in low-dimensional structures*, Reports on Progress in Physics **54**, 169 (1991). (Cit. on p. 9).

[Rot59]   L. M. Roth, B. Lax, and S. Zwerdling, *Theory of Optical Magneto-Absorption Effects in Semiconductors*, Phys. Rev. **114**, 90 (Apr. 1959). (Cit. on p. 17).

[Rya84]   J. F. Ryan, R. A. Taylor, A. J. Turberfield, A. Maciel, J. M. Worlock, A. C. Gossard, and W. Wiegmann, *Time-Resolved Photoluminescence of Two-Dimensional Hot Carriers in GaAs-AlGaAs Heterostructures*, Phys. Rev. Lett. **53**, 1841 (Nov. 1984). (Cit. on pp. 9, 45, 54).

[Rös02]   U. Rössler and J. Kainz, *Microscopic interface asymmetry and spin-splitting of electron subbands in semiconductor quantum structures*, Solid State Communications **121**, 313 (Feb. 2002). (Cit. on p. 18).

[Rös10]   C. Rössler, T. Feil, P. Mensch, T. Ihn, K. Ensslin, D. Schuh, and W. Wegscheider, *Gating of high-mobility two-dimensional electron gases in GaAs/AlGaAs heterostructures*, New Journal of Physics **12**, 043007 (2010). (Cit. on pp. 34, 64, 91).

[Sal01a]   G. Salis, D. T. Fuchs, J. M. Kikkawa, D. D. Awschalom, Y. Ohno, and H. Ohno, *Optical Manipulation of Nuclear Spin by a Two-Dimensional Electron Gas*, Phys. Rev. Lett. **86**, 2677 (Mar. 2001). (Cit. on pp. 26, 28, 100).

[Sal01b]   G. Salis, D. D. Awschalom, Y. Ohno, and H. Ohno, *Origin of enhanced dynamic nuclear polarization and all-optical nuclear magnetic resonance in GaAs quantum wells*, Phys. Rev. B **64**, 195304 (Oct. 2001). (Cit. on pp. 28, 100).

[Sap92]   V. F. Sapega, M. Cardona, K. Ploog, E. L. Ivchenko, and D. N. Mirlin, *Spin-flip Raman scattering in $GaAs/Al_xGa_{1-x}As$ multiple quantum wells*, Phys. Rev. B **45**, 4320 (Feb. 1992). (Cit. on p. 17).

[Sax81]   A. K. Saxena, *Electron mobility in $Ga_{1-x}Al_xAs$ alloys*, Phys. Rev. B **24**, 3295 (Sept. 1981). (Cit. on p. 8).

[Sch03a]   J. Schliemann, A. Khaetskii, and D. Loss, *Electron spin dynamics in quantum dots and related nanostructures due to hyperfine interaction with nuclei*, Journal of Physics: Condensed Matter **15**, R1809 (2003). (Cit. on p. 28).

[Sch03b]   J. Schliemann, J. C. Egues, and D. Loss, *Nonballistic Spin-Field-Effect Transistor*, Phys. Rev. Lett. **90**, 146801 (Apr. 2003). (Cit. on p. 3).

[Sch10]   D. Schuh, private communication (Jan. 2010). (Cit. on pp. 32, 33).

[Sch12]   D. Schuh, private communication (June 2012). (Cit. on pp. 35, 92).

[Sch26]   E. Schrödinger, *An Undulatory Theory of the Mechanics of Atoms and Molecules*, Phys. Rev. **28**, 1049 (Dec. 1926). (Cit. on pp. 1, 12).

[Sch93]   E. F. Schubert. *Doping in III-V Semiconductors (Cambridge Studies in Semiconductor Physics and Microelectronic Engineering)*. Cambridge University Press, 1993. ISBN: 0521419190 (cit. on pp. 35, 127).

[Sch96]   K. L. Schumacher, D Collings, R. T. Phillips, D. A. Ritchie, G. Weber, J. N. Schulman, and K. Ploog, *Inter- and intrasubband relaxation times in $Al_{0.35}Ga_{0.65}As$ quantum wells measured by femtosecond time-resolved differential transmission*, Semiconductor Science and Technology **11**, 1173 (1996). (Cit. on p. 46).

[Sha77]   J. Shah, R. F. Leheny, and W. Wiegmann, *Low-temperature absorption spectrum in GaAs in the presence of optical pumping*, Phys. Rev. B **16**, 1577 (Aug. 1977). (Cit. on p. 46).

[Sha79]   C. V. Shank, R. L. Fork, R. F. Leheny, and J. Shah, *Dynamics of Photoexcited GaAs Band-Edge Absorption with Subpicosecond Resolution*, Phys. Rev. Lett. **42**, 112 (Jan. 1979). (Cit. on p. 46).

[Sha84]   J. Shah, A. Pinczuk, H. L. Stormer, A. C. Gossard, and W. Wiegmann, *Hot electrons in modulation-doped GaAs-AlGaAs heterostructures*, Appl. Phys. Lett. **44**, 322 (Feb. 1984). (Cit. on p. 9).

[She03]   E. Y. Sherman, *Random spin–orbit coupling and spin relaxation in symmetric quantum wells*, Appl. Phys. Lett. **82**, 209 (Jan. 2003). (Cit. on pp. 24, 44, 90).

[Shi95]   A. Shields, M. Pepper, D. Ritchie, M. Simmons, and G. Jones, *Quenching of excitonic optical transitions by excess electrons in GaAs quantum wells*, Phys. Rev. B **51**, 18049 (June 1995). (Cit. on pp. 45, 63).

[Sih04]   V. Sih, W. H. Lau, R. C. Myers, A. C. Gossard, M. E. Flatté, and D. D. Awschalom, *Control of electron-spin coherence using Landau level quantization in a two-dimensional electron gas*, Phys. Rev. B **70**, 161313 (Oct. 2004). (Cit. on p. 75).

[Sli78]   C. P. Slichter. *Principles of magnetic resonance.* 2. rev. and exp. edition, Harper & Row, New York, 1978 (cit. on p. 19).

[Slu96]   M. Slutzky, O. Entin-Wohlman, Y. Berk, A. Palevski, and H. Shtrikman, *Electron-electron scattering in coupled quantum wells*, Phys. Rev. B **53**, 4065 (Feb. 1996). (Cit. on p. 9).

[Sne91]   M. J. Snelling, G. P. Flinn, A. S. Plaut, R. T. Harley, A. C. Tropper, R. Eccleston, and C. C. Phillips, *Magnetic g factor of electrons in $GaAs/Al_xGa_{1-x}As$ quantum wells*, Phys. Rev. B **44**, 11345 (Nov. 1991). (Cit. on p. 17).

[Ste83]   D. Stein, K. v. Klitzing, and G. Weimann, *Electron Spin Resonance on GaAs-$Al_xGa_{1-x}As$ Heterostructures*, Phys. Rev. Lett. **51**, 130 (July 1983). (Cit. on p. 17).

[Sti07a] D. Stich, J. Zhou, T. Korn, R. Schulz, D. Schuh, W. Wegscheider, M. W. Wu, and C. Schüller, *Dependence of spin dephasing on initial spin polarization in a high-mobility two-dimensional electron system*, Phys. Rev. B **76**, 205301 (2007). (Cit. on pp. 14, 25, 66, 67, 106).

[Sti07b] D. Stich, J. H. Jiang, T. Korn, R. Schulz, D. Schuh, W. Wegscheider, M. W. Wu, and C. Schüller, *Detection of large magnetoanisotropy of electron spin dephasing in a high-mobility two-dimensional electron system in a [001] $GaAs/Al_xGa_{1-x}As$ quantum well*, Physical Review B **76**, 073309 (2007). (Cit. on pp. 21, 55).

[Sti07c] D. Stich, J. Zhou, T. Korn, R. Schulz, D. Schuh, W. Wegscheider, M. W. Wu, and C. Schüller, *Effect of Initial Spin Polarization on Spin Dephasing and the Electron g Factor in a High-Mobility Two-Dimensional Electron System*, Physical Review Letters **98**, 176401 (2007). (Cit. on pp. 2, 3, 20, 66, 67, 70).

[Sti69]   G. Stillman, C. Wolfe, and J. Dimmock, *Magnetospectroscopy of shallow donors in GaAs*, Solid State Communications **7**, 921 (July 1969). (Cit. on pp. 45, 81, 82).

[Sti71]   G. Stillman, D. M. Larsen, C. Wolfe, and R. Brandt, *Precision verification of effective mass theory for shallow donors in GaAs*, Solid State Communications **9**, 2245 (Dec. 1971). (Cit. on pp. 45, 81, 82).

[Str81]   G. B. Stringfellow, W. Koschel, F. Briones, J. Gladstone, and G. Patterson, *Photoluminescence of carbon-implanted GaAs*, Appl. Phys. Lett. **39**, 581 (Oct. 1981). (Cit. on pp. 44, 88).

[Stu10]   M. Studer, M. P. Walser, S. Baer, H. Rusterholz, S. Schön, D. Schuh, W. Wegscheider, K. Ensslin, and G. Salis, *Role of linear and cubic terms for drift-induced Dresselhaus spin-orbit splitting in a two-dimensional electron gas*, Phys. Rev. B **82**, 235320 (Dec. 2010). (Cit. on p. 53).

[Sun10]   B. Y. Sun, P. Zhang, and M. W. Wu, *Spin relaxation in n-type (111) GaAs quantum wells*, J. Appl. Phys. **108**, 093709 (Nov. 2010). (Cit. on p. 14).

[Syp07]   M. Syperek, D. R. Yakovlev, A. Greilich, J. Misiewicz, M. Bayer, D. Reuter, and A. D. Wieck, *Spin Coherence of Holes in GaAs/(Al,Ga)As Quantum Wells*, Phys. Rev. Lett. **99**, 187401 (Oct. 2007). (Cit. on p. 11).

[Sze81]   S. M. Sze. *Physics of Semiconductor Devices*. Wiley-Interscience, 1981. ISBN: 0471056618 (cit. on pp. 5, 6, 8).

[Tar09]   S. A. Tarasenko, *Spin relaxation of conduction electrons in (110)-grown quantum wells: A microscopic theory*, Phys. Rev. B **80**, 165317 (Oct. 2009). (Cit. on pp. 24, 43, 83).

[Teh88]   C. Teh and F. Weichman, *Photoluminescence decay mechanism of the ≈1.49 eV emission in LEC-grown semi-insulating GaAs*, Journal of Luminescence **40 & 41**, 359 (Feb. 1988). (Cit. on p. 89).

[Teh90]   C. K. Teh, J. Tuszyński, and F. L. Weichman, *The decay of carbon, luminescence in liquid-encapsulated Czochralski-grown semi-insulating GaAs*. Journal of Materials Research **5**, 365 (1990). (Cit. on p. 89).

[Tor56]   H. C. Torrey, *Bloch Equations with Diffusion Terms*, Phys. Rev. **104**, 563 (Nov. 1956). (Cit. on p. 16).

[Uma09]   V. Umansky, M. Heiblum, Y. Levinson, J. Smet, J. Nübler, and M. Dolev, *MBE growth of ultra-low disorder 2DEG with mobility exceeding $35 \cdot 10^6$ cm^2/Vs*, Journal of Crystal Growth **311**, 1658 (Mar. 2009). (Cit. on pp. 7, 8, 30, 32, 33).

[VD04]   P. Van Dorpe, Z. Liu, W. Van Roy, V. F. Motsnyi, M. Sawicki, G. Borghs, and J. De Boeck, *Very high spin polarization in GaAs by injection from a (Ga,Mn)As Zener diode*, Appl. Phys. Lett. **84**, 3495 (May 2004). (Cit. on p. 14).

[VD05]   P. Van Dorpe, W. Van Roy, J. De Boeck, and G. Borghs, *Nuclear spin orientation by electrical spin injection in an $Al_x Ga_{1-x} As/GaAs$ spin-polarized light-emitting diode*, Phys. Rev. B **72**, 035315 (July 2005). (Cit. on p. 26).

[Var67]   Y. Varshni, *Temperature dependence of the energy gap in semiconductors*, Physica **34**, 149 (1967). (Cit. on pp. 6, 59).

[Vur01]   I. Vurgaftman, J. R. Meyer, and L. R. Ram-Mohan, *Band parameters for III–V compound semiconductors and their alloys*, J. Appl. Phys. **89**, 5815 (June 2001). (Cit. on p. 6).

[Völ11]   R. Völkl, M. Griesbeck, S. A. Tarasenko, D. Schuh, W. Wegscheider, C. Schüller, and T. Korn, *Spin dephasing and photoinduced spin diffusion in a high-mobility two-dimensional electron system embedded in a GaAs-AlGaAs quantum well grown in the [110] direction*, Phys. Rev. B **83**, 241306 (June 2011). (Cit. on pp. 20, 86).

[Win03]   R. Winkler. *Spin-orbit Coupling Effects in Two-Dimensional Electron and Hole Systems (Springer Tracts in Modern Physics)*. Springer, 2003. ISBN: 3540011870 (cit. on pp. 14, 53, 56, 82, 90, 129).

[Win04]   R. Winkler, *Spin orientation and spin precession in inversion-asymmetric quasi-two-dimensional electron systems*, Phys. Rev. B **69**, 045317 (Jan. 2004). (Cit. on pp. 2, 13, 23).

[Wol01]   S. A. Wolf, D. D. Awschalom, R. A. Buhrman, J. M. Daughton, S. von Molnár, M. L. Roukes, A. Y. Chtchelkanova, and D. M. Treger, *Spintronics: A Spin-Based Electronics Vision for the Future*, Science **294**, 1488 (2001). (Cit. on p. 2).

[Wu10]   M. Wu, J. Jiang, and M. Weng, *Spin dynamics in semiconductors*, Physics Reports **493**, 61 (Aug. 2010). (Cit. on p. 2).

[Xu99]   J. Xu, E. Towe, Q. Yuan, and R. Hull, *Beryllium doping and silicon amphotericity in (110) GaAs-based heterostructures: structural and optical properties*, Journal of Crystal Growth **196**, 26 (Jan. 1999). (Cit. on pp. 35, 91, 127).

[Yaf63]   Y. Yafet. "g Factors and Spin-Lattice Relaxation of Conduction Electrons". In: *Solid State Physics*. Ed. by F. Seitz and D. Turnbull. Vol. 14. Academic Press, 1963 (cit. on p. 18).

[Yan10]   C. L. Yang, J. Dai, W. K. Ge, and X. Cui, *Determination of the sign of g factors for conduction electrons using time-resolved Kerr rotation*, Appl. Phys. Lett. **96**, 152109 (Apr. 2010). (Cit. on p. 50).

[Yug07]   I. A. Yugova, A. Greilich, D. R. Yakovlev, A. A. Kiselev, M. Bayer, V. V. Petrov, Y. K. Dolgikh, D. Reuter, and A. D. Wieck, *Universal behavior of the electron g factor in $GaAs/Al_xGa_{1-x}As$ quantum wells*, Phys. Rev. B **75**, 245302 (June 2007). (Cit. on pp. 8, 17, 50, 57, 84, 105).

[Yug09]   I. A. Yugova, A. A. Sokolova, D. R. Yakovlev, A. Greilich, D. Reuter, A. D. Wieck, and M. Bayer, *Long-Term Hole Spin Memory in the Resonantly Amplified Spin Coherence of InGaAs/GaAs Quantum Well Electrons*, Physical Review Letters **102**, 167402 (2009). (Cit. on pp. 41, 100).

[Zut04]   I. Zutic, J. Fabian, and S. Das Sarma, *Spintronics: Fundamentals and applications*, Rev. Mod. Phys. **76**, 323 (Apr. 2004). (Cit. on pp. 2, 12, 20).

[Țif03]   I. Țifrea and M. E. Flatté, *Electric Field Tunability of Nuclear and Electronic Spin Dynamics due to the Hyperfine Interaction in Semiconductor Nanostructures*, Phys. Rev. Lett. **90**, 237601 (June 2003). (Cit. on p. 28).

[Țif04]   I. Țifrea and M. E. Flatté, *Nuclear spin dynamics in parabolic quantum wells*, Phys. Rev. B **69**, 115305 (Mar. 2004). (Cit. on p. 28).

[Țif11]   I. Țifrea and M. E. Flatté, *Nonequilibrium nuclear polarization and induced hyperfine and dipolar magnetic fields in semiconductor nanostructures*, Phys. Rev. B **84**, 155319 (Oct. 2011). (Cit. on pp. 28, 103).

Appendices

Appendix A

Sensitivity of double-sided doped high-mobility GaAs/AlGaAs heterostructures on above-barrier illumination

In PL experiments on the samples F and G at $T = 4\,\mathrm{K}$ a different sensitivity of the carrier density n on the intensity $I_{532\,\mathrm{nm}}$ of the the weak above-barrier illumination could be observed. It was discussed in Sec. 4.3 in detail that the linear dependence of the carrier density n of a 2DES and the spectral width ΔE of the corresponding PL line allows for the determination of the carrier density n. Whereas in sample G extremely low intensities $I_{532\,\mathrm{nm}}$ are sufficient for a drastic change of the spectral width ΔE of the PL line, higher intensities are necessary in sample F to achieve the same effect (see Fig. A.1). The corresponding carrier densities n extracted from the PL traces are shown in Fig. A.2. Panel (a) shows the dependence of the carrier density n of both samples on $I_{532\,\mathrm{nm}}$: the carrier density in both samples decreases when $I_{532\,\mathrm{nm}}$ is increased.
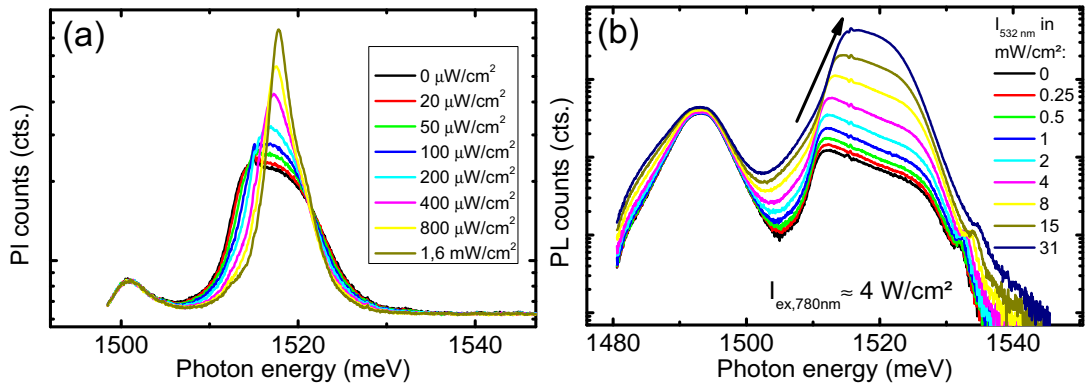
Figure A.1: *(a) PL of sample G under the conditions of optical gating. Low illumination intensities $I_{532\,\mathrm{nm}}$ of the green laser light are sufficient for a drastic change of the PL linewidth. (b) PL of sample F under the conditions of optical gating. An increase of the above-barrier illumination leads to a blue shift of the low energy edge of the PL. In comparison with sample G, here higher illumination intensities $I_{532\,\mathrm{nm}}$ are necessary for a reduction of the spectral width of the PL line.*
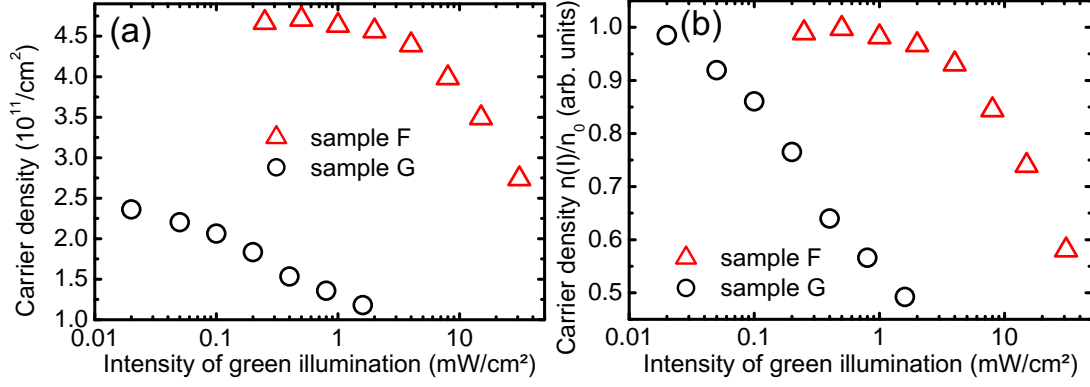
Figure A.2: *(a) Carrier densities n extracted from the PL data shown in Fig. A.1. The carrier density of both samples decreases, when the intensity $I_{532\,nm}$ of the above-barrier illumination is increased. Whereas low illumination intensities $I_{532\,nm} \approx 100\,\mu W/cm^2$ are sufficient for a significant reduction of the carrier density n in sample G, higher intensities $I_{532\,nm} > 1\,mW/cm^2$ are necessary for this purpose in sample F. (b) This can be seen more easily from the normalized carrier densities $n(I_{532\,nm})/n$.*

Whereas low illumination intensities $I_{532\,nm} \approx 100\,\mu W/cm^2$ are sufficient for a significant reduction of the carrier density n in sample G, higher intensities $I_{532\,nm} > 1\,mW/cm^2$ are necessary for this purpose in sample F. Panel (b) shows the relative change $n(I_{532\,nm})/n$ of the carrier density, normalized to the values n_0 without additional illumination. For a reduction of the carrier density to one half of the initial value, in sample F an intensity $I_{532\,nm}$ is necessary, being about a factor of 20 higher than in sample G. Hence, sample G can be qualitatively denoted as more sensitive on above-barrier illumination.

For a quantitative analysis, the model presented in Eq. (2.11) in Sec.2.1.3 can be used[1]:

$$I_{532\,nm} = C(n_0 - n_s)\exp(-D\sqrt{n_s}). \tag{A.1}$$

Here, $I_{532\,nm}$ is the intensity required to achieve a steady-state carrier density[2] n_s. Fig. A.3 shows the steady-state carrier densities n_s and the corresponding illumination intensities $I_{532\,nm}$, as well as a fit to the data using the model in Eq. (A.1). The values
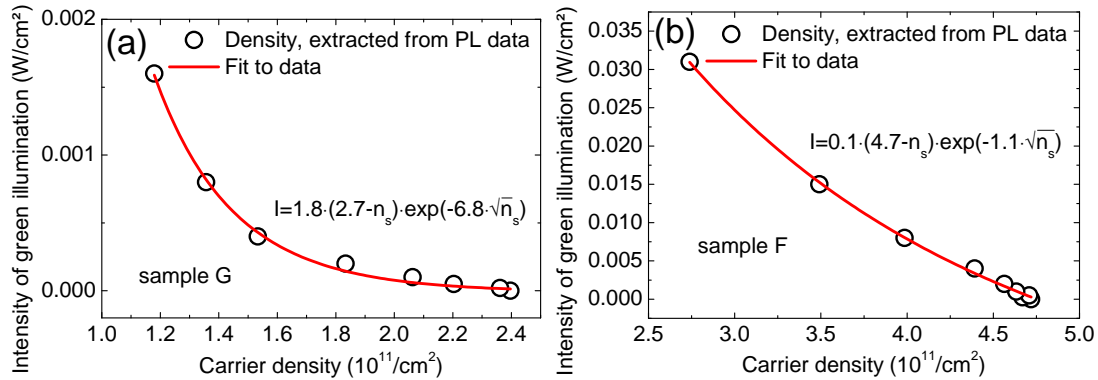

Figure A.3: *Required illumination intensities $I_{532\,nm}$ for achieving a certain steady-state carrier density n_s in sample G (a) and sample F (b). The red lines represent a fit to the data, using the model in Eq. (2.11).*

---

[1]It should be noted again (see also Sec. 2.1.3) that this model was developed for an asymmetric QW. An appropriate model for a symmetric QW is still lacking.

[2]It should be noted that the carrier density n_s is inserted into Eq. (A.1) in units of $10^{11} cm^{-2}$.

for C and D resulting from the fit are written down in Fig. A.3. The value of $D \approx 6.8$ in sample G is significantly higher than in sample F ($D \approx 1.1$). Besides the parameter D, also C should be taken into account for the characterization of the sensitivity [Loi12]. Considering the change $\Delta n = n_0 - n_s$ of the carrier density n_0 when the intensity $I_{532\,\mathrm{nm}}$ is hitting the sample, one can define the sensitivity $S = \Delta n / I_{532\,\mathrm{nm}}$ by rewriting Eq. (A.1):

$$S = \frac{\Delta n}{I_{532\,\mathrm{nm}}} = \frac{\exp(D\sqrt{n_0 - \Delta n})}{C}. \tag{A.2}$$

The calculated values of S for the samples F and G are depicted in Fig. A.4. The value $S \approx 75$ of sample F is clearly lower than that of sample G, where $S \approx 10^4$. For the calculation of S the term $\sqrt{n_0 - \Delta n}$ in the exponent was approximated as $\sqrt{0.75 \cdot n_0}$. The error bars mark the limiting values of S for $0 < \Delta n < n_0/2$, corresponding to the experimentally accessed range of Δn. Here, $\Delta n = n_0/2$ corresponds to the situation, where the carrier density n is reduced to one half of the initial carrier density n_0. The case $\Delta n = 0$ is equivalent to situation without above-barrier illumination. The
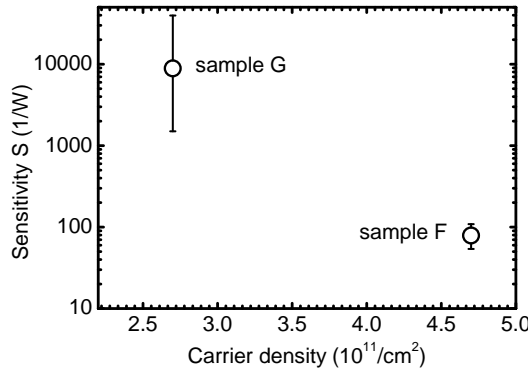
Figure A.4: *Calculated values for the sensitivity S of sample F and G. The sensitivity of sample G clearly exceeds the sensitivity of sample F. The error bars mark the limiting values of S, assuming $0 < \Delta n < n_0/2$.*

determined values of S are within their error bars in agreement with the qualitative observation, that the sensitivity of sample G is drastically higher than that of sample G. Therefore, the analysis of the spectral width of the PL line, which yields the carrier density n_s under the condition of optical gating, can be used for the estimation of the sensitivity S of a sample on weak above-barrier illumination.

Due to the similar growth structure of samples F and G, the different sensitivity of both samples on above-barrier illumination can not be easily explained. Most likely the substrate temperature T_δ during the growth of the SPSL layers (see Sec. 3.1.2) is crucial for this different behavior. T_δ was shown to influence the incorporation of the amphoteric Si donor atoms on Ga or As sites [Sch93; Xu99]. In sample F, the substrate temperature was reduced prior to the growth of the single SPSL layers from $T \approx 480\,\mathrm{K}$ to about $T_\delta \approx 440\,\mathrm{K}$. In contrast, the substrate temperature was kept constant during the growth of sample G at $T = T_\delta \approx 480\,\mathrm{K}$. Due to the reduced temperature T_δ during the growth of the SPSL layers in sample F, a smaller amount of Si atoms is expected to be incorporated on As sites. In consequence, less holes created by Si atoms incorporated on As sites[3] have to be compensated by donor electrons, provided by Si atoms on Ga sites. Therefore, a higher doping efficiency is possible, what could explain the higher carrier density n observed in sample F.

---

[3]Incorporated on As sites, the Si atoms act as acceptors.

The influence of the amount of Si atoms acting as acceptors in the SPSL layers on the sensitivity S is not completely clear up now. In a detailed study of S on comparable samples with a similar growth scheme [Loi12], lower values for S were found if the substrate temperature T_δ during the growth of the SPSL layers was reduced. A dependence of S on other parameters, as for example the doping concentration in the SPSL layers, the resulting carrier density n or the electron mobility μ could not be found.

In conclusion, the sensitivity S of dsd high-mobility heterostructures using the growth scheme as presented in Sec. 3.1.2 can be strongly different, as was shown in particular for samples F and G. The sensitivity S is most likely connected with the growth conditions during the SPSL growth. Lower substrate temperatures T_δ, promoting the incorporation of the amphoteric Si dopant atoms on Ga sites, were found to result in a lower sensitivity S. The microscopic reason for this is not clear yet.

Appendix B

Simulation of the asymmetric band profile of sample C using nextnano^3
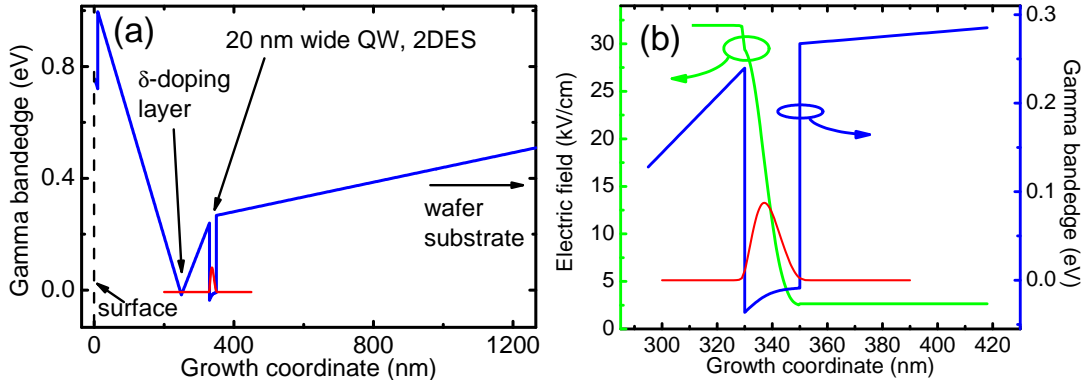
Figure B.1: *(a) Calculated Γ bandedge of the conduction band. The 2DES resides in the asymmetric 20 nm wide QW. (b) Electric field in the vicinity of the 2DES, relevant for the Rashba field Ω_R.*

In Chap. 5 results concerning the relative strength of the Dresselhaus and the Rashba contribution to the SO field $\boldsymbol{\Omega} = \boldsymbol{\Omega}_D + \boldsymbol{\Omega}_R$ were presented, expressed by the ratio β/α. Here, a simulation of the band profile of sample C will be presented, allowing for the calculation of the Rashba parameter α.

Using the nextnano^3 semiconductor simulation software, the band profile of sample C was simulated in the effective mass approximation. Panel (a) of Fig. B.1 shows the calculated band edge of the conduction band at the Γ point. Due to the δ-doping layer, the conduction band in the 20 nm wide GaAs QW is located below the Fermi energy, resulting in the formation of a 2DES. The electric field E_z connected with the band gradient[1] in the vicinity of the QW is depicted in panel (b) of Fig. B.1. The average value of the electric field is $E_z \approx 17\,\mathrm{kV/cm}$. This results in $\alpha = 2\alpha_R E_z \approx 1.7\,\mathrm{meV\mathring{A}}$, legitimating the assumption $\alpha \approx 1.7\,\mathrm{meV\mathring{A}}$, made in Chap. 5.

---

[1]It should be noted, that the band gradient is the same in the conduction as well as in the valence band, due to the constant band gap E_G in the GaAs QW. For the Rashba field, the band gradient in the valence band is of importance [Win03; Eld11], which is in this case equal to the gradient of the conduction band.

Appendix C

Estimating the degree of nuclear spin polarization in sample G

Here, the degree of nuclear spin polarization should be estimated, corresponding to the Overhauser-type shift observed in the RSA spectra, taken at a temperature of $T = 1.2\,\text{K}$ under the conditions of optical gating. First, the maximum value of the Overhauser field will be calculated, using the expression in Eq. (2.72):

$$\vec{B}_n^k = \frac{2\mu_0}{3} \frac{g_0}{g} \sum_\alpha \mu_{I,\alpha} \vec{I}_\alpha \left| \psi_k(\vec{r}_\alpha) \right|^2 .\tag{C.1}$$

Here, the sum collects the contributions of different nuclear species (^{69}Ga, ^{71}Ga and ^{75}As) to the Overhauser field. It is assumed, that all nuclear spins in the illuminated area of the QW (diameter D of the laser $D \approx 50\,\mu$m, QW width $d = 30\,$nm) are spin polarized. The constants used for the calculation are

$$\mu_0 = 4\pi \cdot 10^{-7} \frac{\text{Vs}}{\text{Am}},\tag{C.2}$$

$$\mu_B = 9.274... \cdot 10^{-24} \frac{\text{J}}{\text{T}},\tag{C.3}$$

$$\mu_I = 5.05... \cdot 10^{-27} \frac{\text{J}}{\text{T}},\tag{C.4}$$

$$\eta_{Ga} = 2.7 \cdot 10^3 \quad \text{and}\tag{C.5}$$

$$\eta_{As} = 4.5 \cdot 10^3.\tag{C.6}$$

The considered cylindric volume has the height $d = 30\,$nm, equal to the QW width. The area A of top or bottom of the cylinder is taken to be equal to the area

$$A = \frac{\pi D^2}{4}$$

of the laser spot. The wave function $\psi_k(\vec{r}_\alpha) = \phi_k(\vec{r}_\alpha) u_k(\vec{r}_\alpha)$ is written as a product of the envelope function $\phi_k(\vec{r}_\alpha)$ and the Bloch function $u_k(\vec{r}_\alpha)$, as introduced in Sec. 2.3.2. Thus, $\left| \psi_k(\vec{r}_\alpha) \right|^2$ can be written as $\eta \left| \phi_k(\vec{r}_\alpha) \right|^2$, where the envelope function $\phi_k(\vec{r}_\alpha)$ is assumed to be constant within and zero outside the considered volume. Thus, Eq. (C.1) can be rewritten as

$$\vec{B}_n^k = \frac{2\mu_0}{3} \frac{g_0}{g} \sum_\alpha \mu_{I,\alpha} \eta_\alpha \left| \phi_k(\vec{r}_\alpha) \right|^2 \vec{I}_\alpha.\tag{C.7}$$

The assumptions for the normalized wave function $\phi_k(\vec{r}_\alpha)$ yield

$$|\phi_k(\vec{r}_\alpha)|^2 = \frac{1}{V} = \frac{4}{\pi d D^2} = 1.698... \cdot 10^{16} \frac{1}{\text{m}^3}. \tag{C.8}$$

In addition, the number $\#$ of unit cells in the volume V has to be estimated. At room temperature, the cubic lattice constant a of zinkblende-type GaAs has the value $a = 5.6533\,\text{Å}$ [Lev99]. Thus, $\# \approx 3.29 \cdot 10^{11}$ cubic unit cells can be found in the volume V. Each cubic unit cell of GaAs contains 4 Ga and 4 As atoms, due to the diatomic basis with one Ga and one As atom per site of the underlying face-centered cubic (fcc) Bravais lattice. Considering the two isotopes ^{69}Ga and ^{71}Ga of Gallium and their relative natural abundance of 0.6 and 0.4, the sum $\sum_\alpha \mu_{I,\alpha} \eta_\alpha$ can be estimated as

$$\sum_\alpha \mu_{I,\alpha} \eta_\alpha \approx 4 \cdot ((0.6 \cdot 2.016 + 0.4 \cdot 2.562) \cdot 2.7 + 1.439 \cdot 4.5) \cdot 10^3 \mu_N \approx 50.0 \mu_N, \tag{C.9}$$

where $\mu_{I,^{69}Ga} = 2.016\mu_N$, $\mu_{I,^{71}Ga} = 2.562\mu_N$ and $\mu_{I,^{75}As} = 1.439\mu_N$ are the nuclear magnetic momenta of the corresponding isotopes of Ga and As. This leads to a maximum value of the Overhauser field

$$\vec{B}_n^k = \frac{4\mu_0}{3g} \sum_\alpha \mu_{I,\alpha} \eta_\alpha |\phi_k(\vec{r}_\alpha)|^2 \vec{I}_\alpha \approx \frac{4\mu_0 \#}{3gV} \sum_\alpha \mu_{I,\alpha} \eta_\alpha \vec{I}_\alpha \approx 6\,\text{T}, \tag{C.10}$$

where a value $|g| \approx 0.39$ is assumed for the electron g factor[1].

For a comparison of the experimentally observed Overhauser shift ($\approx 2\,\text{mT}$, see Fig. 6.34(b)) with the maximum achievable value of about $6\,\text{T}$, the geometry of the experimental setup has to be considered: as it is depicted in Fig. C.1, the sample was rotated by a small angle, in order to adjust an angle $\alpha \approx \pm 1°$ between the sample normal and the direction of the inciding laser beam. In consequence of the different refractive indices of vacuum ($n_0 = 1$) and GaAs ($n_{\text{GaAs}} \approx 3$), the refracted beam is closer to the sample normal. Following Snellius law

$$n_0 \sin\alpha = n_{\text{GaAs}} \sin\alpha', \tag{C.11}$$

the angle $\beta = \alpha - \alpha'$ between the inciding and the refracted beam can be estimated as

$$\beta \approx \alpha \left(1 - \frac{n_0}{n_{\text{GaAs}}}\right) \approx \frac{2}{3}\alpha, \tag{C.12}$$

where the small-angle approximation $\sin\alpha \approx \alpha$ was used. In consequence of the conservation of angular momentum, the optically oriented spin polarization resulting from the absorption of the circularly polarized pump beam initially points along the direction of the refracted beam. Therefore, the angle between the spin orientation and the magnetic field, being oriented perpendicular to the inciding laser beam, deviates by the angle β from the right angle. This leads in the presence of a non-zero magnetic field B to electron spin precession on a conical surface. Simultaneous flip-flop processes (c.f. Eq. (2.70)) of electron and nuclear spins at an arbitrary electron spin precession phase lead to polarized nuclear spins, oriented - like the electron spins - parallel to the conical surface. Due to the randomly occuring flip-flop processes, after a certain time the orientation of the nuclear spins can be taken to be equally distributed around the

---

[1]This value was extracted from RSA measurements under similar experimental conditions. Due to the reduction of the carrier density n resulting from optically gating sample G, the absolute value of the g factor slightly increases.
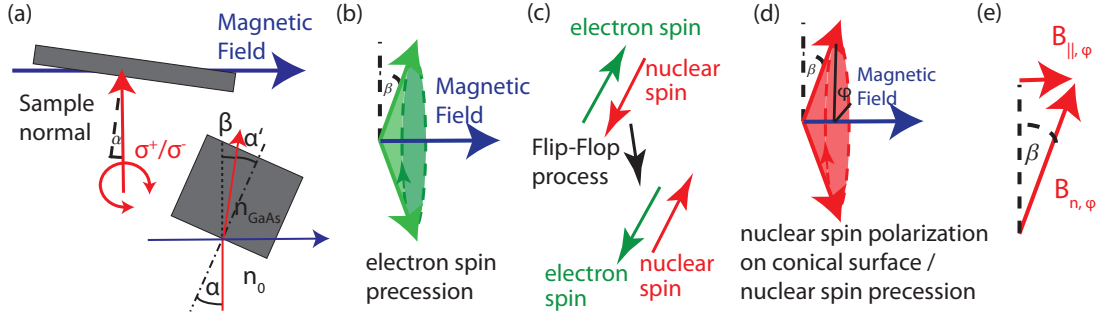
Figure C.1: *(a) Relevant geometry of the sample normal, the direction of the incident pump beam and the magnetic field B. The incident pump beam is refracted towards the sample normal, due to the different refractive index of GaAs. (b) The optically oriented spin ensemble points initially along the direction of the refracted pump beam. If a non-zero magnetic field B is applied, the electron spin ensemble precesses on a conical surface about the magnetic field axis. (c) Due to flip-flop processes, electron spin polarization is transferred to the nuclear spin system at arbitrary phases of electron spin precession. (d) This leads to nuclear spins, oriented parallel to the conical surface of the electron spin precession. (e) The component $B_{||}$ of the Overhauser field parallel to the external field most likely governs the observable shift in the RSA spectra.*

conical surface[2]. The nuclear spin ensemble oriented parallel to the conical surface has a component $B_{||}$ parallel to the external magnetic field B, which most likely governs the experimentally observable shift in the RSA spectra. The component $B_{||}$ parallel to the external magnetic field is connected via the relation

$$B_{||} = B_n \sin(\beta) = \sum_\varphi B_{n,\varphi} \sin(\beta) \tag{C.13}$$

with the total Overhauser field B_n, which is produced of all nuclear spin subsets, being oriented parallel to the conical surface, including an angle φ with the sample plane. Thus, the total Overhauser field B_n can be calculated from the experimentally accessible shifts (up to $2.5\,\text{mT}$) to be about $B_n \approx 200\,\text{mT}$, for a small angle $\alpha \approx \pm 1°$ between the sample normal and the direction of the incident pump beam. This corresponds to a nuclear spin polarization of about 3-4 %, isotropically distributed on the surface of the electron spin precession cone.

---

[2]Similar to electron spin precession in the external magnetic field B, also the nuclear spin ensemble can be expected to precess about B. However, due to the drastically smaller nuclear g factor, the Larmor frequencies of the electron and the nuclear spins are clearly different. Thus, on the timescale of electron spin precession, the nuclear spin orientation can be taken as static.

List of own publications

M. Griesbeck, M.M. Glazov, T. Korn, E. Ya. Sherman, D. Waller, C. Reichl, D. Schuh, W. Wegscheider, and C. Schüller, *Cyclotron effect on coherent spin precession of two-dimensional electrons*, Phys. Rev. B **80**, 241314 (2009)

T. Korn, M. Kugler, M. Griesbeck, R. Schulz, A. Wagner, M. Hirmer, C. Gerl, D. Schuh, W. Wegscheider, and C. Schüller, *Engineering ultralong spin coherence in two-dimensional hole systems at low temperatures*, New Journal of Physics **12**, 043003 (2010)

V. Lechner, L.E. Golub, F. Lomakina, V.V. Bel'kov, P. Olbrich, S. Stachel, I. Caspers, M. Griesbeck, M. Kugler, M.J. Hirmer, T. Korn, C. Schüller, D. Schuh, W. Wegscheider, and S. D. Ganichev, *Spin and orbital mechanisms of the magnetogyrotropic photogalvanic effects in GaAs/Al$_x$Ga$_{1-x}$As quantum well structures*, Phys. Rev. B **83**, 155313 (2011)

R. Völkl, M. Griesbeck, S.A. Tarasenko, D. Schuh, W. Wegscheider, C. Schüller, and T. Korn, *Spin dephasing and photoinduced spin diffusion in a high-mobility two-dimensional electron system embedded in a GaAs-(Al,Ga)As quantum well grown in the [110] direction*, Phys. Rev. B **83**, 241306 (2011)

M. Kugler, K. Korzekwa, P. Machnikowski, C. Gradl, S. Furthmeier, M. Griesbeck, M. Hirmer, D. Schuh, W. Wegscheider, T. Kuhn, C. Schüller, and T. Korn, *Decoherence-assisted initialization of a resident hole spin polarization in a p-doped semiconductor quantum well*, Phys. Rev. B **84**, 085327 (2011)

M. Griesbeck, M.M. Glazov, E.Ya. Sherman, T. Korn, D. Schuh, W. Wegscheider, and C. Schüller (Invited talk), *Anisotropic spin dephasing in a (110)-grown high-mobility GaAs/AlGaAs quantum well measured by resonant spin amplification technique*, Proceedings of SPIE **8100**, 810015 (2011)

M. Griesbeck, M.M. Glazov, E.Ya. Sherman, D. Schuh, W. Wegscheider, C. Schüller, and T. Korn, *Strongly anisotropic spin relaxation revealed by resonant spin amplification in (110) GaAs quantum wells*, Phys. Rev. B **85** 085313 (2012)

List of symbols and abbreviations

Abbreviation	Description	introduced on page
$|\uparrow\rangle, |\downarrow\rangle$	Spin-up, spin-down state	18
a	Lattice constant	6
A	Vectorpotential of the magnetic field	11
$\mathcal{A}$	Amplitude of long-lived tail of spin polarization	26
α	Rashba parameter, $\alpha = 2\alpha_R E_z$	14
$\tilde{\alpha}$	Varshni parameter	6
α'	Absorption coefficient	16
α_c	Dimensionless parameter, which determines the strength of the Dresselhaus SO field; $\alpha_c = 0.07$	12
α_R	Rashba coefficient, $\alpha_R = 5$ eÅ^2	14
a_B	Effective Bohr radius in GaAs, $a_B \approx 114$ Å	21
$a_{\boldsymbol{k}}$	Function with periodicity of the lattice	18
$\boldsymbol{B}$	External magnetic field	11
$\mathcal{B}$	Amplitude of coherent spin oscillations	26
β	Dresselhaus parameter, $\beta = \gamma\langle k_z^2\rangle = \gamma\left(\frac{\pi}{d}\right)^2$	13
$\tilde{\beta}$	Varshni parameter, $\tilde{\beta} \approx \Theta_D$	6
$b_{\boldsymbol{k}}$	Function with periodicity of the lattice	18
BAP	Bir-Aronov-Pikus	20
$\vec{B}_e^i$	Knight field	27
$\vec{B}_n^k$	Overhauser field	27
BIA	Bulk inversion asymmetry	12
γ	Dresselhaus spin splitting constant	12
$\hat{\Gamma}$	Spin relaxation rates tensor	16
$\Gamma_{[001]}$	Spin dephasing rate for spins oriented along the [001] direction	52
Γ_ϕ	In-plane spin dephasing rate	61
Γ_{ij}	Elements of the spin relaxation rates tensor	24
Γ_{BAP}	BAP relaxation rate, $\Gamma_{BAP} = 1/\tau_{\mathrm{BAP}}$	20
c	Speed of light, $c = 299\,792\,458\,\mathrm{m/s}$	12
C	Parameter depending on τ and k_F	24
C_2	Symmetry point group (two-fold axial symmetry)	17
C_{2v}	Symmetry point group (Elements: $\mathcal{I}, \sigma_v/\sigma_v', C_2$)	17
CCD	Charge-coupled device	45
cf	Continuous flow	46
cw	Continuous wave	10
d	Quantum well width	7
DISP	Degree of initial spin polarization	66
DNP	Dynamical nuclear polarization	26
2DES	Two-dimensional electron system	7
DP	Dyakonov-Perel'	18

Abbreviation	Description	introduced on page
DPSS	Diode-pumped solid state laser	93
η	Enhanced probability density of $u_k(\vec{r_i})$ at $\vec{r_i}$	28
ee	Electron-electron	9
δE	Spectral width of the high-energy tail of the PL, $\delta E \propto k_B T_e$	45
ΔE	Spectral width of PL, $\Delta E = E_F - E_G$	44
E_c	Confinement energy	53
E_F	Fermi energy	7
E_G	Band gap energy	6
ΔE_L	Landau level spacing, $\Delta E_L = \hbar \omega_c$	75
ΔE_λ	Spectral width of the laser	75
$E_{\uparrow,\downarrow}(\boldsymbol{k})$	Energy of an electron state with wave vector $\boldsymbol{k}$ and spin $\mid\uparrow\rangle$, $\mid\downarrow\rangle$	19
E_{Ph}	Phonon energy	8
E_{Phot}	Photon energy	93
ΔE_{SO}	Spin-orbit splitting	18
ESR	Electron spin resonance	17
E_T	Thermal energy, $E_T = k_B T$	75
EY	Elliot-Yafet	18
E_z	Built-in growth axis electric field	7
$f_{\rm rep}$	Laser repetition frequency, $f_{\rm rep} = 80\,{\rm MHz}$	16
$\varphi_{\boldsymbol{k}}$	Angle between the $\boldsymbol{k}$ vector and the x axis	25
ϕ	Angle between the magnetic field and the [100] crystallographic direction	50
$\phi_k(\vec{r_i})$	Electron envelope function	28
FWHM	Full width at half maximum	42
g	Electron spin g factor, Landé factor	17
$\hat{\boldsymbol{g}}$	g factor tensor	16
g_0	Free electron g factor, $g_0 = 2.00231930436170(76)$	17
$g(\phi)$	In-plane g factor	50
GaMnAs	Galliummanganesearsenide, a diluted magnetic semiconductor	14
g_I	Nuclear g factor: $g_I(^{69}{\rm Ga}) = 2.0166$, $g_I(^{71}{\rm Ga}) = 2.5623$, $g_I(^{75}{\rm As}) = 1.4395$	26
g_{ij}	Elements of the g factor tensor $\hat{\boldsymbol{g}}$	17
$\hbar$	Planck´s constant, $\hbar = 1.05457266 \cdot 10^{-34}{\rm Js}$	7
$\hat{H}$	Hamilton operator	11
$\widehat{\mathcal{H}_{HF}}$	Hamilton operator of Fermi contact hyperfine interaction	26
$H(\tilde{q})$	Factor describing the weakening of the ee interaction in quasi-2DES	9
$\widehat{H_{SO}}$	Spin-orbit Hamiltonian	12
I	Laser intensity	11
$I_{532\ {\rm nm}}$	Intensity of the above-barrier illumination	93
$\hat{\boldsymbol{I}}$	Nuclear spin operator	26
$\hat{I}_\pm$	Ladder operators of nuclear spin, $\hat{I}_\pm = \hat{I}_x \pm i\hat{I}_y$	26
$\mathcal{I}$	Identity of the C_{2v} point group	17
I_{ex}	Excitation intensity	51
InAs	Indiumarsenide	15
InSb	Indiumantimonide	17
J	Total angular momentum	15
$\mid j_I m_I\rangle, \mid j_S m_S\rangle$	Spin states of nuclear / electron spin	26
κ	Dielectric constant, in GaAs $\kappa \approx 13$	90
$\boldsymbol{k}$	Electron wave vector	6
k_B	Boltzmann constant, $k_B = 8.6173324 \cdot 10^{-5}\,{\rm eV/K}$	9
$\langle k_z \rangle$	Quantum mechanical expectation value of k_z	12

Abbreviation	Description	introduced on page
$\langle k_z^2 \rangle$	Quantum mechanical expectation value of k_z^2	12
λ_{ex}	Excitation wavelength	70
l	Length of delay line, $l = 30\,\mathrm{cm}$	40
LCR	Liquid crystal retarder	100
μ	Electron mobility	8
μ_0	Vacuum permeability, $\mu_0 = 4\pi \times 10^{-7}\,\mathrm{Vs/(Am)}$	26
μ_B	Bohr magneton, $\mu_B = 9.274\,009\,68 \times 10^{-24}\,\mathrm{J/T}$	26
μ_I	Nuclear magnetic moment, $\mu_I = g_I \mu_N$	26
m_0	Electron rest mass, $m_0 = 9.109\,382\,15 \times 10^{-31}\,\mathrm{kg}$	12
m_j	z component of the total angular momentum J	15
μ_N	Nuclear magneton, $\mu_N = 5.050\,783\,24 \times 10^{-27}\,\mathrm{J/T}$	26
μ_S	Magnetic moment of an electron	17
MBE	Molecular beam epitaxy	1
$m_{e,h}^*$	Effective mass	7
∇	Nabla operator, $\nabla = (\partial_x, \partial_y, \partial_z)$	11
n	Carrier density	9
n'	Subband index	7
n_0	Carrier density without illumination	11
n_d	Donor density on each side of the QW	90
$n_{e_{\uparrow,\downarrow}}$	Electron density with spin-up / spin-down	14
δn	Asymmetric carrier density, located somewhere outside the QW	90
N	Number of random walk steps	19
N^+	Number of ionized donors	10
NiCr	nickel/chromium alloy	37
NMR	Nuclear magnetic resonance	27
n_{opt}	Density of optically generated electrons	16
N_{Ph}	Number of photons in a single laser pulse	16
n_s	Steady-state carrier density under the conditions of optical gating	11
ODMR	Optically detected magnetic resonance	17
p	Hole concentration	20
$\hat{\boldsymbol{p}}$	Electron momentum operator	12
P	Degree of spin polarization, $P = \frac{n_{e_\uparrow} - n_{e_\downarrow}}{n_{e_\uparrow} + n_{e_\downarrow}}$	14
$\bar{P}$	Mean laser power	16
$P_{532\ \mathrm{nm}}$	Laser power of the above-barrier illumination	93
PL	Photoluminescence	9
PLE	Photoluminescence excitation	45
PPC	Persistent photoconductivity	33
PSH	Persistent spin helix	22
$\boldsymbol{q}$	Phonon wave vector	8
$\tilde{q}$	Transferred wave vector	9
qubit	Quantum bit	2
QW	Quantum well	9
r	Focal radius of laser beam	16
$\vec{r}_i$	Position of the i-th nucleus	28
R_d	Distance of the ionized donors from the center of the 2DES	90
RSA	Resonant spin amplification	41
σ^+ / σ^-	Photon helicity	15
$\hat{\boldsymbol{\sigma}}$	Vector of Pauli spin matrices	12
σ_v / σ_v'	Mirror planes of the C_{2v} point group	17
$\boldsymbol{s}$	Total spin of an electron spin ensemble	16
$\hat{S}_\pm$	Ladder operator of electron spin, $\hat{S}_\pm = \hat{S}_x \pm i\hat{S}_y$	26
SDA	Spin dephasing anisotropy	21
SDT	Spin dephasing time	17

Abbreviation	Description	introduced on page
sFET	Spin field effect transistor	2
Si	Silicon	31
SIA	Structure inversion asymmetry	12
SO	Spin-orbit	8
SOF	Spin-orbit field	1
SOI	Spin-orbit interaction	1
ssd	Single-sided doped	7
$s_{x,y,z}$	x, y or z components of the spin ensemble	17
$s_{0,x,y,z}$	Initial value of the components $s_{x,y,z}$	17
SPSL	Short-period superlattice	33
Θ	Faraday rotation angle	39
Θ_D	Debye temperature	6
τ	Microscopic scattering time	9
τ_{BAP}	BAP spin relaxation time	20
$1/\tau_b$	Damping rate of coherent spin oscillations	26
$1/\tau_s$	Damping rate of long-lived tail of spin polarization	26
τ_p	Momentum scattering time	8
τ_{ee}	Electron-electron scattering time	8
τ_{PL}	Minority carrier lifetime	10
τ_{RSA}	Decay time of the amplitude $s(B)$ of the RSA peaks	102
Δt	Time interval	19
T_1	Spin-lattice relaxation time	18
T_2	Spin dephasing time	18
$\overline{T}$	Average spin dephasing time	23
$\overline{T_{B\|\|[110]}}$	Average spin dephasing time, $B\|\|[110]$	47
$\overline{T_{B\|\|[1\bar{1}0]}}$	Average spin dephasing time, $B\|\|[1\bar{1}0]$	47
T_δ	Temperature of the wafer substrate during growth of the SPSL doping layers	127
T_ϕ	In-plane spin dephasing time	61
T_e	Temperature of the electron system	9
T_L	Lattice temperature	9
T_{rep}	Laser repetition period, $T_{rep} = 12.5\,\mathrm{ns}$	42
TRDT	Time-resolved differential transmission	46
TRFR/TRKR	Time-resolved Faraday/Kerr rotation	39
TRPL	Time-resolved photoluminescence	45
$T_{xx,yy,zz}$	SDT for spins oriented along the x, y or z direction	17
$T_{[001],[1\bar{1}0],[110]}$	SDT for spins parallel to the $[001]$, $[1\bar{1}0]$, $[110]$ axis	22
$\Delta T_{[110]}$	Uncertainty of $T_{[110]}$	61
U_G	Applied gate voltage	10
$u_k(\vec{r}_i)$	Bloch function	28
Ψ	Wavefunction	12
$|\psi_k(\vec{r}_i)|^2$	Probability density of an electron at position $\vec{r}_i$	27
$\psi("\uparrow", \boldsymbol{k}, \boldsymbol{r})$	Electron Bloch state having mainly $|\uparrow\rangle$ character	18
$\boldsymbol{v}$	Semi-classical velocity of the electron	11
v_k	Fermi velocity of the electrons	21
$V(\lambda)$	Wavelength-dependent Verdet constant	70
$V(\boldsymbol{r})$	Spin-independent lattice potential	12
$V(\hat{z})$	Confinement potential in z direction	11
ω_c	Cyclotron frequency, $\omega_c = \frac{eB}{m_e^*}$	11
$\omega(\boldsymbol{q})$	Phonon frequency	8
$\tilde{\Omega}$	Modified Larmor frequency	23
$\Omega(\boldsymbol{k})$	Effective magnetic field, SO field	12
Ω_D, $\boldsymbol{\Omega_k}$	Dresselhaus-type SO field	12, 25
$\Omega_{D,\,2D,\,001}$	Dresselhaus field of a (001)-grown 2DES	13
$\boldsymbol{\Omega}_D^{(110)}(\boldsymbol{k})$	Dresselhaus field of a (110)-grown 2DES	13

Abbreviation	Description	introduced on page
Ω_{eff}	Modified Larmor frequency, $\Omega_{eff} = \sqrt{\omega_c^2 + \Omega_{k_F}^2}$	26
$\boldsymbol{\Omega}_L$	Larmor frequency, $\boldsymbol{\Omega}_L = \mu_B \hat{g} \cdot \boldsymbol{B}/\hbar$	16
$\Omega_{SIA,\,2D}$, Ω_R	Rashba-type SO field	13
x, y, z	coordinate axes, forming a right-handed triple	13
X	X valley in AlAs	34

Danksagung

Lebenslauf

Michael Griesbeck, geboren am 01.10.1982 in Kemnath.

September 1989 - Juni 2002	Schulzeit in Cham.
Juli 2002 - April 2003	Zivildienst.
Oktober 2003 - September 2008	Studium der Physik an der Universität Regensburg.
Oktober 2005	Vordiplom in Physik.
September 2008	Physik Diplom. Diplomarbeit unter Anleitung von Prof. Dr. Christian Schüller: "Experimente zur Spindynamik in Halbleitern".
Seit Oktober 2008	Vorbereitung der Dissertation.